Characterization of Passive Spectral Regrowth in Radio Frequency Systems

by
Joshua Michael Wetherington

A dissertation submitted to the Graduate Faculty of
North Carolina State University
in partial fulfillment of the
requirements for the Degree of
Doctor of Philosophy

Electrical Engineering

Raleigh, North Carolina

2013

APPROVED BY:

Dr. Randy Avent	Dr. Griff Bilbro
Dr. Mohammed Zikry	Dr. Michael B. Steer Chair of Advisory Committee

Report Documentation Page

Form Approved
OMB No. 0704-0188

1. REPORT DATE	2. REPORT TYPE	3. DATES COVERED
01 AUG 2013	**Final**	**1 Aug 2010 - 31 Dec 2016**

4. TITLE AND SUBTITLE
Characterization of Passive Spectral Regrowth in Radio Frequency Systems / PhD Dissertation

5a. CONTRACT NUMBER
N/A

5b. GRANT NUMBER
N00014-10-1-0958

5c. PROGRAM ELEMENT NUMBER
N/A

6. AUTHOR(S)
Joshua M. Wetherington Electrical & Computer Engineering North Carolina State University

5d. PROJECT NUMBER
N/A

5e. TASK NUMBER
N/A

5f. WORK UNIT NUMBER
N/A

7. PERFORMING ORGANIZATION NAME(S) AND ADDRESS(ES)
North Carolina State University Electrical & Computer Engineering 890 Oval Dr., 3114 Engineering Building II Raleigh, NC 27695

8. PERFORMING ORGANIZATION REPORT NUMBER
61

9. SPONSORING/MONITORING AGENCY NAME(S) AND ADDRESS(ES)
Office of Naval Research (ONR) 875 North Randolph Street - Suite 1425 Code 03R Arlington, VA 22203-1995

10. SPONSOR/MONITOR'S ACRONYM(S)
ONR

11. SPONSOR/MONITOR'S REPORT NUMBER(S)
N/A

12. DISTRIBUTION/AVAILABILITY STATEMENT
Approved for public release, distribution unlimited

13. SUPPLEMENTARY NOTES
N/A, The original document contains color images.

14. ABSTRACT

Passive spectral regrowth is the generation of nonlinear frequency content as a signal passes through a passive system. The nonlinearity may be a result of the intermodulation between individual signal components or signal components coupling to and mixing with energy in non-electromagnetic domains. Passive spectral regrowth is much weaker than regrowth in active devices due to the lack of gain, however characterization of the new spectral content is growing in importance as the sensitivity of radio-frequency (RF) receivers improves. Passive components at the end of an RF chain, including the antenna, can produce distortion that is difficult to remove using conventional filtering techniques. Alternatively, understanding of the nonlinear mixing may be exploited in RF sensing for unique characterization of remote or difficult-to-reach objects. To better understand passive spectral regrowth, an investigation is undertaken to experimentally and analytically characterize the nonlinear effects of spectral-regrowth-generating phenomena on an RF signal. Detection of low-level passive spectral regrowth close in frequency to a high-power stimulus signal requires extreme dynamic range measurement capability not available on commercial, o-the-shelf equipment. To enable these measurements, a high-dynamic-range nonlinear measurement system is built using analog cancellation. Automated analog cancellation with careful attention to signal path calibration and non-iterative phase calculation is key to achieving up to 140 dB of dynamic range in two-tone characterization with tones separated by at least 1 kHz. The primary nonlinear mechanism studied is acousto-electromagnetic interaction. Acoustoelectromagnetic scattering is conventionally analyzed as introducing a Doppler frequency shift only, but with increasingly sophisticated ability to analyze radar returns, it is necessary to strip away previously held assumptions and characterize other possibly detectable acoustic modulation processes including time-varying path loss, time-varying radar cross section, and amplitude modulation associated with special relativity. The fundamental physical mechanisms and assumptions of RF scattering by a vibrating object are explored for a simple vibrating plate, from which several modulation processes are abstracted and the fundamental limits of what can be sensed are derived. Acousto-electromagnetic analysis is repeated at a higher system level, in determining the modulation appearing on RF signals in an acoustically-stimulated antenna. As RF systems are further integrated, single aperture systems have become more common, thus increasing the importance of understanding passive spectral regrowth in these structures. The dynamic range limits of a single aperture system are explored, and acoustically-induced modulation is demonstrated in a log-periodic dipole array antenna.

15. SUBJECT TERMS

16. SECURITY CLASSIFICATION OF:			17. LIMITATION OF ABSTRACT	18. NUMBER OF PAGES	19a. NAME OF RESPONSIBLE PERSON
a. REPORT	b. ABSTRACT	c. THIS PAGE			
unclassified	**unclassified**	**unclassified**	**SAR**	**164**	

ABSTRACT

WETHERINGTON, JOSHUA MICHAEL. Characterization of Passive Spectral Regrowth in Radio Frequency Systems. (Under the direction of Dr. Michael B. Steer.)

Passive spectral regrowth is the generation of nonlinear frequency content as a signal passes through a passive system. The nonlinearity may be a result of the intermodulation between individual signal components or signal components coupling to and mixing with energy in non-electromagnetic domains. Passive spectral regrowth is much weaker than regrowth in active devices due to the lack of gain, however characterization of the new spectral content is growing in importance as the sensitivity of radio-frequency (RF) receivers improves. Passive components at the end of an RF chain, including the antenna, can produce distortion that is difficult to remove using conventional filtering techniques. Alternatively, understanding of the nonlinear mixing may be exploited in RF sensing for unique characterization of remote or difficult-to-reach objects. To better understand passive spectral regrowth, an investigation is undertaken to experimentally and analytically characterize the nonlinear effects of spectral-regrowth-generating phenomena on an RF signal. Detection of low-level passive spectral regrowth close in frequency to a high-power stimulus signal requires extreme dynamic range measurement capability not available on commercial, off-the-shelf equipment. To enable these measurements, a high-dynamic-range nonlinear measurement system is built using analog cancellation. Automated analog cancellation with careful attention to signal path calibration and non-iterative phase calculation is key to achieving up to 140 dB of dynamic range in two-tone characterization with tones separated by at least 1 kHz.

The primary nonlinear mechanism studied is acousto-electromagnetic interaction. Acousto-electromagnetic scattering is conventionally analyzed as introducing a Doppler frequency shift only, but with increasingly sophisticated ability to analyze radar returns, it is necessary to strip away previously held assumptions and characterize other possibly detectable acoustic modulation processes including time-varying path loss, time-varying radar cross section, and amplitude modulation associated with special relativity. The fundamental physical mechanisms and assumptions of RF scattering by a vibrating object are explored for a simple vibrating plate, from which several modulation processes are abstracted and the fundamental limits of what can be sensed are derived. Acousto-electromagnetic analysis is repeated at a higher system level, in determining the modulation appearing on RF signals in an acoustically-stimulated antenna. As RF systems are further integrated, single aperture systems have become more common, thus increasing the importance of understanding passive spectral regrowth in these structures. The dynamic range limits of a single aperture system are explored, and acoustically-induced modulation is demonstrated in a log-periodic dipole array antenna.

BIOGRAPHY

Joshua Michael Wetherington received the B.S. and M.S. degrees in Electrical Engineering from North Carolina State University, Raleigh, NC in 2009 and 2011, respectively. He has been working toward the Ph.D. in Electrical Engineering as a research assistant for the Electronics Research Laboratory at NC State University since 2010.

Mr. Wetherington's primary research interests include RF system design, RF measurement, and nonlinear RF effects. Prior to beginning his Ph.D research, he was with Sony Ericsson Mobile Communications, Inc., Morrisville, NC from 2007 to 2009, where he was an RF Hardware Co-op Engineer. In 2012, he interned as an Electrical Engineer at the Army Research Laboratory, Adelphi, MD. After graduation, Mr. Wetherington will join the Wireless Research Center of North Carolina, Wake Forest, NC.

ACKNOWLEDGEMENTS

I would like to thank my graduate advisor, Dr. Michael Steer, for providing me with this research opportunity at NC State and for guiding me through a maze of ideas, publications, and red ink. I would like to thank the members of my committee Dr. Randy Avent, Dr. Griff Bilbro, and Dr. Mohammed Zikry for their input and feedback on my research. I would like to thank the former RF and antenna engineers at Sony Ericsson that taught me more than I ever needed to know about cell phones and wireless hardware and inspiring me to pursue RF engineering as a career. I would also like to thank the hundreds of professors and engineers that I have consulted with and discussed careers, research, and engineering over the years. Giving advice is truly an engineer's favorite past-time.

I would like to thank my graduate student colleagues Spencer Johnson, Austin Pickles, Peter Gadfort, Dr. Chris Saunders, Dr. Glen Garner and others at NC State for their technical support and brainstorming. I would also like to thank my undergraduate assistants Matt Purvis, Ian Kilgore, and Rongjin Wang for being quick learners and producing mountains of raw research-enabling data.

Lastly, I would like to thank all my family and friends who have supported me through all my crazy ideas and encouraged me to explore and excel at anything I put my mind to.

TABLE OF CONTENTS

List of Tables . . . . . **vii**

List of Figures . . . . . **viii**

Chapter 1 Introduction **1**
1.1 Motivation 1
1.2 Overview 2
1.3 Original Contributions 4
1.3.1 High performance automated analog canceller 4
1.3.2 Compact analytical acousto-electromagnetic scattering theory 4
1.3.3 Sensitive vibration detection using analog cancellation 4
1.3.4 Characterization of acoustic modulation on single aperture systems 5
1.4 Dissertation Outline 5
1.5 Published Works 6
1.5.1 Journal Articles 6
1.5.2 Conference Articles 6
1.5.3 Technical Reports 6
1.6 Unpublished Works 6

Chapter 2 Literature and Concepts Review **8**
2.1 Introduction 8
2.2 Nonlinear Systems 9
2.2.1 Modeling 9
2.2.2 Series Approximation 10
2.2.3 Signal Modulation 12
2.2.4 Time-Frequency Analysis 17
2.3 Passive Spectral Regrowth 18
2.3.1 Material Nonlinearities 18
2.3.2 Acousto-Electromagnetic Effects 20
2.3.3 Filter Transient Effects 22
2.4 High-Dynamic-Range Nonlinear Measurement 22
2.4.1 Filtering 24
2.4.2 Feedforward Cancellation 26
2.4.3 Nonlinear Phase Measurement 28
2.5 Summary 28

Chapter 3 Robust Analog Canceller for High-Dynamic-Range Radio Frequency Measurement **30**
3.1 Introduction 30
3.2 Analog Canceller 32
3.2.1 Feedforward Cancellation Theory 32
3.2.2 Calibration 34
3.2.3 Analog Canceller Performance 38

3.2.4 Summary . . . 40
3.3 Cancellation Architecture for High Dynamic Range . . . 41
3.3.1 Noise and Interference Suppression . . . 42
3.3.2 Measurement and Calibration Accuracy . . . 43
3.4 Application to Two-Tone Non-linear Distortion Measurement . . . 44
3.4.1 System and Component Linearity . . . 45
3.4.2 Bandwidth Limitations . . . 46
3.5 Measurement . . . 47
3.5.1 Cancellation and Dynamic Range . . . 47
3.5.2 PIM in Laboratory Terminations . . . 51
3.6 Extension . . . 54
3.7 Summary . . . 55

Chapter 4 Radio Frequency Scattering by Vibrating Structures . . . 57
4.1 Introduction . . . 57
4.2 Vibration Modulation Analysis . . . 59
4.2.1 Doppler Phase Modulation . . . 60
4.2.2 Amplitude Modulation Due to Special Relativity . . . 64
4.2.3 Far-Field Path Loss Modulation . . . 67
4.2.4 Modulation of Radar Cross Section . . . 71
4.2.5 Extraordinary Geometry Effects . . . 74
4.2.6 Reflection Coefficient Modulation . . . 78
4.2.7 Combined Modulation Effects . . . 78
4.2.8 Comparison of Modulation Tones . . . 80
4.3 Vibration Detection . . . 81
4.3.1 Architecture . . . 82
4.3.2 Range Considerations . . . 83
4.4 Spectral Measurement . . . 85
4.5 Summmary . . . 89

Chapter 5 Passive Spectral Regrowth in Single Aperture Systems . . . 90
5.1 Introduction . . . 90
5.2 Single Aperture Dynamic Range . . . 92
5.3 Acoustic Modulation in Single Apertures . . . 95
5.3.1 Doppler Scattering . . . 95
5.3.2 RF Spectral Measurement . . . 97
5.3.3 Vibration Measurement . . . 100
5.4 Summary . . . 102

Chapter 6 Conclusion . . . 109
6.1 Summary of Research and Original Contributions . . . 109
6.2 Future Research . . . 110

References . . . 113

Appendices **122**
Appendix A Automated Analog Canceller System Documentation 123
A.1 Introduction 123
A.2 User Interface 123
A.3 Hardware 124
A.4 Canceller Algorithms 127
A.5 Sample Measurement Walkthrough 130
A.5.1 Setup 131
A.5.2 Reading the Output 133
Appendix B LabVIEW Analog Canceller VI Directory 135
B.1 Control Files 135
B.2 Support Files 136
B.3 Sweep Files 142
Appendix C MATLAB functions 144
C.1 Nonlinear Intermodulation 144
C.2 Projected Cancellation from Amplitude-to-Phase Error 145
C.3 Calculated Modulation Tone Power 147

LIST OF TABLES

Table 3.1 Cancellation statistics for a sweep of initial phase separation of the stimulus tone and the feedforward tone at 460 MHz. (Av. = average, Md. = median) 40

Table 4.1 Comparison of sideband tone power for various modulation types 80

Table 5.1 Primary theoretical transverse mechanical modes of individual antenna elements. (L – cm, f_V – Hz) 108

Table A.1 Hardware used in analog canceller on controller "TERROR" 126

LIST OF FIGURES

Figure 2.1 Input amplitude spectrum (left) and output amplitude spectrum (right) of a fifth-order nonlinear function, $f(x) = x^5$, with a single-tone sinusoidal input, $x = \cos(2\pi 10t)$. 11
Figure 2.2 Input amplitude spectrum (left) and output amplitude spectrum (right) of a fifth-order nonlinear function, $f(x) = \frac{1}{10}x^5$, with a two-tone sinusoidal input, $x = \cos(2\pi 10t) + \cos(2\pi 12t)$. 12
Figure 2.3 Typical modulation spectrum for low-level nonlinear interactions with an incident RF signal. 15
Figure 2.4 Displacement of a moving surface relative to a monostatic radar antenna. 21
Figure 2.5 Dynamic range problem of measuring small signals in the presence of large signals. 23
Figure 2.6 Ideal extension of dynamic range using filtering. 24
Figure 2.7 Undesirable attenuation of small signals within filter bandwidth. 25
Figure 2.8 Ideal extension of dynamic range using feedforward cancellation. 27
Figure 2.9 Basic block diagram using feedfoward analog cancellation for nonlinear measurement. 27

Figure 3.1 Basic block diagram for signal cancellation employing a feedforward path with amplitude and phase shifting to generate an anti-phase version of the test signal. The DUT could also be replaced with a wireless channel and either a single or separate antennas for transmission and reception. . 32
Figure 3.2 Maximum theoretical analog cancellation, $C_{A,\mathrm{dB}}$, as a result of projected phase shift error caused by amplitude mismatch during the reference measurement. Phase separation is the phase difference of the signal to be cancelled at (C) and the cancelling signal (B) as shown in Fig. 3.1. It is assumed that the unshifted cancellation signal has a larger amplitude than the original signal. 35
Figure 3.3 Measured amplitude error versus phase setting of the cancellation signal: (a) using baseline or fixed-phase calibration; and (b) using in-line calibration. 36
Figure 3.4 Flow chart detailing steps during signal cancellation procedure. 37
Figure 3.5 Calculated maximum analog cancellation using the measured amplitude mismatch in Fig. 3.3: (a) using baseline calibration; and (b) using in-line calibration. 38
Figure 3.6 Measured analog cancellation versus initial phase separation: (a) no target (single iteration); (b) forced two iterations; and (c) with cancellation target C_T of 40 dB. 39
Figure 3.7 Block diagram of a single-channel analog cancellation system, in a configuration for testing distortion generated in the DUT. 41
Figure 3.8 Dual-channel high-dynamic range cancellation system for passive intermodulation distortion (PIM) measurement with both transmission and reflection configurations. 45

Figure 3.9 Relationships between several measurement quantities assuming sufficient analog cancellation (C_A) (logarithmic scale). The DUT input power is reduced by the insertion loss (IL) in a transmission measurement and by the return loss (RL) in a reflection measurement. With a wireless channel, this would include appropriate portions of the link loss. 48
Figure 3.10 Worst-case third-order intermodulation dynamic range (DR_{IM3}) achieved in two-port transmission configuration over frequency separation during automated two-tone testing at 26.5 dBm at a center frequency of 460 MHz. 49
Figure 3.11 Third-order intermodulation dynamic range (DR_{IM3}) achieved for the lower IM3 product in two-port transmission configuration over frequency separation during automated two-tone testing at 26.5 dBm at a center frequency of 460 MHz. 50
Figure 3.12 Worst-case third-order intermodulation dynamic range achieved in one-port reflection measurement over frequency separation during automated two-tone testing at 26 dBm at a center frequency of 460 MHz. 51
Figure 3.13 Measured third-order passive intermodulation distortion (lower IM3) of common laboratory 2 W N-type terminations using a two-tone test at 460 MHz. Measurement taken with 26 dBm input power for each tone. . . 52
Figure 3.14 Measured third-order passive intermodulation distortion (upper IM3) of common laboratory 2 W N-type terminations using a two-tone test at 460 MHz. Measurement taken with 26 dBm input power for each tone. . . 53
Figure 3.15 Measured third-order passive intermodulation distortion (lower IM3) of common laboratory high-power, finned N-type terminations using a two-tone test at 460 MHz. Measurement taken with 26 dBm input power for each tone. 54
Figure 3.16 Measured third-order passive intermodulation distortion (upper IM3) of common laboratory high-power, finned N-type terminations using a two-tone test at 460 MHz. Measurement taken with 26 dBm input power for each tone. 55

Figure 4.1 General modulation spectrum of an RF signal scattered from a vibrating object. 60
Figure 4.2 Displacement of a moving surface relative to a monostatic radar antenna. 62
Figure 4.3 A plate vibrating rotationally around an axis in a rocking motion. 72
Figure 4.4 Expected power relative to the RF carrier tone of the first eight normalized modulation sideband tones for a linearly vibrating plate using $\beta = 0.03\lambda$, $R_0 = 3\lambda$, $\lambda = \frac{1}{3}$ m, and $f_V = 1$ kHz 81
Figure 4.5 Expected relative power of the first four normalized modulation tone amplitudes on a rocking plate with various rotational amplitudes, $a = 0.9\lambda$ and $\lambda = \frac{1}{3}$ m. The first eight predicted Doppler PM tones from a linearly vibrating plate ($\beta = 0.03\lambda$) are included for reference. 82
Figure 4.6 Basic vibration detector architecture. 83
Figure 4.7 Physical configuration of bistatic radar vibration detector inside of an anechoic chamber. 84

Figure 4.8 Measured first-order modulation tone power for a vibrating flat rectangular plate versus the vibration displacement amplitude as measured by a laser Doppler vibrometer. The theoretical curve is from (4.85) and normalized. 86
Figure 4.9 Measured first-order modulation tone power for a vibrating flat rectangular plate buried in sand. The independent axis represents the LDV-measured displacement for the same actuator drive power with the freely hanging plate. The theoretical curve (based on (4.85)) is normalized to match the measured RF amplitude. 87
Figure 4.10 Measured RF power spectrum offset from 900 MHz for a rocking flat rectangular aluminum plate with $\varphi \approx 2^{\circ}$. Four independent trials are shown for the plate both while stationary and in motion. 88

Figure 5.1 Narrowband power spectrum of the log-periodic dipole array antenna centered at 500 MHz. 93
Figure 5.2 Wideband power spectrum of the log-periodic dipole array antenna centered at 500 MHz. 94
Figure 5.3 Narrowband power spectrum of the non-resonant antenna centered at 500 MHz. 95
Figure 5.4 Wideband power spectrum of the non-resonant antenna centered at 500 MHz. 96
Figure 5.5 Narrowband power spectrum of the low-PIM termination (PE6152A) centered at 500 MHz. 97
Figure 5.6 Wideband power spectrum of the low-PIM termination (PE6152A) centered at 500 MHz. 98
Figure 5.7 Dynamic range of measurement system using the low-PIM termination (a), the log-periodic dipole antenna (b), and the non-resonant antenna (c). Measurement density above 50 kHz is only 3 points per decade due to the increase in required measurement bandwidth. 99
Figure 5.8 Top view of experimental set-up in anechoic chamber, including antenna, acoustic source, and laser doppler vibrometer (LDV). 100
Figure 5.9 Side view of log-periodic dipole array antenna and cut-away showing an individual antenna element. 101
Figure 5.10 Narrowband RF spectrum with acoustic intermodulation. The RF carrier is 500 MHz at 27 dBm, with a 1 kHz acoustic tone at 100 mV drive voltage. 102
Figure 5.11 Wideband RF spectrum with acoustic white noise and without an acoustic signal. The RF carrier is 500 MHz at 27 dBm. 103
Figure 5.12 Intermodulation power versus RF drive power. The RF carrier is 500 MHz, with a 1 kHz acoustic tone at 100 mV drive voltage producing an SPL of 80 dB. 104
Figure 5.13 Intermodulation power versus acoustic drive power. The RF carrier is 500 MHz at 27 dBm, with a 1 kHz acoustic tone. Acoustic drive power is the power driving the input of the studio monitor and is directly proportional to sound pressure level (SPL). 104

Figure 5.14 Intermodulation power versus RF frequency for single tone acoustic excitation at frequency, f_{AC}. The RF tone power is 27 dBm and the drive of the acoustic tones at 100 mV producing an SPL of 80 dB. 105
Figure 5.15 Intermodulation power versus acoustic frequency for multiple RF frequencies. The RF tone power is at 27 dBm, with the acoustic tone driven at 100 mV drive voltage producing an SPL of 80 dB. 106
Figure 5.16 Averaged surface velocity response over all elements (a), with 500 MHz RF intermodulation response (b). 107

Figure A.1 Example front panel user interface. 124
Figure A.2 Hardware architecture for single-channel cancellation. 125
Figure A.3 Hardware architecture for dual-channel cancellation. 125
Figure A.4 Phase ambiguity from application of the phase-shift equation (A.1). . . . 128
Figure A.5 Procedural flow for a non-iterative feedforward cancellation measurement. 128
Figure A.6 Procedural flow for an efficient, semi-iterative feedforward cancellation measurement. 130
Figure A.7 Front panel user interface for "TwoTone_Cancel_Simple.vi". 131
Figure A.8 Measurement with poor cancellation depth. 134

Chapter 1

Introduction

1.1 Motivation

Modern radio frequency (RF) systems suffer from a multitude of noise problems as more systems are integrated into a single structure. A major source of this noise is electrical interference from co-located or common aperture communications and sensing systems. Unintentional signal interaction between various systems generates additional spectral content potentially within the receiver bandwidth of multiple systems. This receiver interference can be interpreted as spreading the bandwidth of the offending signal and is commonly known as spectral regrowth.

Extensive research and development has gone into understanding spectral regrowth inherent in active nonlinear devices, however passive spectral regrowth is often difficult to trace to an exact nonlinear phenomenon. As more bandwidth and flexibility is demanded from RF systems, the filtering needed to remove nonlinear distortion has been unable to provide adequate performance or is impractical, as in the case of passive spectral regrowth generated in antennas. The difficulty in removing this interference underscores the importance of understanding the sources of spectral regrowth in order to prevent distortion generation. Interference in receivers operating near the thermal noise floor of the communication channel can be driven by co-located high power transmitters. Analysis and measurement of these effects require a large power dynamic range exceeding 180 dB. This is a difficult figure to reach both physically and numerically, further complicating characterization of passive spectral regrowth.

In remote sensing, enhanced characterization of passive spectral regrowth may lead to new physical sensing modalities, extending current sensing methods or inspiring new techniques. As receiver performance improves, detection of these modalities could provide unique characterization of unknown objects.

1.2 Overview

Spectral regrowth has traditionally been used to describe the increase in adjacent channel power due to finite bandwidth signals passing through a nonlinear power amplifier [1–4]. Here, spectral regrowth is more broadly defined as an increase in power at any frequency not included in the system input. This is inherently a nonlinear operation, as the output cannot be described as a scaled version of the input. In particular, passive spectral regrowth refers to nonlinear spectral generation in devices and components without gain. Physical devices with gain, such as amplifiers, are inherently nonlinear and can only be treated as linear elements through a small signal approximation. Passive components are typically very weakly nonlinear, producing detectable spectral regrowth only in cases of very high power signals or through multi-physics cross-domain coupling. In new RF systems, with a multitude of co-located radios operating across a wide range of frequency bands, the source of generated broadband interference may be unknown. Systems designers are interested in understanding spectral regrowth both to improve radio performance, and to exploit them for remote sensing of unique signatures.

A major source of passive spectral regrowth is passive intermodulation (PIM). PIM is primarily known as an interference-generating phenomenom in RF circuits. PIM has been attributed to both point-source junction nonlinearities [5–12] and to distributed nonlinearities [13–16]. Discrete PIM results from the nonlinear interaction of dissimilar materials, or materials with a rough contacting surface. This produces a large amount of distortion, but can generally be improved through better manufacturing and maintenance processes. Distributed PIM is generated by nominally homogeneous, nonlinear materials. Typically, detectable distributed nonlinear effects arise due to coupled multi-physics interactions such as ferromagnetism [17, 18] and electro-thermal coupling [15, 16].

Other sources of passive spectral regrowth do not easily fit the traditional definition of PIM. These alternative mechanisms are typically studied for their applications in nonlinear radar and standoff detection. Remote RF probing of a target object can generate substantial loss in the reflected signal power due to omni-directional signal spreading, but exploitation of the nonlinear spectral content allows for frequency discrimination of the return signature and improved detection dynamic range. The reflected nonlinear signal may be generated by re-radiated PIM-like effects such as nonlinear junctions or materials [19–23], but may also be generated in perfectly linear circuits, where time-domain effects such as energy storage in filters can introduce transients into a reflected signal [24–26]. Using bandlimited Fourier analysis, transients can generate complicated spectral signatures, but are intermittent, making physical description difficult.

In addition to electrical nonlinearities, motion of a reflecting target is also known to generate spectral regrowth. Since common motion is much slower than RF propagation, a moving reflec-

tor is often modeled as introducing a frequency or phase shift on the scattered signal, according to Doppler theory. Radar systems used for vibration and motion detection operate primarily in the time-domain, mostly ignoring spectral interpretations [27–30]. Thorough analysis of the scattering requires application of special relativity [31–39]. Secondary nonlinear effects such as dielectric permittivity fluctuation [40] or microphonics [41, 42] may also contribute to spectral regrowth in vibrating structures.

Each of these mechanisms for passive spectral regrowth can be treated as a type of modulation on the RF signal passing through or incident on the nonlinear device or structure. From a fundamental perspective, modulation must increase the bandwidth of a signal, as information is being added to the carrier. Demodulating the enhanced signal allows for extraction of the added information and therefore characterization of the nonlinear process. This characterization relies on appropriate demodulation, otherwise the extracted information is meaningless. In the absence of knowing the exact physical mechanism, direct frequency domain measurements of the nonlinear effects are necessary. Often, only knowing the amplitude and phase at a single point are not enough, so both theory and detection must be developed further to determine unique signatures for identification of the different sources of passive spectral regrowth.

Detection of passive spectral regrowth or, more broadly, detection of small signals in the presence of large signals is a long-standing and difficult problem. Typically, the large signal is a stimulus to drive the nonlinear system and generate the small signal, or passive spectral regrowth. Sensing and measurement equipment have a limited dynamic range for detecting power, generally set by digitization of the input signal. To improve dynamic range, the large signal must be removed prior to measurement. Traditionally, filters are used to remove the large signals [43]. However, finite filter skirts limit how close in frequency the large and small signals can be without removing the small signal as well. For sufficiently separated signals, filters can provide the highest dynamic range currently possible [44]. Alternatively, feed-forward cancellation can be used to remove the large signal. This technique has been widely used in feedforward linearization [45–47], and more recently for nonlinear distortion measurement [48–52]. These methods are primarily limited to power measurement, however phase measurement has been enabled using non-linear vector network analyzers [53–55] and phase cancellation [56].

The focus of this work is on developing a theoretical and experimental framework for exploring passive spectral regrowth. This framework is established in application to passive spectral regrowth caused by coupling of vibration and electromagnetics (EM) in systems. Analysis of the physics of acousto-EM coupling is extended through study and elimination of common approximations, which may no longer be valid at the low signal levels desired. Stripping away these approximations exposes the phenomena involved in passive spectral regrowth, but also complicates numerical and simulation analysis. Thus, engineering equations and interpretation are analytically derived from a systems perspective that can be used to discriminate nonlin-

ear sources. An experimental, high-dynamic range nonlinear measurement system is built using feedforward analog cancellation to observe passive spectral regrowth and verify theoretical findings. Performance of the system exceeds contemporary systems, and the ultimate performance limitations are established through detailed analysis of the hardware and software architecture.

1.3 Original Contributions

A number of original research initiatives were undertaken and are described in this dissertation. These contributions to the field of RF and microwave engineering are summarized below.

1.3.1 High performance automated analog canceller

A significant obstacle to high dynamic range measurement is the necessity of measuring very small signals in the presence of high power stimulus signals. With limited dynamic range at the receiver, the performance of the detector is dependent on the ability to remove the large signals masking the desired small signals. At very narrow bandwidths of hertz to thousands of hertz, filters cannot be constructed to remove the high power signal masking the detection of the signal of interest. Analog cancellation is a strong alternative, and a robust automated canceller system has been developed. The canceller is adapted from previous systems to take advantage of careful attention to signal level calibration, architectural refinements, and an intelligent cancellation algorithm to achieve up to 70 dB of cancellation.

1.3.2 Compact analytical acousto-electromagnetic scattering theory

RF scattering from vibrating structures is traditionally based on the quasi-static Doppler effect. As receiver performance improves, many of the engineering approximations and assumptions are no longer valid, as previously insignificant errors are not on the same order as receiver signal levels. Vibratory scattering is re-examined by removing approximations and analyzing the core physical principles. Simple, intuitive models are determined for the scattering and solutions are interpreted as modulation on a scattered wave, a convenient model for RF analysis and measurement.

1.3.3 Sensitive vibration detection using analog cancellation

The enhanced analog canceller is combined with ground-penetrating radar to achieve extremely sensitive vibration detection, including vibrating buried targets. The detected spectral regrowth on the reflected RF signal is interpreted as modulation, allowing for insight on the generating structure. Combining system analysis from the high dynamic range measurement system and vibratory scattering leads to fundamental limits on detection capability.

1.3.4 Characterization of acoustic modulation on single aperture systems

As multi-function radios and systems converge into a single structure, there is increasing demand for these systems to use a common aperture, i.e., a single antenna. The sources of passive spectral regrowth observed on these antennas is often unknown and difficult to trace. Passive spectral regrowth from acousto-electromagnetic interaction of a broadband antenna is observed and fully characterized, and the results are interpreted to provide insight into acousto-electromagnetic coupling.

1.4 Dissertation Outline

Chapter 2 of this dissertation presents a literature review of nonlinear systems analysis and modeling and detection of passive spectral regrowth.

Chapter 3 discusses feedforward analog cancellation and its implementation as a high dynamic range broadband measurement system. The hardware and software architecture required for extending high performance cancellation beyond previous results is presented, including careful attention to signal level calibration, architectural refinements, and an intelligent cancellation algorithm. The canceller-based measurement system is built, and the effective dynamic range is both measured and demonstrated through detection of low-level electro-thermal passive intermodulation in RF terminations. The performance limits of the measurement system are presented, as well as the connections to limitations of the canceller and system architecture.

Chapter 4 analyzes the generation of passive spectral regrowth in RF scattering from vibrating structures. Characterization of potentially detectable spectral content, interpreted as acoustic modulation of the RF signal, is undertaken starting with first-principles physics, and analyzing and eliminating approximations and assumptions with an error of similar magnitude to the proposed low-level signals. Through this investigation, simple, engineering expressions are derived and compared for their relative importance to detectable passive spectral regrowth. A prototype vibration detection radar is developed using analog cancellation and preliminary measurements are taken to demonstrate improved sensitivity and to verify derived acoustic modulation theory.

Chapter 5 explores the effects of passive spectral regrowth on a single, isolated aperture. The canceller-based measurement system is re-configured for single-channel reflection measurements to probe the antenna feed for passive spectral regrowth, and the dynamic range and limitations of the measurement system are discussed. Significant spectral content is observed on a broadband log-periodic dipole array antenna from induced acoustic modulation and measurements are correlated with the active acoustic stimulus.

Chapter 6 concludes with a summary of the presented work and its implications for future

research.

1.5 Published Works

1.5.1 Journal Articles

J. M. Wetherington and M. B. Steer, "Robust analog canceller for high-dynamic range radio frequency measurement," *IEEE Trans. Microw. Theory and Tech.*, vol. 60, no. 6, pp. 1709–1719, Jun. 2012.

J. M. Wetherington and M. B. Steer, "Standoff acoustic modulation of radio frequency signals in a log-periodic dipole array antenna," *IEEE Antennas and Wireless Propag. Lett.*, vol. 11, pp. 885–888, 2012.

1.5.2 Conference Articles

J. M. Wetherington and M. B. Steer, "Characterization of the dynamic range of a single aperture communications system," *2012 Workshop on Integrated Nonlinear Microwave and Millimetre-Wave Circuits (INMMIC)*, Sep. 2012, pp. 1–3.

M. B. Steer, J. R. Wilkerson, N. M. Kriplani, and J. M. Wetherington, "Why it is so hard to find small radio frequency signals in the presence of large signals," *2012 Workshop on Integrated Nonlinear Microwave and Millimetre-Wave Circuits (INMMIC)*, Sep. 2012, pp. 1–3.

1.5.3 Technical Reports

J. M. Wetherington and G. J. Mazzaro, "High dynamic range nonlinear measurement using analog cancellation," Army Research Laboratory, Adelphi, MD, Rep. ARL-TR-6234, Oct. 2012.

1.6 Unpublished Works

J. M. Wetherington and M. B. Steer, "Radio frequency scattering by vibrating structures," *submitted to IEEE Sensors J.*.

J. M. Wetherington and M. B. Steer, "Sensitive vibration detection using ground-penetrating radar," *submitted to IEEE Microw. Wireless Compon. Lett.*.

M. B. Steer, J. R. Wilkerson, and J. M. Wetherington, "Investigation of Close-In Passive Intermodulation Distortion on Antennas", *2013 IEEE Antennas and Propagation Society International Symposium (APS/URSI)*, Jul. 2013.

Chapter 2

Literature and Concepts Review

2.1 Introduction

Linear systems analysis is an extremely useful and powerful tool for engineering design and development. Ideal linear systems operate with predictable behavior that can be abstracted and simplified for quick calculation and intuitive understanding. Real systems are never linear in the ideal sense, however typically the error associated with the linear assumption is well within the operating tolerance, i.e., below the noise floor, of the system. As RF receiver performance improves, this approximation is no longer valid. Characterization and modeling of spectral regrowth is needed to better understand the nonlinear effects on a radio frequency (RF) system.

Nonlinear generation has been observed and studied in electric circuits since at least the 1920s [57]. Early on, it was understood that approximations were necessary to develop engineering intuition from typically intractable nonlinear differential equations. This practice continues to the present, with a large number of models of varying accuracy and simplicity. Design of inherently nonlinear devices, such as amplifiers and mixers, rely heavily on techniques that ameliorate the high levels of existing distortion, such as filtering and predistortion. Passive spectral regrowth that occurs in the front end of radios and in signals reflected from nonlinear targets occurs at much lower levels. As the physical mechanisms of passive nonlinear generation are poorly understood, the weak signature makes it more troublesome to both find the physical source of distortion and predict behavior. This puts greater emphasis on physical-based modeling and understanding of passive spectral regrowth, as well as improving existing measurement and detection methods.

2.2 Nonlinear Systems

A linear system, by definition is one that observes both the additive and homogeneous properties of superposition [58]. That is, a system H is linear for input signals $s_1(t)$ and $s_2(t)$ and scalars α and β if and only if

$$H[\alpha s_1(t) + \beta s_2(t)] = \alpha H[s_1(t)] + \beta H[s_2(t)]. \tag{2.1}$$

Linear systems are often assumed to be operating in steady state conditions, a combination referred to as linear time-invariant (LTI). Analysis of LTI systems is very powerful, in that it allows for direct prediction of the output of the system based on any combination of inputs. This lends itself well to Fourier analysis, the decomposition of a signal into a orthogonal set of sinusoidal components. These sinusoids represent the frequency spectrum of the signal. As the output of an LTI system is a superposition of its inputs, any frequencies not appearing in the Fourier series decomposition of the input signal will not appear at the output. This greatly simplifies system analysis, so that the system transfer function is uniquely identified using only amplitude and phase for a given frequency component. Nonlinear systems do not obey superposition, and therefore frequencies may appear in the output signal that were not present in the input. In remaining consistent with common usage, a nonlinear system is defined here as non-LTI, as opposed to strictly failing linearity conditions.

2.2.1 Modeling

Modeling of nonlinear systems is typically classified as either behavioral or physical [59]. These classifications are not mutually exclusive, however the extent to which each type of model is used can have implications for how nonlinear processes are interpreted and handled in a designed system.

Physical models are based on known physical mechanisms, derived independently of the phenomena the models are designed to predict. Physically-linked parameters allow for greater intuition and flexibility in design, as system outputs can be better predicted over a wide range of inputs. Use of physical models implies ideal isolation and decoupling from mechanisms not described in the model, thus physical models are most accurate under highly-controlled laboratory conditions. In less rigorous, commercially-developed systems, it is impossible to completely decouple the physical process under study from all other interactions. Mathematically, nonlinear system models are complex and difficult to evaluate, so simplifying the interaction between processes is necessary to maintain tractability in analysis. This interaction occurs at very low levels and can be approximated as insignificant in many systems, however often this low-level coupling is the source of passive spectral regrowth. Even for numerical simulation of the full

physics, passive spectral regrowth may be undetectable due to discretization error in simulating the differential equations. To account for the discrepancy with observed passive spectral regrowth, physical models may be extended through behavioral modeling.

Behavioral models are built by correlating the measured response of the system directly to a given input, a statistical approach independent of the physical mechanisms involved. By abstracting unknown physical parameters and locally limiting the approximation, behavioral modeling is the most accurate and efficient approach for characterizing a specific system under specified circumstances, ideal for low-cost, quick design. However, behavioral models cannot provide intuitive feedback to design improvement and are not easily transferable. Instead, many RF engineers will adapt a hybrid model, starting with known physical models and adding behavioral "correction" factors.

2.2.2 Series Approximation

Nonlinear systems, whether using physical or behavioral models, rely on approximations for tractability and numerical efficiency. For all but the simplest systems and inputs, constituent differential equations typically have no analytic solution. The most common approach to evaluating these systems is to use a power series representation of the nonlinear function, $f(x)$, that is

$$f(x) = \sum_{n=0}^{\infty} a_n x^n = a_0 + a_1 x + a_2 x^2 + a_3 x^3 + \ldots, \tag{2.2}$$

where a_n are the Taylor series coefficients of the function centered at zero [60], and are implicitly assumed to be constants. The a coefficients may be derived analytically from physical models, or may represent a best-fit approximation for behavioral models. Approximation for evaluation of the infinite series is made for small-signal inputs, i.e., $x \ll 1$, by eliminating all terms higher than a given order. The highest order term not evaluated in the summation is an approximation of the error for this approach.

The power series approximation provides insight into the generation of nonlinear spectral content. In (2.2), the first two terms, a_0 and $a_1 x$, produce constant and linear outputs, representatively. A linear system can always be represented as a combination of these two terms. The nonlinear terms, i.e., $n \geq 2$, represent self-modulation of the input signal. Physically, the self-modulation can be interpreted as an input-dependent system response, such as gain compression in an amplifier. For a discrete-tone, continuous-wave (CW) sinusoidal input, this self-modulation generates harmonic tones at integer multiples of the input frequency, as demonstrated in Fig. 2.1 for $f(x) = x^5$, with $x = \cos(2\pi 10t)$. Even-order nonlinear terms will produce DC tones and even-multiple harmonics up to the order of the term, and odd-order nonlinear terms will produce fundamental tones and odd-multiple harmonics up to the order of the term.

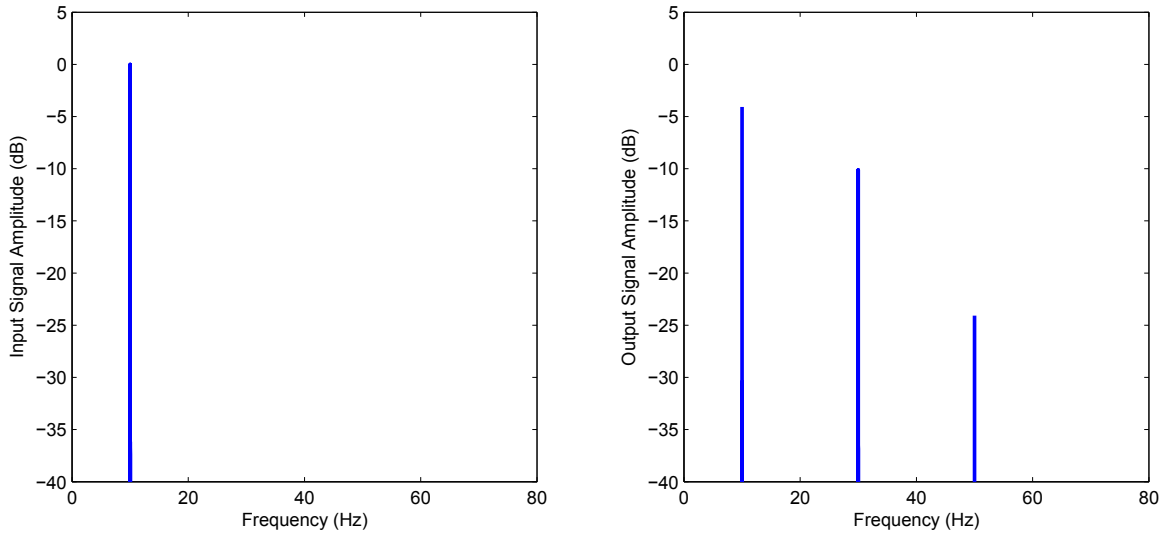

Figure 2.1: Input amplitude spectrum (left) and output amplitude spectrum (right) of a fifth-order nonlinear function, $f(x) = x^5$, with a single-tone sinusoidal input, $x = \cos(2\pi 10t)$.

In communications, harmonic distortion is easily mitigated through filtering due to the wide separation between the input tone and lowest-order distortion tone.

Single-frequency CW signals are used in certain types of radar systems [61], but, in general, are not useful for practical RF applications. Instead, real finite-bandwidth signals are modeled as the combination of many individual frequency components, as indicated by Fourier decomposition [62–64]. Through the self-modulation process demonstrated by the single-tone input, mixing will occur between the individual tones, also known as intermodulation. The simplest form of intermodulation occurs with a two-tone input, as demonstrated in Fig. 2.2 for $f(x) = \frac{1}{10}x^5$, with $x = \cos(2\pi 10t) + \cos(2\pi 12t)$. The even- and odd-order behavior is similar to the single tone scenario, with the exception of added intermodulation tones in close proximity to the fundamental and harmonic tones. Odd-order nonlinearities are of the greatest interest, due to generation of intermodulation tones around the input fundamental frequencies. In a communications system, these intermodulation tones will appear either in-band with the desired signal, or as interference in adjacent channels. The close spacing, based on the separation of the input tones, prohibits the use of filtering to discriminate the nonlinear tones from the desired fundamental tones.

Two-tone characterization is typically used as a metric for device nonlinearity, particularly the amplitude of the third-order intermodulation products (IM3). This metric is beginning to lose favor as the two-tone power series model is a poor representation of modern, digitally-modulated signals [2, 64–66]. Accurate simulation of spectral regrowth, predominantly in RF

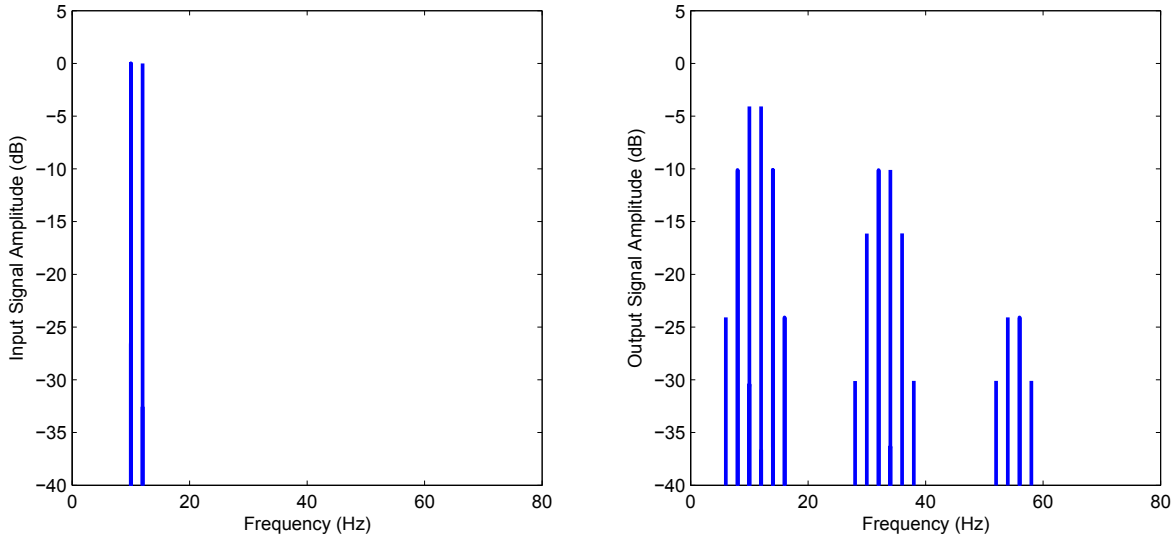

Figure 2.2: Input amplitude spectrum (left) and output amplitude spectrum (right) of a fifth-order nonlinear function, $f(x) = \frac{1}{10}x^5$, with a two-tone sinusoidal input, $x = \cos(2\pi 10t) + \cos(2\pi 12t)$.

amplifiers, requires the use of Volterra analysis [63, 67–69]. The Volterra series extends the standard nonlinear power series expansion to include memory effects. Volterra methods require greatly increased complexity in return for better accuracy, and are primarily limited to statistical, behavioral analysis. A simpler, multi-slice behavioral model of nonlinearity has also been demonstrated which is capable of capturing memory effects and is amenable to direct measurement [70, 71].

2.2.3 Signal Modulation

Power series expansion is a useful tool for modeling nonlinear processes, but it cannot as easily capture spectrum regrowth in linear, periodic time-varying systems. The simplest of these linear, time-varying systems is an ideal mixer.

In a superheterodyne or direct conversion radio, the received RF signal must be down-converted to baseband frequencies near DC to accommodate quantization and detection by digital circuitry. The down-conversion is performed by a mixer, which uses the multiplication properties of sinusoids to produce an output that is frequency-shifted from the input. While spectral content is generated that was not present in the original signal, an ideal mixer is canonically a linear element. This can be shown using (2.1), defining the system function for

an ideal multiplying mixer as

$$H_m[y] = y\cos(\omega_m t) \tag{2.3}$$

where ω_m is the frequency of the mixing signal. To test for superposition, the input, y, is assumed to be a combination of complex signals,

$$y = \alpha s_1(t) + \beta s_2(t). \tag{2.4}$$

Substituting this input into (2.3) produces

$$H_m[\alpha s_1(t) + \beta s_2(t)] = [\alpha s_1(t) + \beta s_2(t)]\cos(\omega_m t) \tag{2.5}$$

$$H_m[\alpha s_1(t) + \beta s_2(t)] = \alpha s_1(t)\cos(\omega_m t) + \beta s_2(t)\cos(\omega_m t) \tag{2.6}$$

$$H_m[\alpha s_1(t) + \beta s_2(t)] = \alpha H_m[s_1(t)] + \beta H_m[s_2(t)]. \tag{2.7}$$

The last statement is the definition of superposition, and therefore $H_m[y]$ is a strictly linear function. However, since the ideal mixer is functionally dependent on time, it fails LTI criterion, and thus can be classified as a nonlinear device using the broader spectral definition. Ideal mixers cannot be realized at RF frequencies, so in practice mixers are based on nonlinear devices and designed to produce an appropriate spectrum [61].

For the ideal mixer, a power series expansion does not produce an efficient interpretation of the spectral output. Instead, the system may be treated as introducing modulation on the input signal. Signal modulation represents a stronger analytical model for spectral regrowth based on the interaction of time-varying phenomena without a strong bi-directional coupling. In the ideal mixer, the mixing sinusoid has no input dependence, thus it is linear.

Signal modulation can be generally classified as amplitude modulation (AM), frequency modulation (FM), or phase modulation (PM). These represent variations induced by an external source on each of the three fundamental components of a sinusoidal phasor. Mathematically, FM and PM are very similar processes, as frequency is the time-derivative of the angle of a sinusoidal phasor. There are physical differences in the efficient detection of either FM or PM, but in signal analysis this difference lies in interpreting the modulation signal as itself or as the derivative of itself. For sinusoidal modulation signals, common for physical processes such as vibration, this difference results only in a constant as the derivative of a sinusoid remains a sinusoid. As a result, a modulated sinusoid of frequency ω may be represented by the general form

$$s(t) = A(t)\cos\left[\omega t + \phi(t)\right], \tag{2.8}$$

where $A(t)$ and $\phi(t)$ represent amplitude and phase modulation, respectively. These modulation

terms can be represented as

$$A(t) = A_0 \left[1 + m_A x_A(t)\right] \tag{2.9}$$

$$\phi(t) = \phi_0 + m_\phi x_\phi(t), \tag{2.10}$$

where A_0 and ϕ_0 are constant scalars that do not contribute to modulation and m_A and m_ϕ are the modulation indexes of AM and PM, respectively, for the modulation signals $x_A(t)$ and $x_\phi(t)$. Using this terminology, the effects of AM and PM can be mathematically separated and analyzed independently for signatures that can be used to discriminate the two processes.

The simplest case of amplitude modulation is the ideal mixer considered above. For the ideal mixer, the modulation term is $A(t) = \cos(\omega_m t)$ and directly modulates the amplitude of the input signal y. For a sinusoidal input, $y = \cos(\omega_{\mathrm{RF}} t)$, the amplitude-modulated signal is

$$s_A(t) = A(t)\cos(\omega_{\mathrm{RF}} t) \tag{2.11}$$

$$s_A(t) = \cos(\omega_m t)\cos(\omega_{\mathrm{RF}} t) \tag{2.12}$$

$$s_A(t) = \tfrac{1}{2}\cos[(\omega_m + \omega_{\mathrm{RF}})t] + \tfrac{1}{2}\cos[(\omega_m - \omega_{\mathrm{RF}})t], \tag{2.13}$$

producing two modulation tones at sum and difference frequencies, and suppressing the input tone. This is known as double-sideband suppressed carrier AM (DSB-SC AM) [58]. Using the general AM representation with the same input gives an amplitude-modulated signal

$$s_A(t) = A_0 \left[1 + m_A x_A(t)\right]\cos(\omega_{\mathrm{RF}} t) \tag{2.14}$$

$$s_A(t) = A_0 \cos(\omega_{\mathrm{RF}} t) + m_A x_A(t)\cos(\omega_{\mathrm{RF}} t). \tag{2.15}$$

The modulation signal $x_A(t)$ may be represented by a Fourier series, so that

$$x_A(t) = \sum_{n=1}^{\infty} a_n \cos(n\omega_m t). \tag{2.16}$$

Using the expanded modulation signal, the amplitude-modulated signal, $s_A(t)$, is

$$s_A(t) = A_0 \cos(\omega_{\mathrm{RF}} t) + \sum_{n=1}^{\infty} m_A a_n \cos(n\omega_m t)\cos(\omega_{\mathrm{RF}} t) \tag{2.17}$$

$$s_A(t) = A_0 \cos(\omega_{\mathrm{RF}} t) + \sum_{n=1}^{\infty} \frac{m_A a_n}{2}\left\{\cos[(\omega_{\mathrm{RF}} + n\omega_m)t] + \cos[(\omega_{\mathrm{RF}} - n\omega_m)t]\right\} \tag{2.18}$$

$$s_A(t) = \sum_{n=-\infty}^{\infty} A_n \cos[(\omega_{\mathrm{RF}} + n\omega_m)t], \tag{2.19}$$

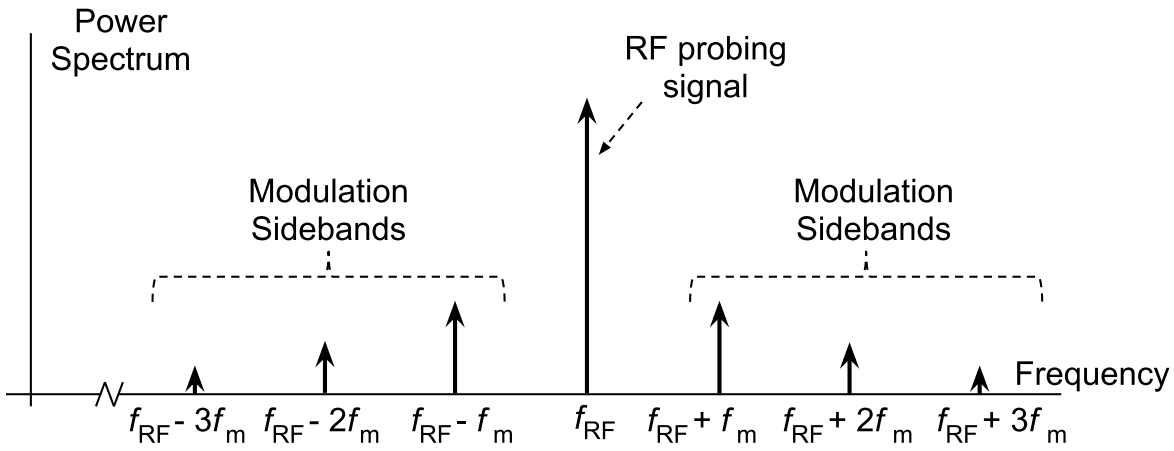

Figure 2.3: Typical modulation spectrum for low-level nonlinear interactions with an incident RF signal.

where

$$A_{n\neq 0} = \frac{m_A a_{|n|}}{2}. \tag{2.20}$$

The derived modulation spectrum, (2.19), is a collection of tones representing the modulation signal spectrum up-converted and mirrored around the RF carrier tone. The shape and power of the spectrum is dependent on A_n, which may be interpreted as an AM conversion factor for relating the spectrum of the modulating process to the detected RF modulation sidebands. A sample spectrum is shown in Fig. 2.3. Typically, a majority of the power in the modulation signal is concentrated in lower-order harmonics. As a result, the largest modulation tones in the RF modulation sidebands will be the lowest-order tones, closest to the RF carrier tone.

The modulation spectrum for PM can be similarly derived. Using the general PM representation in (2.10) and the same single-tone RF input tone, the phase-modulated signal is

$$s_\phi(t) = \cos\left[\omega_{\mathrm{RF}} t + \phi(t)\right] \tag{2.21}$$

$$s_\phi(t) = \cos\left[\omega_{\mathrm{RF}} t + \phi_0 + m_\phi x_\phi(t)\right]. \tag{2.22}$$

Beginning with the simplest case for the modulation signal, $x_\phi(t) = b\cos(\omega_m t)$, the phase-modulated signal, $s_\phi(t)$ is

$$s_\phi(t) = \cos\left[\omega_{\mathrm{RF}} t + \phi_0 + m_\phi b\cos(\omega_m t)\right]. \tag{2.23}$$

Using the Jacobi-Anger expansion, $s_\phi(t)$, is re-written

$$s_\phi(t) = \sum_{i=-\infty}^{\infty} J_i\left(m_\phi b\right) \cos\left(\omega_{\mathrm{RF}} t + \phi_0 + i\omega_m t + i\frac{\pi}{2}\right), \tag{2.24}$$

where $J_i(x)$ is the i-th order Bessel function of the first kind. Unlike the AM case, a single-tone modulating signal, $x_\phi(t)$, yields an infinite-bandwidth modulated signal, $s_\phi(t)$, with tones in the modulation sidebands spaced apart by ω_m. For $m_\phi b \ll 1$, representing weak nonlinear interaction, $J_{i+1}\left(m_\phi b\right) \ll J_i\left(m_\phi b\right)$ and a spectrum is generated similar to Fig. 2.3. Only the lowest-order tones are detectable above the system noise floor and the expanded signal bandwidth may be considered finite for practical purposes.

The PM analysis can be expanded for more complex signals. Again, using the Fourier series expansion of the modulation signal,

$$x_\phi(t) = \sum_{n=1}^{\infty} b_n \cos(n\omega_m t), \tag{2.25}$$

the phase-modulation signal signal, $s_\phi(t)$, is

$$s_\phi(t) = \cos\left[\omega_{\mathrm{RF}} t + \phi_0 + m_\phi \sum_{n=1}^{\infty} b_n \cos(n\omega_m t)\right]. \tag{2.26}$$

This can be re-written as

$$s_\phi(t) = \cos\left[\omega_{\mathrm{RF}} t + \phi_0 + \Phi_1 + m_\phi b_1 \cos(\omega_m t)\right], \tag{2.27}$$

where

$$\Phi_1 = m_\phi \sum_{n=2}^{\infty} b_n \cos(n\omega_m t). \tag{2.28}$$

Using the Jacobi-Anger expansion, (2.27) becomes

$$s_\phi(t) = \sum_{i_1=-\infty}^{\infty} J_{i_1}\left(m_\phi b_1\right) \cos\left(\omega_{\mathrm{RF}} t + \phi_0 + \Phi_1 + i_1\omega_m t + i_1\frac{\pi}{2}\right) \tag{2.29}$$

Drawing out the $n = 2$ term of Φ_1, the modulated signal can be written

$$s_\phi(t) = \sum_{i_1=-\infty}^{\infty} J_{i_1}\left(m_\phi b_1\right) \cos\left(\omega_{\mathrm{RF}} t + \phi_0 + i_1\omega_m t + i_1\frac{\pi}{2} + \Phi_2 + m_\phi b_2 \cos(2\omega_m t)\right), \tag{2.30}$$

where

$$\Phi_2 = m_\phi \sum_{n=3}^{\infty} b_n \cos(n\omega_m t). \tag{2.31}$$

The Jacobi-Anger expansion is again applied, resulting in

$$s_\phi(t) = \sum_{i_1=-\infty}^{\infty} \sum_{i_2=-\infty}^{\infty} J_{i_1}(m_\phi b_1)\, J_{i_2}(m_\phi b_2) \cos\left(\omega_{\mathrm{RF}} t + \phi_0 + (i_1 + 2i_2)\omega_m t + (i_1 + i_2)\frac{\pi}{2} + \Phi_2\right). \tag{2.32}$$

For a modulation signal approximated by an M-th order Fourier series,

$$x_{\phi,M}(t) = \sum_{n=1}^{M} b_n \cos(n\omega_m t), \tag{2.33}$$

the expansion process may be repeated recursively, so that the phase-modulated signal is

$$s_\phi(t) = \sum_{i_1=-\infty}^{\infty} \cdots \sum_{i_M=-\infty}^{\infty} \left[J_{i_1}(m_\phi b_1) \ldots J_{i_M}(m_\phi b_M)\right] \tag{2.34}$$

$$\times \cos\left(\omega_{\mathrm{RF}} t + \phi_0 + \sum_{k=1}^{M} k i_k \omega_m t + \sum_{k=1}^{M} i_k \frac{\pi}{2}\right). \tag{2.35}$$

This result is an M-dimensional summation of tones, generating a more complicated spectrum than the simple PM case, but again with modulation sideband tones spaced apart by ω_m. As $m_\phi b \ll 1$ and $b_{n+1} \ll b_n$, the additional tones generated in the expanded analysis are generally insignificant.

Unlike inherently nonlinear processes, time-varying systems are not easily expanded into power series for spectral analysis. Periodic time-varying systems may be modeled as modulating the incident signal. Both amplitude and phase modulation generate extensive spectral regrowth, despite operating as linear processes, making them strong models for multi-domain interactions without bidirectional coupling. These situations arise when the modulating signal is strongly biased and either unaffected or only weakly affected by feedback from the incident signal.

2.2.4 Time-Frequency Analysis

Neither power series nor modulation provide a convenient model for analyzing non-periodic time-varying systems. In these systems, transient effects and rapidly changing conditions correspond to variations of the instantaneous spectrum over time. The mathematical Fourier transform implies an integration over infinite time. For periodic functions, this is easily reconciled as evaluation of a finite length of time may be extended to infinite time by periodicity. Applying the finite-time Fourier transform to a transient signal ignores the assumption of periodicity, thus

the resulting spectrum may be seen as a mathematical artifact with less value. Nonetheless, non-periodic systems produce spectral regrowth by definition, as the Fourier transform of a finite-time signal produces an infinite-bandwidth spectrum. Analysis of these systems requires time-domain considerations. This may be handled as a strictly time-domain analysis for decaying exponential transients [72,73] or using joint time-frequency analysis for rapidly time-varying conditions [39].

2.3 Passive Spectral Regrowth

Spectral regrowth occurs in non-LTI systems either due to nonlinear effects or time-varying conditions. Specifically, passive spectral regrowth may be defined as additional frequency content generated in passive devices or structures, i.e., without gain. Active devices such as amplifiers and mixers require an external large-signal electrical bias to produce an output signal with higher power than the input signal. In the case of amplifiers, this is effectively a conversion of DC power to AC power [61]. Passive devices do not have an external electrical bias to draw power from, thus the output signal can be no higher in power than the input signal. Although active devices typically provide much stronger spectral regrowth, largely due to the presence of gain, passive spectral regrowth is more difficult to mitigate. Components such as the antenna are highly vulnerable to passive spectral regrowth due to high-power RF signals and no current feasible method for linearization. The only alternative is prevention, which requires a strong understanding of the nonlinear processes involved. The most common known passive sources of spectral regrowth are discussed here, including material nonlinearities, acousto-electromagnetic effects, and filter transient effects. All these effects may occur in either the RF radio front-end, or in remote targets. With any system connected to a physical aperture, both types of generation must be considered in the system design. To a lesser extent, but for maximum performance, all parts of the system must be evaluated for radiative coupling potential.

2.3.1 Material Nonlinearities

Inherent nonlinear mechanisms in passive components are commonly referred to as passive intermodulation (PIM). These processes fit the strict definition of nonlinear, as a combination of superimposed input signals will produce additional signals generated from mixing between the individual input signals, or intermodulation. Thus, these passive nonlinearities cannot be characterized by a single-tone input, requiring a finite-bandwidth signal composed of at least two or more discrete tones. Physical descriptions of passive intermodulation processes are based primarily on electrical junction nonlinearities or multi-physics, coupled domain interaction.

The oldest known class of passive nonlinearities is commonly termed the “rusty bolt” ef-

fect [5–10, 12], arising primarily from empirical evidence of loose, corroded, or dirty contacts generating nonlinear characteristics in RF connectors and adapters. Phenomenological studies of these effects commonly show dependence on materials used and connector tightness. Physical characterization of the "rusty bolt" effect is complicated by the wide variety of nonlinear mechanisms that may occur on a very small local scale and may have randomly distributed discrete sources over both a single component and throughout an entire batch of identical components. This has led to a multitude of suggested guidelines on connector tightening, better materials, and general construction and care of sensitive components [6, 7, 9].

Many of the underlying physical mechanisms of the "rusty bolt" effect have been tied to electrical junction nonlinearities resulting from metal-metal or metal-insulator-metal (MIM) contact. With a dirty or corrosive layer acting as an insulator, the quantum current tunneling from one metal to the other is described by the Simmons' model [74], a strongly nonlinear exponential function, and a potential source of spectral regrowth [12, 75, 76]. This effect is likely insignificant in the presence of any other nonlinear phenomenon [59, 76]. Nonlinear contact resistance results from mechanical or thermal stress warping the contact area between two surfaces. The uneven surface mating leads to a concentration of current over a smaller surface area, increasing current density and exacerbating nonlinear generation [77, 78].

Aside from the stress-induced "rusty bolt" phenomena, some materials exhibit inherent nonlinear behavior, often resulting from multi-physics coupled-domain interactions. These interactions include ferromagnetic, electro-thermal, and piezoelectric. Usually very weak, these coupled-domain effects are much stronger in distributed structures such as transmission lines, where they gain the advantage of being generated over the entire length of the line [14]. Junction nonlinearities, in contrast, are more likely to occur as localized discrete point sources.

Ferromagnetic nonlinearity results from hysteresis, or memory, of the induced magnetic field in certain materials such as iron, steel, cobalt, and nickel [59]. This effectively creates a time-varying magnetic bias coupled to the incident EM wave, inducing intermodulation with a delayed version of the signal [17, 79, 80]. Spectral regrowth from passive intermodulation is strongest in components that intentionally exploit ferromagnetic materials to generate a magnetic bias, such as in circulators [81], but is also present in components with no designed bias [9, 17, 80].

Electro-thermal interaction is caused by the coupled dependence of temperature and resistance in lossy components [15, 16, 79, 82]. In a lossy material, power is dissipated as heat when a current passes through a resistance. The resistance of nearly every material exhibits some temperature-dependence, generally characterized as the temperature coefficient of resistance (TCR). This creates a feedback loop, where excess thermal energy from dissipated electrical power modulates the equivalent resistance, in turn affecting power dissipation. Larger, distributed structures that are better able to "sink" excess heat produce reduced spectral re-

growth. Unlike many other sources of spectral regrowth, electro-thermal interaction has shown excellent agreement between theoretical physical models and measurements, primarily due to success in isolating the generating phenomenon.

Piezoelectric materials are common in surface-acoustic-wave (SAW) or bulk-acoustic-wave (BAW) analog filters [59]. Stress and strain of the material can affect EM and acoustic propagation characteristics, as well as the conversion factor between the two domains [83, 84]. The exact nonlinear coupling mechanism is unknown and under continued investigation.

2.3.2 Acousto-Electromagnetic Effects

Unlike material nonlinearities, acousto-electromagnetic (acousto-EM) effects are the results of acoustic modulation of the electrical properties of the propagation medium. Unlike piezoelectricity, acousto-EM interaction relies on an external source to drive the acoustic modulation, as opposed to self-generation of coupled acoustic and EM signals. Thus, acousto-EM interaction may occur in any material or medium and is not restricted to materials with special piezoelectric properties. Acoustic stimulus may be induced intentionally to trigger a measurable response, as in proposed systems for landmine detection [27, 85] or medical imaging [86], or the structure may vibrate on its own accord, as in a plane or vehicle. Acousto-EM interaction may result in direct modulation of the EM signal by mechanical scattering and resonance or modulation of the electrical characteristics of the device or structure.

The most common example of spectral regrowth from acousto-EM interaction is the Doppler effect [31–39]. Relative motion between the source and an observer leads to a shift in the observed frequency. In radar applications, this leads to spectral regrowth in the reflected signal from a moving target of interest. The motion of the reflector relative to the source modulates the distance traveled, and thus the phase of the reflected signal. This is pictured in Fig. 2.4. Using this, the reflected signal, $s(t)$, is

$$s(t) = \cos[\omega_{\mathrm{RF}} t + 2kr(t)], \tag{2.36}$$

where ω_{RF} is the frequency of the transmitted wave, k is the wavenumber of the transmitted wave, and $2r(t)$ is the round-trip distance between the source and the reflector. Time-varying displacement of the reflector appears in the reflected signal as phase modulation. For a reflector with constant velocity, $r(t) = R_0 - d(t)$ where $d(t) = vt$, the reflected signal is

$$r(t) = \cos[\omega_{\mathrm{RF}} t - 2kvt + 2kR_0] \tag{2.37}$$

$$r(t) = \cos\left[\omega_{\mathrm{RF}}\left(1 - \frac{2v}{c}\right)t + 2kR_0\right]. \tag{2.38}$$

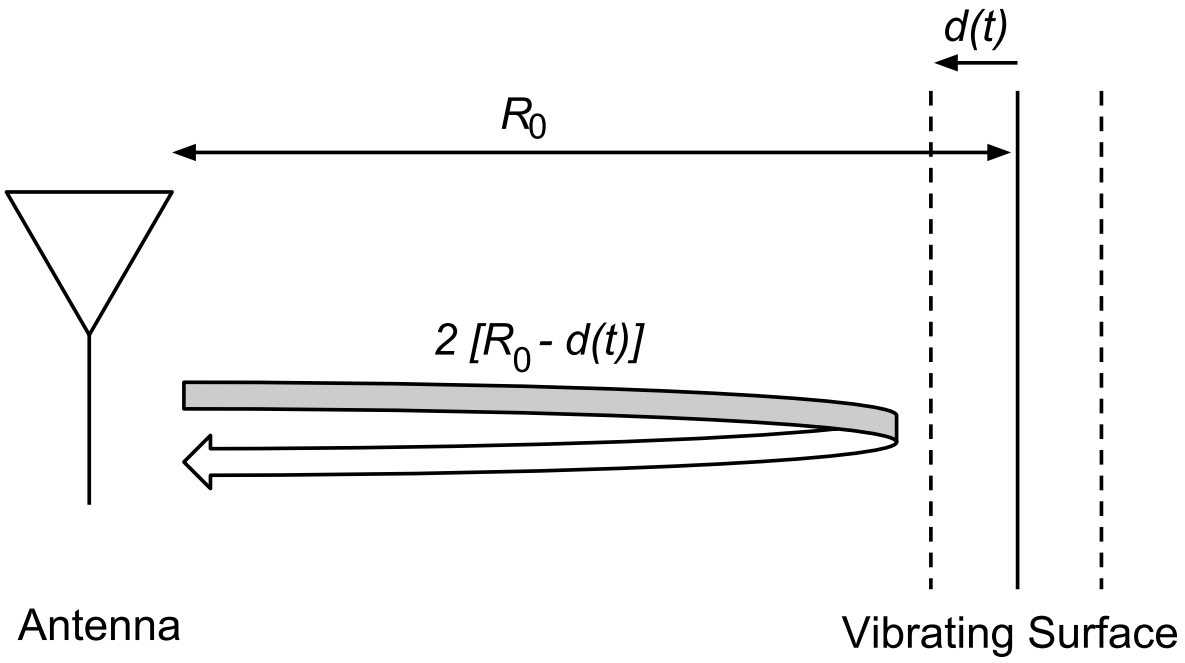

Figure 2.4: Displacement of a moving surface relative to a monostatic radar antenna.

Thus the linear motion of the reflector has generated spectral content at an offset, $\Delta\omega = \frac{2v}{c}$, from the original carrier frequency. In the case of a vibrating reflector, $d(t) = \beta\cos(\omega_V t)$, a broad spectrum of content is generated, (2.24) as derived in Section 2.2.3.

Acoustically-induced vibration may also modulate the electrical fields in a material or structure. The coupling of acoustic energy into an electrical signal in circuits is known as microphonics. Microphonics is conventionally known for generating an additional acoustic "buzz" in amplifier vacuum tube triodes [41]. In a microphonic tube, the grid is less mechanically stable than the cathode or plate. Vibration of the grid relative to the cathode or plate modulates the fields present in the tube, introducing oscillation into the triode operating current. The microphonic effect has also been demonstrated in off-the-shelf capacitors [42]. This effect is also likely caused by a mechanical resonance in the construction of the component. Connected to an antenna or other radiating element, these microphonic effects will appear as spectral regrowth of a transmitted signal.

In addition to mechanical resonances, acoustically-induced vibration may modulate the electrical permittivity of a dielectric [40]. Instantaneous changes in the permittivity are introduced due to vibration as the bulk density of the material varies with displacement, causing changes in charge center separation. Using a very high power acoustic stimulus tuned to the mechanical resonance of a dielectric cylinder, simulation demonstrated that nonlinear dielectric scattering

is a significant contributor to the total scattering response in some cases. While the development in [40] is for a plane wave impinging on a dielectric cylinder, a similar relationship may also hold for radiating components, such as antennas.

Spectral regrowth may also be possible due to Bragg scattering in air for propagating EM and acoustic signals at proper wavelengths. Bragg scattering is exploited in radio-acoustic sounding systems (RASS) to measure meteorological conditions in the lower atmosphere [87]. The Bragg scattering condition occurs when the acoustic wavelength is one-half the RF wavelength. Changes in atmospheric conditions have a much larger effect on acoustic propagation than on RF propagation. Thus, for a certain acoustic and RF frequency, the power of the backscattered RF signal indicates the wavelength of the acoustic signal, which can be fit to theoretical models to predict current conditions. Although the RASS only considers linear scattering, it proves the concept of coupled acoustic and EM waves in air and provides the basic mechanism for a potentially ubiquitous nonlinear process.

2.3.3 Filter Transient Effects

As discussed in Section 2.2.4, strictly linear systems may also produce spectral regrowth due to non-periodic or transient responses. This phenomenon has been observed in high-order bandpass filters, which develop a long-tail transient response through energy storage [72]. High performance filters with steep skirts required for new communications systems can only be realized with high-order designs. These high-order designs lead to strong internal resonances with low loss. In a pulsed or switched-tone radio, energy stored in these resonances from the "on" state will exponentially decay when the signal is off. This stored response cannot be predicted by steady-state analysis, and must necessarily generate spectral regrowth as a nonlinear process. Description of this effect in the frequency-domain can be misleading, however, as the common approach to removing extra spectral content, i.e., more filtering, would paradoxically degrade performance.

2.4 High-Dynamic-Range Nonlinear Measurement

One of the key challenges in characterizing passive spectral regrowth is measurement. Many sources of passive spectral regrowth are weakly nonlinear, requiring a high-power stimulus signal to produce detectable low-level spectral content. The measure of the ability of a system to detect small signals in the presence of large signals is known as dynamic range. An example of a small signal falling below the dynamic range of a receiver is shown in Fig. 2.5.

The definition of dynamic range is dependent on context, as it is often re-defined for a specific application. In RF amplifiers, spurious-free dynamic range (SFDR) is defined as the

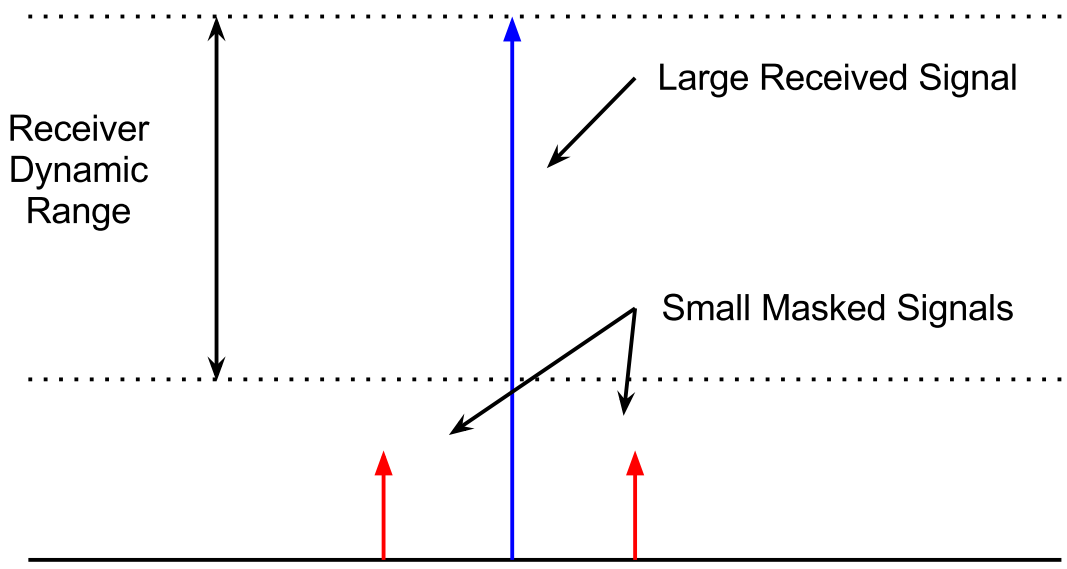

Figure 2.5: Dynamic range problem of measuring small signals in the presence of large signals.

ratio of signal power to the noise floor at the maximum signal power where distortion tone power is below the noise floor [61]. Amplifiers are strongly nonlinear devices and the power of the strongest distortion tone, the third-order intermodulation (IM3) product, typically follows a predictable 3:1 logarithmic slope versus input power as predicted by the power series expansion discussed in Section 2.2.2. This predictable behavior makes SFDR a useful metric for design and characterization of amplifiers, but SFDR does not adequately cover the needs of defining dynamic range for a small signal measurement system. Here, dynamic range is defined as the ratio of measurement input signal power to the minimum discernible signal (MDS) at a given frequency offset from the input signal carrier frequency. This definition is broad enough to cover broadband spectral regrowth, as well as account for any type of noise or distortion providing interference up to minimum detectable signal.

Receivers used for nonlinear measurement are designed to be very linear to maximize dynamic range. Laboratory spectrum analyzers, essentially a software-defined receiver, can achieve over 80 dB of SFDR [52], but still fall short of detecting passive spectral regrowth 100 dB or more below the high-power input stimulus and do not generally offer phase-measurement capability. In order to enable measurement of small signals, high-power signal or signals must first be removed. Discussed here are the two most successful architectures for removing high-powers, filtering and feedforward cancellation. In addition to extending dynamic range, several additional considerations must be taken in receivers to enable phase measurement, a potential

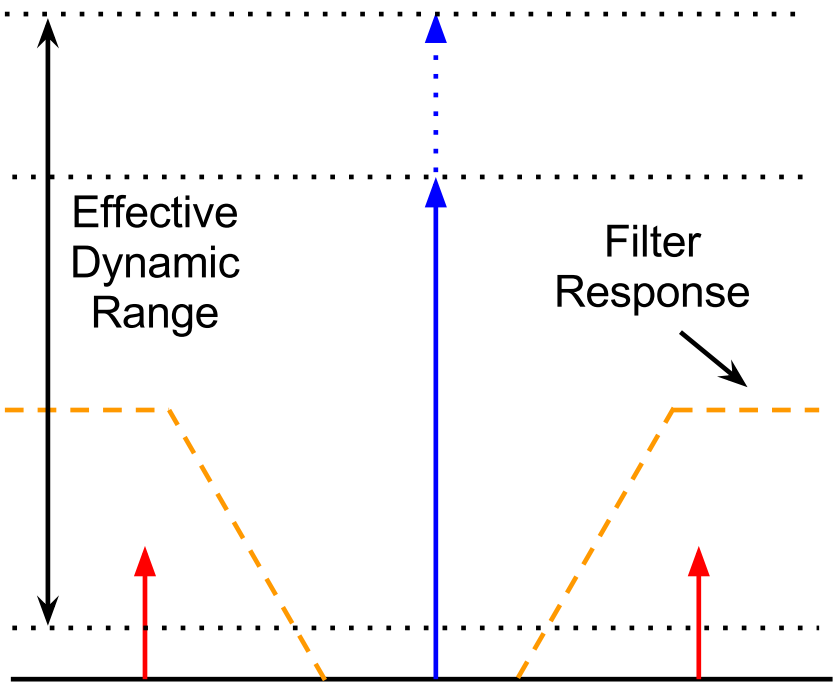

Figure 2.6: Ideal extension of dynamic range using filtering.

crucial discriminator of sources of passive spectral regrowth.

2.4.1 Filtering

Traditionally, removing unwanted frequency content is referred to as filtering. Physical analog filters are built to resonate across particular bandwidths, allowing certain frequencies to pass and strongly attenuating others, known as passbands and stopbands, respectively. Ideal filters transition directly from the passband to the stopband. Real filters have a finite transition band between the passbands and stopbands, referred to as the filter skirt and characterized by the roll-off of signal rejection. In the context of high-dynamic-range nonlinear measurement, a bandstop filter is used to remove, or notch, the high-power spectral content, as shown in Fig. 2.6. In this figure, the small tones previously below the receiver dynamic range are now detectable due to the power reduction of the large tone. The dynamic range, as defined above, has increased since the input signal power has not changed, but the MDS has decreased. Filtering is widely used in commercial implementations of nonlinear measurement systems [43], and can achieve the highest dynamic range with careful design. In particular, analog filtering must be used, as noise introduced by analog-to-digital converters (ADC) will greatly overwhelm small signals with the large interfering signal still present.

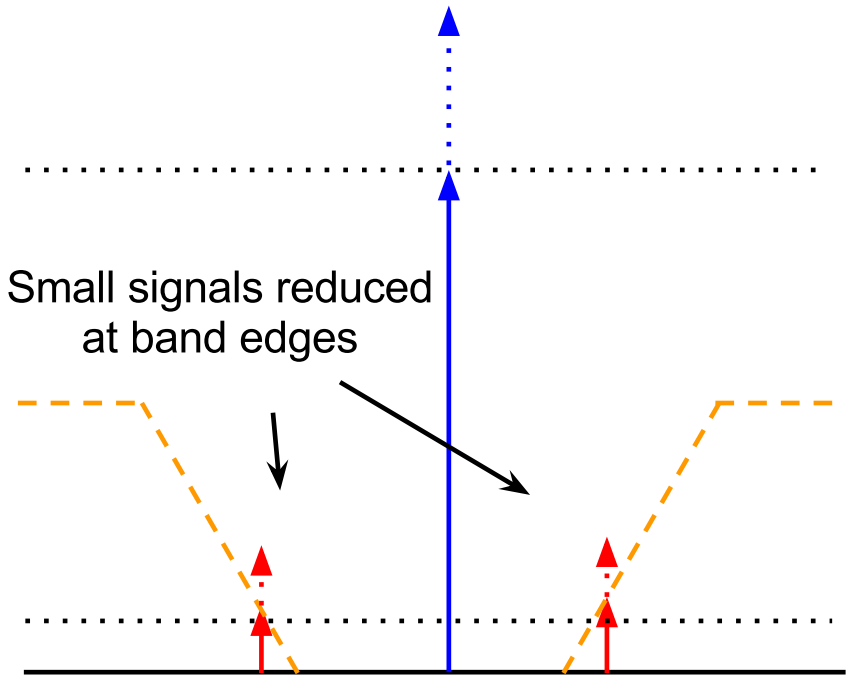

Figure 2.7: Undesirable attenuation of small signals within filter bandwidth.

The ideal extension of dynamic range using filtering is only possible if the desired small signals are completely within the passband of the filter. To accurately measure small signals very close in frequency to the large interferer, a very narrow stopband and sharp filter roll-off is needed. Suppressing small signals at a 1 kHz offset from a 1 GHz carrier tone require a filter with a quality factor (Q) of greater than 10^6, much higher than possible in physical filter implementations. Signals not entirely within the passband will be attenuated, as shown in Fig. 2.7, greatly reducing the effectiveness of the technique. This limits filter-based nonlinear measurements systems to a minimum frequency offset. For two-tone third-order intermodulation (IM3) testing, the IM3 tone occurs at a frequency offset equal to the frequency separation of the two input tones. Thus filter-based systems have a minimum tone separation, limiting detection of tone-separation-dependent phenomena such as electro-thermal passive intermodulation.

In addition to minimum bandwidth limitations, filter-based systems also suffer from poor tuning performance. Performance of state-of-the-art electronically tunable filters [88] typically falls well below the high performance characteristics of fixed-frequency filters in current systems. Instead, broadband filters or switched filter banks are needed. Broadband filters, used for testing specific fixed communications bands [43], impose large restrictions on minimum frequency offset. Switched filter banks allow much greater flexibility in frequency tuning, but can be prohibitively

expensive or physically large.

With transmission line resonators, filter-based systems have been demonstrated that can achieve over 190 dB of dynamic range [44]. In this type of system, the device under test (DUT) is placed at specific points along a $\frac{\lambda}{2}$ microstrip resonator to align with a standing wave. The voltage or current maxima presented to the DUT provides a higher power input tone stimulus for the nonlinear mechanism, but does not propagate through the system, reducing residual system nonlinear products. In addition, the resonator system provides a means of discriminating between primarily voltage-driven or current-driven nonlinearities, a characteristic that provides deep insight into the physical processes involved. Unfortunately, use of the resonator exacerbates bandwidth problems of filter-based systems, limiting measurements to a specific bandwidth associated with the standing wave resonance.

2.4.2 Feedforward Cancellation

To address many of the bandwidth concerns associated with filter-based systems, feedforward analog cancellation has been introduced as a new alternative for high-dynamic-range nonlinear measurement [48–51]. Analog cancellation has been widely used in linearizing power amplifiers [89], and as radar reverse-power cancellers [90–93], but analog cancellers did not achieve sufficient performance for detection of passive spectral regrowth until recently [52, 94].

In an analog canceller, the undesired signal is combined with an equal amplitude, oppositely phased signal. This results in destructive interference, removing or reducing the power of the undesired tone. For nonlinear measurement, the large interfering signal is cancelled, extending the effective dynamic range as shown in Fig. 2.8. The combination of the measurement signal and the cancellation signal occurs after the measurement signal has passed through the nonlinearity. Since the small tones generated by the nonlinearity are not present in the cancellation signal, they pass through the combination with no change. The general structure for implementing analog cancellation for nonlinear measurement is shown in Fig. 2.9.

In general, dynamic range of a canceller-based system is dependent on the achievable cancellation of the stimulus tone. Thus, accurate control of the feedforward signal is critically important to maximizing cancellation. This control may be generalized as inducing a variable amplitude and phase shift on the cancellation signal, as pictured in Fig. 2.9, and implemented as variable attenuators and delay lines or vector modulators. The limit to achievable cancellation, C_A, given an amplitude error, ϵ_α, and phase error, ϵ_ϕ, is

$$C_{A,\mathrm{dB}} = -10\log\left[1+\epsilon_\alpha^2 - 2\epsilon_\alpha\cos(\epsilon_\phi)\right]. \tag{2.39}$$

The amplitude error, ϵ_α, is the amplitude ratio of the cancellation and measurement tones. The phase error, ϵ_ϕ is the deviation of the phase difference between the two tones from anti-phase

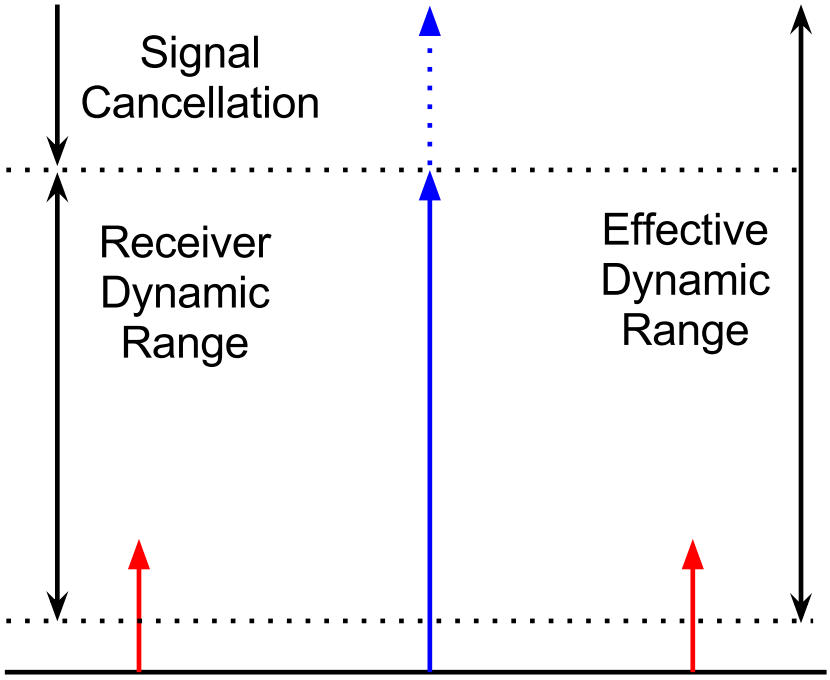

Figure 2.8: Ideal extension of dynamic range using feedforward cancellation.

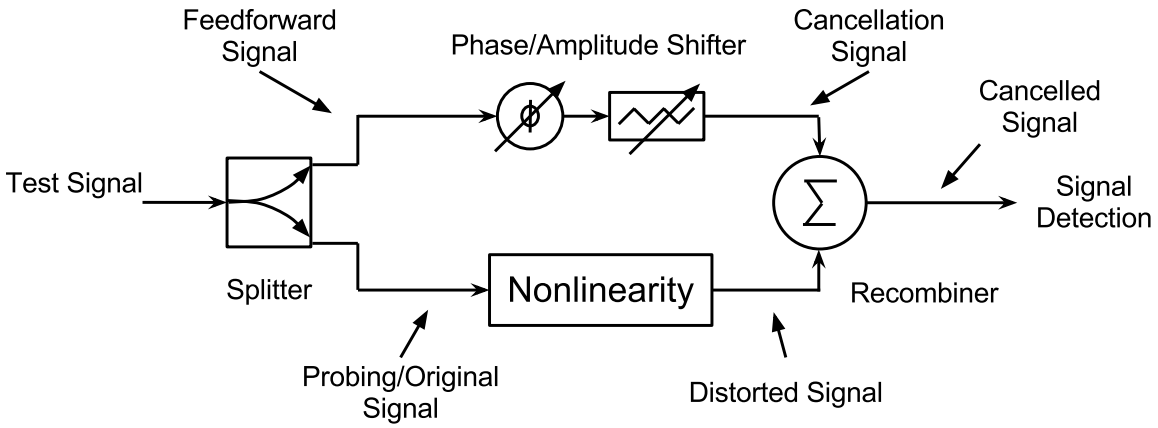

Figure 2.9: Basic block diagram using feedfoward analog cancellation for nonlinear measurement.

matching. For ideal cancellation, $\epsilon_\alpha = 1$ and $\epsilon_\phi = 0$, resulting in $C_{A,\mathrm{dB}} = \infty$. To achieve a minimum of 40 dB of cancellation, the amplitude mismatch can be no more than 0.1 dB and the phase error can be no more than 0.6°. Manual tuning is not sufficient to achieve this level of

accuracy, and automated control with feedback is necessary. Typical automated control schemes implement derivative-based iterative techniques to slowly, but consistently reach the intended cancellation state. These techniques can require a large number of iterations to reach moderate levels of cancellation and cannot absolutely converge due to dithering of the error signal [50–52]. In response, a more efficient, directly convergent algorithm has been developed [50, 52] that eliminates the need for the iterative approach, but relies on high measurement accuracy and is less applicable to time-dynamic systems.

2.4.3 Nonlinear Phase Measurement

Power is the most directly detectable characteristic of a signal, however, as high-dynamic-range solutions have been developed more attention has turned to accurate phase measurement of nonlinear spectral content. The primary difficulty in phase measurement lies in generation of a calibrated reference phase to produce a traceable phase response. Establishing a phase reference between tones of separate frequencies is non-trivial, since the tones inherently advance in phase at different rates. A variety of nonlinear vector network analyzers (NVNA) have been introduced to attempt to measure the nonlinear phase directly, generally sacrificing some dynamic range in order to produce an absolute or relative nonlinear reference signal [53–55]. An alternative measurement system based on cancellation has also been introduced which functionally operates as a feedforward linearizer, drawing phase information about the nonlinear tones from the phase of the feedforward signal [56]. Solving the issues associated with nonlinear phase measurement will be key to developing new techniques and methodologies in discriminating sources of passive spectral regrowth.

2.5 Summary

Passive spectral regrowth is a weakly nonlinear process gaining importance as receiver performance improves for both communications and sensing. Thus far, it has been difficult to consolidate theory and measurements of spectral regrowth, mostly due to the extremely difficult detection problem and the complicated multi-physics coupling potentially involved. Standard methods of nonlinear analysis and measurement and known theoretical models were reviewed to gain the basis for understanding passive spectral regrowth.

A nonlinear system is defined as a system that generates additional spectral content not present in the input of the system. This is a colloquial definition and contains all non-linear-time-invariant (non-LTI) systems. Nonlinear systems may be describing using physical models, based on theoretical principles, or behavior models, based on measured and statistical data. For strictly nonlinear systems, i.e., failing superposition, power series approximation provides the

most useful framework for analyzing and understanding complex, intractable models. Linear, periodic time-varying systems may be best represented mathematically using signal modulation, which provides greater physical insight than power series. Non-periodic time-varying systems defy simple characterization and must be considered directly in the time domain.

Passive spectral regrowth is the appearance of nonlinear frequency content in passive devices or structures. Passive spectral regrowth is typically much weaker than spectral regrowth in active structure, due to the lack of electrical gain. Primary sources of passive spectral regrowth are identified as material nonlinearities, acousto-electromagnetic (acousto-EM) effects and filter transient effects. Many of these nonlinear mechanisms contain quantum-level or multi-physics interactions that are difficult to isolate and poorly understood.

Weak nonlinear mechanisms make the detection of passive spectral regrowth difficult. High-power stimulus signals are required to generate low-power nonlinear frequency content, requiring extensive measurement dynamic range at the receiver. High-dynamic-range measurement systems typically use either analog filtering or feedforward cancellation to remove the high-power stimulus before passing the signal to the receiver, creating a larger effective dynamic range. As the dynamic range of measurement systems improve, more attention is being paid to the fundamental signal characteristics of spectral regrowth, including both amplitude and phase.

Chapter 3

Robust Analog Canceller for High-Dynamic-Range Radio Frequency Measurement

3.1 Introduction

There are many situations in which small RF signals must be detected in the presence of large RF signals. These include characterization of materials; detection of buried objects by examining the nonlinear response to electromagnetic probing signals; satellite navigation receivers operating near high power cellular phone systems or in the presence of jammers that intentionally attempt to deny satellite-based navigation; high power RF transmitters of digitally-modulated signals that transmit unintended signals (so-called spectral regrowth) that can disrupt other radios operating in adjacent bands; systems that characterize the distortion performance of analog circuits using two-tone testing (in which the frequency spacing of the tones is ideally swept); and nonlinear radar that attempts to detect the presence of electronics by detecting harmonics and intermodulation products in the reflected RF signal. The detection problem in all of these systems is the characterization of small RF signals in the presence of large signals. Systems such as commercial radios use bandpass filters (as well as regulated air space and centralized dynamic power control) to minimize large interfering signals.

The increasing sensitivity of modern radio, radar, and sensor systems has led to greater attention to ultra-low distortion products resulting from passive intermodulation distortion (PIM), or the mixing products created when multiple tones interact in presumably linear passive components. Although these mixing products can be 100 dB or more below the power level of the carrier signals, technologies such as GPS and spread spectrum modulation continually push the minimum detectable signal levels lower. Therefore, in order to understand the origins of

PIM, it has become necessary to extend the performance of high-dynamic range measurement systems.

Traditional non-linear distortion measurement systems apply a high power stimulus, typically a two-tone signal, to a device-under-test (DUT), sometimes in a wireless channel. The carrier signals are then removed at the output of the DUT or receive antenna to prevent masking of mixing products and to improve the sensitivity of the receiver. Commercial systems use filtering to isolate the high-power stimulus from the generated low-power intermodulation products [43]. Systems such as these can measure very small intermodulation products, but the finite slope of the filters in transitioning from passband to stopband prevent measurement of closely spaced tones. More advanced systems, such as that reported in [44], expand the capabilities of the filtering system by using a resonator to generate higher power levels in the DUT, however, there is a minimum ability to shift frequency bands or measure when the tone spacing is small.

The second class of non-linear distortion measurement systems uses the concept of analog cancellation of the stimulus signal to extend the dynamic range of a receiver-based measurement instrument. Feedforward cancellation is a well-known technique for signal and noise suppression and active cancellers have been widely applied as reverse power cancellers (RPCs) for continuous wave radar [90–93], for co-channel and adjacent channel distortion measurement [48–51], and for passive intermodulation distortion measurement [52, 94]. These cancellers typically employ a combination of amplitude and phase shifters or a vector modulator which require manual or slow iterative tuning for optimal cancellation.

A recent implementation [52] reported an analog canceller using digitally-controlled vector modulators to automate the cancellation process leading to a high dynamic range distortion measurement system. The system achieved up to 50 dB of analog cancellation and was used to characterize PIM of microwave components from 1 Hz to 10 kHz [15, 16]. Key to achieving this performance was replacing the Newton or quasi-Newton iterative commonly used in vector-modulator based cancellers by a predictive formula that determines the appropriate settings at each iteration of the canceller. The derivative-based procedure necessarily requires an error signal and the dithering of this error determines the extent of cancellation achievable.

In [52] the primary limits to analog cancellation and thus system dynamic range were established as carrier phase noise and amplitude measurement error leading to a decrease in cancellation depth. The system presented in this chapter improves the automated analog cancellation performance through careful attention to signal level calibration, architectural refinement, and an intelligent cancellation algorithm.

Section 3.2 presents the theory behind the analog canceller developed including an in-line calibration procedure that calibrates the system at the same time as the canceller operates. The architecture of the new canceller is presented in Section 3.3 along with implementation details. Section 3.4 describes a high dynamic range PIM measurement system that utilizes the analog

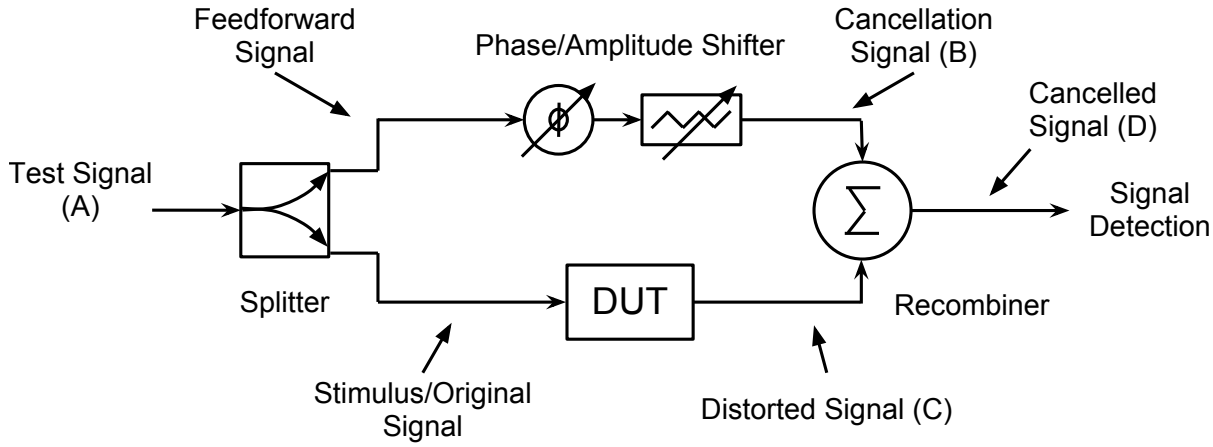

Figure 3.1: Basic block diagram for signal cancellation employing a feedforward path with amplitude and phase shifting to generate an anti-phase version of the test signal. The DUT could also be replaced with a wireless channel and either a single or separate antennas for transmission and reception.

canceller. The measurement section, Section 3.5, first defines various dynamic range measures to be used with analog cancellers and PIM measurement systems. Then the application of the two-tone PIM measurement system is used to measure the PIM of off-the-shelf lossy microwave components from the electro-thermal region below 100 Hz of tone separation up to 100 MHz. It is shown that there are sources of PIM beyond the electro-thermal sources of PIM that dominate at low tone-spacings.

3.2 Analog Canceller

This section describes the approach to reliably achieving analog cancellation exceeding 70 dB. Even the most subtle issues must be addressed to achieve such cancellation levels automatically.

3.2.1 Feedforward Cancellation Theory

The input to an analog canceller is a signal that needs to be transmitted to a DUT but be suppressed before signal detection. In many cases this input signal is a high-power signal needed to drive an antenna and wireless channel, or to drive distortion in microwave components to measurable levels. Reflection or leakage of the high-power signal into receiver circuitry can saturate it, greatly reducing sensitivity of the receiver. In the analog canceller here, a test signal is split into two paths, providing a stimulus signal to the DUT and a feedforward signal to phase and amplitude shifters, see Fig. 3.1. Nonlinearities in the DUT create a distorted signal at the output, while shifting on the feedforward path outputs a cancellation signal. These signals

are then recombined for detection and measurement. The feedforward signal (B) destructively interferes with the signal from the DUT (C) so that the undesired original tones are suppressed, i.e. cancelled, at a final combination point to produce the cancelled signal (D). In the ideal case, the feedforward signal has the same amplitude, but opposite phase, as the test signal resulting in total cancellation. Thus the original signal is cancelled leaving only distortion products at the output of the canceller. The cancelled signal is then detected using a conventional receiver, a vector signal analyzer, or a spectrum analyzer.

The canceller uses measurements of the amplitude of the signal at the output of the canceller with and without the cancellation signal applied. Without loss of generality, α is the voltage amplitude of an original component of the distorted signal when the shifters are adjusted so that there is no cancellation signal and β is the voltage amplitude of the same component with the cancellation signal applied. In the absence of nonidealities, perfect cancellation is obtained when $\beta = 0$. Nonidealities include amplitude imbalance, ϵ_α, phase imbalance, ϵ_ϕ, and group delay effects for finite bandwidth signals. Restricting the development to discrete stimulus signals (as in two-tone testing), the amplitude and phase imbalances result in a limit to the achievable cancellation [52]:

$$C_{A,\mathrm{dB}} = -10 \log \left[1 + \epsilon_\alpha^2 - 2\epsilon_\alpha \cos\left(\epsilon_\phi\right)\right] \tag{3.1}$$

where $C_{A,\mathrm{dB}}$, the analog cancellation, is the ratio (in decibels) of the power of the original signal to the power of the cancelled signal as measured at the cancellation reference plane at the output (D). In (3.1) the amplitude imbalance, ϵ_α, is a linear voltage ratio of the cancellation and original tones. With ideal amplitude matching of the original and cancellation signals, i.e. $\epsilon_\alpha = 1$, and no offset from anti-phase matching, i.e. $\epsilon_\phi = 0$, then $C_{A,\mathrm{dB}} = \infty$ dB and perfect cancellation is achieved.

As in [52], only signal amplitude measurements are needed to determine the correct amplitude and phase for the cancellation signal. A power measurement of the distorted signal determines the target amplitude for the cancellation signal. A reference measurement combining the original signal and an equal amplitude cancellation signal with an arbitrary phase separation, $\Delta\phi$, will ideally result in a measured power that is solely dependent on $\Delta\phi$. Therefore the additional phase shift, ϕ_s, of the feedforward signal needed to completely cancel the original signal is

$$\phi_s = \pi \pm 2 \arccos\left(\frac{\beta}{2\alpha}\right) = \pm 2 \arcsin\left(\frac{\beta}{2\alpha}\right) \tag{3.2}$$

which can be derived from the vector addition of equal amplitude discrete tones [52]. The symmetry of the unit circle yields two solutions, only one of which will provide the desired cancellation. The correct sign in (3.2) can be determined by taking an additional amplitude measurement at a second reference phase separation.

Equation (3.2) contains no inherent phase shift error, that is, for the combination of two ideal tones on a perfectly linear cancellation signal path, ϵ_ϕ will always be zero for the predicted phase shift. In reality, even small errors (or noise) in the signal amplitude of the cancellation signal or slight non-linearities in the cancellation signal path can severely degrade actual cancellation. From (3.1), a 0.1 dB amplitude mismatch or a 0.6° phase mismatch limits cancellation to under 40 dB ($C_{A,\mathrm{dB}} < 40$ dB). Amplitude error is mostly due to nonlinearities in the cancellation path, however phase error is dominated by amplitude error in the reference measurement embedding itself in the application of (3.2) in determining the required phase shift for cancellation. The combination of mismatched original and unshifted cancellation signals produces an incorrect value for β, propagating into an error in the calculated required phase shift, ϕ_s. Subsequent iterations correct for this error but it is desirable to achieve maximum cancellation with no or few iterations. The amplitude-to-phase error propagation is also dependent on the phase separation of the signals during the reference measurement, as a result of vector addition. A plot of the maximum analog cancellation for several values of amplitude mismatch is shown in Fig. 3.2. For phase separations less than 90°, this limit on cancellation can exceed the limit imposed directly by amplitude mismatch. As the tones spread farther apart, the effect of amplitude-to-phase error becomes much less significant. Due to relying only on amplitude measurements, amplitude mismatch has a significant effect on cancellation error, and highly accurate calibration is required to characterize the cancellation path so that maximum analog cancellation can be achieved.

3.2.2 Calibration

In [52] calibration was performed prior to canceller operation. The baseline calibration fine-tunes the scaling of the cancellation amplitude for a cancellation phase of 0°. In the absence of phase-dependent amplitude variations, this calibration can be applied at arbitrary phases during testing. However, using this fixed-phase calibration, a phase-periodic amplitude error is measured, shown as Curve (a) in Fig. 3.3. One potential solution to this issue is to expand the calibration to include a full sweep of cancellation phase shift. This extra dimension significantly expands the amount of time spent during the calibration, mostly dependent on the density of the phase points calibrated. Loosely spaced phase points provide a faster calibration, but it cannot accurately capture local non-linearities, and it will inherently suffer from interpolation error. A tighter grid of calibration points would provide a better approximation of the amplitude non-linearity, but the extended time required decreases system throughput and introduces error from time-dependent nonidealities due to, for example, temperature and humidity variability, and power supply variation due to battery depletion.

To avoid the problems inherent to grid-based calibration, here calibration is incorporated

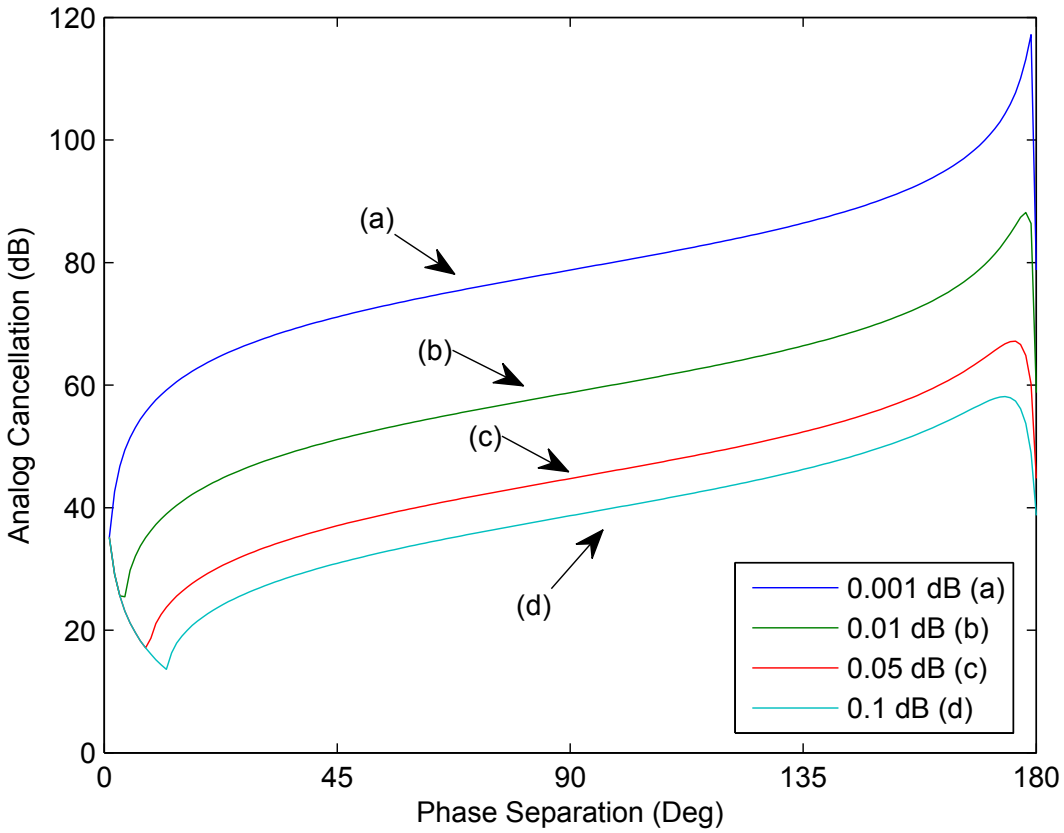

Figure 3.2: Maximum theoretical analog cancellation, $C_{A,\mathrm{dB}}$, as a result of projected phase shift error caused by amplitude mismatch during the reference measurement. Phase separation is the phase difference of the signal to be cancelled at (C) and the cancelling signal (B) as shown in Fig. 3.1. It is assumed that the unshifted cancellation signal has a larger amplitude than the original signal.

into the operation of the canceller, capturing nonlinear effects in-line with the measurement. The in-line calibration operates at the frequency and phase shift required for cancellation, dramatically decreasing the amount of time spent calibrating and eliminating all phase-interpolation error. Calibrating the cancellation amplitude at test time also eliminates time-dependent effects. To minimize the effect that in-line calibration could have on extending test time, the baseline fixed-phase calibration is still performed prior to canceller operation. This reduces each in-line calibration step to a single measurement for correcting the fixed-phase error. The flow implementing the integrated in-line calibration and cancellation procedure is shown in Fig. 3.4. Amplitude measurements at two separate references phases are required to determine the two unknowns of the required phase shift for cancellation, magnitude and sign. These reference

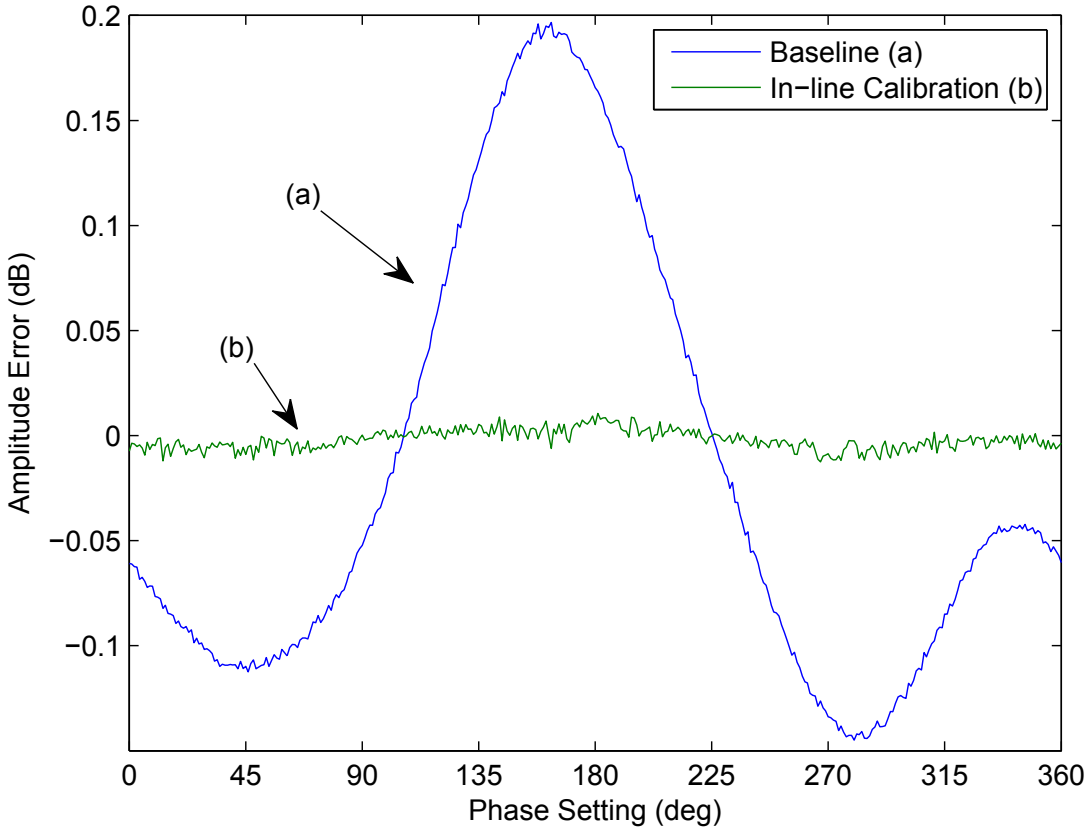

Figure 3.3: Measured amplitude error versus phase setting of the cancellation signal: (a) using baseline or fixed-phase calibration; and (b) using in-line calibration.

phases can be arbitrarily chosen, however for mathematical simplicity they are usually chosen to be 90° apart.

The improvements obtained by using in-line calibration can be understood by examining Figs. 3.3 and 3.5. Fig. 3.3 compares the measured amplitude error, ϵ_α, following in-line calibration and initial fixed-phase (baseline) calibration of the canceller system of Fig. 3.1. Fig. 3.5 presents the analog cancellation achievable using the two calibration methods (without canceller iteration). The phase setting in Figs. 3.3 and 3.5 is the phase shift of the cancellation tone added by the phase shifter of Fig. 3.1, as opposed to the phase separation between the cancellation and original tones as in Fig. 3.2.

As seen in Fig. 3.3, the baseline calibration has a roughly sinusoidal dependence on phase shift ranging between +0.2 dB and −0.15 dB. In-line calibration provides a dramatic improvement. The effect of in-line calibration on cancellation is shown in Fig. 3.5, where the maximum

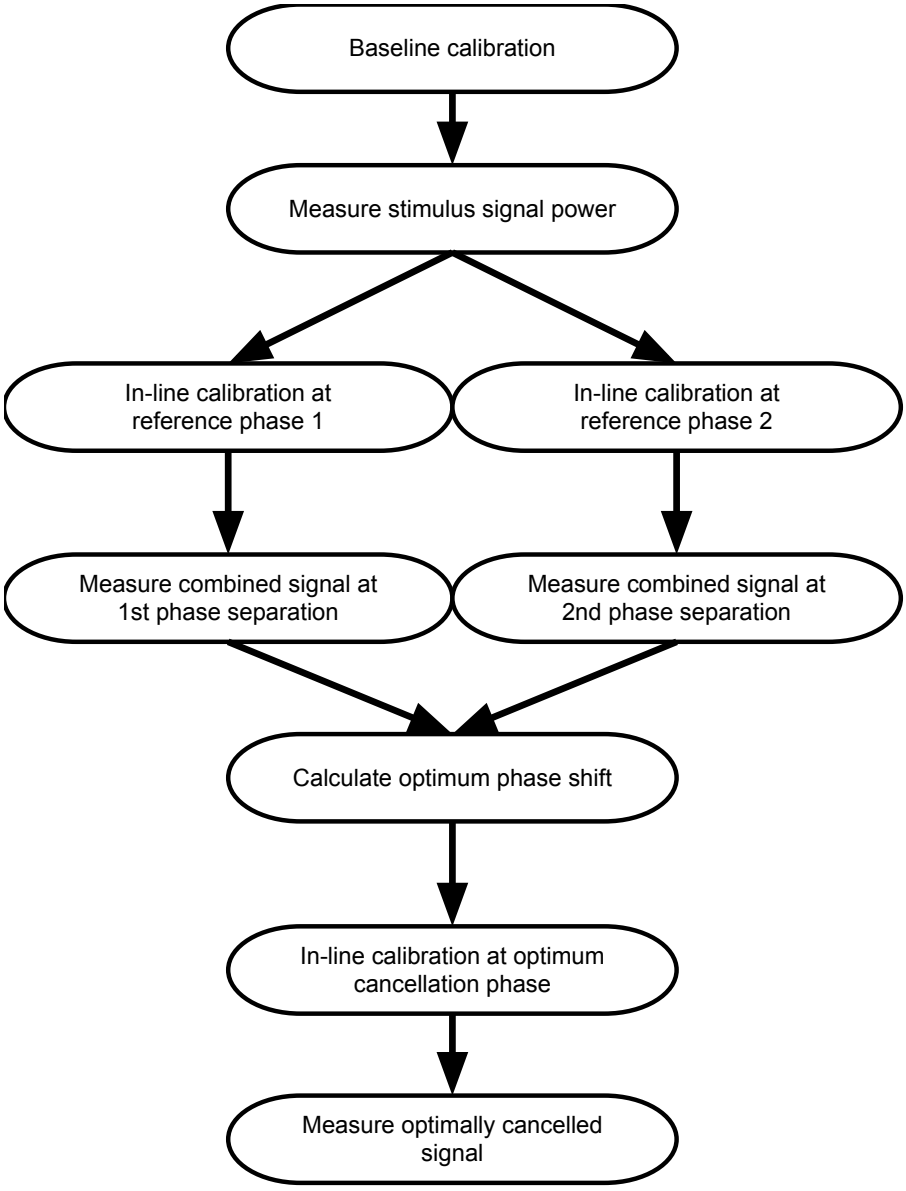

Figure 3.4: Flow chart detailing steps during signal cancellation procedure.

cancellation predicted from amplitude mismatch on the calibrated path exceeds 60 dB across essentially the entire range, as opposed to only a few points exceeding 60 dB using baseline calibration. On average, maximum cancellation (from amplitude mismatch alone) is improved by 30 dB by using in-line calibration.

The statistical nature of cancellation is seen in Fig. 3.5. With systematic amplitude error mostly minimized, noise dominates the remaining effective mismatch and initial cancellation

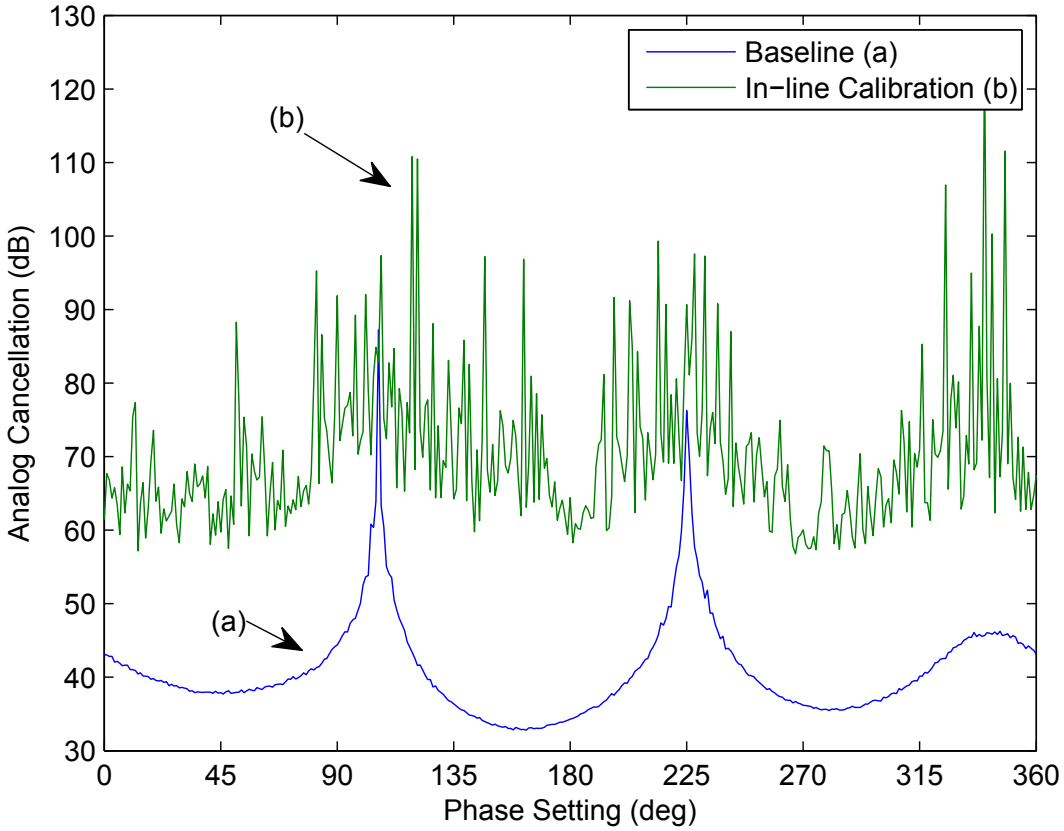

Figure 3.5: Calculated maximum analog cancellation using the measured amplitude mismatch in Fig. 3.3: (a) using baseline calibration; and (b) using in-line calibration.

error, creating the jagged shape of the in-line calibrated curve, Curve (b), in Figs. 3.3 and 3.5. The variation evident in the curve is partially due to environmental conditions (including temperature, radio frequency interference, and power supply noise), but is also affected by hardware considerations such as quantization error. This is discussed in more depth in Section 3.3.

3.2.3 Analog Canceller Performance

The phase separation of the signal to be cancelled and the cancelling signal of an isolated cancelling scenario cannot be known a priori so, in effect, the initial phase separation will be uniformly distributed between 0° and 360°. Thus the maximum cancellation possible without iteration will have a statistical distribution. In application as an analog canceller in a measurement or wireless system, re-using the phase separation from the previous time instant or measurement can significantly improve cancellation levels in practice without iteration. However,

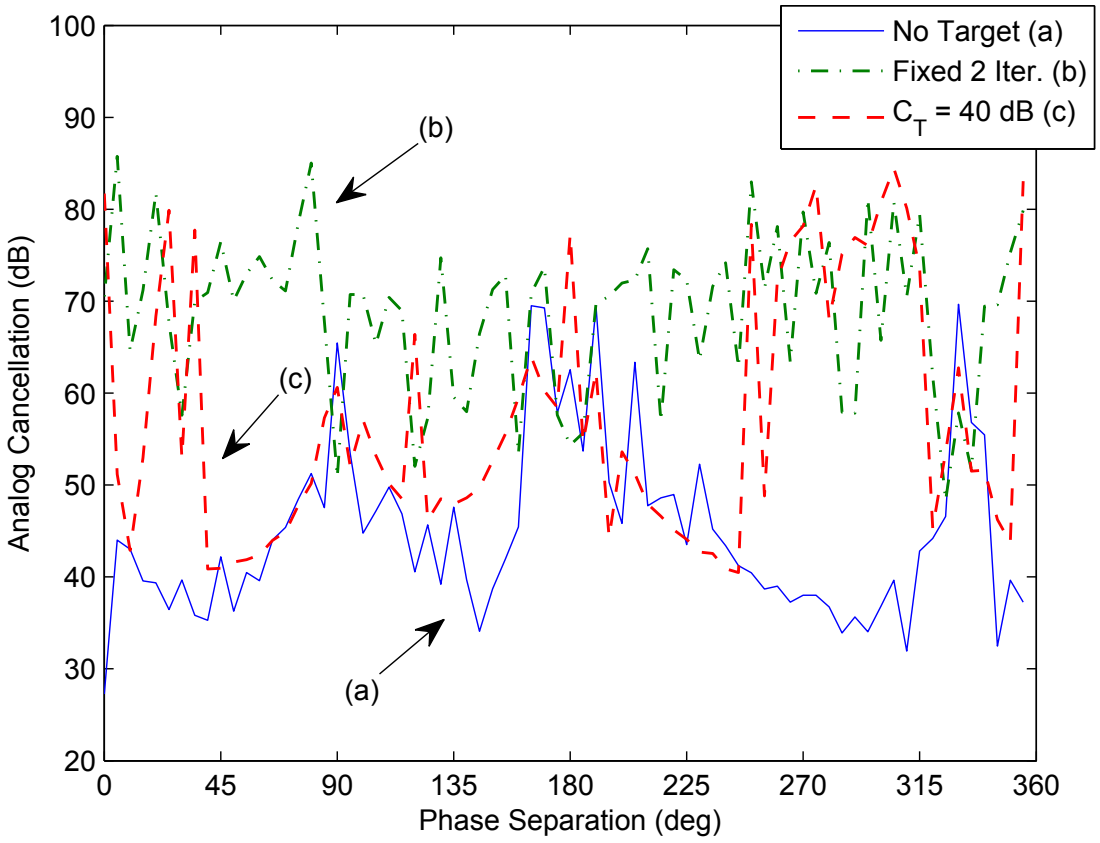

Figure 3.6: Measured analog cancellation versus initial phase separation: (a) no target (single iteration); (b) forced two iterations; and (c) with cancellation target C_T of 40 dB.

to ensure optimum cancellation performance, an iterative cancellation procedure is required.

The cancellation performance improvement as phase separation approaches 180° is primarily due to reduction of amplitude-to-phase error and the reduced impact of phase-dependent nonlinear effects. As the phase shift required at each iteration gets smaller, the cancellation path appears more linear, improving the accuracy of the required phase shift calculated using (3.2). Thus the cancellation procedure in Fig. 3.4 can be applied iteratively to obtain a target cancellation, C_T. By setting a cancellation target, the number of iterations at an arbitrary phase can be kept to a minimum while guaranteeing a certain level of performance. On average less than three iterations is required for a minimum cancellation of 70 dB. Measured results from applying the iterative cancellation procedure over a range of initial phase separations is shown in Fig. 3.6. Curve (a) in Fig. 3.6 shows the analog cancellation obtained using a single pass of the cancellation procedure as shown in Fig. 3.4. This is referred to as single iteration, or no target.

Table 3.1: Cancellation statistics for a sweep of initial phase separation of the stimulus tone and the feedforward tone at 460 MHz. (Av. = average, Md. = median)

Target C_T (dB)	Iterations				Meas. analog cancellation (dB)			
	Av.	Max	Md.	σ	Av.	Max	Min	σ
0	1.00	1	1	0.00	45.0	69.7	27.3	9.5
30	1.01	2	1	0.12	46.4	79.3	31.2	10.4
40	1.31	2	1	0.46	56.9	84.5	40.5	13.3
50	1.72	3	2	0.48	67.0	84.5	50.3	10.0
60	2.01	4	2	0.49	73.5	87.6	62.5	4.9
70	2.63	11	2	1.24	75.3	90.0	70.3	4.0
–	Forced 2 Iter.				68.6	85.8	48.3	8.7

When the initial phase separation is near 180° a cancellation of 70 dB is achieved but otherwise it is as low as 27 dB. Using a second iteration, Curve (b) of Fig. 3.6, the maximum cancellation is 86 dB and the minimum cancellation is 48 dB. With a target cancellation $C_T = 40$ dB, Curve (c) in Fig. 3.6, the maximum number of iteration is 2 and the average number of iterations is 1.3. The results are summarized in Table 3.1 for several cancellation targets.

3.2.4 Summary

The nature of the phase shift equation, (3.2), suggests that the optimum phase shift is obtained as a directly convergent result from amplitude measurements, enabling very high cancellation in only a single iteration. Reliance on a single iteration magnifies the effect of path nonlinearities in degradation of cancellation, but phase correction from additional iterations can recover high cancellation performance. The hardware concerns generating these nonlinearities, as well as other mentioned throughout this section are discussed in Section 3.3.

The analog canceller achieves 70–90 dB cancellation given sufficient iterations. For high cancellation targets of 70 dB or more, the iteration count can grow dramatically in a few cases. Unlike other Newton-like iterative techniques utilizing power gradients or least squares approximations that provide incremental improvement through iteration[1], each iterative step here is designed to be terminal and will only provide improvement if the path nonlinearities are significantly reduced from the previous iteration. For iterations that end near the cancellation target, the very small phase differences between iterations often produce identical results, eliminating

[1]However, as noted previously, Newton-like iterative schemes necessarily require an error signal and the dithering of this error limits the analog cancellation that can be achieved to much lower levels than that reported here.

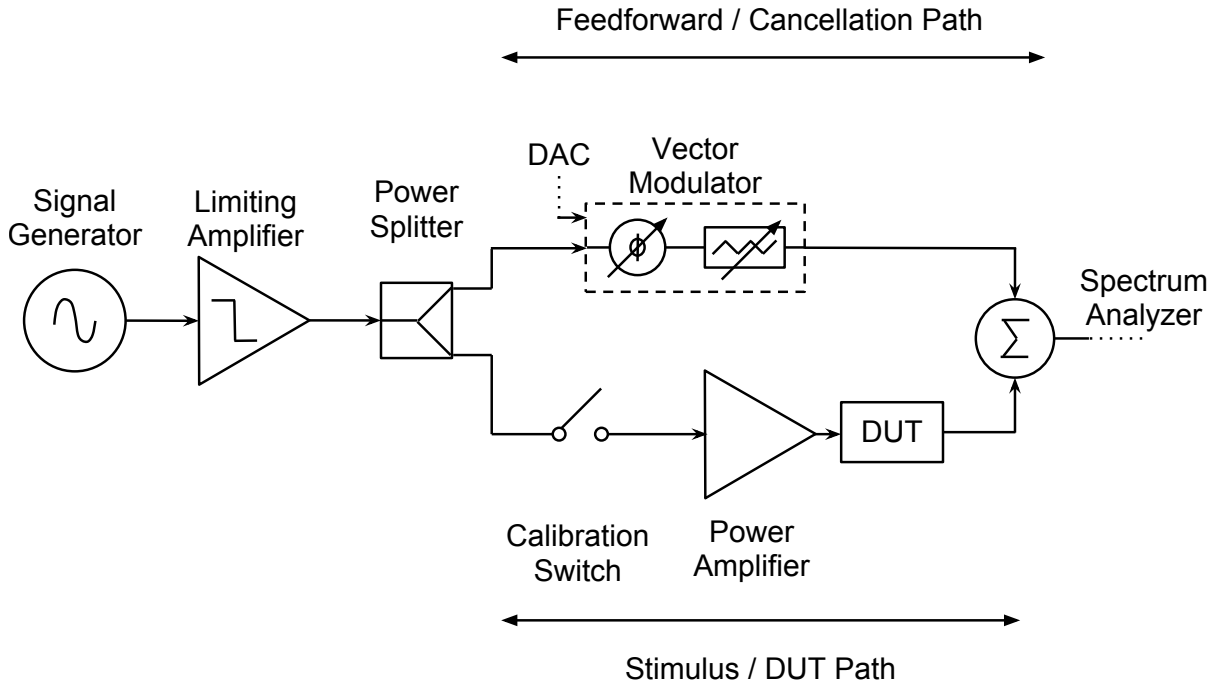

Figure 3.7: Block diagram of a single-channel analog cancellation system, in a configuration for testing distortion generated in the DUT.

any potential for incremental improvement. However, in application in measurement or wireless receiver systems, this phase tracking ensures that the canceller can maintain high levels of analog cancellation without iteration. For significant phase changes, such as changes to the wireless channel or a large frequency shift, the full iterative cancellation may be required to recover optimum cancellation performance.

3.3 Cancellation Architecture for High Dynamic Range

The performance of a canceller in measurement is quantified in terms of the cancellation dynamic range, which is distinct from the analog cancellation performance, C_A. Cancellation performance is the ratio of the original signal power to the cancelled signal power. Cancellation dynamic range, DR_C, as it is defined here, is an asynchronous form of dynamic range that compares the highest-power signal that can be cancelled with the minimum detectable signal after analog cancellation. Ideally DR_C would be the product of the dynamic range of the receiver (measurement) equipment DR_R, and the analog cancellation, C_A. However various constraints reduce the achievable DR_C.

The implementation of the analog canceller is shown in Fig. 3.7. This is the minimum

configuration for implementing single-channel cancellation, and is a subset of a larger system for multi-channel cancellation described later in this chapter. The primary features are the split paths emerging from a single source, a digitally-controlled vector modulator for automated phase and amplitude shifting, and a high-power microwave switch on the stimulus channel. The microwave switch enables automated calibration of the feedforward channel as described in the previous section by breaking the DUT path, allowing the vector modulator output to pass uncancelled to the measurement receiver. In the feedforward path, the output of the power splitter is input to the LO port of the vector modulator. The software-controlled DAC drives the I and Q inputs of the vector modulator to set the phase and power of the cancellation tone. A spectrum analyzer is used here as a receiver but a vector signal analyzer or a radio receiver could also be used. Key to ensuring high levels of cancellation performance and cancellation dynamic range are noise and interference suppression and measurement and calibration accuracy.

3.3.1 Noise and Interference Suppression

Major sources of noise and interference in the feedforward cancellation path result from coupling of spurious frequency content from external sources and from summation of random noise components at the recombiner. These interfering sources are inherently suppressed through cancellation and close attention to radiative shielding.

Spurious frequency content in the canceller (spurs) primarily derive from power line noise, switching noise in power supplies, and leakage of intermediate frequency (IF) signals from signal sources. In the system of Fig. 3.7, amplitude-related spurs emanating from the signal source are eliminated by the limiting amplifier through a mirroring effect [52]. Phase-related spurs from the signal generator are minimal. Line noise and switching noise are introduced into the system in the active components such as the amplifiers and vector modulators. Either DC power from batteries or a highly regulated power supply will reduce line or switching spurs below that of the low-level signal components to be measured [52]. With battery-based DC power it is important to ensure sufficient shielding or RF suppression on power cables to prevent coupling into the supply lines or into the battery components.

In systems employing a wireless channel as the DUT, spurious RF emissions are a major source of interference. These external spurs couple into the system at the transmit and receive antennas and are not suppressed through cancellation. Since it is often impractical to eliminate the sources of these emissions, it is necessary to contain much of the equipment and cabling in an isolated, shielded environment.

3.3.2 Measurement and Calibration Accuracy

This section considers measurements and calibration accuracy and discusses how the various sources of error affect overall dynamic range and cancellation performance. The system dynamic range is application specific and in Section 3.4 this is presented relative to a two-tone distortion measurement system. The discussion below, however, applies to all systems using the analog canceller presented in this chapter.

Quantization error inherent to digital control of the vector modulator is the ultimate limit on achievable cancellation. The quantization errors are also correlated with the measurement accuracy of the receiver (here a spectrum analyzer) since the calibration of the power output of the vector modulator can be no more accurate than the repeatability of the spectrum analyzer, and the finite steps of the vector modulator output limit the ability of the calibration to make the minute adjustments required for precise amplitude matching. While the relative accuracy of the spectrum analyzer measurements can be improved by averaging more data points, the speed of the measurement can be severely degraded, especially when extremely narrow resolution bandwidths are used. As mentioned in Section 3.2, small changes due to time-dependent effects can overwhelm the sensitivity of the calibration, which prove to be detrimental over extended averaging measurements. The trade-off between time and accuracy is heavily hardware and application-dependent, relying on the performance of the measurement equipment and the type and accuracy of measurements desired.

The ability to make small adjustments to the output power of the vector modulator is most crucial to ensuring very high levels of cancellation. Here, a Hittite HMC497LP4 vector modulator is used with a 16-bit digital-to-analog converter (DAC) to implement the automated phase and amplitude shifting. The DAC provides DC voltages to differentially drive the in-phase (I) and quadrature (Q) ports of the vector modulator. Due to the limited bit resolution of the DAC and fixed output range, the minimum output voltage step is fixed. When presented directly to the vector modulator, the voltage output will ideally increment linearly, based on the capability of the circuitry. Since the voltage output of the vector modulator will generally be less than both of the voltage inputs at the I/Q ports, the conversion gain will be less than unity. As a result of this, the step resolution at the output of the vector modulator will be smaller than the voltage step of the DAC. By extension of this effect, any attenuation between the vector modulator and the combination of the feedforward and original signals will also linearly improve the adjustment resolution. With the voltage output accuracy fixed linearly, the relative power output accuracy in decibels will increase at higher power levels, since the step size becomes much smaller in relation to the output power. These observations mesh well with the reported results of [52], which experimentally claimed higher accuracy at high vector modulator output power and also better success with cancellation at low signal levels.

Through exploitation of these effects, the effective accuracy in decibels of the vector modulators can be increased arbitrarily to at least the measurement accuracy of the spectrum analyzer. However, attenuation of the vector modulator power can directly reduce achievable cancellation dynamic range. A potential solution to this is attenuation of the DAC output signal power to overcome the fixed output range, thus allowing higher resolution but reducing the maximum tuning range. In measurement, the reduction of tuning range is acceptable since system signal levels are generally known, but in wireless systems the signal to be cancelled may vary wildly in power, increasing the significance of this trade-off.

In addition to the restrictions on cancellation, the power handling capability of the receiver (spectrum analyzer) and the vector modulator loosely set limits on the theoretical cancellation dynamic range of the system. While the maximum obtainable cancellation dynamic range of the system could be at the extreme ends of the power handling range of the receiver, attenuation in the system will change this significantly. With attenuation, the power output of the vector modulators will be less than the maximum power specifications and can be significantly less than the output power from the DUT, requiring similar attenuation in the DUT path. If it is the smaller signal, the maximum power level of the vector modulator roughly sets the highest signal level able to be cancelled, also setting the high end of the cancellation dynamic range. Sometimes, due to high loss in the DUT or removal of the amplifier, the stimulus signal can instead limit the cancellation dynamic range ceiling. The low end of the cancellation dynamic range is set by the noise floor at the output of the system, which determines the minimum detectable signal, except in cases where spurious frequency content has not been suppressed. At frequencies near the carrier signal, the phase noise of the vector modulator will dominate the noise floor. Attenuation at the vector modulator output can reduce this phase noise, but the noise floor at the output will not drop below the noise floor of the receiver. In addition, any attenuation or gain after the vector modulator can only negatively affect, if at all, the cancellation dynamic range since both the highest-power cancellable signal and the noise floor are affected simultaneously, with excess noise in the amplifier or attenuation slightly degrading the noise floor.

3.4 Application to Two-Tone Non-linear Distortion Measurement

By extending the feedforward cancellation system to two channels, it can be used in two-tone non-linear distortion reflection or transmission measurements as shown in Fig. 3.8. This hardware implementation of the system is similar to that described in [52], but with the addition of calibration switches to implement the in-line calibration procedure, and a directional coupler

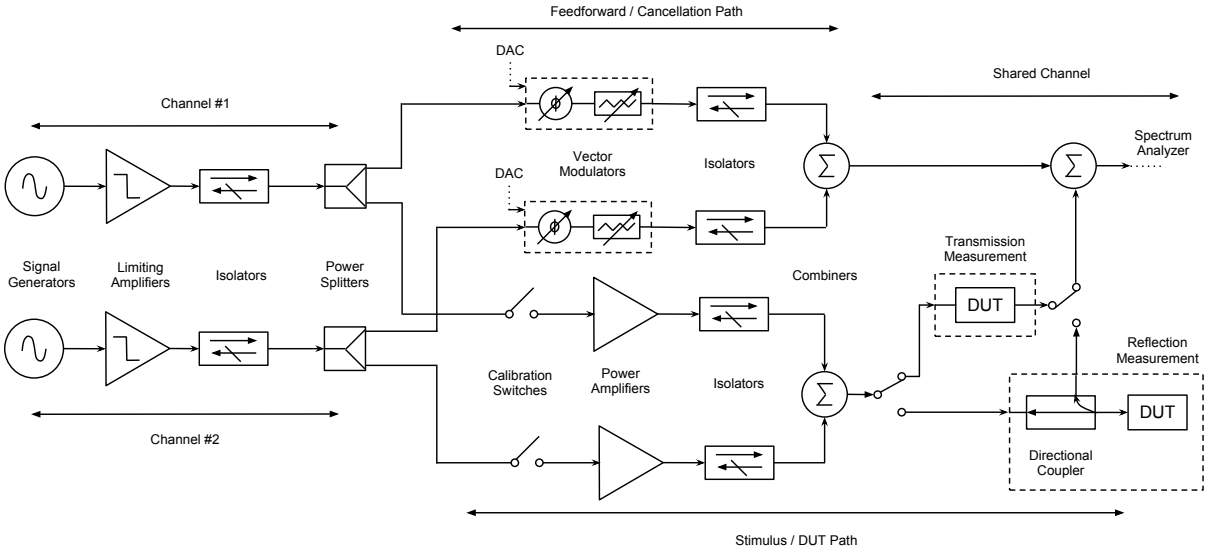

Figure 3.8: Dual-channel high-dynamic range cancellation system for passive intermodulation distortion (PIM) measurement with both transmission and reflection configurations.

to enable one-port reflection measurements. The system can be implemented as shown in the figure to enable both reflection and transmission PIM measurements through the use of switches, however for best performance one fixed configuration with direct cable connections is preferred. The other key addition to this system, relative to Fig. 3.7, are the isolators, which help ensure system linearity but impose half-octave bandwidth restrictions.

3.4.1 System and Component Linearity

System linearity is crucial to high-dynamic range non-linear distortion measurement. Often residual system PIM establishes the minimum measurable distortion level, limiting the dynamic range. In order to suppress residual intermodulation products, interchannel coupling must be minimized, and the shared DUT channel must be kept as linear as possible.

Mixing products in passive system components can be kept to a minimum by using large connectors such as DIN- and N-type with silver-plating [95]. Where attenuation or termination is necessary, very long slightly-lossy low-PIM cables act as attenuators or terminations and produce significantly lower distortion than similar lumped components. Similarly, other components such as combiners and directional couplers also benefit from transmission line implementations over lumped element versions. These choices for passive components reduce current density therefore improving linearity.

Active components such as power amplifiers and vector modulators, however, are strongly non-linear requiring emphasis on reducing interchannel coupling. The system is especially sen-

sitive to coupling prior to the active amplification stages, as any intermodulation products generated experience significant gain. Coupling is also extremely detrimental at the input of the isolators as these are strongly non-linear in the presence of multiple tones.

The use of separate channels and isolators, as shown in Fig. 3.8, prevent a majority of undesired tone mixing, but radiated coupling between the channels, and the finite reverse leakage of the isolators prevents complete isolation. Radiated coupling is primarily a consequence of the very high power levels required to generate measurable PIM in the DUT. High quality double- or triple-shielded cabling can be used, but often does not sufficiently reduce radiated signal levels. Extra shielding is needed, such as using RF absorber and Faraday cages around sensitive spots. To ensure maximum radiated isolation, each cable or component should be shielded against any other cable or component carrying the opposite channel signal [52]. High quality, high-isolation isolators can be used to improve problems with reverse signal leakage, although these isolators typically suffer from very narrow fractional-octave bandwidth limitations. Alternatively, multiple isolators can be used in series to achieve a high-degree of isolation with adequate bandwidth with a small increase of insertion loss.

3.4.2 Bandwidth Limitations

The narrowest bandwidth components in the system are the isolators in the individual channels prior to combination, and they only need to accommodate a single tone within their bandwidth. Thus the isolators directly limit the frequency range of the two-tone test but only indirectly limit the frequency separation of the tones. Other bandwidth-limited components in the individual channels such as the amplifiers can be easily selected to have wider bandwidth than the isolators in the system and thus impose no restrictions on bandwidth as long as the components share a sufficient common bandwidth. For the components in the shared signal path, bandwidth limitations come from the couplers and combiners. Since both tones and their intermodulation products need to be in the passband of these components, the maximum frequency separation allowed can be no larger than their total bandwidth divided by the order of the intermodulation products being measured. For example, in order to be able to measure third-order intermodulation products, a coupler with 300 MHz bandwidth with a centered two-tone stimulus can support a maximum frequency separation of 100 MHz. For practical purposes, the intermodulation products may still need to be well inside the characterized bandwidth of a component to avoid extra loss at the edge of the pass band that could drive extremely low-level products below the noise floor. Although very large frequency separations with regard to the center frequency are possible in the described system, PIM characterization with more than 2% fractional tone separation may be better served by systems utilizing duplexing and notch filters, to take advantage of the filtering performance advantage.

The system presented in this chapter has been built to operate at a center frequency range of 400–650 MHz, which is primarily limited by the narrow bandwidth isolators in the system. Replacing these, as well as other components in the system with higher frequency models should allow the architecture to be extensible to all modern RF communications bands. The Hittite HMC497LP4 vector modulator, the key component in the architecture, can be used up to 4 GHz, and vector modulators up to 60 GHz have been demonstrated [96].

3.5 Measurement

In distortion measurement systems, intermodulation dynamic range, $\mathrm{DR_{IM}}$, is usually defined as the ratio of the DUT input signal power to the minimum detectable signal (MDS). DR_C, however, relates the MDS to the maximum cancellable signal at the output of the DUT. This MDS is due to either residual intermodulation products, carrier phase noise, or the receiver noise floor. $\mathrm{DR_{IM}}$ is a measure that is ideally independent of both the DUT characteristics and the measurement configuration (transmission or reflection), since the DUT input power and the MDS are independent of the loss of the DUT. In practice, $\mathrm{DR_{IM}}$ can be quite different as the MDS can change depending on the configuration. The relationships of these measures and various signal power levels are shown in Fig. 3.9. Analog cancellation, C_A, extends the cancellation dynamic range, DR_C, beyond that of the receiver, DR_R. Increasing the DUT insertion loss (IL) for two-port measurements or DUT return loss (RL) for one-port measurements reduces the output power of the DUT, decreasing the achievable DR_C, but also decreases the required C_A needed to reduce the signal power to below the maximum undistorted received signal level. $\mathrm{DR_{IM}}$ can be determined by directly combining the measured DR_C with the RL or IL from the DUT. Passive components will always experience some loss, ensuring that the $\mathrm{DR_{IM}}$ will be greater than the DR_C for such components.

3.5.1 Cancellation and Dynamic Range

Third-order intermodulation dynamic range, $\mathrm{DR_{IM3}}$, was measured for the two-port transmission configuration with a fully-automated two-tone frequency sweep. The DUT for the measurement was replaced with a through connection, and the worst-case $\mathrm{DR_{IM3}}$ was determined by comparing the power of an individual input tone to the larger of the two measured third order intermodulation (IM3) products. The performance is shown in Fig. 3.10 for both non-iterative, Curve (a), and targeted cancellation, Curves (b) and (c), techniques. The minimum $\mathrm{DR_{IM3}}$ for the non-iterative measurement is 85 dBc at 1 Hz frequency separation, with an average analog cancellation C_A of 51 dB and minimum C_A of 34 dB. With a cancellation target, $C_T = 60$ dB, the $\mathrm{DR_{IM3}}$ at 1 Hz increased to 94 dBc, with an average C_A of 63 dB. The 12 dB cancellation

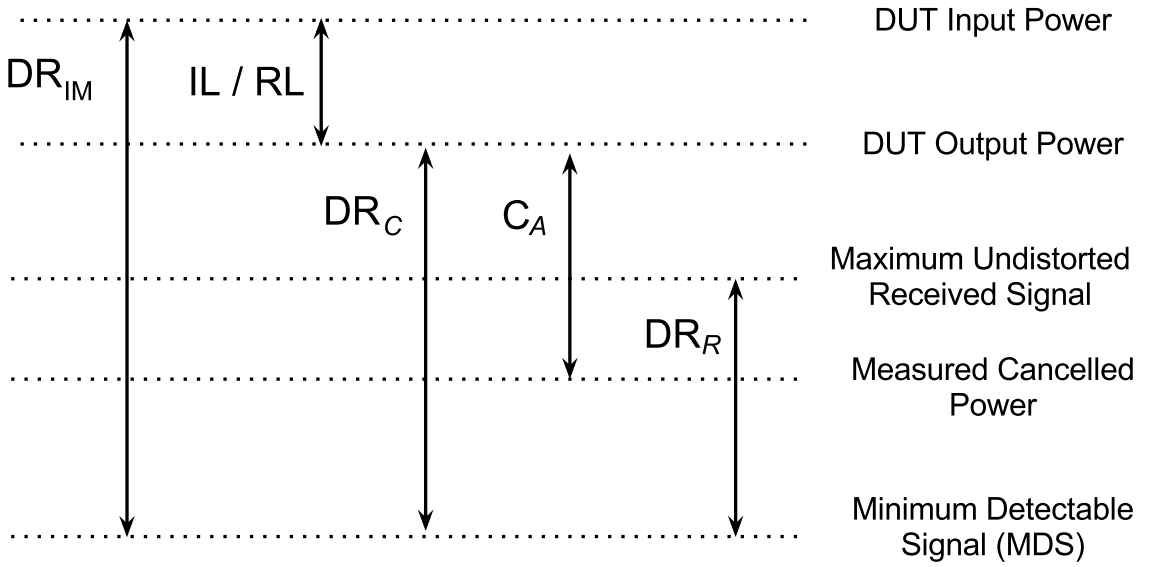

Figure 3.9: Relationships between several measurement quantities assuming sufficient analog cancellation (C_A) (logarithmic scale). The DUT input power is reduced by the insertion loss (IL) in a transmission measurement and by the return loss (RL) in a reflection measurement. With a wireless channel, this would include appropriate portions of the link loss.

improvement is obtained at a cost of 1.4 additional iterations on average. Since both channels are being cancelled concurrently, the analog cancellation performance during the two-tone test can not be expected to necessarily match the measured results from Table 3.1. The $\mathrm{DR_{IM3}}$ is lowest for small tone separations, Δf, below 100 Hz, and for separation approaching 1 MHz. The dynamic range for small tone separations is primarily limited by the phase noise of the carrier tone bleeding into the frequency of the IM3 products. The phase noise, which is the minimum detectable signal at low frequency separations, is dependent on the power of the cancelled signal and thus small tone separations directly benefit from increased levels of cancellation. As Δf approaches 100 Hz the minimum detectable signal becomes the noise floor determined by the system thermal noise and the resolution bandwidth of the receiver. This reduces the dependence of $\mathrm{DR_{IM}}$ on analog cancellation and flattens out the $\mathrm{DR_{IM3}}$ curves. A minimum $\mathrm{DR_{IM3}}$ of 113 dBc is achieved from 100 Hz to 30 kHz. Above 100 kHz, the self-generated upper IM3 products experience considerable growth independent of the lower IM3 product, dominating the minimum detectable signal power and sharply degrading system performance. The mechanism behind this growth is currently unknown. Additional unidentified spurious tones at 10 MHz and 100 MHz further degrade performance independent of center frequency. Higher $\mathrm{DR_{IM3}}$ was obtained for the lower IM3 tone, see Fig. 3.11, however for equal power input tones the IM3

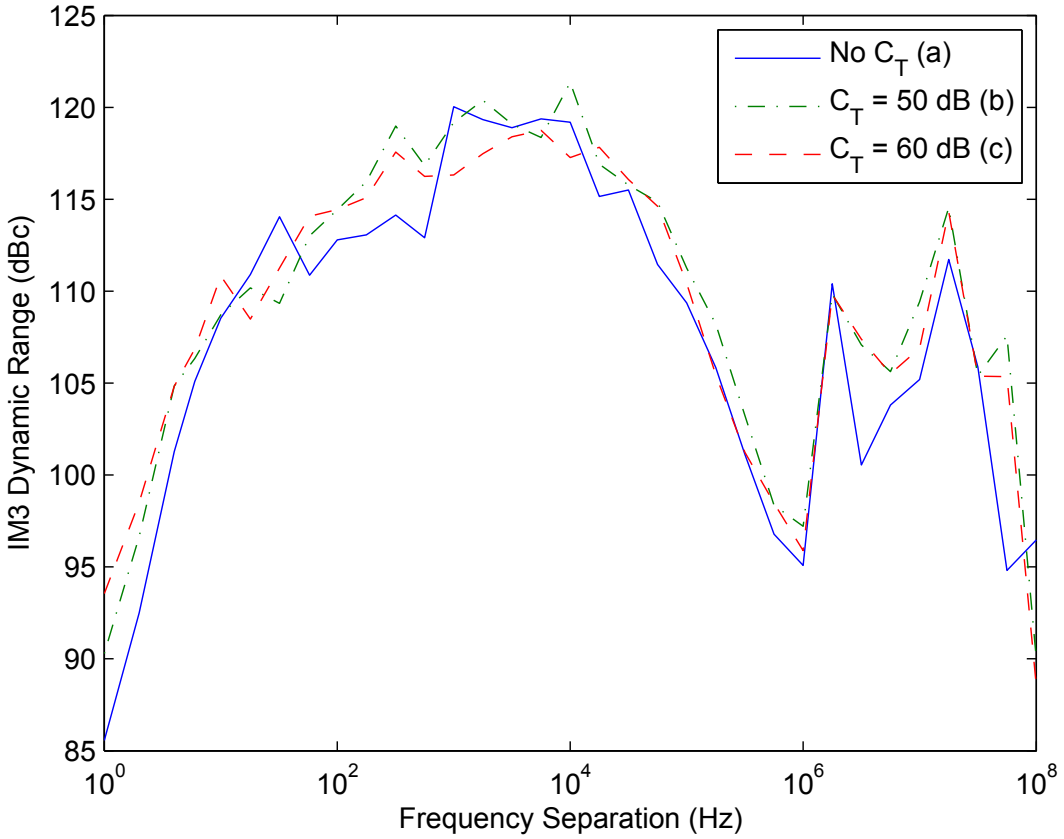

Figure 3.10: Worst-case third-order intermodulation dynamic range (DR_{IM3}) achieved in two-port transmission configuration over frequency separation during automated two-tone testing at 26.5 dBm at a center frequency of 460 MHz.

products would normally be expected to be symmetric. While DR_{IM3} for the lower IM3 products is nearly identical to worst-case DR_{IM3} below 100 kHz, the sharp degradation in performance is not seen above 100 kHz. The lower IM3 curves appear much flatter as expected as the MDS approaches the system noise floor. Again degradations around 10 MHz and 100 MHz are due to spurious frequency content. At 1 MHz, the DR_{IM3} for the lower IM3 product is 22 dB higher than the DR_{IM3} of the upper IM3 product, improving from 95 dBc to 117 dBc.

The large return loss encountered in many one-port reflection measurements results in DR_{IM} being higher in reflection than in transmission. DR_{IM} in reflection was measured using a low-PIM termination realized as a terminated 75 m long, low-PIM cable as the DUT. This termination does not produce PIM measurable in this system. The power of each tone input to the cable was 26 dBm and the cable has a return loss of 25 dB. The DR_{IM3} characteristic is shown in

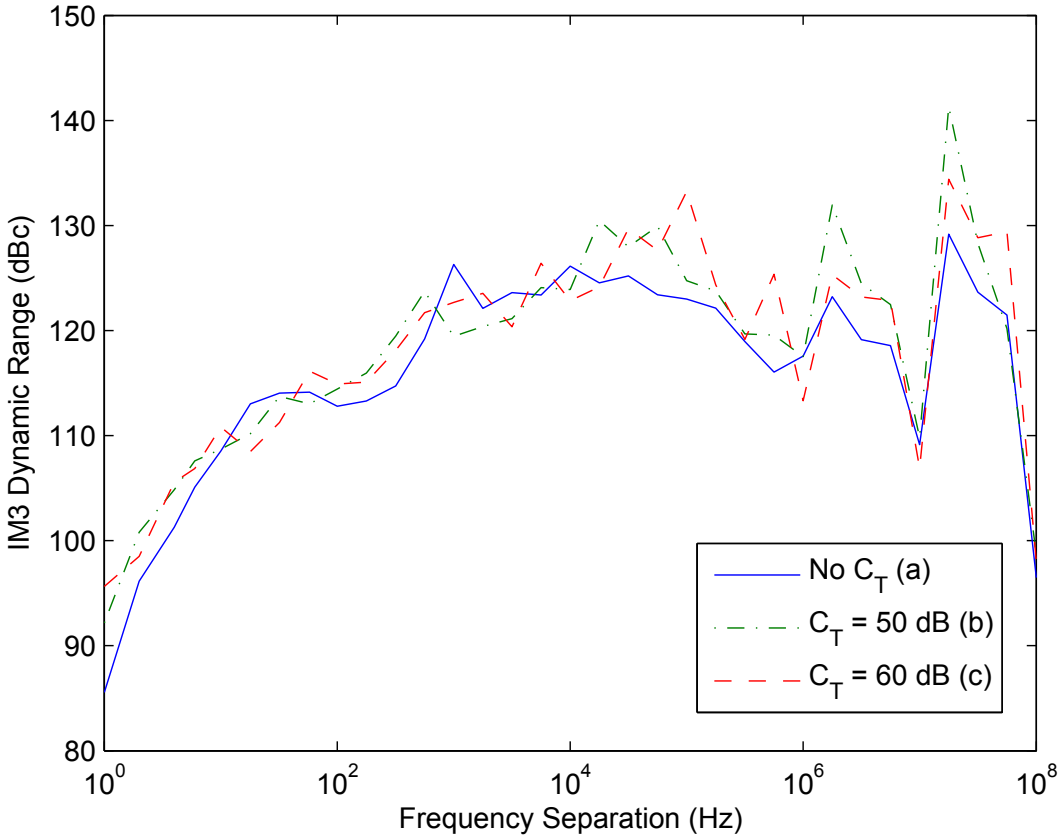

Figure 3.11: Third-order intermodulation dynamic range (DR_{IM3}) achieved for the lower IM3 product in two-port transmission configuration over frequency separation during automated two-tone testing at 26.5 dBm at a center frequency of 460 MHz.

Fig. 3.12. The additional return loss, RL, improves DR_{IM3} for the reflection measurement over the transmission measurement, reaching 139 dBc at 100 kHz, with a minimum of 99 dBc at 1 Hz. Compared to non-iterative analog cancellation, iterative analog cancellation improves DR_{IM} only at low tone separations. At 1 Hz, DR_{IM3} improves from 99 dBc to 111 dBc with a cancellation target, C_T, of 50 dB. The average cancellation of each curve is 47 dB for a single iteration, Curve (a) of Fig. 3.12, and 54 dB for a C_T of 50 dB, Curve (b) of Fig. 3.12. The higher cancellation was obtained at a cost of 1.1 extra iterations on average. The effect of extra cancellation on dynamic range is much less prominent as return loss increases, since the reduction of DUT output power reduces the analog cancellation, C_A, required for signals to be within a receiver dynamic range, DR_R, of the MDS. Again, the growth of system-generated IM3 products at 10 MHz and 100 MHz sharply degrades performance at those separations.

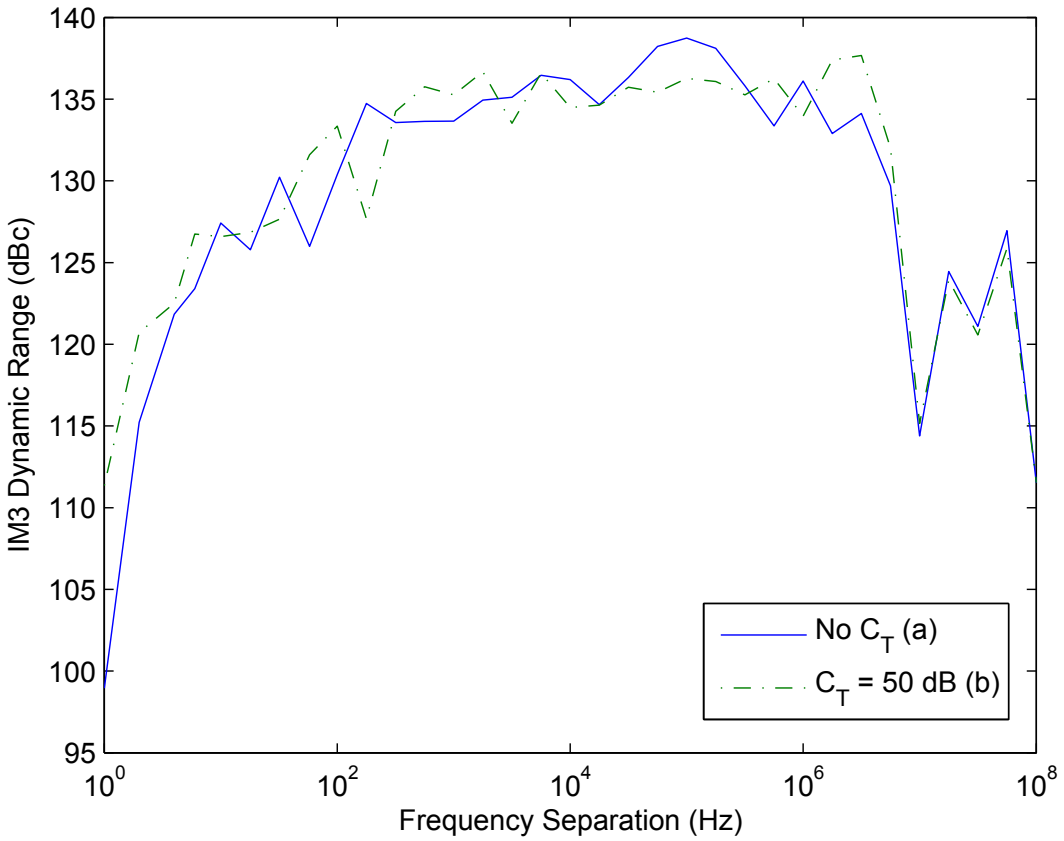

Figure 3.12: Worst-case third-order intermodulation dynamic range achieved in one-port reflection measurement over frequency separation during automated two-tone testing at 26 dBm at a center frequency of 460 MHz.

3.5.2 PIM in Laboratory Terminations

Several pairs of standard laboratory N-type terminations were characterized over a wide range of frequency separations. For each pair of terminations the return losses were very similar and well within specifications. Figs. 3.13 and 3.14 show the response of the Pasternack PE6154 and PE6152 N-type 2 W terminations. Each figure also contains the distortion characteristic of the low-PIM cable, which represents the lowest measurable distortion level in the system. Despite very similar sizes and construction, the PE6152 terminations had roughly 30 dB lower measured IM3 distortion than the PE6154. While the IM3 characteristics of the PE6154 terminations diverge above 100 Hz, the PE6152 terminations performed very similarly, albeit only slightly above the measurement threshold. The electro-thermal theory of intermodulation distortion predicts a 10 dB per decade slope [15]. From 1–100 Hz, the PE6154 and PE6152 terminations

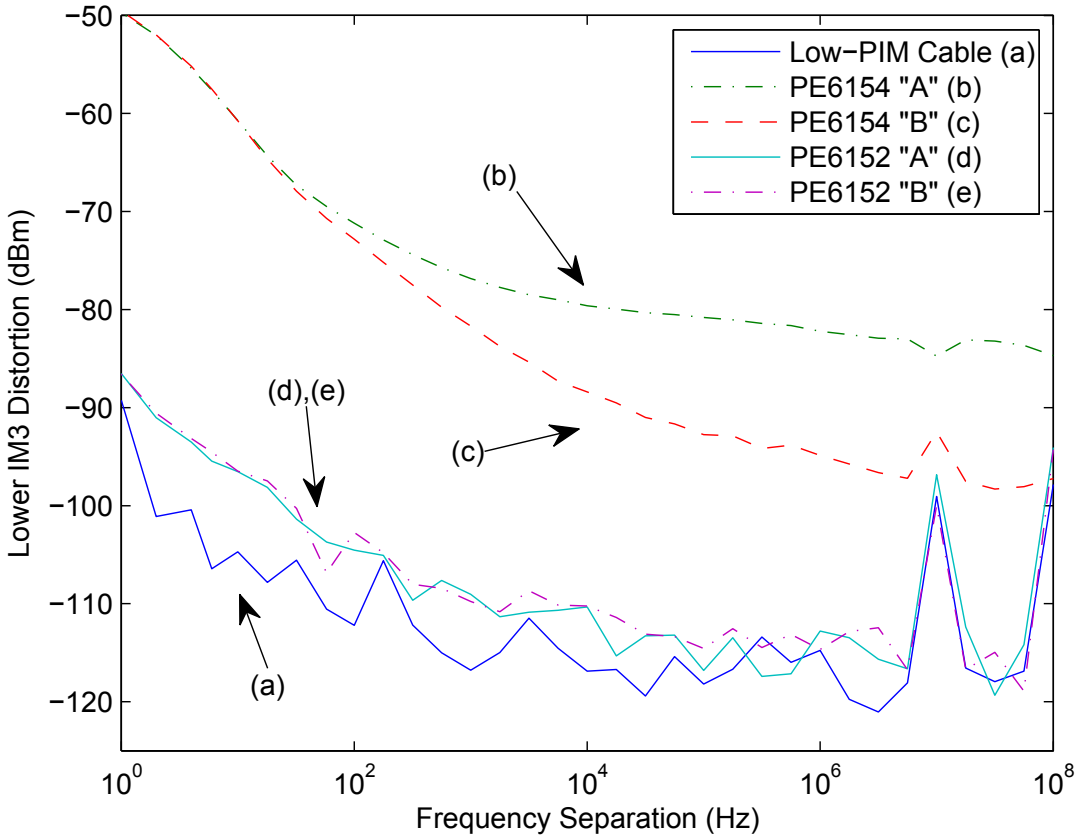

Figure 3.13: Measured third-order passive intermodulation distortion (lower IM3) of common laboratory 2 W N-type terminations using a two-tone test at 460 MHz. Measurement taken with 26 dBm input power for each tone.

follow this prediction very well, but begin to flatten out above 100–1000 Hz. For the PE6152 terminations, the flattening can be explained by the approach to the system noise floor, however the divergence and flattening of PIM of the PE6154 terminations cannot be explained simply by electro-thermal effects.

In addition to the 2 W terminations, pairs of the Pasternack PE6097 (5 W) and Pasternack PE6035 (10 W) high-power N-type terminations were also measured, shown in Figs. 3.15 and 3.16. Unlike the simple 2 W terminations, these high-power terminations have large finned aluminum heatsinks attached which are roughly the size of the body of the termination. While having PIM generally lower than that of the PE6154 terminations, the PIM of the high-power terminations varied more between terminations of the same type. The characteristic shape of these terminations is most exaggerated for the PE6097 terminations and features a mild slope

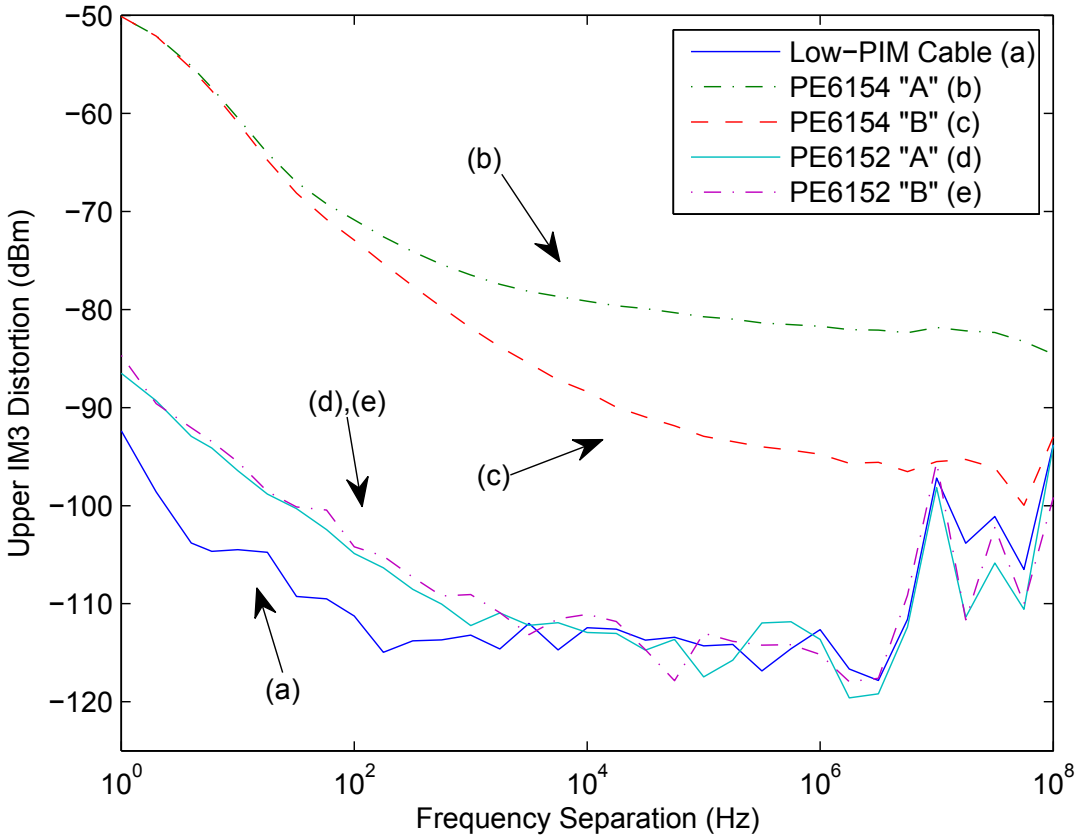

Figure 3.14: Measured third-order passive intermodulation distortion (upper IM3) of common laboratory 2 W N-type terminations using a two-tone test at 460 MHz. Measurement taken with 26 dBm input power for each tone.

from 1–1000 Hz followed by a much steeper slope from 1–10 kHz and a roughly flat response above 10 kHz. Simple electro-thermal theory does not suffice to explain these characteristics and the physical phenomenology is not well understood. It is noted that these characteristics are repeatable after disconnection and reconnection cycles and independent of center frequency over the range of the isolators.

It was previously demonstrated that for single-metal attenuators [97], terminations [15], and transmission lines [16], electro-thermal effects were the dominant source of PIM. The devices examined here contain multiple conductors and magnetic materials (nickel and stainless steel) and work remains to explain the non-electro-thermal PIM with dependence on frequency separation in a two-tone test.

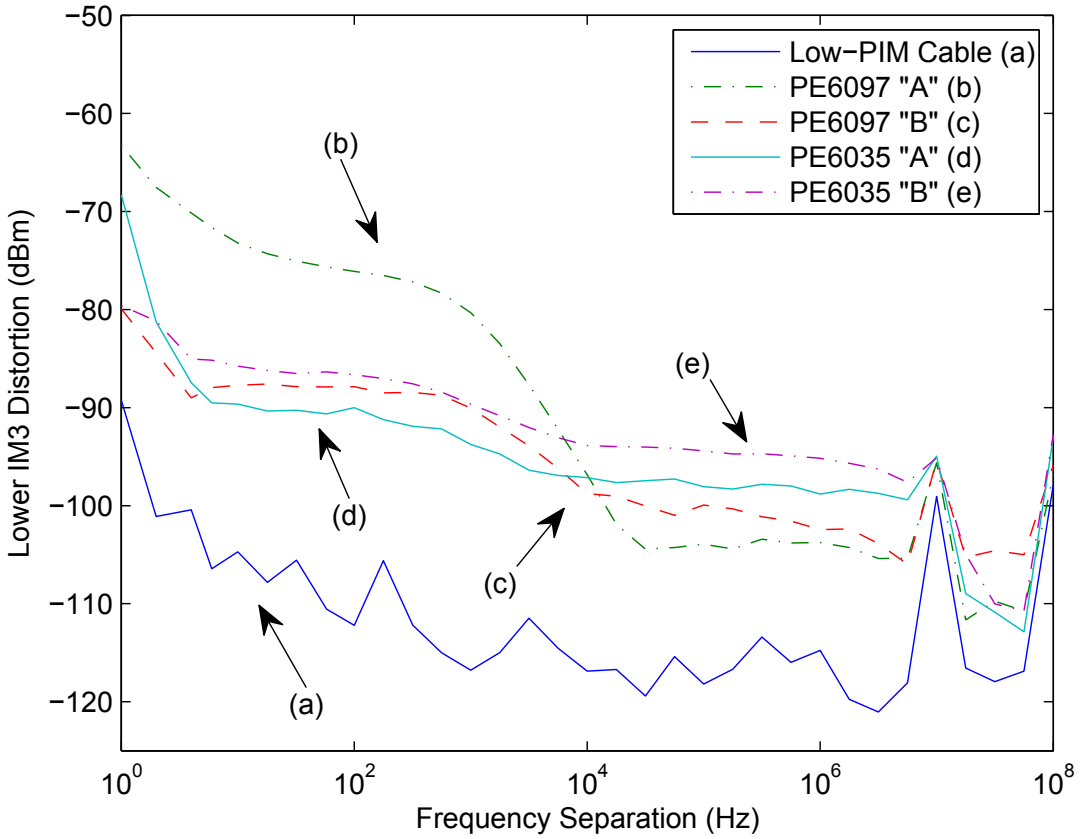

Figure 3.15: Measured third-order passive intermodulation distortion (lower IM3) of common laboratory high-power, finned N-type terminations using a two-tone test at 460 MHz. Measurement taken with 26 dBm input power for each tone.

3.6 Extension

The improved analog cancellation system developed here was applied to a passive intermodulation distortion measurement system, however, as noted in the introduction, analog cancellation is a widely used technique for a variety of applications. The analog canceller has been developed without loss of generality such that many of the improvements presented here could be adapted to fit a variety of these applications. In particular, replacement of the DUT with an antenna creates a structure very similar to the reflected power cancellers presented in [90–93]. With tighter integration, many of the existing limits on current performance could be improved, such as better resolution for the vector modulation amplitude tuning, or improved system linearity. In applications such as ground-penetrating radar, the improvement in noise and carrier suppression should enable better resolution for processing and detection.

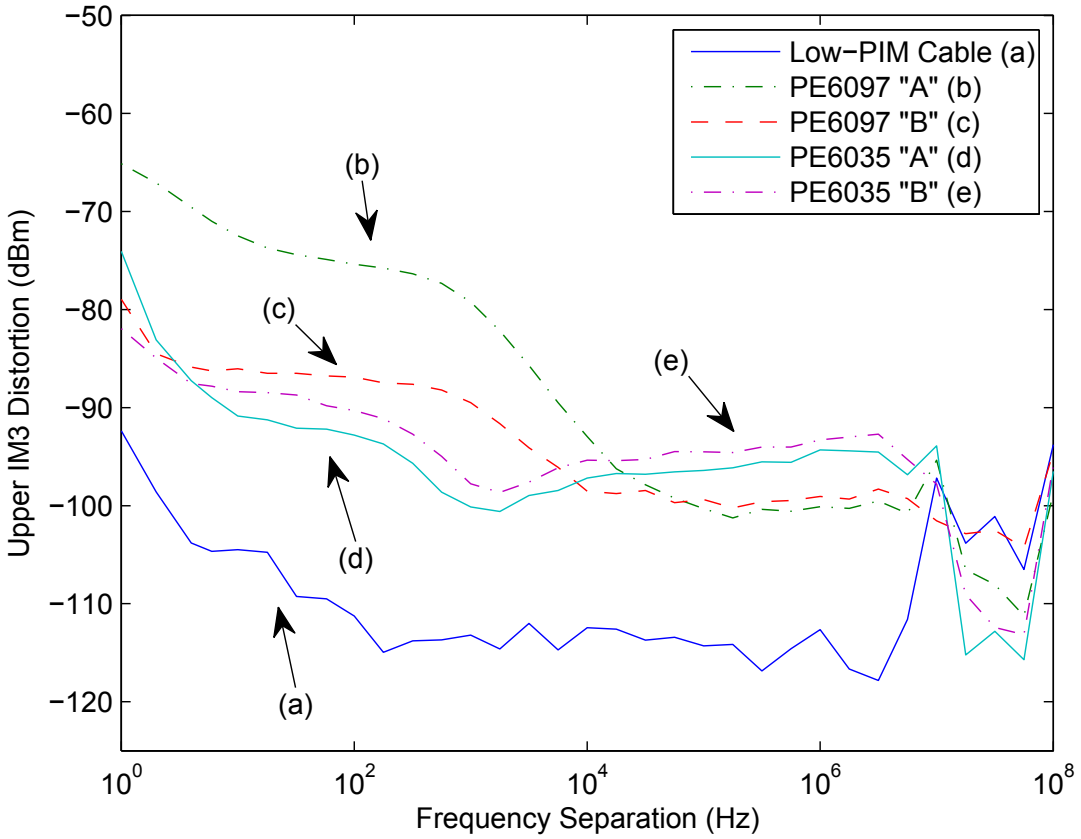

Figure 3.16: Measured third-order passive intermodulation distortion (upper IM3) of common laboratory high-power, finned N-type terminations using a two-tone test at 460 MHz. Measurement taken with 26 dBm input power for each tone.

3.7 Summary

An automated analog cancellation system was presented that exceeds or meets the performance of manually-tuned systems. A minimum of 70 dB of analog cancellation is achieved by integrating the calibration procedure in-line with canceller operation in a weakly iterative process. The extension in cancellation has been applied to intermodulation distortion measurement and a full discussion of the system features and cancellation dynamic range presented. The analog cancellation performance in the system exceeded the cancellation needed to maximize the effective dynamic range of current receiver systems, decoupling the sensitivity of the analog canceller system from system accuracy. In one-port reflection testing, the intermodulation dynamic range begins to approach the reported performance of filter-based commercial and high-performance intermodulation measurement systems, without the minimum frequency separation limit im-

posed by filters. Using this system, several common laboratory terminations were characterized over a frequency separation sweep of 1 Hz to 100 MHz with a center frequency of 460 MHz, for a maximum fractional tone separation of 21.7%. The sweep from very small frequency separations to very large would ordinarily require a combination of the previous systems, but has been achieved here without requiring any re-configuration.

Acknowledgment

The authors would like to thank Dr. J. Wilkerson for providing portions of the software. The authors also wish to thank Dr. A. Khalil and E. Peek of Hittite Microwave Corp. for discussions regarding vector modulators and providing vector modulators with superior performance.

Chapter 4

Radio Frequency Scattering by Vibrating Structures

4.1 Introduction

Radio frequency (RF) probing and characterization of vibrating objects provides a means of sensing that exploits acousto-electromagnetic interactions. Vibrations are induced on the remote object by a stimulant in a physical domain orthogonal to the RF sensing probe, using, for example, an acoustic or seismic wave. The transfer of energy from the acoustic to the electrical domain, i.e. the interaction of the vibrating object with an incident electromagnetic (EM) wave, creates a modulated reflected or scattered wave with characteristics unique to the structure or composition of the vibrating object. Information contained in the returned signal from the interaction can help inform a decision about the unknown object. In addition, RF probing allows for non-contact characterization of buried objects, or of features within the vibrating object itself, allowing for safe, stand-off, non-destructive evaluation. Examples of such sensing and imaging systems are used in landmine detection [27,85], evaluation of structural integrity [86,98], and medical imaging [86].

One of the greatest challenges in remote probing is detecting and characterizing an object based on unique features of a reflected EM signal. The traditional understanding of RF scattering from a vibrating surface is based solely on the Doppler effect [31–39]. More accurate analysis of the scattering, especially for complex motion, is limited to full-field EM solutions [40, 85, 99] or arbitrary waveform analysis [38, 39], both of which require numerical simulation and provide little intuition into the fundamental processes involved. Many of the unique characteristics of the reflected EM signal, such as modulation introduced by vibration, occur at small signal levels outside the dynamic range of conventional sensors. The strongest frequency component of a received EM signal corresponds to the transmitted signal itself, while the dynamic range of

the receiver limits the information that can be extracted from low-level sideband modulation. Recent advances in analog cancellation have significantly improved the dynamic range of RF sensors and the detection of sidebands in a reflected signal [52, 100–102]. It is therefore necessary to re-examine broad assumptions about the physical mechanisms that result in scattering. Reconsidering the assumptions leads to greater understanding of the fundamental limits of RF sensing systems and to the determination of new sensing modalities that either interfere with measurement or can be exploited for enhanced characterization.

Another major challenge in remote RF probing is detecting the modulated reflected signal in the presence of the directly reflected carrier [102]. The power of the modulation sidebands can be much smaller than the reflected carrier signal with the usefulness of the GPR system dependent on the ability to resolve low level sidebands typically within ten to a few thousand Hertz of the carrier frequency. The highest performance non-contact techniques for measuring vibration are laser-based, however line-of-sight operation restricts their expanded use [103]. As an alternative, microwave Doppler radar systems have been presented [27–30]. These systems use phase demodulation of the Doppler-modulated reflected signal and function primarily as time-domain position sensors, with a measurement resolution of micrometers when operating at 20–40 GHz at 1–2 m standoff from the target [28–30], but also as low as 1 nm when operating at 8 GHz very close-in to the target [27]. An alternative technique [104] exploits knowledge of the nonlinear modulation spectrum to reduce complexity but at a cost of significantly degraded measurement sensitivity.

In this chapter, compact analytical solutions are presented that lead to intuitive understanding of the physics behind modulation appearing on a reflected wave. (From an RF sensing perspective, it is nearly always better to detect modulation than to directly analyze the RF waveform.) Four modulation effects are identified for a simple vibrating plate. These are (1) traditional Doppler phase modulation (described in Section 4.2.1), (2) amplitude modulation deriving from special relativity [105] (described in Section 4.2.2), (3) path loss modulation (described in Section 4.2.3), and (4) modulation of radar cross section (RCS) (described in Section 4.2.4). Uniquely identifying these processes is important to correctly interpret scattered signals and sensor design. That is, measurement systems designed to only measure Doppler-type modulation may yield limited characterization. The effect of geometry and orientation beyond simple RCS modulation is discussed in Section 4.2.5. Additional modulation sources for non-perfectly reflecting targets are discussed in Section 4.2.6. The various types of modulation introduced are compared and explored in Sections 4.2.7 and 4.2.8, leading to the general result that each modulation process may be considered separably and then linearly or multiplicatively combined. Section 4.3 discusses the architecture and theoretical limitations of a vibration detection system based on analog cancellation [100] using the derived vibration modulation theory. Radar scattering measurements are presented in Section 4.4 verifying the dominance of Doppler

modulation and the significance of rotational modulation as an orthogonal sensing modality, as well as demonstrating ground-pentrating capability for the vibration detection system.

4.2 Vibration Modulation Analysis

The modulation of an EM signal can be generally partitioned into phase and amplitude modulation. The information in each of these modes will be interpreted differently depending on the sensing system and processing of the received signal. The following development aims to determine the fundamental limits of what can be sensed.

A monochromatic EM signal undergoing both amplitude and phase modulation can be represented as

$$s(t) = A(t)\cos\left[\omega t + \phi(t)\right], \tag{4.1}$$

where $A(t)$ is the amplitude modulation (AM) and $\phi(t)$ is the phase modulation (PM) of a sinusoid of frequency ω. These analog modulation terms are conventionally represented as

$$A(t) = A_0\left[1 + m_A x_A(t)\right] \tag{4.2}$$

$$\phi(t) = \phi_0 + m_\phi x_\phi(t), \tag{4.3}$$

where A_0 and ϕ_0 are constant scaling terms that do not contribute to modulation, and m_A and m_ϕ are the modulation indexes of AM and PM, respectively, coupling the modulating signals $x_A(t)$ and $x_\phi(t)$ to the incident wave. Specifically, for a vibrating object the modulating signal, $x(t)$, is often a sinusoid with vibrational radian frequency, ω_V. As a result, the modulation index, m_A or m_ϕ, is usually a function of the vibrational displacement amplitude, β. In special circumstances, PM can be interpreted as frequency modulation, as is the case for the conventional Doppler frequency shift.

The periodic modulation of an RF carrier tone, especially for small modulation indexes, has an insignificant impact on the amplitude of the primary tone, with the dominant observable effect being the tones introduced on either side of the carrier as shown in Fig. 4.1. Mathematically, this modulation spectrum can be represented as the Fourier series,

$$s(t) = \sum_{n=-\infty}^{\infty} A_n \cos(\omega_{\mathrm{RF}} + n\omega_V)t \tag{4.4}$$

where A_n is the amplitude of the sideband tone at a radian frequency offset of $n\omega_V$ from the RF carrier. The multiple discrete tones on each side of the carrier result when the modulation signal, $x_A(t)$ or $x_\phi(t)$, is periodic but not a simple sinusoid. For example, with acousto-EM interaction, $x(t)$ can have significant harmonic content at multiples of the vibration frequency,

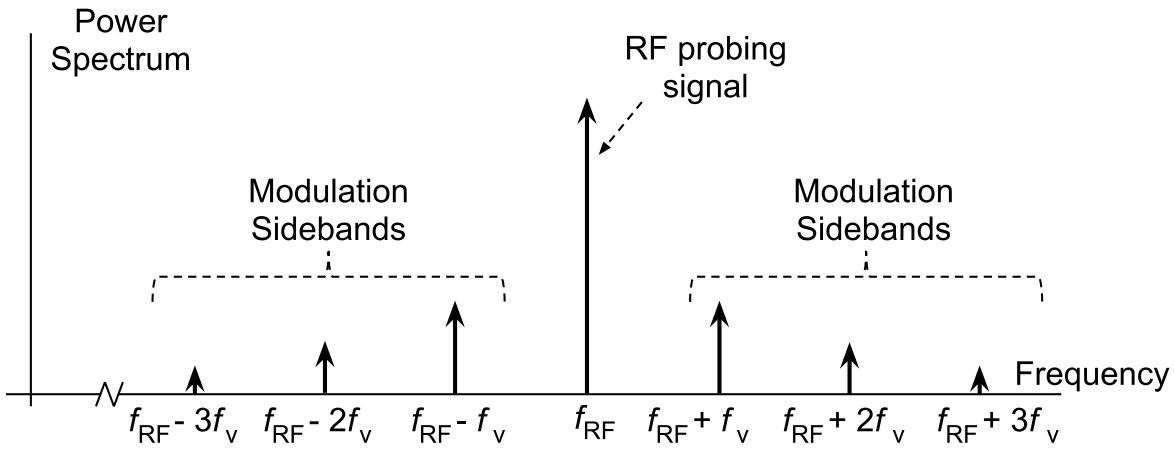

Figure 4.1: General modulation spectrum of an RF signal scattered from a vibrating object.

ω_V. For a small modulation index and as the harmonic order increases, A_n falls off quickly and drops below the noise floor of the RF sensor. This is the case for the modulation of a signal reflected from a vibrating surface.

In the following sections various modulation processes are explored for vibrating objects, starting with the most common, the Doppler effect. Extracting the theoretical modulation spectrum for each of these processes permits comparison of their contributions to the net scattering effect and potentially enables orthogonal sensor modalities leading to better characterization of remote vibrating objects.

4.2.1 Doppler Phase Modulation

The Doppler effect has been extensively studied in applications where a moving surface affects an incident field, particularly the returns of an EM radar signal [31–39]. It is primarily known for inducing a frequency shift on a carrier wave when the transmitting source and receiver are in linear relative motion. For an object in periodic motion, i.e. vibrating, a full modulation spectrum such as Fig.4.1 is produced.

The physical phenomenon producing the Doppler scattering effect is special relativity, with the illuminated object vibrating relative to both the transmitter and the receiver (which could be colocated). For a perfectly conducting reflecting surface (i.e., a mirror) it can be shown, using relativistic boundary conditions and the D'Alembert solution [38], that the reverse-traveling (scattered) waveform, $g(t)$, is a time-shifted version of $f(t)$, the forward-traveling (incident) wave,

$$g\left(t + \frac{r(t)}{c}\right) = -\gamma(t) f\left(t - \frac{r(t)}{c}\right), \tag{4.5}$$

where $r(t)$ is the position of the reflecting surface, c is the speed of light,

$$\gamma(t) = \frac{1 - \dfrac{v(t)}{c}}{1 + \dfrac{v(t)}{c}}, \tag{4.6}$$

and $v(t)$ is the time-derivative of $r(t)$.

A compact analytical solution for $g(t)$ is only possible when $r(t)$ can be represented as a low-order polynomial, such as when the reflecting surface is moving with constant velocity as then $r(t)$ is linear with respect to time [38]. When the motion is complex, such as with periodic vibration, approximation is needed to obtain an analytic result for $g(t)$ and its modulation components. The most common approximation uses the quasi-stationary approach, in which the motion of the reflecting surface is considered to be very slow relative to the speed of the EM signal, that is, $|v_{\text{peak}}| \ll c$, where v_{peak} is the peak velocity. At each instant in time, the motion of the boundary is approximated as having a constant velocity so that $r(t) = vt$. Inserting this motion into (4.5) and using variable substitution yields the general solution

$$g(t) = -\left(\frac{1 - v/c}{1 + v/c}\right) f\left[\left(\frac{1 - v/c}{1 + v/c}\right) t\right]. \tag{4.7}$$

For a sinusoidally-varying incident EM wave with radian frequency ω_{RF}, the scattered wave is

$$g(t) = -\left(\frac{1 - v/c}{1 + v/c}\right) \cos\left[\left(\frac{1 - v/c}{1 + v/c}\right) \omega_{\text{RF}} t\right]. \tag{4.8}$$

To simplify (4.8) for analysis and complete the quasi-stationary approximation, a Maclaurin series expansion is used, that is

$$\left(\frac{1 - v/c}{1 + v/c}\right) = 1 + 2\sum_{m=1}^{\infty} (-1)^m \left(\frac{v}{c}\right)^m \approx 1 - \frac{2v}{c} + \frac{2v^2}{c^2} + \ldots . \tag{4.9}$$

As $v \ll c$, only the first two terms of the series expansion are retained as the phase of the cosinusoid in (4.8), and the amplitude term is approximated as unity. Then (4.8) becomes

$$g(t) \approx \cos\left[\omega_{\text{RF}} t \left(1 - \frac{2v}{c}\right)\right] \approx \cos\left[\omega_{\text{RF}} t - 2k_{\text{RF}} r(t)\right], \tag{4.10}$$

where $k_{\text{RF}} = \omega_{\text{RF}}/c$ is the RF wavenumber. This result, (4.10), is the conventional Doppler equation for vibration. The phase term, $2k_{\text{RF}} r(t)$, can be interpreted as the change in the phase due to the variation of the round-trip distance to the plate, $2r(t)$. As the spatial delay changes over time, phase modulation is induced on the scattered wave. While strictly derived

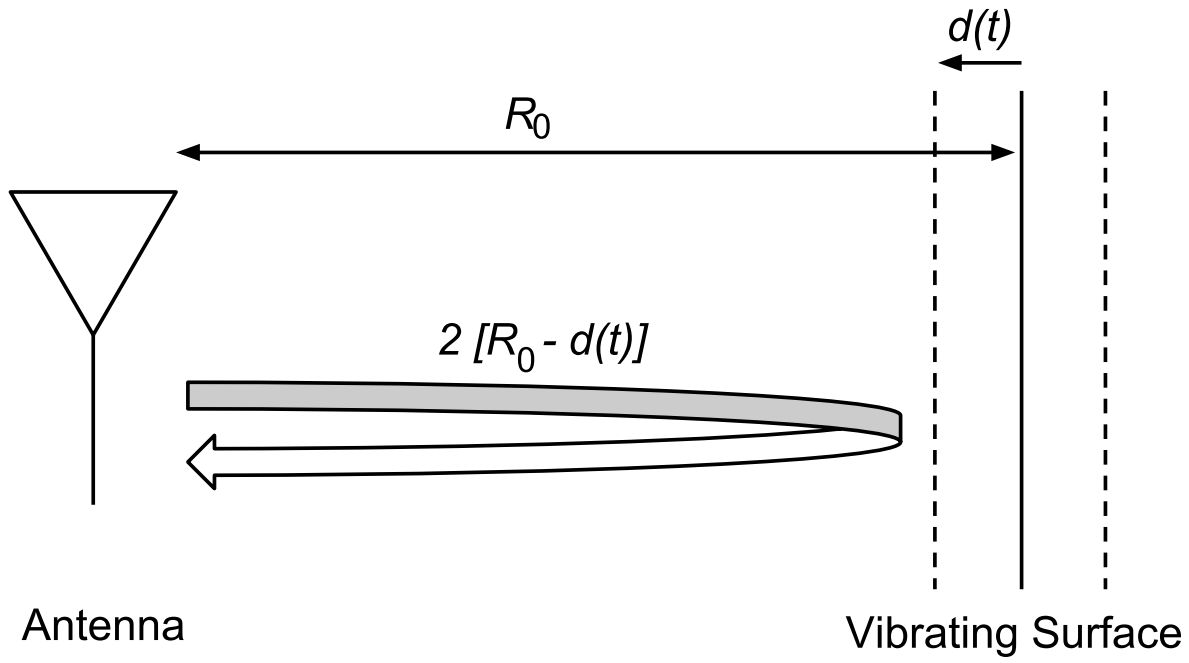

Figure 4.2: Displacement of a moving surface relative to a monostatic radar antenna.

for constant velocity motion, (4.10) is often used for arbitrary $r(t)$, neglecting errors introduced by higher orders of motion. The error of the quasi-stationary approach has been shown to be bounded on the order of $|v_{\text{peak}}|/c$ [34]. For a sinusoidally vibrating surface at 1 kHz with a peak displacement of 1 mm, the peak velocity is $\pm 2\pi$ m/s and the error is less than one part in 10^7. Since $|v_{\text{peak}}| \ll c$, the error is generally negligible.

Using (4.10), the received modulated reflection from a moving plane mirror as shown in Fig. 4.2 is

$$s(t) = \alpha_0 \cos\left[\omega_{\text{RF}} t - \phi_D(t)\right], \tag{4.11}$$

where

$$\phi_D(t) = 2k_{\text{RF}}\left[R_0 - d(t)\right] = \phi_0 - 2k_{\text{RF}} d(t), \tag{4.12}$$

α_0 is the received RF signal amplitude, R_0 is the average separation of the object and the co-located transmitter and receiver, and $d(t)$ is the time-varying surface displacement. The amplitude modulation term from special relativity, $\gamma(t)$, which was dropped in (4.10), is multiplicative and will be considered separately. With sinusoidal surface displacement and ignoring the constant phase term (as it introduces no modulation), the normalized, phase-modulated

reflected signal is

$$s'(t) = \cos\left(\omega_{\mathrm{RF}} t + 2k_{\mathrm{RF}}\beta\cos\left(\omega_V t\right)\right), \tag{4.13}$$

where β is the vibrational displacement amplitude and ω_V is the angular frequency of vibration. To obtain a simple expression for the modulation spectrum, (4.13) is expanded into its complex exponential form, so that

$$\begin{aligned} s'(t) =& \tfrac{1}{2} e^{\jmath\omega_{\mathrm{RF}} t} e^{\jmath 2k_{\mathrm{RF}}\beta\cos(\omega_V t)} + \tfrac{1}{2} e^{-\jmath\omega_{\mathrm{RF}} t} e^{-\jmath 2k_{\mathrm{RF}}\beta\cos(\omega_V t)} \\ =& \tfrac{1}{2} e^{\jmath\omega_{\mathrm{RF}} t} e^{\jmath 2k_{\mathrm{RF}}\beta\cos(\omega_V t)} + \tfrac{1}{2} e^{-\jmath\omega_{\mathrm{RF}} t} e^{\jmath 2k_{\mathrm{RF}}\beta\cos(\omega_V t - \pi)}. \end{aligned} \tag{4.14}$$

Using the Jacobi-Anger expansion, (4.14) can be written as

$$\begin{aligned} s'(t) =& \frac{1}{2} e^{\jmath\omega_{\mathrm{RF}} t} \sum_{n=-\infty}^{\infty} \jmath^n J_n(2k_{\mathrm{RF}}\beta) e^{\jmath n\omega_V t} + \frac{1}{2} e^{-\jmath\omega_{\mathrm{RF}} t} \sum_{n=-\infty}^{\infty} \jmath^n J_n(2k_{\mathrm{RF}}\beta) e^{\jmath n\omega_V t} e^{-\jmath n\pi}) \\ =& \frac{1}{2} \sum_{n=-\infty}^{\infty} \jmath^n J_n(2k_{\mathrm{RF}}\beta) e^{\jmath(\omega_{\mathrm{RF}} t + n\omega_V t)} + \frac{1}{2} \sum_{n=-\infty}^{\infty} \jmath^{-n} J_n(2k_{\mathrm{RF}}\beta) e^{-\jmath(\omega_{\mathrm{RF}} t - n\omega_V t)}, \end{aligned} \tag{4.15}$$

where $J_n(x)$ is the n^{th}-order Bessel function of the first kind. As the summation over n is infinite, $-n$ can be directly substituted for n in the second term and the complex terms combined, so that

$$\begin{aligned} s'(t) =& \frac{1}{2} \sum_{n=-\infty}^{\infty} \jmath^n J_n(2k_{\mathrm{RF}}\beta) e^{\jmath(\omega_{\mathrm{RF}} t + n\omega_V t)} + \frac{1}{2} \sum_{n=-\infty}^{\infty} \jmath^n J_{-n}(2k_{\mathrm{RF}}\beta) e^{-\jmath(\omega_{\mathrm{RF}} t + n\omega_V t)} \\ =& \frac{1}{2} \sum_{n=-\infty}^{\infty} \jmath^n J_n(2k_{\mathrm{RF}}\beta) e^{\jmath(\omega_{\mathrm{RF}} t + n\omega_V t)} + \frac{1}{2} \sum_{n=-\infty}^{\infty} \jmath^n (-1)^n J_n(2k_{\mathrm{RF}}\beta) e^{-\jmath(\omega_{\mathrm{RF}} t + n\omega_V t)} \\ =& \frac{1}{2} \sum_{n=-\infty}^{\infty} e^{\jmath n\frac{\pi}{2}} J_n(2k_{\mathrm{RF}}\beta) e^{\jmath(\omega_{\mathrm{RF}} t + n\omega_V t)} + \frac{1}{2} \sum_{n=-\infty}^{\infty} e^{-\jmath n\frac{\pi}{2}} J_n(2k_{\mathrm{RF}}\beta) e^{-\jmath(\omega_{\mathrm{RF}} t + n\omega_V t)} \\ =& \frac{1}{2} \sum_{n=-\infty}^{\infty} J_n(2k_{\mathrm{RF}}\beta) \left[e^{\jmath\left(\omega_{\mathrm{RF}} t + n\omega_V t + n\frac{\pi}{2}\right)} + e^{-\jmath\left(\omega_{\mathrm{RF}} t + n\omega_V t + n\frac{\pi}{2}\right)} \right] \\ =& \sum_{n=-\infty}^{\infty} J_n(2k_{\mathrm{RF}}\beta) \cos\left[\left(\omega_{\mathrm{RF}} + n\omega_V\right) t + n\frac{\pi}{2} \right]. \end{aligned} \tag{4.16}$$

Since $J_{-n}(x) = (-1)^n J_n(x)$, the phase of the upper and lower sideband tones are the same. For very small vibrations (i.e., $\beta \ll \lambda$),

$$J_n(x) \approx \frac{x^n}{2^n n!}. \tag{4.17}$$

Thus substituting (4.17) in (4.16), the amplitude of the n-th Doppler sideband tone relative to

the RF carrier tone is

$$A_{\text{Doppler},n} \approx \frac{1}{n!}\left(k_{\text{RF}}\beta\right)^n = \frac{1}{n!}\left(\frac{\beta\omega_{\text{RF}}}{c}\right)^n = \frac{(2\pi)^n}{n!}\left(\frac{\beta}{\lambda}\right)^n. \tag{4.18}$$

For very small vibrations, higher-order tones will decrease steeply in power. Only the lowest-order tones are likely to be measurable. Using only first-order terms, the modulated signal is approximated as

$$\begin{aligned} s'(t) &\approx \cos\left(\omega_{\text{RF}}t\right) \pm k_{\text{RF}}\beta\cos\left[\omega_{\text{RF}}t \pm \left(\omega_V t + \frac{\pi}{2}\right)\right] \\ &\approx \cos\left(\omega_{\text{RF}}t\right) - k_{\text{RF}}\beta\sin\left[\left(\omega_{\text{RF}} + \omega_V\right)t\right] - k_{\text{RF}}\beta\sin\left[\left(\omega_{\text{RF}} - \omega_V\right)t\right], \end{aligned} \tag{4.19}$$

which is the original RF signal with two modulation tones, one on each side of the RF tone. It should be noted that this approximation, sometimes referred to as narrow-band angle modulation [58], is indistinguishable from AM. For example, the amplitude modulation of a signal can be described by

$$s'(t) = \left[1 + m_D x(t)\right]\cos\left(\omega_{\text{RF}}t\right), \tag{4.20}$$

where

$$m_D x(t) = -2k_{\text{RF}}\beta\sin\left(\omega_V t\right) = -\frac{2\beta\omega_{\text{RF}}}{c}\sin\left(\omega_V t\right). \tag{4.21}$$

The trigonometric expansion of (4.20) is identical to (4.19). However, no physical vibrational mechanism is known to directly produce this form of AM, so that any received signal having the form of (4.19) will be due to Doppler scattering.

In this subsection, Doppler phase modulation of an EM wave scattered from a vibrating object was derived from first principles starting with the special relativity principle. The quasi-stationary approach was used to simplify intractable equations by assuming that the vibrating object was moving at a much slower rate than the EM wave, that is $|v_{\text{peak}}| \ll c$. This led to the familiar result for the Doppler effect (4.16).

4.2.2 Amplitude Modulation Due to Special Relativity

In the quasi-stationary derivation of the Doppler equation (4.13), the amplitude modulation term, $\gamma(t)$ in (4.5), was considered to be a constant. This subsection considers non-constant $\gamma(t)$ for a sinusoidally vibrating target. As with the development of the Doppler equation, a nonlinear equation of motion, $r(t)$, is used.

Considering only the amplitude term from special relativity, and no Doppler phase modulation, the received modulated signal is

$$s(t) = \gamma(t)\cos(\omega_{\text{RF}}t). \tag{4.22}$$

To obtain the modulation spectrum, $\gamma(t)$ is expanded using a Maclaurin series, so that

$$\gamma(t) = \frac{1 - v(t)/c}{1 + v(t)/c} = 1 + 2\sum_{m=1}^{\infty} (-1)^m \left(\frac{v(t)}{c}\right)^m. \tag{4.23}$$

With sinusoidal motion, $v(t) = \beta\omega_V \cos(\omega_V t)$, where β is the vibrational displacement amplitude and ω_V is the vibrational radian frequency, (4.23) can be written as

$$\gamma(t) = 1 + 2\sum_{m=1}^{\infty} (-1)^m \left(\frac{\beta\omega_V}{c}\right)^m [\cos(\omega_V t)]^m. \tag{4.24}$$

The term, $\cos^m\theta$, has the trigonometric expansion

$$\cos^m\theta = \begin{cases} \dfrac{2}{2^m}\displaystyle\sum_{j=0}^{\frac{m-1}{2}} \binom{m}{j} \cos\left[(m-2j)\,\theta\right] & \text{for odd } m \\ \dfrac{1}{2^m}\binom{m}{\frac{m}{2}} + \dfrac{2}{2^m}\displaystyle\sum_{j=0}^{\frac{m}{2}-1} \binom{m}{j} \cos\left[(m-2j)\,\theta\right] & \text{for even } m, \end{cases} \tag{4.25}$$

where $\binom{m}{j}$ is the binomial coefficient. In (4.25) it is seen that odd powers of cosine produce odd harmonic tones and the even powers produce DC and even harmonic tones. Thus (4.24) can be partitioned into even and odd components,

$$\gamma(t) = \gamma_{\text{odd}}(t) + \gamma_{\text{even}}(t), \tag{4.26}$$

where $\gamma_{\text{odd}}(t)$ collects the terms in $\gamma(t)$ with m odd, corresponding to the odd-order sideband tones of the RF signal, and $\gamma_{\text{even}}(t)$ collects the terms in $\gamma(t)$ with m even, corresponding to the even-order sideband tones. First, considering only the odd tones:

$$\begin{aligned} \gamma_{\text{odd}}(t) =& 2\sum_{\substack{m=1 \\ m \text{ odd}}}^{\infty} (-1)^m \left(\frac{\beta\omega_V}{c}\right)^m \frac{2}{2^m} \sum_{j=0}^{\frac{m-1}{2}} \binom{m}{j} \cos\left[(m-2j)\omega_V t\right] \\ =& 4\sum_{\substack{m=1 \\ m \text{ odd}}}^{\infty} \sum_{j=0}^{\frac{m-1}{2}} (-1)^m \left(\frac{\beta\omega_V}{2c}\right)^m \binom{m}{j} \cos\left[(m-2j)\omega_V t\right]. \end{aligned} \tag{4.27}$$

With $n = m - 2j$, $p = \frac{1}{2}(m-n)$, and re-arranging,

$$\begin{aligned}
\gamma_{\text{odd}}(t) =& 4 \sum_{\substack{m=1 \\ m \text{ odd}}}^{\infty} \sum_{\substack{n=1 \\ n \text{ odd}}}^{m} (-1)^m \left(\frac{\beta\omega_V}{2c}\right)^m \binom{m}{\frac{m-n}{2}} \cos(n\omega_V t) \\
=& 4 \sum_{\substack{n=1 \\ n \text{ odd}}}^{\infty} \sum_{\substack{m=n \\ m \text{ odd}}}^{\infty} (-1)^m \left(\frac{\beta\omega_V}{2c}\right)^m \binom{m}{\frac{m-n}{2}} \cos(n\omega_V t) \\
=& 4 \sum_{\substack{n=1 \\ n \text{ odd}}}^{\infty} \sum_{p=1}^{\infty} (-1)^{2p+n} \left(\frac{\beta\omega_V}{2c}\right)^{2p+n} \binom{2p+n}{p} \cos(n\omega_V t) \\
=& \sum_{\substack{n=1 \\ n \text{ odd}}}^{\infty} F_{\gamma,n \text{ odd}} \cos(n\omega_V t), \qquad (4.28)
\end{aligned}$$

where $F_{\gamma,n \text{ odd}}$ represents the n-th Fourier series coefficient for all odd sideband tones. Following a similar development with $\gamma_{\text{even}}(t)$, the expression for the n-th Fourier series coefficient for the even sideband tones yields

$$\gamma_{\text{even}}(t) = F_{\gamma,0} + \sum_{\substack{n=1 \\ n \text{ even}}}^{\infty} F_{\gamma,n \text{ even}} \cos(n\omega_V t), \qquad (4.29)$$

where $F_{\gamma,n \text{ even}} = F_{\gamma,n \text{ odd}} = F_{\gamma,n}$. Collecting even and odd contributions yields the amplitude modulation term,

$$\gamma(t) = \gamma_{\text{odd}}(t) + \gamma_{\text{even}}(t) = F_{\gamma,0} + \sum_{n=1}^{\infty} F_{\gamma,n} \cos(n\omega_V t), \qquad (4.30)$$

having the Fourier series coefficients,

$$F_{\gamma,0} = 1 + 2\sum_{p=1}^{\infty} \left(\frac{\beta\omega_V}{2c}\right)^{2p} \binom{2p}{p} \qquad (4.31)$$

$$F_{\gamma,n} = 4\left(\frac{\beta\omega_V}{2c}\right)^n (-1)^n \sum_{p=0}^{\infty} \left(\frac{\beta\omega_V}{2c}\right)^{2p} \binom{2p+n}{p}. \qquad (4.32)$$

Using the assumption that $\beta\omega_V = |v_{\text{peak}}| \ll c$, the Fourier series coefficients can be approxi-

mated using only the $(p = 0)$ term so that

$$F_{\gamma,0} \approx 1 \tag{4.33}$$

$$F_{\gamma,n} \approx 4 \left(\frac{\beta \omega_V}{2c} \right)^n . \tag{4.34}$$

Using (4.22) and (4.30), the scattered wave with AM due to special relativity can be written as

$$\begin{aligned} s(t) &= \left[F_{\gamma,0} + \sum_{n=1}^{\infty} F_{\gamma,n} \cos\left(n \omega_V t\right) \right] \cos(\omega_{\mathrm{RF}} t) \\ &= F_{\gamma,0} \cos(\omega_{\mathrm{RF}} t) + \sum_{n=1}^{\infty} \left[\frac{F_{\gamma,n}}{2} \cos\left[\left(\omega_{\mathrm{RF}} \pm n \omega_V \right) t \right] \right] . \end{aligned} \tag{4.35}$$

Thus the power of the n-th special relativity AM sideband tone relative to the RF carrier tone is

$$A_{\gamma,n} \approx \frac{2}{2^n} \left(\frac{\beta \omega_V}{c} \right)^n . \tag{4.36}$$

The ratio of the power of the lowest-order sideband tone of Doppler PM in (4.18) to the power of the lowest-order sideband tone of AM due to special relativity in (4.36) is the ratio of the RF to the vibration frequency, that is

$$\frac{A_{\mathrm{Doppler},1}}{A_{\gamma,1}} = \frac{\omega_{\mathrm{RF}}}{\omega_V}. \tag{4.37}$$

In most standoff sensing applications where RF propagation is required, the vibration frequency will be many orders of magnitude less than RF, so that the special relativity AM term will be negligible. In the case of a hand-held metal-detector, the vibrational frequency and RF could be separated by a factor of ten to a thousand so that it may be possible to partition modulation due to special relativity into phase (i.e. Doppler) and amplitude components.

In this subsection, special relativity amplitude modulation, commonly dropped due to the quasi-stationary approximation, was expanded into its Fourier series representation, (4.35), and shown to produce sideband tones significantly below the Doppler PM tones.

4.2.3 Far-Field Path Loss Modulation

When characterizing a vibrating object at a standoff distance, the incident power on the object decreases with increasing distance due to spherical spreading of the propagating wave. As the object moves closer or further from the transmitting source, the attenuation, commonly termed path loss, will be modulated. This section examines the contribution from this modulation on the received scattered signal. Path loss modulation is not known to have been previously

reported in the literature. Conventional Doppler analysis assumes an incident plane wave on the target, which experiences no signal attenuation through spherical spreading.

The reflected power received by a radar antenna from a perfectly conductive surface in the far-field is given by the radar equation [61],

$$P_{\mathrm{R}} = \frac{P_{\mathrm{T}} G_{\mathrm{T}} G_{\mathrm{R}} \lambda^2 \sigma}{(4\pi)^3 r_{\mathrm{T}}^2 r_{\mathrm{R}}^2}, \tag{4.38}$$

where P_{T} is the transmitted signal power, G_{T} and G_{R} are the gains of the transmit and receive antennas respectively, λ is the RF wavelength, σ is the radar cross-section, and r_{T} and r_{R} are the distances from the reflector to the transmit and receive antennas respectively. The radar equation, (4.38), assumes ideal linear interaction of the EM wave with the reflecting object and ideal free-space propagation. While other models are available which attempt to account for ground effects and other non-ideal conditions, they are primarily empirical or statistically-based and require some knowledge of the propagation link [23, 61]. In the absence of best-fit models, the physics-based approach works best.

With a monostatic radar, the received signal power is inversely proportional to the fourth power of the standoff distance, the result of spherical spreading of energy in both the transmit and receive propagation paths. As a reflector vibrates, the distance between the radar antenna and target will change, introducing modulation of the effective path loss so that the received signal is

$$s(t) = \alpha_0 A_{\mathrm{PL}}(t) \cos\left(\omega_{\mathrm{RF}} t\right), \tag{4.39}$$

where

$$A_{\mathrm{PL}}(t) \propto \frac{1}{\left[R_0 - d(t)\right]^2}, \tag{4.40}$$

α_0 is the received RF signal amplitude, ω_{RF} is the RF radian frequency, R_0 is the average separation between the reflecting surface and antenna, and $d(t)$ is the time-varying surface displacement. Considering the surface displacement to be sinusoidal, the normalized modulation signal becomes

$$A'_{\mathrm{PL}}(t) = \frac{1}{\left[1 - B\cos\left(\omega_V t\right)\right]^2}, \tag{4.41}$$

where ω_V is the radian frequency of vibration, $B = \beta / R_0$ is the distance-normalized displacement amplitude, and β is the vibrational displacement amplitude of the surface. The radar equation, (4.38), assumes that the target is in the far-field, implying that $R_0 \gg \beta$ and therefore

$B \ll 1$. The modulation tone, (4.41), can be expanded using a Maclaurin series, so that

$$A'_{\mathrm{PL}}(t) = \sum_{m=0}^{\infty} (m+1) \left[B \cos\left(\omega_V t\right)\right]^m . \tag{4.42}$$

As with (4.24), (4.42) can be partitioned into components corresponding to even and odd sideband tones,

$$A'_{\mathrm{PL}}(t) = A'_{\mathrm{PL,odd}}(t) + A'_{\mathrm{PL,even}}(t), \tag{4.43}$$

where $A'_{\mathrm{PL,odd}}(t)$ collects the terms in $A'_{\mathrm{PL}}(t)$ with m odd, and $A'_{\mathrm{PL,even}}(t)$ collects the terms in $A'_{\mathrm{PL}}(t)$ with m even. First, considering only the odd sideband tones:

$$\begin{aligned} A'_{\mathrm{PL,odd}}(t) &= \sum_{\substack{m=1 \\ m \text{ odd}}}^{\infty} (m+1)\, B^m \frac{2}{2^m} \sum_{j=0}^{\frac{m-1}{2}} \binom{m}{j} \cos\left[(m-2j)\,\omega_V t\right] \\ &= \sum_{\substack{m=1 \\ m \text{ odd}}}^{\infty} \sum_{j=0}^{\frac{m-1}{2}} (m+1)\, 2 \left(\frac{B}{2}\right)^m \binom{m}{j} \cos\left[(m-2j)\,\omega_V t\right]. \end{aligned} \tag{4.44}$$

With $n = m - 2j$, $p = \frac{1}{2}(m-n)$, and re-arranging the summations,

$$\begin{aligned} A'_{\mathrm{PL,odd}}(t) &= \sum_{\substack{m=1 \\ m \text{ odd}}}^{\infty} \sum_{\substack{n=1 \\ n \text{ odd}}}^{m} 2\,(m+1) \left(\frac{B}{2}\right)^m \binom{m}{\frac{m-n}{2}} \cos\left(n\omega_V t\right) \\ &= \sum_{\substack{n=1 \\ n \text{ odd}}}^{\infty} \sum_{\substack{m=n \\ m \text{ odd}}}^{\infty} 2\,(m+1) \left(\frac{B}{2}\right)^m \binom{m}{\frac{m-n}{2}} \cos\left(n\omega_V t\right) \\ &= \sum_{\substack{n=1 \\ n \text{ odd}}}^{\infty} \sum_{p=0}^{\infty} 2\,(2p+n+1) \left(\frac{B}{2}\right)^{2p+n} \binom{2p+n}{p} \cos\left(n\omega_V t\right) \\ &= \sum_{\substack{n=1 \\ n \text{ odd}}}^{\infty} F_{\mathrm{PL},n \text{ odd}} \cos\left(n\omega_V t\right), \end{aligned} \tag{4.45}$$

where $F_{\mathrm{PL},n \text{ odd}}$ represents the n-th Fourier series coefficient for all odd sideband tones. Following a similar development with $A'_{\mathrm{PL,even}}(t)$, the expression for the n-th Fourier series coefficient for the even sideband tones is

$$A'_{\mathrm{PL,even}}(t) = F_{\mathrm{PL},0} + \sum_{\substack{n=1 \\ n \text{ even}}}^{\infty} F_{\mathrm{PL},n \text{ even}} \cos\left(n\omega_V t\right), \tag{4.46}$$

where $F_{\mathrm{PL},n\ \mathrm{even}} = F_{\mathrm{PL},n\ \mathrm{odd}} = F_{\mathrm{PL},n}$. Collecting the Fourier series representations for both even and odd sideband tones yields

$$A'_{\mathrm{PL}}(t) = A'_{\mathrm{PL,odd}}(t) + A'_{\mathrm{PL,even}}(t) = F_{\mathrm{PL},0} + \sum_{n=1}^{\infty} F_{\mathrm{PL},n} \cos\left(n\omega_V t\right), \tag{4.47}$$

with Fourier series coefficients,

$$F_{\mathrm{PL},0} = \sum_{p=0}^{\infty} (p+1) \left(\frac{B}{2}\right)^{2p} \binom{2p+1}{p+1} \tag{4.48}$$

$$F_{\mathrm{PL},n} = 2\left(\frac{B}{2}\right)^{n} \sum_{p=0}^{\infty} (p+1) \left(\frac{B}{2}\right)^{2p} \binom{2p+1+n}{p+1}. \tag{4.49}$$

Using $B \ll 1$, the higher order summation terms in $F_{\mathrm{PL},0}$ and $F_{\mathrm{PL},n}$ will rapidly decrease for $p > 0$. Taking only the first term of the summation, the Fourier coefficients can be approximated as

$$F_{\mathrm{PL},0} \approx 1 \tag{4.50}$$

$$F_{\mathrm{PL},n} \approx 2\,(n+1) \left(\frac{B}{2}\right)^{n}. \tag{4.51}$$

Combining (4.39) and (4.47), the normalized modulated received signal is then

$$\begin{aligned} s'(t) &= A'_{\mathrm{PL}}(t) \cos\left(\omega_{RF} t\right) \\ &= \left[F_{\mathrm{PL},0} + \sum_{n=1}^{\infty} F_{\mathrm{PL},n} \cos\left(n\omega_V t\right)\right] \cos\left(\omega_{\mathrm{RF}} t\right) \\ &= F_{\mathrm{PL},0} \cos\left(\omega_{RF} t\right) + \sum_{n=1}^{\infty} \frac{F_{\mathrm{PL},n}}{2} \cos\left[\left(\omega_{\mathrm{RF}} \pm n\omega_V\right) t\right]. \end{aligned} \tag{4.52}$$

Thus the power of the n-th path-length attenuation sideband tone relative to the RF carrier tone is

$$A_{\mathrm{PL},n} \approx \left(\frac{n+1}{2^n}\right) \left(\frac{\beta}{R_0}\right)^{n}. \tag{4.53}$$

In this subsection, path loss modulation emerged by considering variation in the distance between the vibrating object and the radar antenna. Small changes in distance due to vibration of the target object leads to the appearance of sideband tones, with power proportional to the vibrational displacement amplitude and standoff distance. Far-field assumptions ($\beta \ll R_0$) suggest that sideband tones from path loss modulation will be weak, however, they are functionally independent of RF wavelength, unlike Doppler phase modulation. An ideal propagation

link was assumed in the derivation, but path loss modulation should also appear in non-ideal scenarios, potentially obscured by "excess loss" terms related to terrain effects or destructive interference as in [23].

4.2.4 Modulation of Radar Cross Section

With any target, physical geometry and orientation will significantly impact the scattered signal. The complexity of the target structure and motion create a non-uniform reflector for the incident EM wave. Scattered reflections from various points on the vibrating object will combine coherently, canceling or summing based on spatial and phase relationships and appearing as new modes of modulation on the net scattered wave. When an object is intentionally vibrated by a seismic or acoustic signal, additional modes of motion may also appear as well as or instead of linear vibration. In this and the next subsection, modulation induced by the time-varying spatial orientation and geometry of a vibrating object is examined.

Physical geometric effects are conventionally accounted for using radar cross-section (RCS), σ, as in the radar equation (4.38). A large, complex structure can often be rendered as a collection of simpler, uniform structures which are more easily evaluated [106]. One such simple shape is a flat rectangular plate, for which the physical optics approximation for RCS [107,108] is

$$\sigma_{\text{plate}} = \frac{4\pi A^2}{\lambda^2} \cos^2\theta \left[\frac{\sin(ka\sin\theta)}{ka\sin\theta}\right]^2, \tag{4.54}$$

where A is the area of the plate, λ is the RF wavelength, k is the RF wavenumber, a is the major dimension of the plate, and θ is the angle between the normal area vector of the plate and the propagation vector of the incident wave. The physical optics approximation is known to closely match measurements for small θ (i.e., near normal incidence) [108].

Traditional theoretical treatments of RCS are independent of stand-off distance, a result of assuming the far-field condition of a plane wave incident on the target object. Therefore, the RCS of a linearly vibrating plate will not change, as the plate can be treated as a single, uniform Doppler reflector. However, a plate that vibrates rotationally around its major axis in a rocking motion, as in Fig. 4.3, will modulate its RCS as θ in (4.54) changes over time. (Intuitively, this is the same as considering the net effect of quasi-stationary Doppler modulation across the surface of the plate.) This equivalence is explored in the next section. By taking $\theta = \varphi\sin\omega_V t$, where φ is the rotational amplitude (in radians) of vibration and ω_V is the rocking radian frequency, RCS can be written as

$$\sigma_{\text{plate}} \propto \cos^2(\varphi\sin\omega_V t)\left[\frac{\sin(ka\sin(\varphi\sin\omega_V t))}{ka\sin(\varphi\sin\omega_V t)}\right]^2. \tag{4.55}$$

From the radar equation, (4.38), the received signal amplitude is proportional to the square

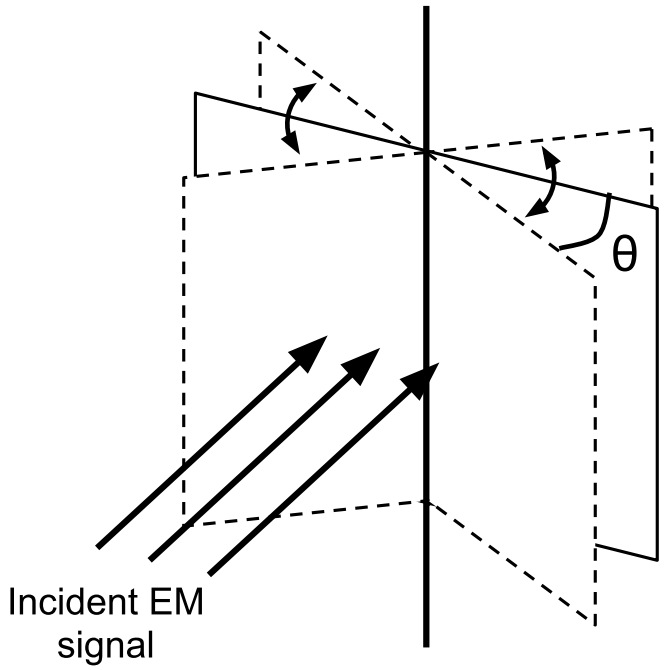

Figure 4.3: A plate vibrating rotationally around an axis in a rocking motion.

root of the RCS, so that the normalized amplitude modulation term derived from time-varying RCS is

$$A'_{\mathrm{RCS}}(t) = \cos\left(\varphi \sin \omega_V t\right) \left[\frac{\sin\left(ka \sin\left(\varphi \sin \omega_V t\right)\right)}{ka \sin\left(\varphi \sin \omega_V t\right)}\right]. \tag{4.56}$$

Note that the plate RCS equation, (4.54), is only valid at small angles near normal incidence, i.e. for a rocking plate, $\varphi \ll 1$. This situation is of interest for very low-level vibrations. Taking $\varphi \ll 1$ and using the small angle approximations for sine and cosine, (4.56) simplifies to

$$A'_{\mathrm{RCS}}(t) = \frac{\sin\left(ka\varphi \sin \omega_V t\right)}{ka\varphi \sin \omega_V t}. \tag{4.57}$$

Using the Jacobi-Anger expansion, (4.57) becomes

$$\begin{aligned} A'_{\mathrm{RCS}}(t) &= \frac{2}{ka\varphi \sin \omega_V t} \sum_{n=0}^{\infty} J_{2n+1}(ka\varphi) \sin\left[(2n+1)\omega_V t\right] \\ &= \frac{2}{ka\varphi} \sum_{n=0}^{\infty} J_{2n+1}(ka\varphi) \frac{\sin\left[(2n+1)\omega_V t\right]}{\sin \omega_V t}. \end{aligned} \tag{4.58}$$

The ratio of sines in (4.58) is the Dirichlet kernel, which has the trigonometric expansion

$$\frac{\sin\left[(n+\frac{1}{2})x\right]}{\sin\frac{1}{2}x} = 1 + 2\sum_{m=1}^{n}\cos(mx). \tag{4.59}$$

Then the normalized RCS modulation term becomes

$$\begin{aligned} A'_{\mathrm{RCS}}(t) =& \frac{2}{ka\varphi}\sum_{n=0}^{\infty} J_{2n+1}(ka\varphi)\left(1 + 2\sum_{m=1}^{n}\cos(2m\omega_V t)\right) \\ =& \frac{2}{ka\varphi}\sum_{n=0}^{\infty} J_{2n+1}(ka\varphi) + \frac{2}{ka\varphi}\sum_{n=1}^{\infty}\sum_{m=1}^{n} 2J_{2n+1}(ka\varphi)\cos(2m\omega_V t). \end{aligned} \tag{4.60}$$

The Fourier series of the RCS modulation term is obtained by swapping the order of the summation in (4.60), so that

$$\begin{aligned} A'_{\mathrm{RCS}}(t) =& \frac{2}{ka\varphi}\left[\sum_{n=0}^{\infty} J_{2n+1}(ka\varphi)\right] + \frac{4}{ka\varphi}\sum_{m=1}^{\infty}\left[\sum_{n=m/2}^{\infty} J_{2n+1}(ka\varphi)\right]\cos(2m\omega_V t) \\ =& \frac{2}{ka\varphi}\left[\sum_{n=0}^{\infty} J_{2n+1}(ka\varphi)\right] + \frac{4}{ka\varphi}\sum_{m=1}^{\infty}\left[\sum_{n=0}^{\infty} J_{m+2n+1}(ka\varphi)\right]\cos(2m\omega_V t), \end{aligned} \tag{4.61}$$

where the Fourier coefficients are

$$F_{\mathrm{RCS},0} = \frac{2}{ka\varphi}\left[\sum_{n=0}^{\infty} J_{2n+1}(ka\varphi)\right] \tag{4.62}$$

and

$$F_{\mathrm{RCS},m} = \begin{cases} 0 & \text{if } m \text{ is odd} \\ \dfrac{4}{ka\varphi}\displaystyle\sum_{n=0}^{\infty} J_{m+2n+1}(ka\varphi) & \text{if } m \text{ is even.} \end{cases} \tag{4.63}$$

Using the assumption $\varphi \ll 1$, only the lowest-order Bessel term will dominate each sideband tone, so the Fourier are

$$F_{\mathrm{RCS},0} \approx \frac{2}{ka\varphi}J_1(ka\varphi) \approx 1 \tag{4.64}$$

$$F_{\mathrm{RCS},m_{\mathrm{even}}} \approx \frac{4}{ka\varphi}J_{m+1}(ka\varphi) \approx \frac{2}{(m+1)!}\left(\frac{ka\varphi}{2}\right)^m. \tag{4.65}$$

Thus, the received normalized RCS-modulated signal is

$$s'(t) = A'_{\mathrm{RCS}}(t)\cos(\omega_{RF}t) \tag{4.66}$$

$$= \left[F_{\mathrm{RCS},0} + \sum_{n=1}^{\infty} F_{\mathrm{RCS},2n}\cos(2n\omega_V t)\right]\cos(\omega_{\mathrm{RF}}t) \tag{4.67}$$

$$= F_{\mathrm{RCS},0}\cos(\omega_{RF}t) + \sum_{n=1}^{\infty}\left[\frac{F_{\mathrm{RCS},2n}}{2}\cos\left[\left(\omega_{\mathrm{RF}} \pm 2n\omega_V\right)t\right]\right]. \tag{4.68}$$

Therefore the power of the n-th rocking sideband tone relative to the RF carrier tone can be approximated as

$$A_{\mathrm{RCS},n_{\mathrm{odd}}} = 0 \tag{4.69}$$

$$A_{\mathrm{RCS},n_{\mathrm{even}}} \approx \frac{1}{(n+1)!}\left(k_{\mathrm{RF}}\frac{a\varphi}{2}\right)^n = \frac{(2\pi)^n}{(n+1)!}\left(\frac{a\varphi/2}{\lambda}\right)^n. \tag{4.70}$$

In this subsection, the standard physical-optics approximation for RCS of a flat rectangular plate was used to show that modulation can arise from rotational vibration, such as a rocking motion. The end-result for relative power of the sideband tones has a very similar form to that of the Doppler PM tones, with $a\varphi/2$ in (4.70) replacing the linear displacement amplitude, β, in the Doppler case. A key feature of rocking RCS modulation is the absence of sideband tones resulting from odd harmonics of the vibrational frequency— this provides a means for differentiating RCS modulation from Doppler modulation when the sideband tone powers are nearly equal. The RCS-based derivation in this subsection used the far-field approximation of an incident plane wave on the target object, which may not always be a good assumption. The plane wave assumption and other geometric effects are explored further in the next subsection.

4.2.5 Extraordinary Geometry Effects

Several assumptions, inherent to the concept of RCS, were key to obtaining the previous simple result for rocking RCS modulation. Understanding these assumptions is important to determining the responses from various physical mechanisms and developing new sensor modalities that could be exploited in sensing applications. Non-ideal effects that complicate analysis of finite-sized targets are discussed in this subsection, and RCS modulation is re-derived using a different set of principles from that used in the previous subsection.

The most important consideration used in the derivation of RCS modulation in the previous subsection is the assumption of an incident plane wave on the target object. The radar equation, (4.38), relies on the spherical spreading of a propagating EM wave. Thus the plane wave assumption can be interpreted as a limit on the curvature of the incident wave. For small

objects at a large standoff distance this curvature is negligible, but recent research [109–111] has shown that corrections are necessary for shorter standoffs, such as the detection of vehicles, or even at large distances for large enough targets, such as observing the surface of the Earth from a satellite.

Curvature adds considerable complexity to analyzing modulation induced by a vibrating target. Each point on the target typically reflects the incident wave at slightly different times, and thus slightly different states of motion, eliminating uniformity in the reflection. The angle of incidence also changes for each of these points over space and time, reducing the modulation effect as the EM propagation vector shifts out of phase with the surface displacement vector. Directional antenna patterns will also contribute to errors as power density is reduced on portions of the target off-axis or outside the central beam. A straightforward approach is taken to these considerations in [104], where the displacement of a vibrating plate is expressed as a function of space and the integral of the reflected signal, with a correction factor for the antenna pattern, is taken over the surface of the plate.

RCS modulation may be considered more generally as a type of reflection coefficient modulation. Non-uniform or composite materials will have spatially-varying reflection properties in addition to the time-varying components of motion. This creates a highly complex scattering scenario, in which the reflected signal is often treated statistically instead of analytically. In addition, acoustically-induced vibration has been shown to vary the permittivity of a dielectric target [40], creating an additional vector of complexity.

Additional problems arise in characterizing the actual displacement of a vibrating target. Doppler measurement systems, both radar and laser, yield a linear velocity or displacement, along the primary axis of measurement. In the case of the purely rocking plate shown in Fig. 4.3, a laser focused on the fixed center axis of rotation will measure no displacement, while a laser focused on the edge of the plate will detect pulsed motion due to the plate edge swinging out of sight. Points in-between will present complex, non-sinusoidal motion. As detectable vibration amplitudes continue to decrease (principally due to the increase of dynamic range of measurement systems), it becomes more important to be able to distinguish linear vibrations from other modes of motion which can be dominant if not accounted for.

With the above considerations, it will be shown that the surface integral of the quasi-stationary Doppler effect on the rocking plate is equivalent to the previous RCS-derived result that used the plane wave assumption. The net Doppler effect is taken as the integral of the point-wise Doppler effect response over the area of the plate. Then the received signal is

$$s(t) = \frac{1}{A} \iint_A \cos\left[\omega_{\mathrm{RF}} t - \phi_D(t)\right] dA, \tag{4.71}$$

where A is the area of the plate, ω_{RF} is the RF radian frequency, and $\phi_D(t)$ is the Doppler phase modulation term. Considering the rocking plate in Fig. 4.3, for an incident plane wave the vertical dimension of the plate will appear to be uniform, thus the surface integral simplifies to a one-dimensional integral over the major dimension so that

$$s(t) = \frac{1}{a} \int_{-a/2}^{a/2} \cos\left[\omega_{\mathrm{RF}} t - \phi_D(t)\right] dx, \tag{4.72}$$

where a is the length of the major dimension and x is the position along the major dimension. The Doppler phase term, $\phi_D(t)$ must be modified to account for the phase difference between the left and right sides of the plate, so that

$$\phi_{D,\mathrm{left}}(t) = 2k_{\mathrm{RF}}\beta \cos\left(\omega_V t - \frac{\pi}{2}\right) \tag{4.73}$$

$$\phi_{D,\mathrm{right}}(t) = 2k_{\mathrm{RF}}\beta \cos\left(\omega_V t + \frac{\pi}{2}\right), \tag{4.74}$$

where the displacement amplitude, β, is also a function of x and the rocking vibration amplitude, φ. For small vibrations, $\varphi \ll 1$,

$$\beta = |x \cos\varphi| \approx |x\varphi|. \tag{4.75}$$

Inserting the Doppler phase terms,

$$\begin{aligned} s(t) =& \frac{1}{a} \int_{0}^{a/2} \cos\left(\omega_{\mathrm{RF}} t + 2k_{\mathrm{RF}}\beta \cos\left(\omega_V t + \frac{\pi}{2}\right)\right) dx \\ &+ \frac{1}{a} \int_{-a/2}^{0} \cos\left(\omega_{\mathrm{RF}} t + 2k_{\mathrm{RF}}\beta \cos\left(\omega_V t - \frac{\pi}{2}\right)\right) dx. \end{aligned} \tag{4.76}$$

The Doppler-shifted sinusoids can be re-written in the form of the previously derived Doppler modulation series by substituting the new phase terms ($\omega_V t \pm \frac{\pi}{2}$), for ($\omega_V t$) in (4.16) yielding

$$\begin{aligned} s(t) =& \frac{1}{a} \int_{0}^{a/2} \sum_{n=-\infty}^{\infty} J_n(2k_{\mathrm{RF}}\beta) \cos\left(\omega_{\mathrm{RF}} t + n\omega_V t + n\pi\right) dx \\ &+ \frac{1}{a} \int_{-a/2}^{0} \sum_{n=-\infty}^{\infty} J_n(2k_{\mathrm{RF}}\beta) \cos\left(\omega_{\mathrm{RF}} t + n\omega_V t\right) dx. \end{aligned} \tag{4.77}$$

The phase shift, $n\pi$, in the first integral indicates a possible sign change, and the two integrals

combine to produce

$$\begin{aligned} s(t) =& \frac{1}{a} \int_{-a/2}^{a/2} \sum_{n=-\infty}^{\infty} \left[1 + (-1)^n\right] J_n(2k_{\mathrm{RF}}\beta) \cos\left(\omega_{\mathrm{RF}} t + n\omega_V t\right) dx \\ =& \frac{1}{a} \int_{-a/2}^{a/2} \left\{ \sum_{n=-\infty}^{\infty} J_{2n}(2k_{\mathrm{RF}}\beta) \cos\left(\omega_{\mathrm{RF}} t + 2n\omega_V t\right) \right\} dx. \end{aligned} \tag{4.78}$$

The phase contributions from each side of the plate cancel for odd-order sideband tones and combine for even-order sideband tones. (This provides an intuitive understanding for the suppression of odd harmonic modulation tones obtained in the previous subsection, see (4.70)). Exchanging the integration and summation and substituting for β yields

$$s(t) = \sum_{n=-\infty}^{\infty} \left[\int_{-a/2}^{a/2} \frac{1}{a} J_{2n}(2k_{\mathrm{RF}}|x\varphi|) dx \right] \cos\left(\omega_{\mathrm{RF}} t + 2n\omega_V t\right). \tag{4.79}$$

Using symmetry and variable substitution, a Bessel integral standard form is obtained and can be solved resulting in

$$\begin{aligned} s(t) &= \sum_{n=-\infty}^{\infty} \left[\frac{2}{a} \int_{0}^{a/2} J_{2n}(2k_{\mathrm{RF}} x\varphi) dx \right] \cos\left(\omega_{\mathrm{RF}} t + 2n\omega_V t\right) \\ &= \sum_{n=-\infty}^{\infty} \left[\frac{2}{a} \int_{0}^{k_{\mathrm{RF}} a\varphi} J_{2n}(y) \frac{dy}{2k_{\mathrm{RF}}\varphi} \right] \cos\left(\omega_{\mathrm{RF}} t + 2n\omega_V t\right) \\ &= \sum_{n=-\infty}^{\infty} \left[\frac{1}{k_{\mathrm{RF}} a\varphi} \sum_{m=0}^{\infty} 2J_{2n+2m+1}(k_{\mathrm{RF}} a\varphi) \right] \cos\left(\omega_{\mathrm{RF}} t + 2n\omega_V t\right). \end{aligned} \tag{4.80}$$

The term within in square brackets in (4.80) represents the amplitudes of the harmonic sideband tones. This is the same as the previous result derived using the RCS approximation, (4.70). Note that the odd-order sideband tones are suppressed. Despite starting with phase modulation using the Doppler effect, the result was primarily a consequence of the assumptions rather than the process. Also, a far-field plane wave was assumed, however for low-level vibrations at a moderate stand-off, this should be reasonable.

4.2.6 Reflection Coefficient Modulation

There are several other physical mechanisms that can modulate a reflected signal by effectively changing a target's reflection coefficient. The modulation processes discussed in Sections 4.2.1–4.2.5 are primarily concerned with modulation occurring due to the changes in the path length from the antenna to the target, with the target assumed to be a perfect reflector. However, the perfect reflector condition is not always approximated as vibration may affect the scattering behavior, that is, reflection coefficient, of the target. Any change in scattering behavior may be considered a type of reflection coefficient modulation. Due to the uniqueness of these processes, they are not as amenable to analysis and must be numerically evaluated or experimentally characterized.

With dielectric materials, permittivity has been shown to be modulated by density variations caused by vibration [40]. This affects boundary interaction with an incident wave. The simulated results in [40] suggest that modulation from fluctuation of the dielectric constant can have magnitudes similar to Doppler phase modulation and significantly contributes to the overall response. This may be seen as a similar effect to the phenomenon exploited in radio acoustic sounding systems (RASS), where the reflectivity of the air above the radar sensor is modulated by an acoustic wave, providing information about meteorological conditions in the lower atmosphere [87].

Targets with active circuits may experience microphonic effects, where mechanical vibration modulates an existing electric field. This differs from piezoelectricity in which mechanical stress directly generates a coupled electric field. Microphonics is traditionally associated with amplifier tubes [41], but has also been demonstrated in passive components such as capacitors [42]. Connected to an antenna or other resonant structure, an RF probing signal may be absorbed, couple with the microphonic nonlinearity, and reradiate, as in antenna mode scattering [112]. Modulation sidebands from a vibrating antenna has previously been demonstrated [101], though it is not yet well understood.

4.2.7 Combined Modulation Effects

A signal reflected from a vibrating surface will undergo many forms of modulation as outlined in the previous sections. Combining these effects, the complete model for the modulated return signal for a linearly vibrating plate is

$$s(t) = \alpha_0 A_{\mathrm{PL}}(t)\gamma(t)\cos[\omega_{\mathrm{RF}}t - \phi_{\mathrm{Doppler}}(t)], \tag{4.81}$$

where $A_{\mathrm{PL}}(t)$ is amplitude modulation from path loss variation, $\gamma(t)$ is amplitude modulation from special relativity, $\phi_{\mathrm{Doppler}}(t)$ is phase modulation from the Doppler effect, and α_0 is a

constant accounting for transmitted power and non time-dependent effects of path loss and radar cross section. In this simple case, the AM effects are multiplicative. For more complex motion, such as the rotating plate, the AM effects need to be integrated across the moving surface. Substituting the expressions derived for each of the modulation terms produces the normalized signal

$$s'(t) = \left[F_{\mathrm{PL},0} + \sum_{n=1}^{\infty} F_{\mathrm{PL},n} \cos\left(n\omega_V t\right)\right] \times \left[F_{\gamma,0} + \sum_{n=1}^{\infty} F_{\gamma,n} \cos\left(n\omega_V t\right)\right] \times \left[\sum_{n=-\infty}^{\infty} A_{\mathrm{Doppler},n} \cos\left(\omega_{\mathrm{RF}} t + n\omega_V t + n\frac{\pi}{2}\right)\right]. \tag{4.82}$$

The mixing in (4.82) creates a rich array of sideband tones. Most of these tones have an amplitude that is the product of higher-order coefficients from two or more modulation processes, decaying rapidly with increasing combined order. The primary sideband tones appearing in the spectrum of the scattered signal will be the result of the higher-order terms of one process mixing with the constant or zero-order terms for all other effects. The zero-order terms are approximately unity, so the modulated signal is

$$\begin{aligned} s'(t) \approx & \left[\sum_{n=-\infty}^{\infty} A_{\mathrm{Doppler},n} \cos\left(\omega_{\mathrm{RF}} t + n\omega_V t + n\frac{\pi}{2}\right)\right] \\ & + \left[\sum_{n=1}^{\infty} F_{\mathrm{PL},n} \cos\left(n\omega_V t\right)\right] \cos\left(\omega_{\mathrm{RF}} t\right) + \left[\sum_{n=1}^{\infty} F_{\gamma,n} \cos\left(n\omega_V t\right)\right] \cos\left(\omega_{\mathrm{RF}} t\right) \\ \approx & \cos(\omega_{\mathrm{RF}} t) + \sum_{n=1}^{\infty} \left[A_{\mathrm{Doppler},n} \cos\left(\omega_{\mathrm{RF}} t \pm n\omega_V t \pm n\frac{\pi}{2}\right)\right] \\ & + \sum_{n=1}^{\infty} \left[A_{\mathrm{PL},n} \cos\left(\omega_{\mathrm{RF}} \pm n\omega_V\right) t\right] + \sum_{n=1}^{\infty} \left[A_{\gamma,n} \cos\left(\omega_{\mathrm{RF}} \pm n\omega_V\right) t\right]. \end{aligned} \tag{4.83}$$

This indicates that the various modulation contributions can be approximately superimposed for low-level vibrations. This approximation can be extended to more complex motion as well, as higher orders of motion represent a similar mixing of rapidly decaying high-order sideband tones. Although not explicitly shown, there will also be an arbitrary phase shift of the vibrational displacement relative to the RF signal. This phase shift remains coherent through all processes and can safely be ignored, similar to the constant phase shift introduced by phase modulation due to a static standoff distance.

Table 4.1: Comparison of sideband tone power for various modulation types

Type, equation	n-th order tone amplitude	valid n
Doppler PM, (4.18)	$\frac{(2\pi)^n}{n!}\left(\frac{\beta}{\lambda}\right)^n$	$n = 1, 2, ...$
Special Relativity AM, (4.36)	$\frac{2}{2^n}\left(\frac{\beta\omega_V}{c}\right)^n$	$n = 1, 2, ...$
Path Loss AM, (4.53)	$\frac{n+1}{2^n}\left(\frac{\beta}{R_0}\right)^n$	$n = 1, 2, ...$
Rocking AM, (4.70)	$\frac{(2\pi)^n}{(n+1)!}\left(\frac{a\varphi/2}{\lambda}\right)^n$	$n = 2, 4, ...$

4.2.8 Comparison of Modulation Tones

A summary of the tone amplitudes for each of the modulation processes is shown in Table 4.1. For the linearly vibrating plate, the sideband tone amplitudes for Doppler PM, special relativity AM, and path loss AM are all proportional to the vibrational amplitude raised to the order of the tone. Ignoring constant coefficients, Doppler effect modulation tones will typically be much larger than both the special relativity AM and path loss modulation tones, since typically $\omega_{\mathrm{RF}} \gg \omega_V$ and $R_0 \gg \lambda$. The power relative to the RF carrier tone of the first eight modulation tones for these three processes are shown in Fig. 4.4 using $\beta = \frac{3}{100}\lambda$, $R_0 = 3\lambda$, $\lambda = \frac{1}{3}$ m, and $f_V = 1$ kHz. These conditions represent a radar operating at 900 MHz, with 1 m standoff from an object vibrating with an amplitude of 1 cm at 1 kHz. The full expressions, (4.16), (4.32), and (4.49), were used to generate the curves in Fig. 4.4. For small n, the amplitude of the AM tones will always be significantly less than the amplitude of the PM tones. At best, only the first several tones will be measurable for very low-level vibration with current sensing techniques.

For a rocking plate or a plate with multiple modes of motion, the rotational modulation effect becomes significant. The amplitudes of the rotational modulation tones are proportional to $a\varphi/2$, although all odd harmonic tones are suppressed. From the assumption of $\varphi \ll 1$, the term $a\varphi/2$ can be interpreted as the linear displacement amplitude at the edge of the plate, similar to β. The amplitudes of the first four predicted sideband tones for a rocking plate with $a = 0.9\lambda$ and $\lambda = \frac{1}{3}$ m are shown in Fig. 4.5 for various angular vibration amplitudes. These tones are compared to the Doppler modulation tone amplitudes from Fig. 4.4. When the plate is rocking with an amplitude of 6.6°, the second-order rotational sideband tone is equal to the Doppler sideband tone. For even smaller linear vibrations, this angle decreases linearly, e.g. for a 1 mm linear vibration, only 0.7° of rocking is needed to produce an equal sideband tone. Also, as the rocking modulation is dependent on the major dimension, a, the modulation tone power will increase relative to the Doppler tones as a increases. Thus, a very slight rocking vibration

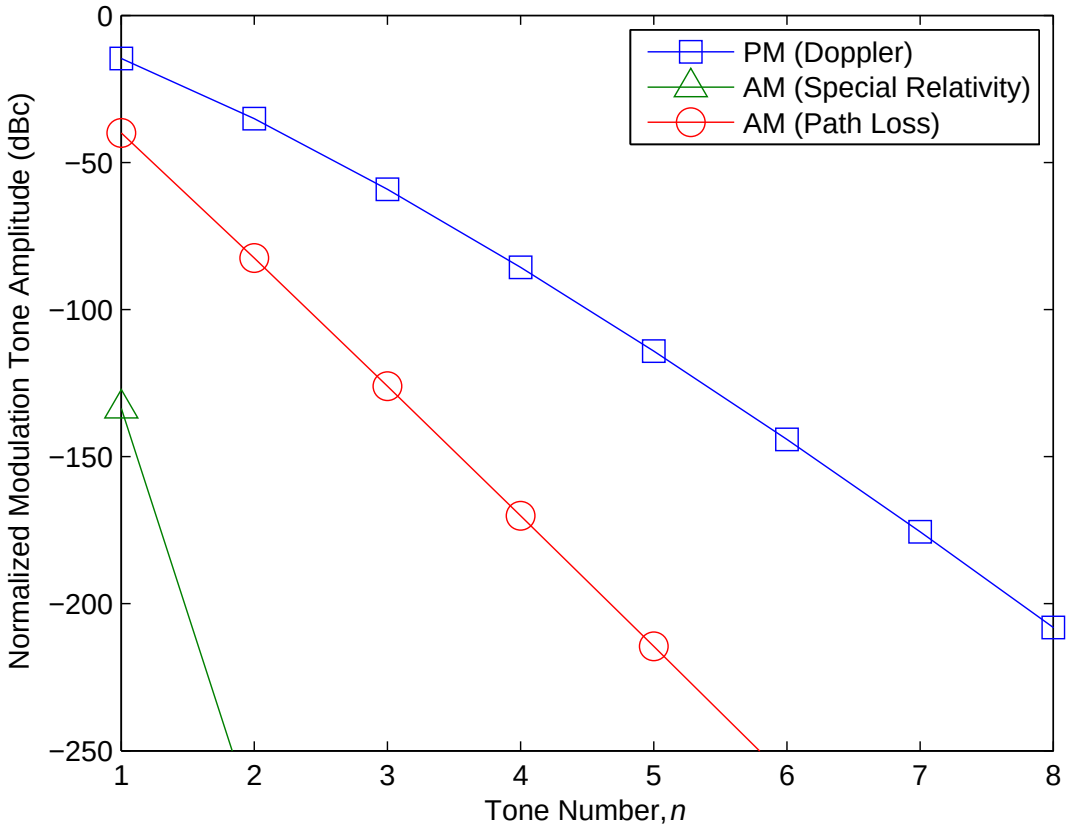

Figure 4.4: Expected power relative to the RF carrier tone of the first eight normalized modulation sideband tones for a linearly vibrating plate using $\beta = 0.03\lambda$, $R_0 = 3\lambda$, $\lambda = \frac{1}{3}$ m, and $f_V = 1$ kHz

in a large object, such as a plane or vehicle, would produce a scattering response comparable to the response when the object is linearly vibrating.

4.3 Vibration Detection

In this section, the design and fundamental limits for a vibration detection system are discussed. Using modulation analysis and results derived in Table 4.1, it should be theoretically possible determine the amplitude and mode of vibration on a remote object from the RF scattering response. The modulation tones inherent to vibration scattering will be much smaller than the RF probing tone used, requiring a high-dynamic-range receiver for detection. To achieve this, feedforward analog cancellation [100] is used to condition the reflected scattered signal before

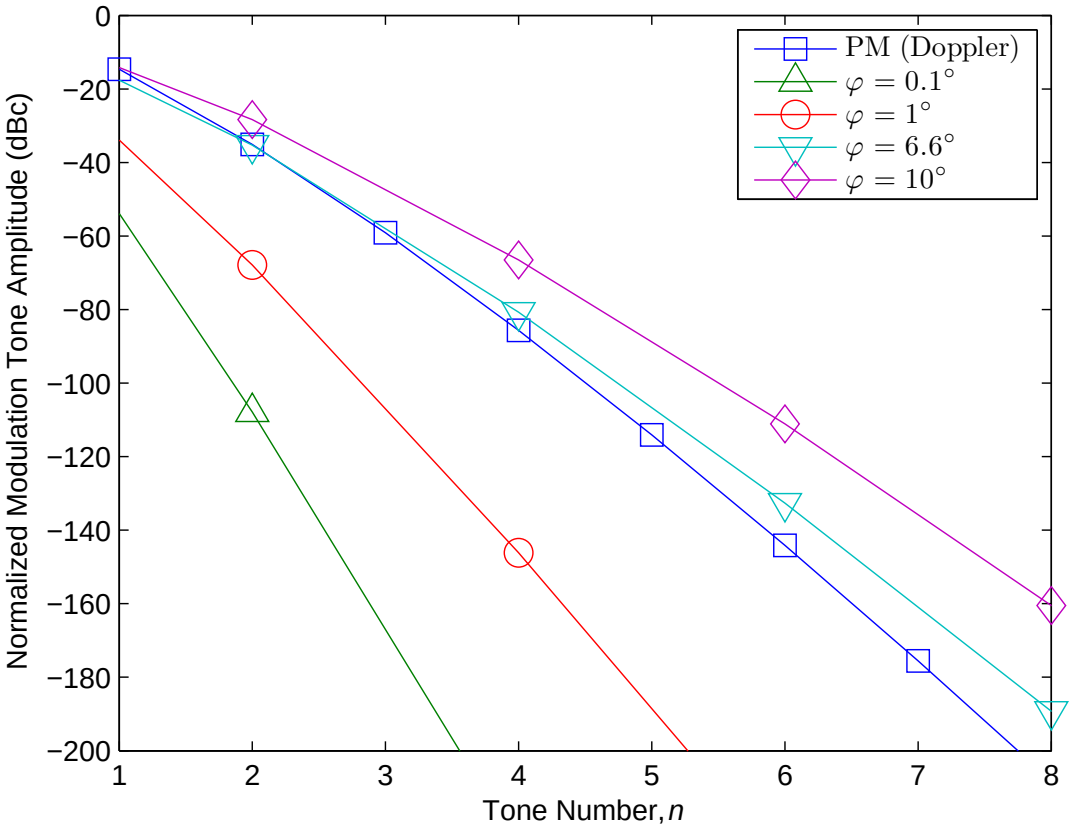

Figure 4.5: Expected relative power of the first four normalized modulation tone amplitudes on a rocking plate with various rotational amplitudes, $a = 0.9\lambda$ and $\lambda = \frac{1}{3}$ m. The first eight predicted Doppler PM tones from a linearly vibrating plate ($\beta = 0.03\lambda$) are included for reference.

passing the signal to the receiver. A theoretical vibration sensitivity limit is derived based on system parameters and range to the vibrating object.

4.3.1 Architecture

The block diagram of the vibration detector, using feedforward analog cancellation [100], is shown in Fig. 4.6. A RF tone is generated and amplified along the probing path, then transmitted to the vibrating object through an antenna (Tx). The reflected signal from the target is received by a second antenna (Rx), then is combined with a feedforward signal. The amplitude and phase of the feedforward signal are controlled automatically using a vector modulator to produce a signal that cancels the unmodulated component of received signal.

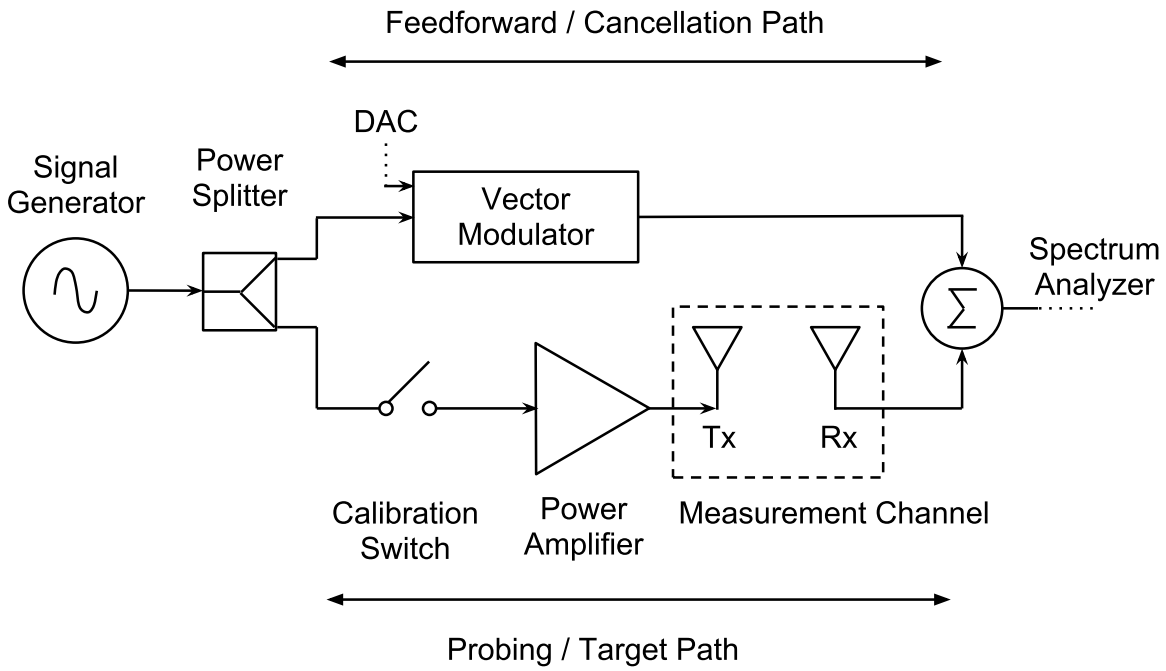

Figure 4.6: Basic vibration detector architecture.

The vibrating target is probed inside of a dual acoustic-RF anechoic chamber [113]. This chamber emulates both RF and acoustic freespace, allowing for more ideal measurement of the interactions of the RF probing tone with the vibrating target. A bistatic antenna configuration was chosen to isolate the forward-traveling measurement signal at the receiver from the reverse-traveling reflected signal from the transmit antenna. With poorly matched antennas, the reflected signal in a monostatic configuration could overwhelm the much smaller received signal, requiring additional dynamic range to discern the very small distortion tones. In the current system, antennas with low directionality were used, generating significant cross-coupling between the transmit and receive antennas and making it impossible to calibrate the propagation loss to and from the target. Without this calibration, it is impossible to correlate RF measurements directly to vibrational displacement, without resorting to multi-order nonlinear techniques [104].

4.3.2 Range Considerations

Doppler scattering modulation is expected to dominate the received modulated signal, with the carrier-normalized amplitude spectrum given by (4.18). The received signal will be further

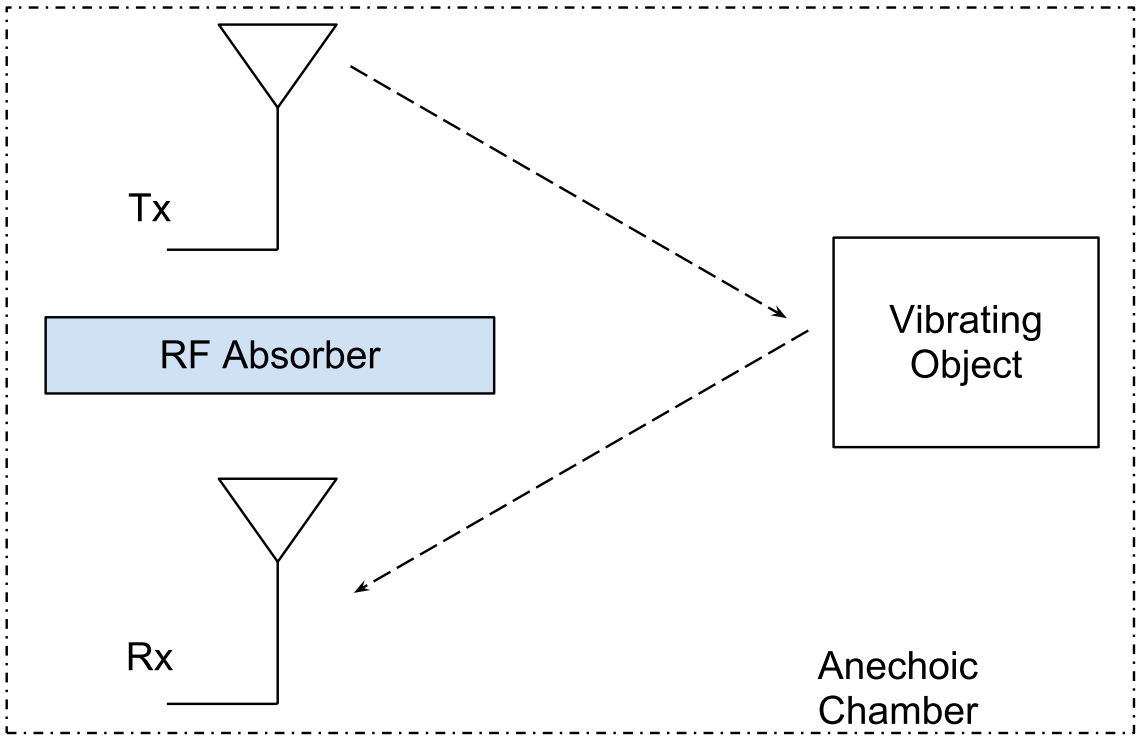

Figure 4.7: Physical configuration of bistatic radar vibration detector inside of an anechoic chamber.

attenuated as described by the radar equation [61], so that the power of the received signal is

$$P_{\mathrm{R}} = \frac{P_{\mathrm{T}} G_{\mathrm{T}} G_{\mathrm{R}} \lambda^2 \sigma}{(4\pi)^3 r_{\mathrm{T}}^2 r_{\mathrm{R}}^2}, \tag{4.84}$$

where P_{T} is the transmitted signal power, G_{T} and G_{R} are the gains of the transmit and receive antennas, σ is the radar cross-section, and r_{T} and r_{R} are the distances between the reflector and the transmit and receive antennas, respectively. Combining (4.18) and (4.84) and setting $r_{\mathrm{T}} = r_{\mathrm{R}} = R$, the expected received power of the n-th Doppler tone is

$$P_{\mathrm{R},n} = P_{\mathrm{T}} \frac{G_{\mathrm{T}} G_{\mathrm{R}} \sigma \lambda^2}{(4\pi)^3 R^4} J_n^2 \left(\frac{4\pi\beta}{\lambda} \right). \tag{4.85}$$

Using the small vibration approximation (i.e., $\beta \ll \lambda$), the received power of the first-order Doppler tone is

$$P_{\mathrm{R},1} = P_{\mathrm{T}} \frac{G_{\mathrm{T}} G_{\mathrm{R}} \sigma \lambda^2}{(4\pi)^3 R^4} \left(\frac{2\pi\beta}{\lambda} \right)^2 = P_{\mathrm{T}} \frac{G_{\mathrm{T}} G_{\mathrm{R}} \sigma \beta^2}{16\pi R^4}. \tag{4.86}$$

Defining the dynamic range of the measurement system as the ratio of the transmitted power to the minimum detectable received tone, $\mathrm{DR} = P_{\mathrm{T}}/P_{\mathrm{R,min}}$, the minimum resolvable vibration amplitude using the first-order Doppler tone is

$$\beta_{\min} = \frac{4R^2}{\sqrt{\mathrm{DR}}}\sqrt{\frac{\pi}{G_{\mathrm{T}}G_{\mathrm{R}}\sigma}}. \tag{4.87}$$

For a system with 140 dB dynamic range, as reported in [114], and assuming $G_{\mathrm{T}}G_{\mathrm{R}}\sigma = 1$, the minimum detectable vibration amplitude at 2 m standoff will be 2.8 μm. With high-gain antennas and small standoffs, the minimum vibration level may be even lower. It may be noted that (4.87) is independent of RF wavelength although quantities within may not be, e.g. dynamic range and antenna gain. This is only true when considering the first-order Doppler tone. The result derived for $\beta_{\min}$ may be considered a fundamental limit for the minimum detectable vibrations based on standoff distance (R) and system capability (DR). Regardless of the technique used, the interaction to be measured, e.g. modulation tone power, must be within the system dynamic range for the vibration to be detected. Inherently, this must be true for any measurement or sensing system.

4.4 Spectral Measurement

To explore the conclusions of the previous sections, the scattering response from a rectangular vibrating aluminum plate was tested using the vibration detection radar operating at 900 MHz and transmitting 1 W total power. The plate dimensions were 30.5 cm $\times$ 10.2 cm $\times$ 0.95 cm and positioned at 2 m standoff. RF scattering responses are presented for a both linearly vibrating and rocking plate to verify the derived modulation theory. Scattering results are also presented for the linearly vibrating plate buried in sand, demonstrating ground-penetrating capability, a key advantage to RF-based vibration detection over laser-based techniques.

Linear vibrations were induced on the aluminum plate using a linear resonant actuator (Precision Microdrives C10-100) bonded to the surface of the plate. The actuator was driven at its resonant vibration frequency, 172 Hz, and the vibration amplitude of the plate was varied by varying the actuator drive signal. The vibrating plate was hung horizontally, and supported by two looped threads, roughly 2 cm from each end of the plate. A laser Doppler vibrometer (LDV) was used to measure the displacement of the plate. The LDV-measured displacement amplitude was observed to be approximately uniform across the face of the plate. A plot of the measured first-order sideband tone power versus plate displacement amplitude is shown in Fig. 4.8 along with predicted results using (4.85). No higher-order tones were observed, as expected since the second-order Doppler tones are predicted to be considerably below the dynamic range of the measurement system. Since the current system does not have

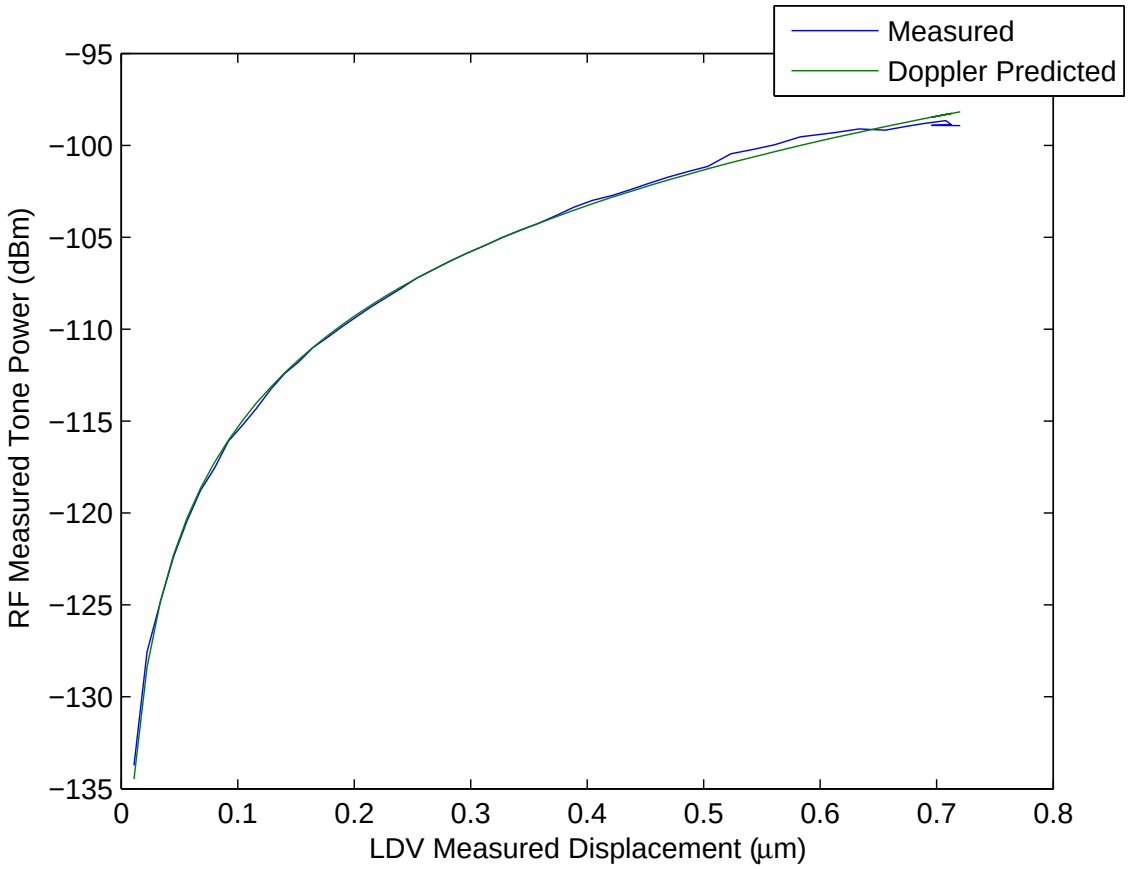

Figure 4.8: Measured first-order modulation tone power for a vibrating flat rectangular plate versus the vibration displacement amplitude as measured by a laser Doppler vibrometer. The theoretical curve is from (4.85) and normalized.

amplitude calibration capability, the measured RF tone power does not correlate absolutely to the displacement amplitude, however normalization of the RF amplitude provides an excellent match to the predicted Doppler modulation tone power. There is a small discrepancy between the measured and predicted responses at the low end where the measured RF tones are near the noise floor of the system and at the high end where the actuator drive begins to compress and the plate vibrations become nonlinear. The smallest displacement detected is 11 nm, where the measured Doppler tone power is approximately at the noise floor of the system. This is not necessarily the measurement resolution of the system, due to the lack of amplitude calibration, however, it can be taken to represent the potential capability of the system.

The experiment was repeated with the vibrating plate buried in a bucket of sand, with approximately 13 cm of sand between the plate and the antennas, still at 2 m standoff. The

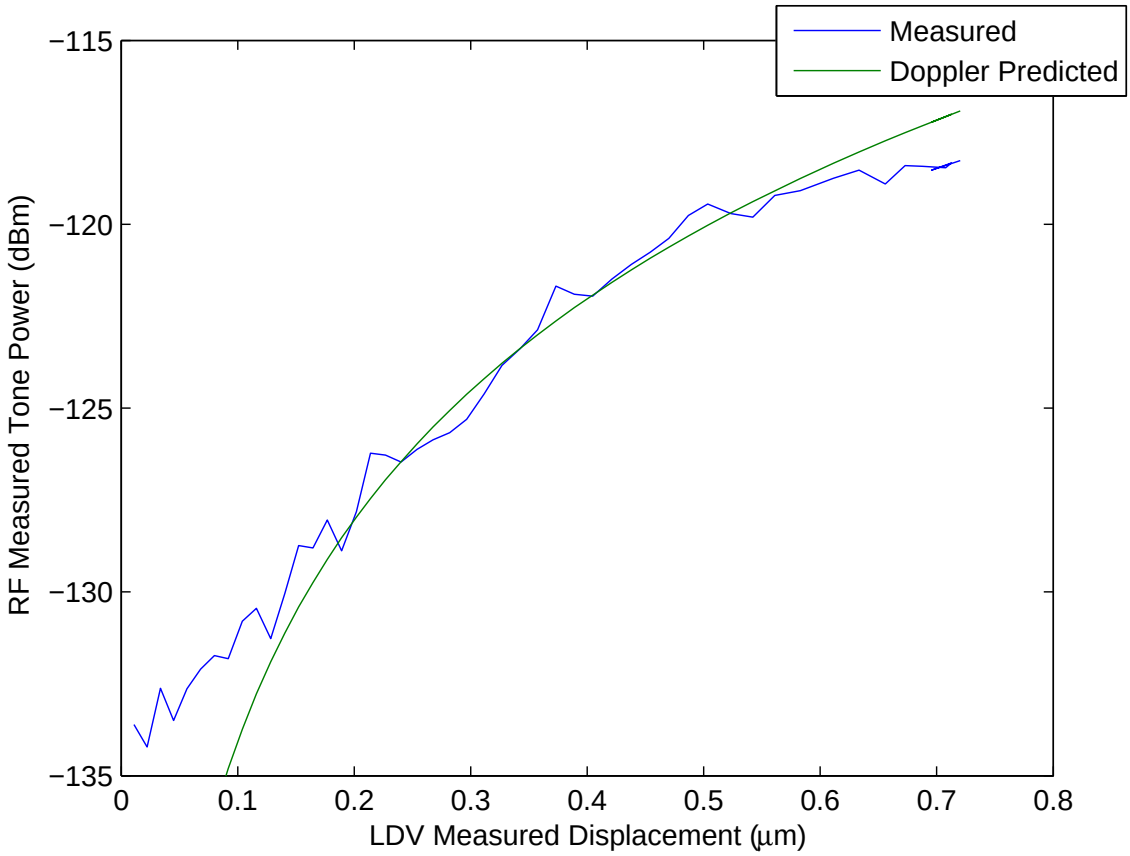

Figure 4.9: Measured first-order modulation tone power for a vibrating flat rectangular plate buried in sand. The independent axis represents the LDV-measured displacement for the same actuator drive power with the freely hanging plate. The theoretical curve (based on (4.85)) is normalized to match the measured RF amplitude.

measured results are shown in Fig. 4.9. The sand physically dampens the vibration amplitude, reducing the measured Doppler tone power. Penetrating sand, instead of air, attenuates the RF signal slightly, however a majority of the decrease in modulation tone power can be assumed to be from dampening of the plate vibration. Since the LDV cannot penetrate sand, the actual vibration displacement amplitude of the plate could not be measured. Thus, the independent axis of Fig. 4.9 refers to the displacement amplitude measured for the same actuator drive signal level with the freely hanging plate. The theoretical curve is a much poorer match, since the displacement amplitude used for prediction is not accurate.

Using the same plate, a rocking motion was induced around the center of the longest dimension. The lowest-order sideband tone in rocking modulation is second-order, so a considerable

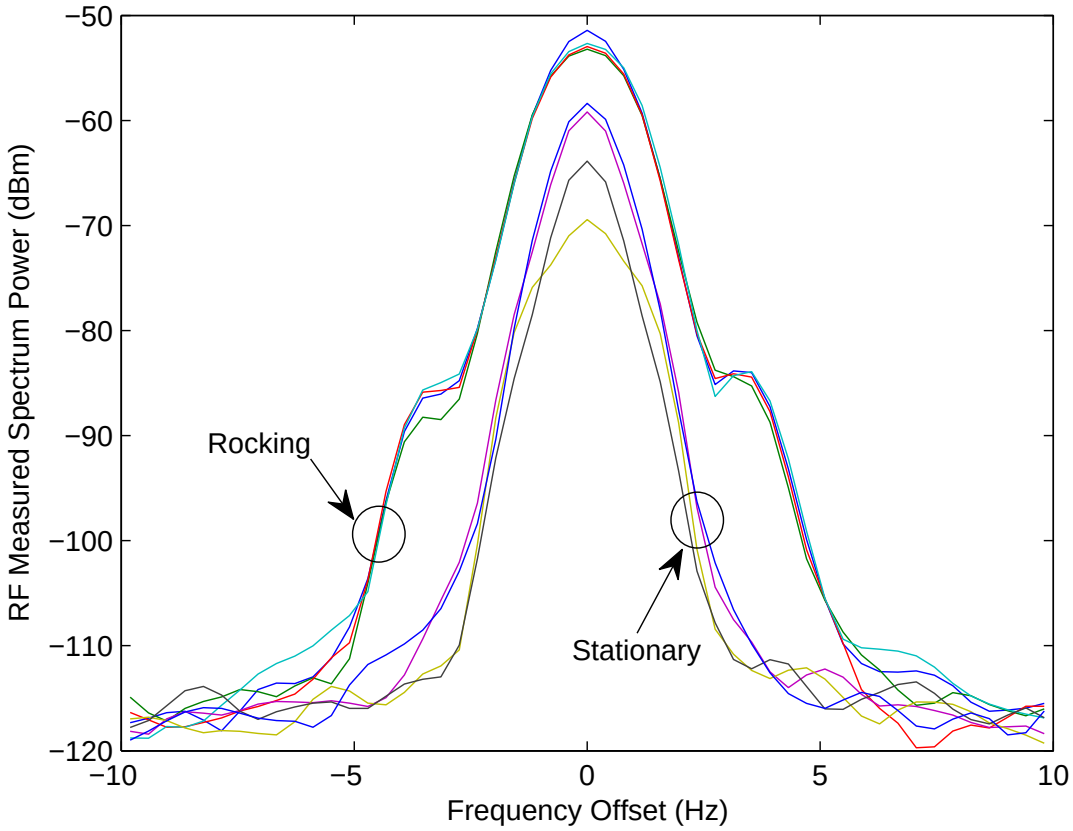

Figure 4.10: Measured RF power spectrum offset from 900 MHz for a rocking flat rectangular aluminum plate with $\varphi \approx 2°$. Four independent trials are shown for the plate both while stationary and in motion.

increase in vibration amplitude was needed relative to the previous experiment, which only observed first-order Doppler modulation. In order to adequately suppress linear vibration and generate a measurable modulation tone from rocking, a much lower frequency was used, producing approximately 0.5 cm of vibration near the edge of the plate ($\varphi \approx 2°$) at a frequency between 1.5 Hz and 2 Hz. Accurate measurement of the vibration amplitude using the LDV is difficult, since the laser-based techniques assume linear motion, while the vibration amplitude on the rocking plate is a rotational quantity. The resulting RF power spectrum is shown in Fig. 4.10. Distinct sidebands appear around 3.5 Hz offset at about 25–30 dB above the noise floor indicated by the stationary response. Despite the vibration amplitude being roughly 10,000 times larger than in the linear case, measured sideband levels were only 10–20 dB higher, a result of the large reduction in power for the second-order rotational tone. The power displayed

at zero offset is the carrier power after undergoing analog cancellation of at least 40 dB [100].

4.5 Summmary

Increasing sensing capability has prompted a re-investigation of many nonlinear phenomena, as new behaviors in measured results are observed. In this chapter, the fundamental physical mechanisms of RF scattering by a vibrating object were explored. The interaction between a vibrating structure and an incident EM wave produces modulation sidebands detectable on the reflected RF wave. Here, four scattering effects were identified by their modulation of the reflected RF wave including Doppler phase modulation, amplitude modulation from special relativity, path loss modulation, and modulation of radar cross section. For a linearly vibrating object, results show that Doppler effect scattering dominates the observable modulation spectrum, while amplitude modulation from special relativity and path loss modulation are predicted to be undetectable by current high dynamic range sensors. RCS modulation has been shown to be significant and measurable for an object vibrating in a rocking motion, although the lowest, second-order effects are more difficult to detect.

A prototype of a vibration detection architecture based on analog cancellation was also presented and shown to be able to detect vibrations as small as 11 nm. The new vibration detection system operates at much lower frequencies than previous radar vibrometers, enabling ground-penetrating capability as shown by detecting vibrations of a plate buried in sand. The theoretical minimum detectable vibration amplitude of the system was shown to be a function of standoff distance and dynamic range and independant of RF wavelength.

Throughout the characterization, common engineering assumptions were re-considered or eliminated to produce accurate results and to provide physical, intuitive meaning to better understand the fundamental limits of the systems involved. This process is key to accurately predicting reflected responses and to uniquely characterizing remote objects. Although analysis here has shown minimal deviation from traditional Doppler analysis, the framework has been established to consider alternative modulation sources in the future.

Chapter 5

Passive Spectral Regrowth in Single Aperture Systems

5.1 Introduction

One problem that plagues mobile communications is being able to simultaneously transmit and receive two or more communications channels. Typically different communications systems use their own transmit and receive antennas, commonly implemented as omnidirectional antennas. The worst case situation is when the transmitter is transmitting a signal that is very close in frequency to a very small signal being received at a co-located second antenna. As mobile antennas are omnidirectional, the large transmit signal is presented to the receiver. The general characteristics of the unwanted signal in the receiver are known but the relationship of the signal at the transmitter electronics to the signal interfering in the receive electronics is not well known. For example, the phase relationship can be variable and there can be rapid variations in amplitude with respect to frequency as the antennas interact with each other, issues related to vehicle movement, and reflections from metallic objects. One of the schemes proposed to reduce co-site interference effects is to use a common aperture, i.e., a single antenna that is used by both communication systems. It has also been proposed to extend this concept and use a common aperture for radar and sensing systems in addition to the communication systems.

Single aperture systems with high power transmitters and sensitive receivers are plagued by co-site interference in which interfering signals prevent the operation of sensitive receivers often without any identifiable pathways relating the frequencies of the transmitted and received signals. Sometimes saturation of a receiver front-end by a transmitted signal is the culprit, but with a filter suppressing the transmit signal, the interference is possibly produced by another mechanism termed passive intermodulation (PIM). Commonly cited physical sources of PIM include ferromagnetism and tunneling [16]. Identification of the sources of PIM is complicated by

the large dynamic range of a transmitted signal with a power of hundreds of watts (>50 dBm) and a sensitive receiver capable of receiving communications signals of hundreds of femtowatts (−100 dBm), and navigation signals of hundreds of attowatts (−130 dBm). At the same time, the transmitted and received signal could be separated by just a few kilohertz. Instrumentation to fully resolve these signals requires a dynamic range of at least 180 dB with signals that could be separated by as little as a few hundred hertz. No laboratory-grade equipment is available to resolve such signals. Recently, measurement systems with enhanced dynamic range incorporating feedforward cancellation [49–52, 100] or resonators [18, 44] have identified phenomena such as electro-thermal interaction [16] and magneto-impedance [80] as significant sources of PIM. Other investigations have shown time-frequency effects as a source of interference [72] that must also be considered to be PIM. These discoveries illustrate that PIM is not only due to electrical nonlinear effects as conventionally thought.

A vibrating structure is known to modulate reflected RF signals producing a received signal comprising the originally transmitted signal and sidebands offset by the frequency of vibration. This Doppler modulation is exploited in land mine detection [27,85] but can be detrimental as in modulation by rotating helicopter rotor-blades [115]. The use of a standoff acoustic tone to drive mechanical vibrations subsequently detected by an RF signal has also been explored [85, 116].

This chapter explores the fundamental limits of performance in a single aperture system. Performance can be characterized in terms of dynamic range and the spurious signals derived from the electronics themselves and from RF interference caused by standoff acoustic excitation of an antenna. Receiver resolution is investigated for a received signal close in frequency to the transmitted signal. In this case, filters cannot be used to discriminate the transmit and receive signals. In addition, military and emergency radios require broad frequency coverage and it is not feasible to use fixed filters to discriminate signals widely-spaced in frequency as can be used with commercial radios. Section 5.2 discusses the antennas used in the investigation and the relevant dynamic range and spurious frequency issues associated with single channel measurement. Close-in reflected frequency responses for a single tone input to the antenna feed are measured using the analog-canceller-based high-dynamic-range measurement system [100]. In Section 5.3.1, basic Doppler scattering theory is reviewed as a phase modulation of the RF carrier signal. Section 5.3.2 presents measurements of close-in nonlinear spectral regrowth is intentionally induced by driving mechanical vibrations on a log-periodic dipole array antenna using an acoustic source. The acousto-electromagnetic (acousto-EM) interaction results in spectral regrowth below the noise floor of conventional instrumentation. Again, the analog canceller-based measurement system is used. Vibration measurements and mechanical resonances of the antenna are discussed in Section 5.3.3 to attempt to close the loop on a theoretical understanding of the acoustic modulation phenomenon.

5.2 Single Aperture Dynamic Range

Two antennas are used in this investigation. The first antenna is a log-periodic dipole antenna. This is a resonant antenna with elements that will vibrate with respect to the main structure of the antenna. The other antenna is a broadband non-resonant antenna, model Elite-530, from Greenwave Scientific, Inc. [117]. This second antenna is a three-dimensional traveling-wave Vivaldi-like antenna. Hereinafter this antenna is referred to as the non-resonant antenna. Passive spectral regrowth is produced in these antennas due to both electro-thermal effects and antenna vibration. This impacts the dynamic range of the single aperture systems, that is, the ability to resolve a small receive signal in close proximity to a high power transmitted signal. In several studies it has been shown that electro-thermal interactions are a major source of passive intermodulation distortion (PIM) with two-tone excitation, however there are a multitude of other PIM sources that have been postulated and continue to to be investigated [15, 16, 44, 95, 97, 100, 101].

To determine the effective dynamic range of the single aperture system, each antenna is excited by a single-tone high power RF signal (1 W) at 500 MHz. The system in [100] is used to measure the reflected signal from the antenna feed and thus determine the minimum discernible signal at a given offset from the carrier (i.e. transmit) frequency. The measurement system uses cancellation to suppress the high input power and extend the dynamic range of the receiver, in this case a spectrum analyzer. This enables better measurement of the physical noise limitations of the system, as opposed to the limitations of the receiver used.

The measured reflected power spectrum of the log-periodic dipole antenna is shown in Figs. 5.1 and 5.2 for a bandwidth of 2 kHz and 100 kHz respectively around the carrier frequency. The same spectra for the non-resonant antenna is shown in Figs. 5.3 and 5.4. Overall, the minimum discernible signal is the minimum sensitivity of the receiver, at roughly -100 dBm. However, the log-periodic dipole antenna shows a large amount of distortion in a 500 Hz band immediately around the carrier frequency. This distortion does not appear on the non-resonant antenna, suggesting that it is an antenna characteristic, as opposed to system-generated noise. It is believed that this noise appearing on the log-periodic antenna is due to low frequency building vibrations driving vibrations on the antenna and modulating the RF signal [100]. On the non-resonant antenna, where the close-in spectrum is not masked by distortion, the minimum discernible signal is determined by the phase noise of the RF signal. With improvements in cancellation of the main RF signal, this phase noise will also decrease [100]. An additional single spurious signal (spur) appears at roughly 29 kHz on both antennas. This indicates system-generated spurs. This spur is believed to be a mixing intermediate frequency leaking from the signal generator used driving for the RF input signal. This spur can be eliminated through better isolation in the signal generator circuitry or through the use of a limiting amplifier [52].

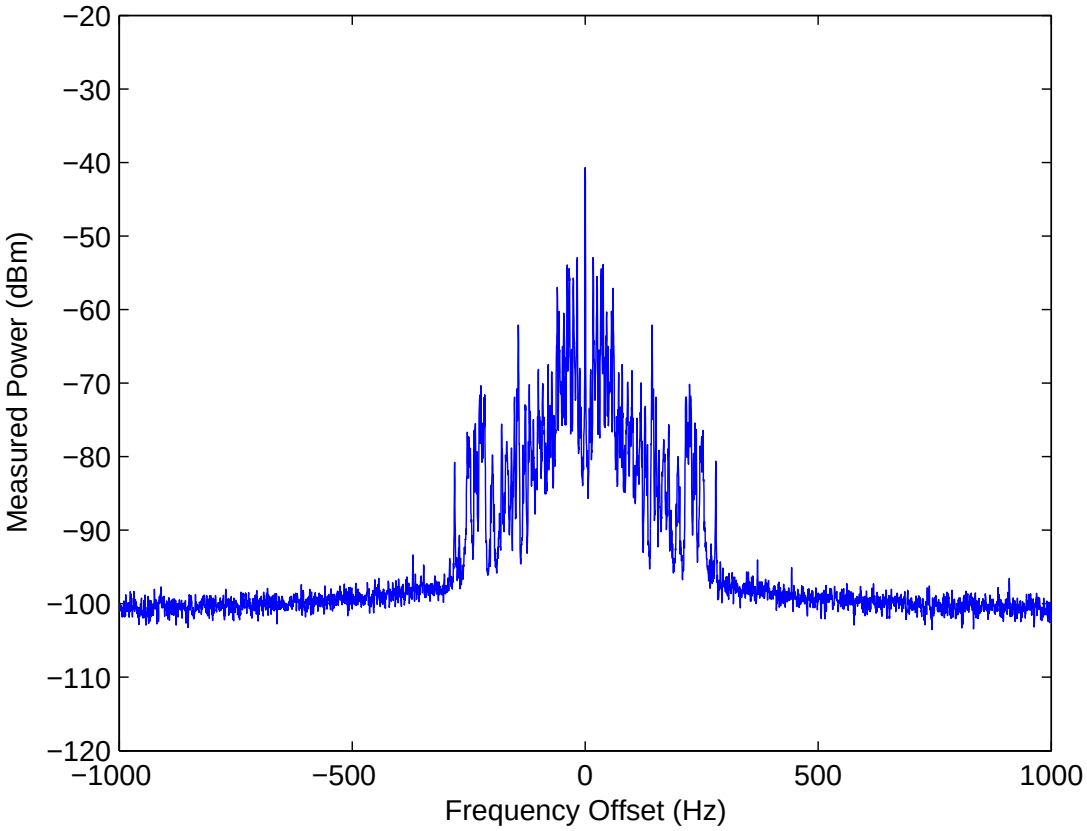

Figure 5.1: Narrowband power spectrum of the log-periodic dipole array antenna centered at 500 MHz.

Although measured in-band, both of the antennas have relatively low return loss in comparison to standard microwave components such as attenuators and terminations. With a high RF signal input power, the antenna reflected signal power will therefore also be substantial. To account for the high signal levels after the signal reflection, additional attenuation was needed, leading to a rise in the measurement noise floor as shown in the previous figures. In the absence of this attenuation, using a low-PIM termination in place of the antenna, it can be shown that the noise floor of the system decreases even further, as seen in Figs. 5.5 and 5.6. The termination used was a Pasternack PE6152, which has been shown to have very low PIM levels [100].

Using the spectral measurements of the two antennas and termination, the full measurement dynamic range of the system can be determined by taking the ratio of the input signal power to the reflected signal power measured. The measured dynamic range of the system is shown in Fig. 5.7. All three curves begin at a minimum at 1 Hz frequency offset and monotonically

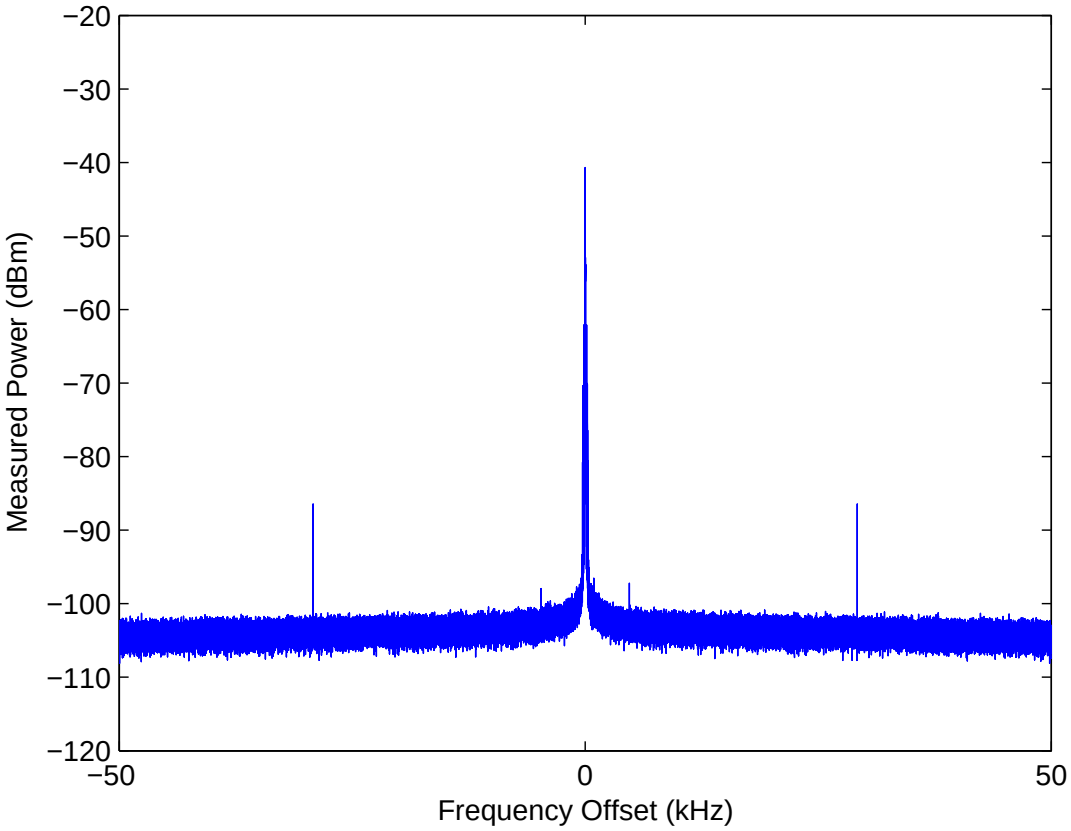

Figure 5.2: Wideband power spectrum of the log-periodic dipole array antenna centered at 500 MHz.

increase until plateauing around 100 kHz, with the exception of the log-periodic dipole antenna due to the excessive low frequency noise. The log-periodic dipole antenna achieves a slightly higher dynamic range than the non-resonant antenna due to slightly higher return loss, but the termination achieves a far higher dynamic range than either antenna reaching a maximum of 147 dBc. The dynamic range measurement was extended beyond the 50 kHz offset of the spectral measurements to 100 MHz using only 3 points per decade. At exactly 5 MHz offset and integer multiples thereof, there is an additional spur that appears due to the receiver. These points are not shown in Fig. 5.7 to give a better representation of the overall dynamic range of the receiver.

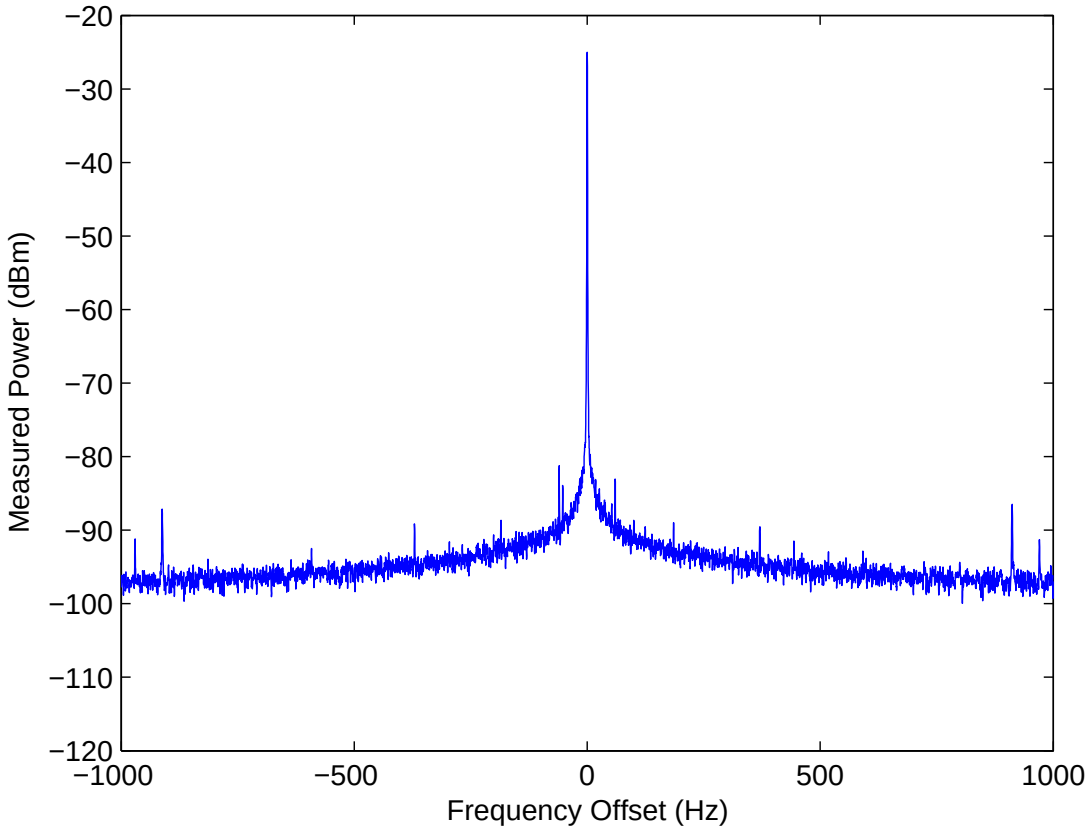

Figure 5.3: Narrowband power spectrum of the non-resonant antenna centered at 500 MHz.

5.3 Acoustic Modulation in Single Apertures

5.3.1 Doppler Scattering

The simplest form of coupling between mechanical vibration and electromagnetic (EM) propagation involves EM scattering from a moving surface, producing the Doppler effect. A sinusoidally vibrating surface phase modulates an incident single-tone EM wave resulting in a reflected signal

$$s(t) = \alpha \cos\left(\omega_{\mathrm{RF}} t + k_{\mathrm{RF}} \beta \cos\left(\omega_V t\right)\right) \tag{5.1}$$

where α is the RF signal amplitude, β is the vibrational displacement amplitude, ω_{RF} and ω_V are the angular frequencies of the RF signal and vibration, respectively, and k_{RF} is the RF

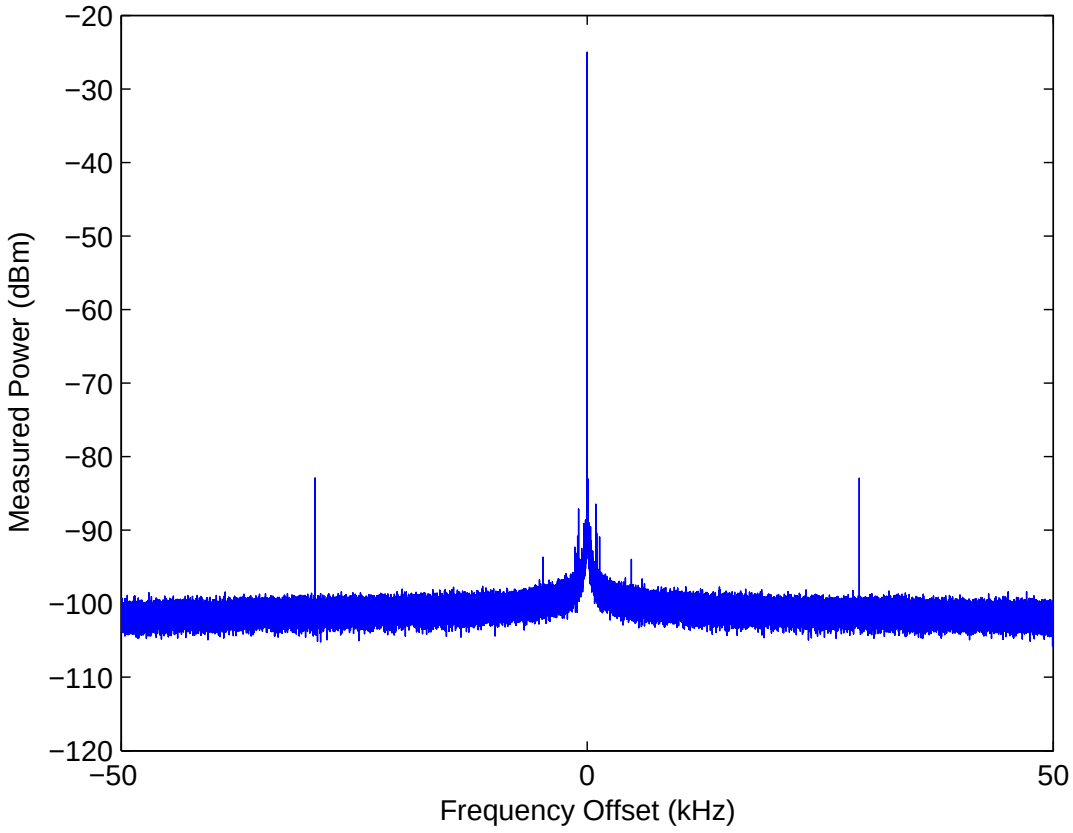

Figure 5.4: Wideband power spectrum of the non-resonant antenna centered at 500 MHz.

wavenumber. Following Fourier series expansion, (5.1) becomes

$$s(t) = \alpha \sum_{n=-\infty}^{\infty} J_n\left(k_{\mathrm{RF}}\beta\right) \cos\left[\left(\omega_{\mathrm{RF}} + n\omega_V\right) t\right] \tag{5.2}$$

where $J_n\left(x\right)$ is the n^{th}-order Bessel function of the first kind. For very small vibrations, $\beta \ll 1$ and (5.2) reduces to

$$s(t) \approx \alpha \left\{ \cos\left(\omega_{\mathrm{RF}} t\right) \pm \frac{k_{\mathrm{RF}}\beta}{2} \cos\left[\left(\omega_{\mathrm{RF}} \pm \omega_V\right) t\right] \right\}. \tag{5.3}$$

The spectrum of this signal is the original RF tone with two nonlinear modulation tones, one on each side of the RF tone.

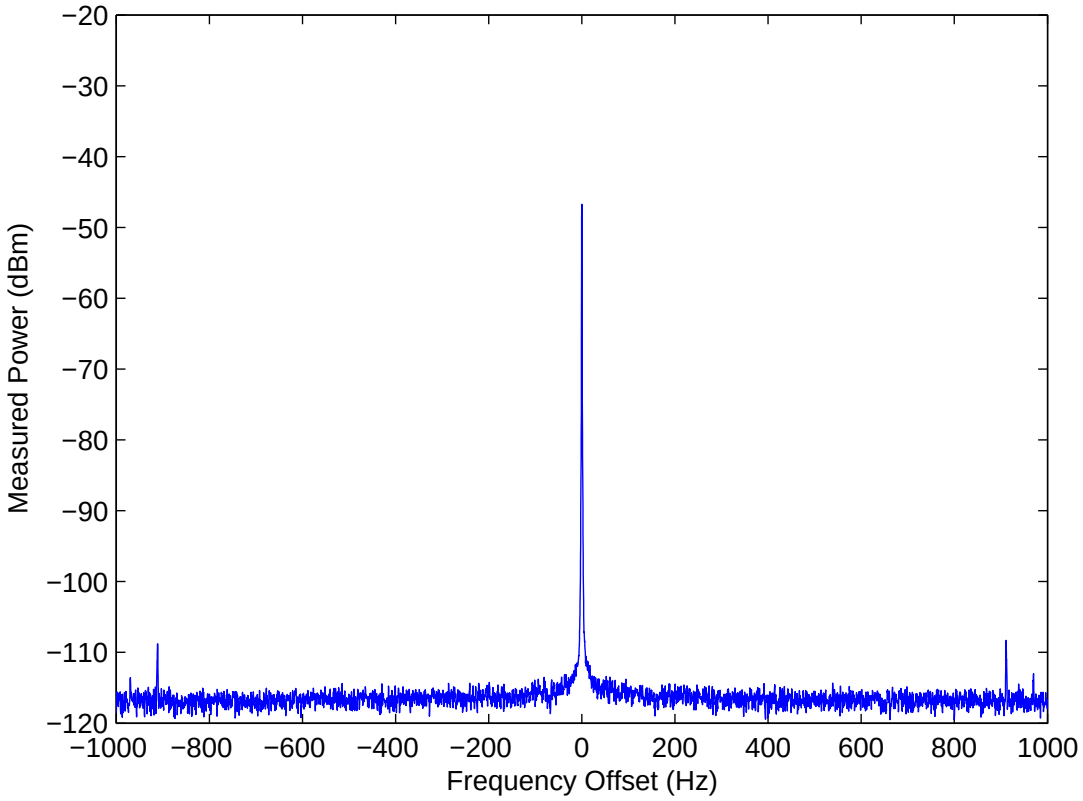

Figure 5.5: Narrowband power spectrum of the low-PIM termination (PE6152A) centered at 500 MHz.

5.3.2 RF Spectral Measurement

The test system is shown in Fig. 5.8 with an antenna, a studio monitor as the acoustic source, and a laser doppler vibrometer (LDV), all in an acoustic-RF anechoic chamber [113]. The side view of the antenna is shown in Fig. 5.9. The antenna was driven by a 27 dBm, 500 MHz RF tone, and the signal reflected at the antenna port was measured using the system in [100]. The resulting power spectra are shown in Figs. 5.10 and 5.11. In the narrowband spectrum, Fig. 5.10, the studio monitor was driven by a 1 kHz tone with 100 mV amplitude producing a measured sound pressure level (SPL) across the antenna averaging 80 dB. The antenna provided a rich acoustic scattering environment and the SPL varied by as much as 10 dB, dependent on frequency and placement of the microphone on the antenna. In the absence of the antenna, the sound level varied by no more than 3 dB. The wideband spectrum, Fig. 5.11, shows an acoustic-free response when the acoustic source is turned off, as well as the response to acoustic

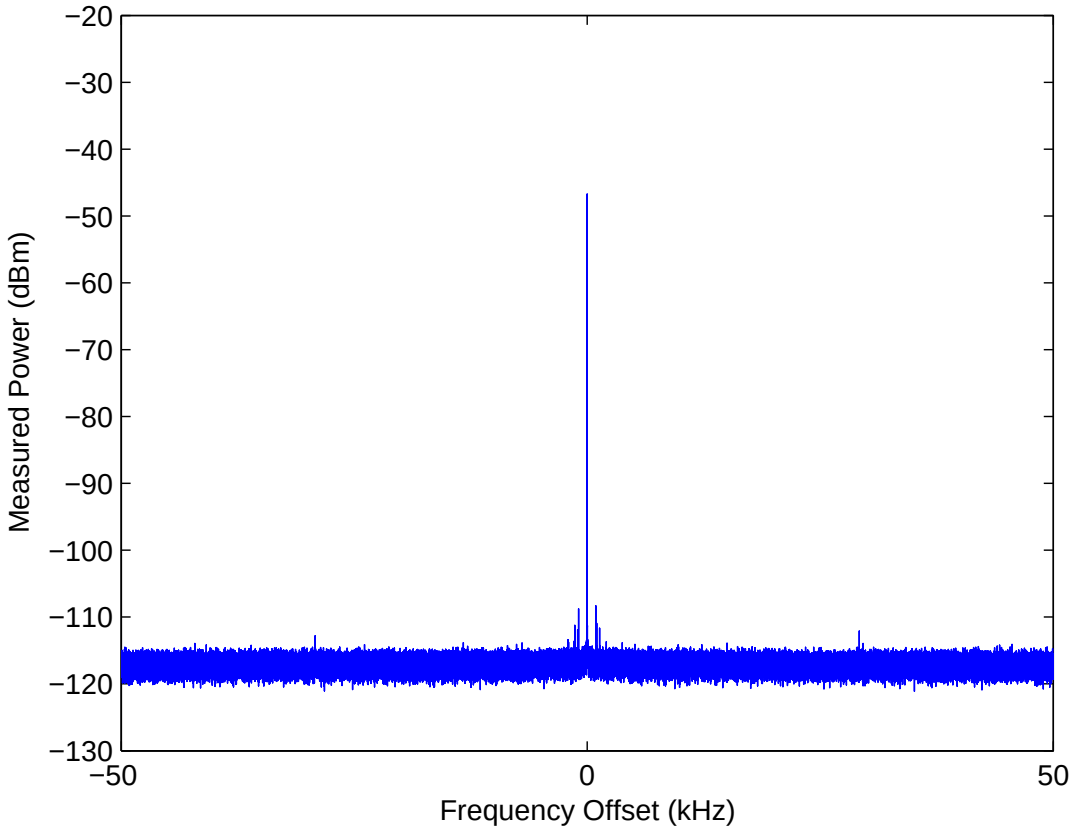

Figure 5.6: Wideband power spectrum of the low-PIM termination (PE6152A) centered at 500 MHz.

white noise. The acoustic-free response is the measurement noise floor.

With a single acoustic tone, Fig. 5.10, clean intermodulation products can be seen at a 1 kHz offset from the RF carrier on both sides. This tone is 100 dB below the RF signal power, which is beyond the dynamic range of previous measurement capability at 1 kHz offset. However, this is a level that can disrupt a sensitive receiver. In addition, "noisy" spurious signals (spurs) appear within 250 Hz of the RF carrier. This noise also appears with the acoustic source off, see Fig. 5.10, and is attributed to vibrations driven by building vibrations. Building noise is common to many acoustic anechoic chambers due to poor isolation at very low frequencies. It should be noted that no 60 Hz sources (the power mains frequency) or low frequency noise are measurable within the system itself, so these spurs are being generated by the antenna. No sideband harmonics of the intermodulation tone are measurable, consistent with the assumption of $\beta \ll 1$ in the Doppler scattering equations.

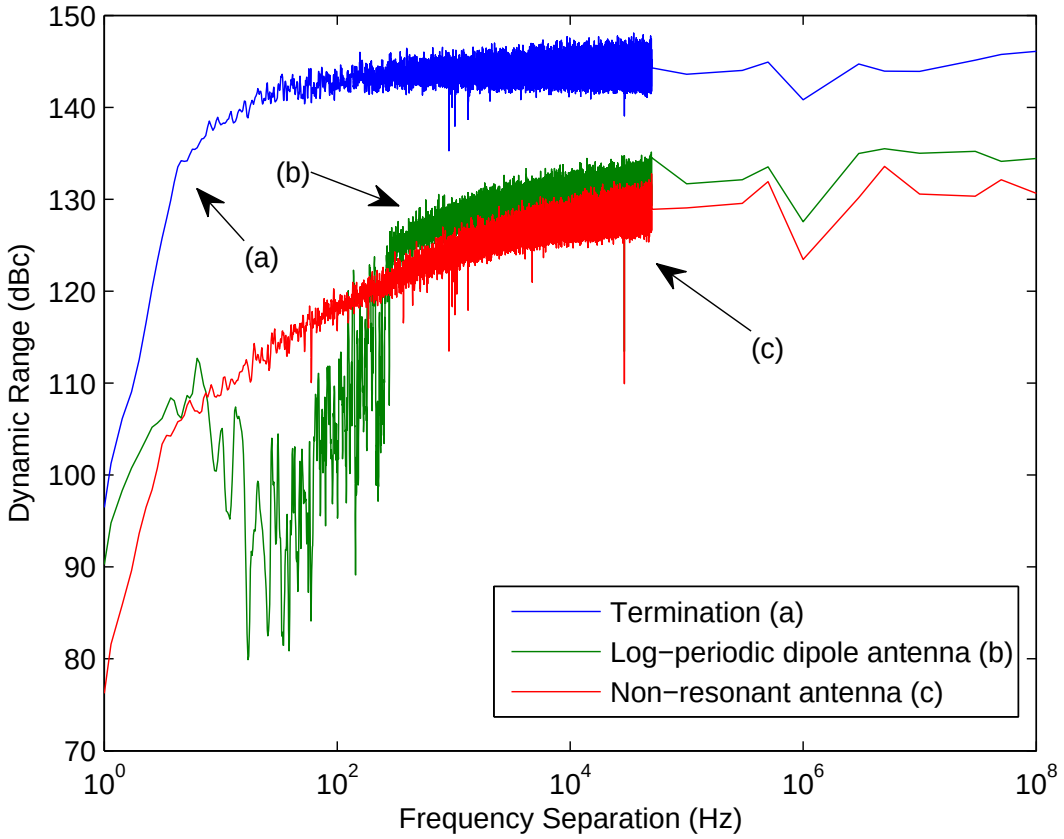

Figure 5.7: Dynamic range of measurement system using the low-PIM termination (a), the log-periodic dipole antenna (b), and the non-resonant antenna (c). Measurement density above 50 kHz is only 3 points per decade due to the increase in required measurement bandwidth.

The interference caused by the acoustic tone was further characterized over RF power (Fig. 5.12), acoustic power (Fig. 5.13), RF frequency (Fig. 5.14), and acoustic frequency (Fig. 5.15). These figures show the power of the major intermodulation tone in a single sideband across a sweep of the respective parameter. Both the RF and acoustic power sweeps, Figs. 5.12 and 5.13, show a 1:1 ratio of the drive power and intermodulation tone power. Figs. 5.14 and 5.15 show an irregular relationship between the intermodulation response and both the RF and acoustic frequencies. The curves in each sweep shift nearly uniformly over the secondary parameter (acoustic frequency in Fig. 5.14 and RF frequency in Fig. 5.15), suggesting that the envelopes of the RF and acoustic responses are not jointly dependent and that the antenna is largely acting as a single solid structure mechanically. Alternatively, the acoustic coupling could be mostly driven by one or a few of the antenna elements with the antenna acting as a single coupled EM

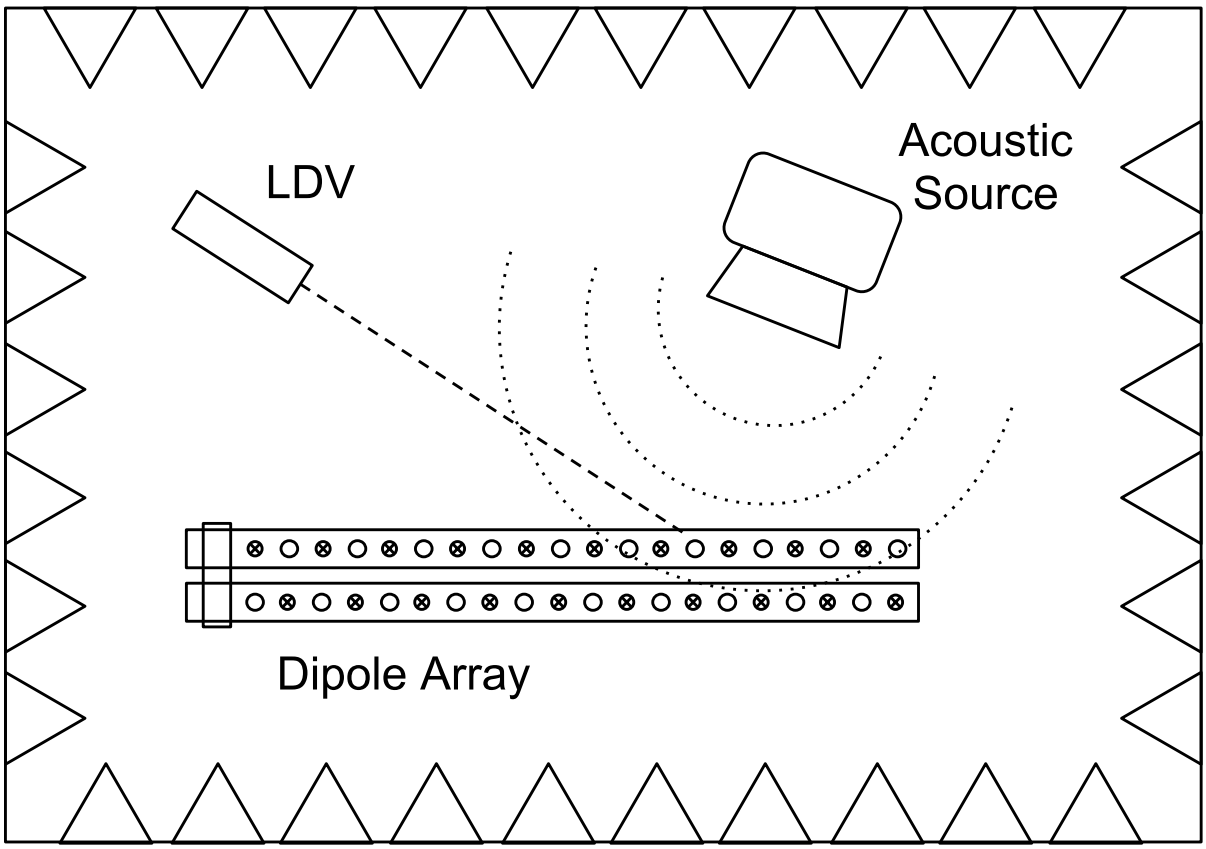

Figure 5.8: Top view of experimental set-up in anechoic chamber, including antenna, acoustic source, and laser doppler vibrometer (LDV).

structure.

The wideband spectrum, Fig. 5.11, shows the RF response when the studio monitor was driven by white acoustic noise. A rich spectrum of distortion appears on the reflected RF signal with notable peaks around 1.69 kHz, 4.86 kHz, 9.55 kHz, and 15.1 kHz. These peaks are believed to correspond to various resonant mechanical modes of the antenna. This spectrum is also similar to the 500 MHz single-tone acoustic frequency sweep, Fig. 5.15, such that the white noise response can be treated as the superposition of individual interfering tones.

5.3.3 Vibration Measurement

The RF response was compared to the mechanical resonances of the antenna using the LDV to measure the surface velocity of the sinusoidal vibration of each antenna element. The LDV was aligned with the free end of each element where displacement is expected to be maximum. At each acoustic frequency, the velocity response was averaged over all elements yielding an

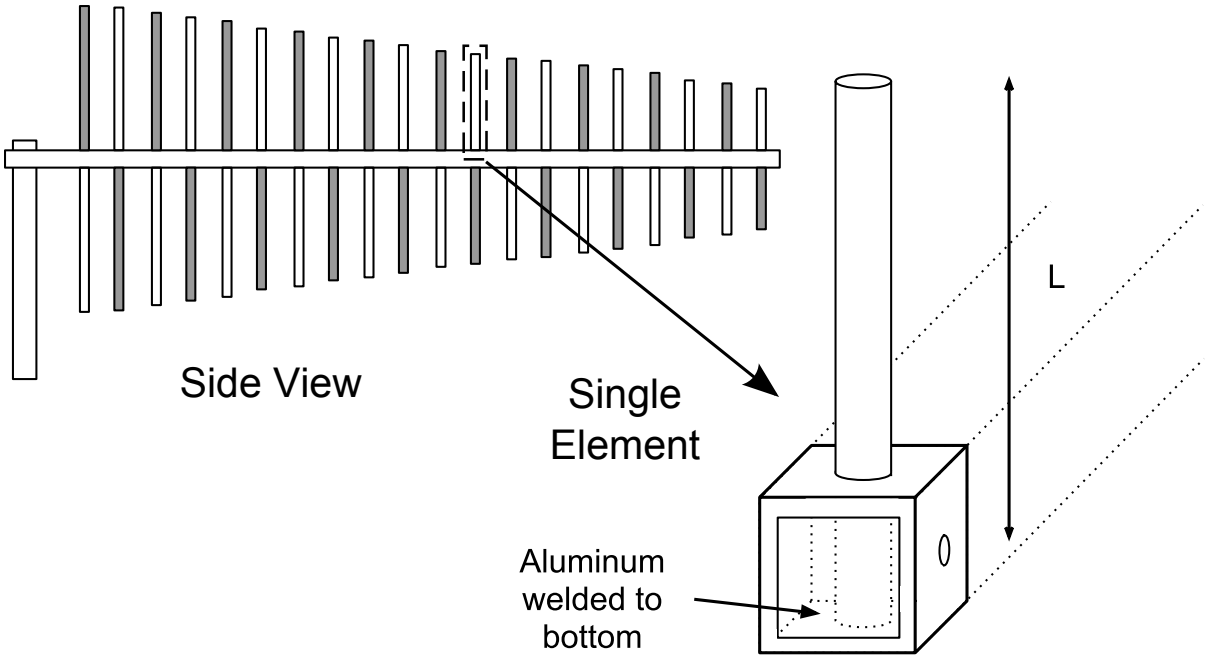

Figure 5.9: Side view of log-periodic dipole array antenna and cut-away showing an individual antenna element.

aggregate characterization of the vibration of the entire structure. This response is shown in Fig. 5.16 superimposed on the 500 MHz RF spectral response from Fig. 5.15. The profile of the velocity response mimics the RF response with mostly coincident peaks and nulls. A majority of the measured surface velocities were 1–2 orders of magnitude above the noise floor of the LDV, however scattering by the rounded elements led to excess noise above 10 kHz.

As shown in Fig. 5.8 the acoustic wave is normally incident at the antenna elements, so vibration will be transverse to the length of an element. If each element vibrates independently, then the vibration of an element can be modeled as the transverse vibration of a fixed, free bar, with n^{th} order resonant frequency [118]

$$f_{V,n} = \frac{\lambda_n^2 \pi \kappa v}{8L^2} \tag{5.4}$$

where κ is the radius of gyration, v is the speed of sound in the element, L is its length, and λ_n is the n^{th} solution to

$$\cosh\left(\lambda_n \frac{\pi}{2}\right) \cos\left(\lambda_n \frac{\pi}{2}\right) = -1. \tag{5.5}$$

Table 5.1 lists the first three transverse vibrational modes of each element. Fig. 5.16 de-emphasizes these individual resonances due to averaging, while the "structural" resonances stand out, such as the wide responses around 4 kHz and 8 kHz.

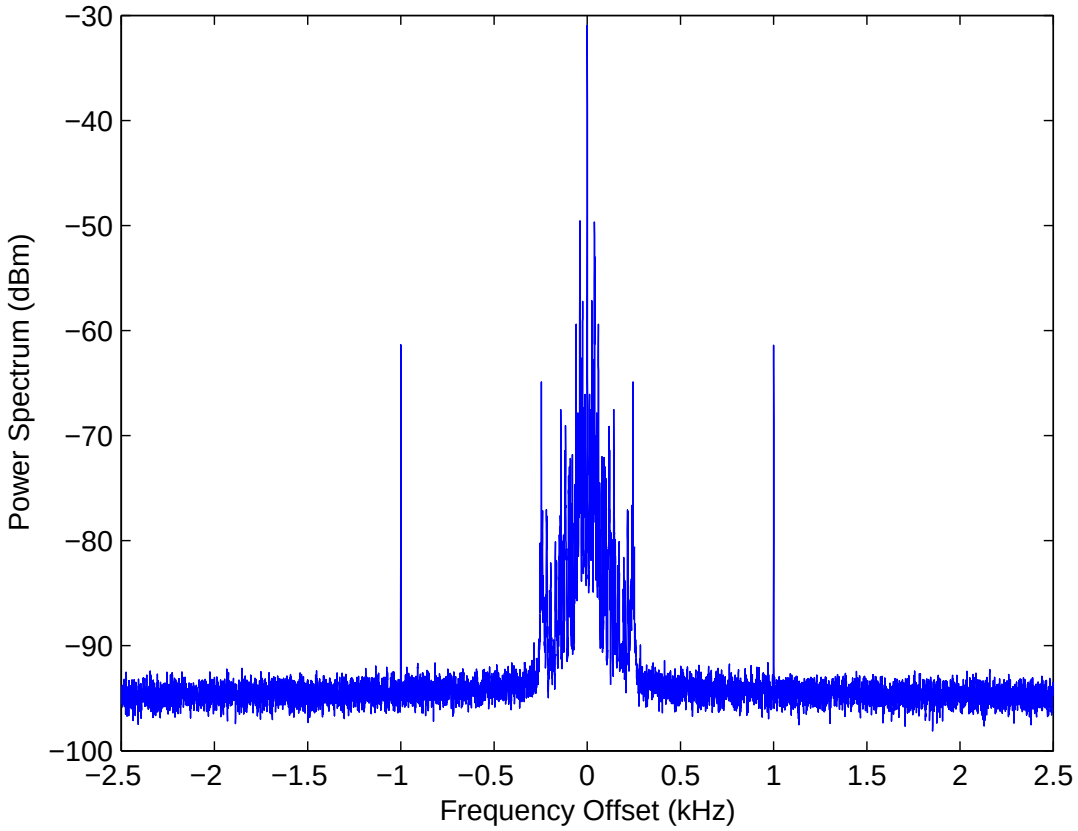

Figure 5.10: Narrowband RF spectrum with acoustic intermodulation. The RF carrier is 500 MHz at 27 dBm, with a 1 kHz acoustic tone at 100 mV drive voltage.

5.4 Summary

This chapter investigated the dynamic range of a resonant and a non-resonant antenna for use in a single aperture system. It was seen that with the resonant antenna that the levels of interference due to spectral regrowth introduced by structure vibrations sets a limit to the minimum discernible receive signal when a common aperture is used for transmit and receive. The non-resonant antenna did not present spurious signals related to vibration. These effects could only be seen using recently developed high-dynamic-range measurement equipment.

Significant levels of acoustic modulation on an RF signal on an antenna were also demonstrated. This modulation results from vibrations caused by an acoustic tone driving mechanical resonances in the antenna, leading to an effect similar to Doppler scattering. In a single aperture, this spurious frequency content can be expected to be a significant source of interference

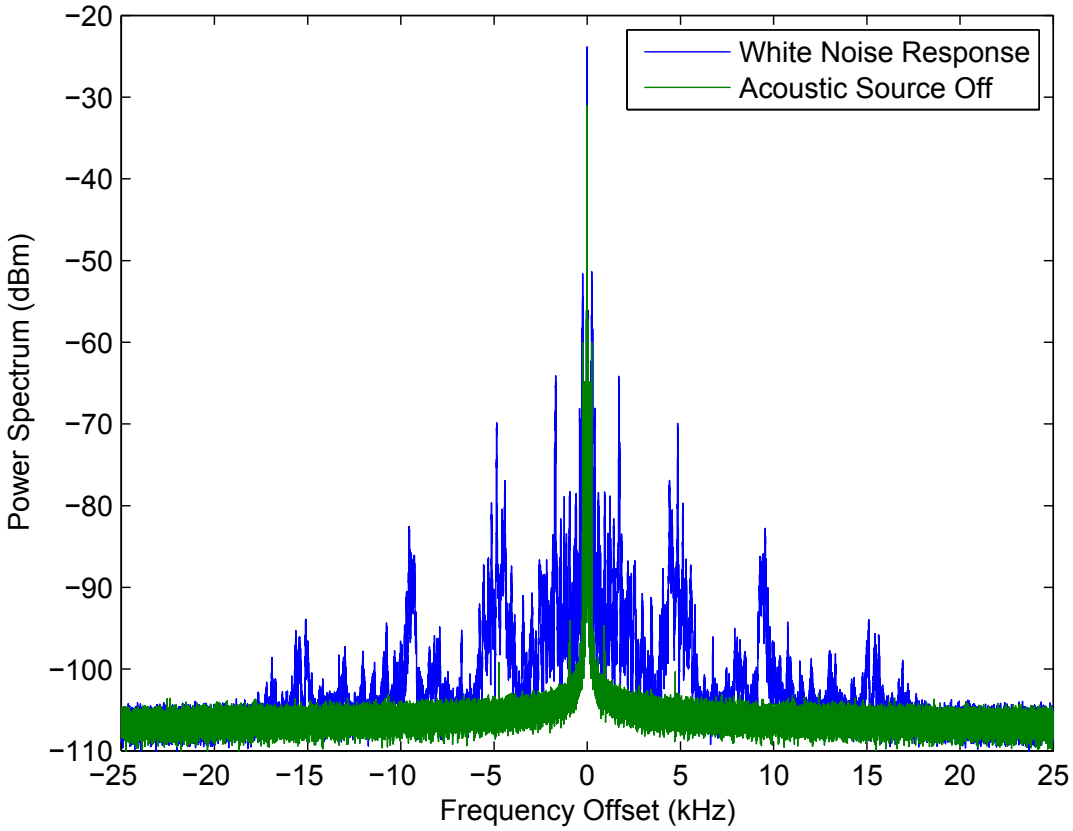

Figure 5.11: Wideband RF spectrum with acoustic white noise and without an acoustic signal. The RF carrier is 500 MHz at 27 dBm.

for sensitive receivers. Within the band of the antenna, the interfering signals can be expected to radiate at the same level that they appear at the antenna feed connection, generating co-site interference as well.

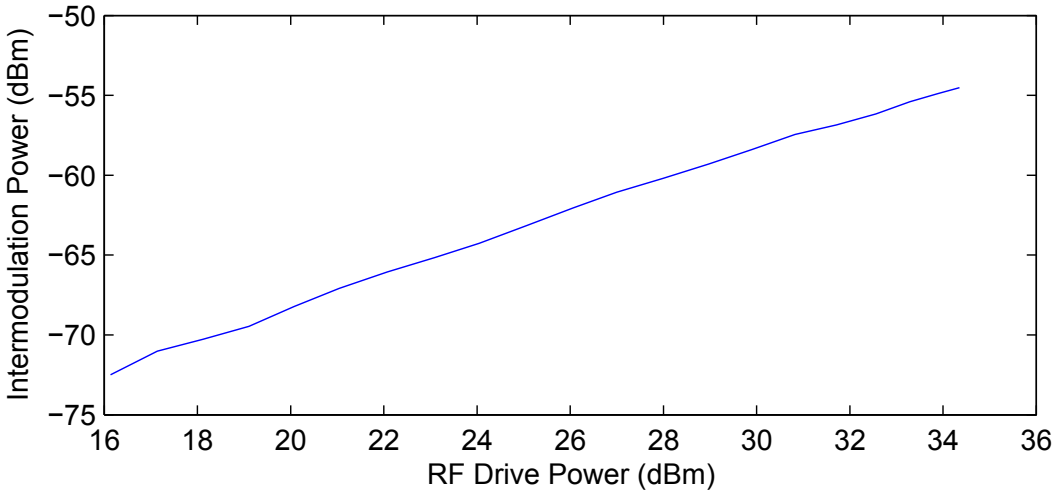

Figure 5.12: Intermodulation power versus RF drive power. The RF carrier is 500 MHz, with a 1 kHz acoustic tone at 100 mV drive voltage producing an SPL of 80 dB.

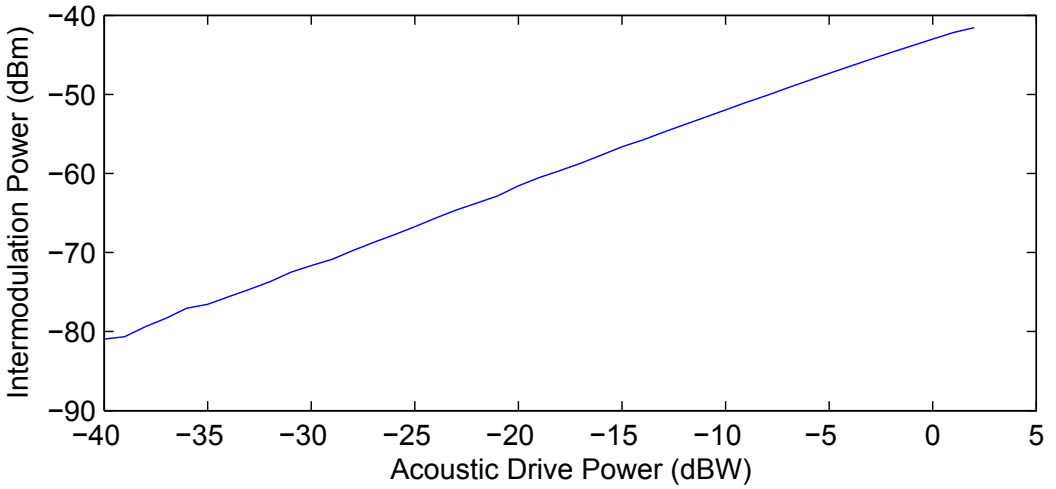

Figure 5.13: Intermodulation power versus acoustic drive power. The RF carrier is 500 MHz at 27 dBm, with a 1 kHz acoustic tone. Acoustic drive power is the power driving the input of the studio monitor and is directly proportional to sound pressure level (SPL).

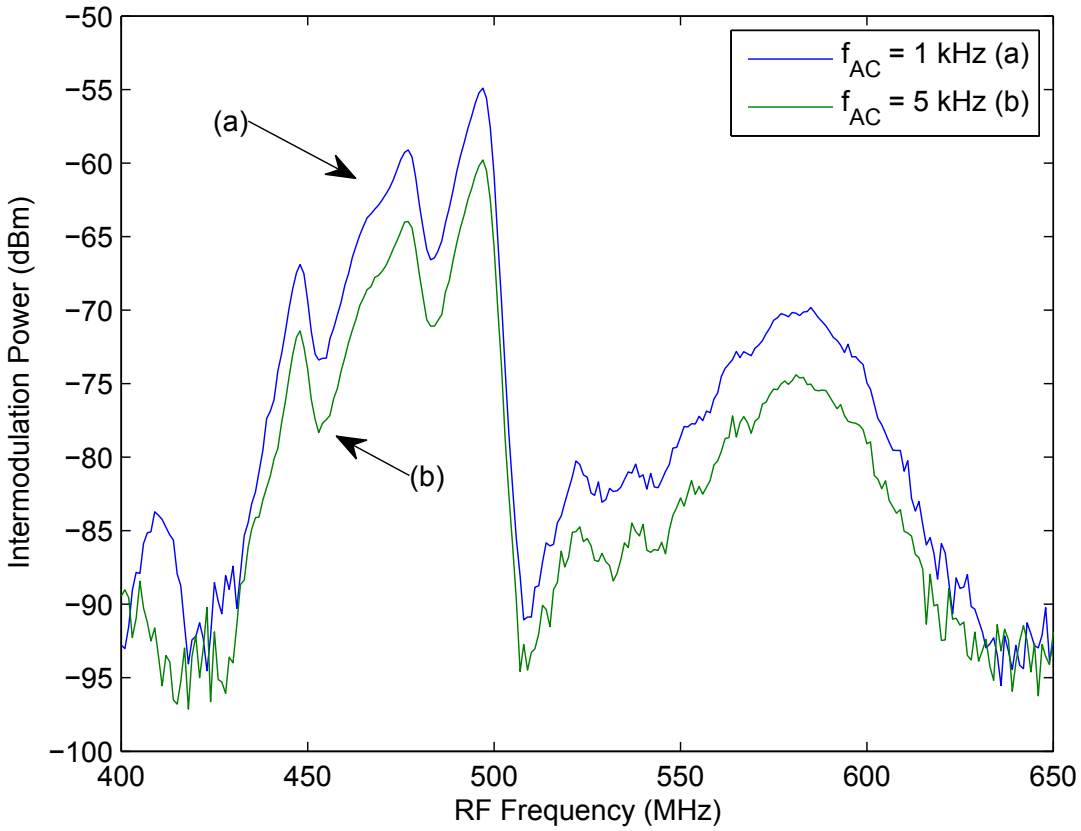

Figure 5.14: Intermodulation power versus RF frequency for single tone acoustic excitation at frequency, f_{AC}. The RF tone power is 27 dBm and the drive of the acoustic tones at 100 mV producing an SPL of 80 dB.

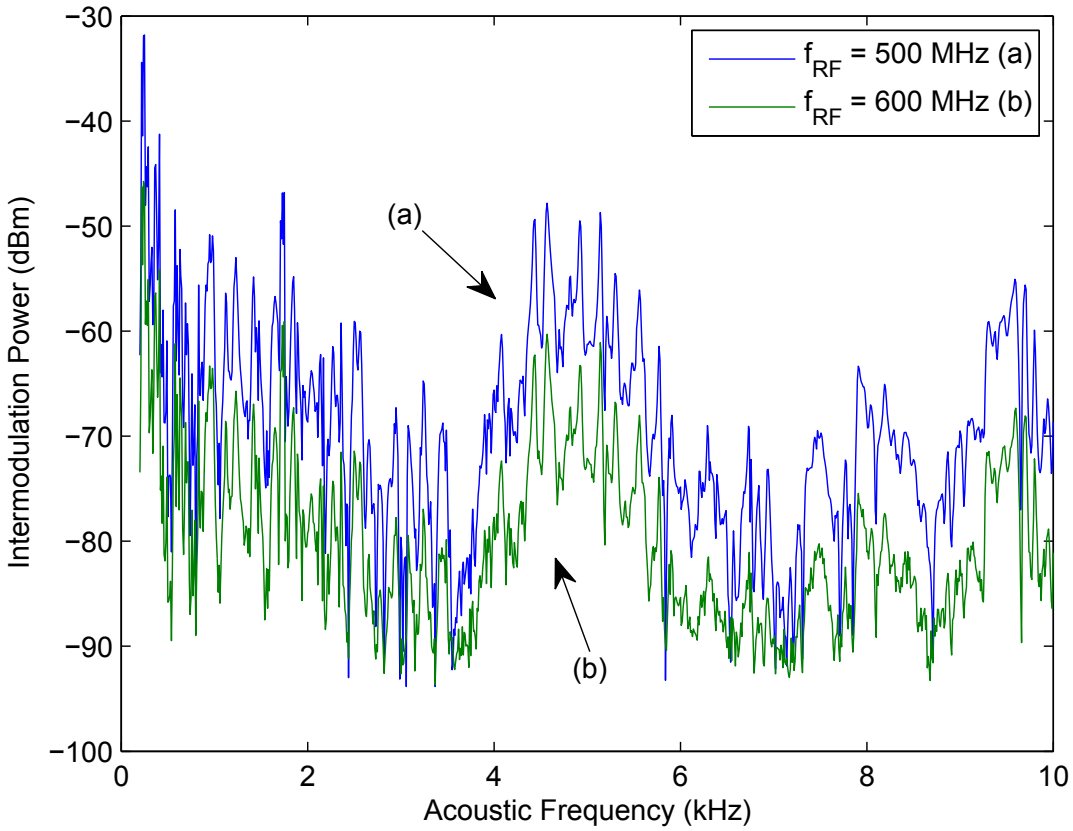

Figure 5.15: Intermodulation power versus acoustic frequency for multiple RF frequencies. The RF tone power is at 27 dBm, with the acoustic tone driven at 100 mV drive voltage producing an SPL of 80 dB.

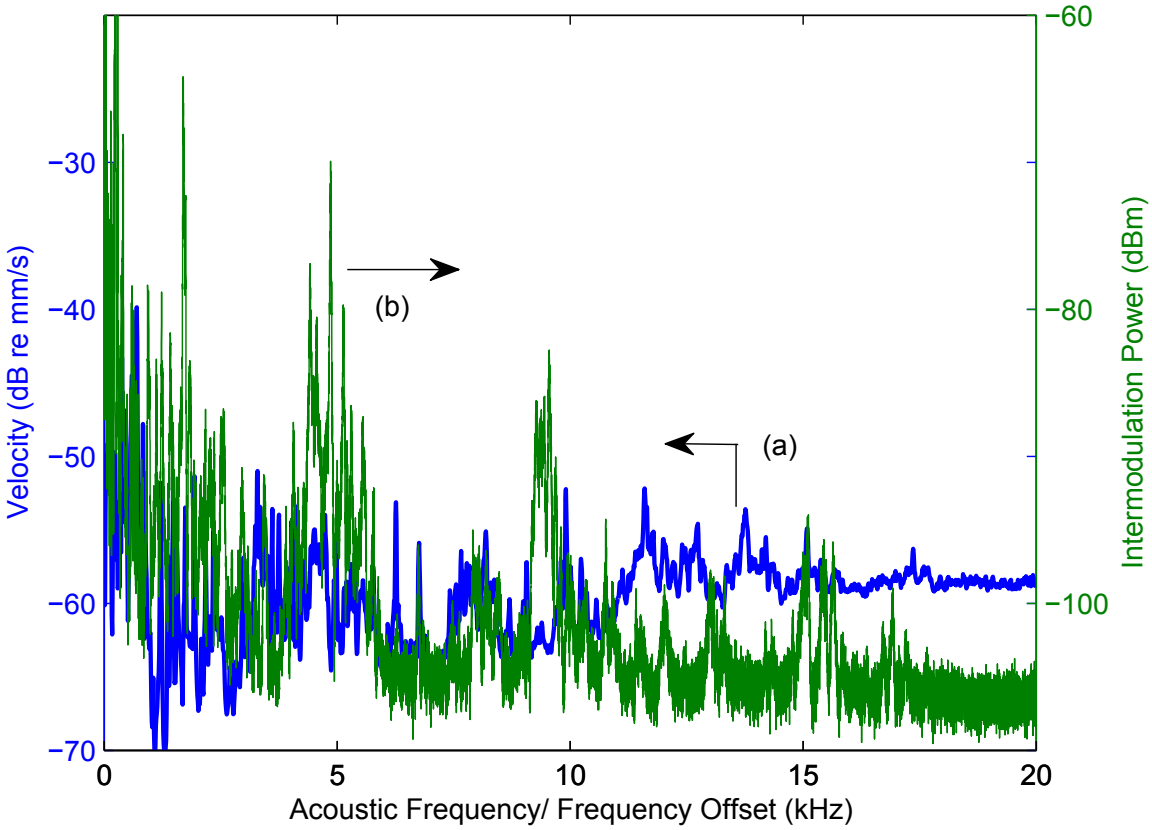

Figure 5.16: Averaged surface velocity response over all elements (a), with 500 MHz RF intermodulation response (b).

Table 5.1: Primary theoretical transverse mechanical modes of individual antenna elements. (L – cm, f_V – Hz)

#	1	2	3	4	5	6	7
L	24.2	23.0	21.7	20.7	19.5	18.5	17.5
$f_{V,1}$	89	98	110	121	137	152	172
$f_{V,2}$	556	615	691	760	856	951	1063
$f_{V,3}$	3051	3377	3794	4169	4698	5220	5833
#	8	9	10	11	12	13	14
L	16.5	15.5	14.8	14.1	13.2	12.5	11.8
$f_{V,1}$	191	216	237	261	298	333	373
$f_{V,2}$	1196	1355	1486	1638	1869	2084	2338
$f_{V,3}$	6562	7436	8156	8986	10253	11434	12830
#	15	16	17	18	19	20	
L	11.1	10.5	10.0	9.5	8.8	8.6	
$f_{V,1}$	422	471	520	576	671	702	
$f_{V,2}$	2643	2953	3256	3608	4204	4402	
$f_{V,3}$	14500	16204	17865	19795	23069	24155	

Chapter 6

Conclusion

6.1 Summary of Research and Original Contributions

This dissertation has explored the characterization of passive spectral regrowth in RF systems, with an emphasis on understanding the fundamental processes involved and how they are translated to detectable phenomena. Increasing sensitivity in radio frequency (RF) systems has increased the need for this fundamental understanding as long-standing approximations and assumptions about the significance of small signals no longer hold. Acousto-electromagnetic interaction has been identified as a major source of passive spectral regrowth, using both analytic methods and newly developed measurement capability.

To enable detection of low-level passive spectral regrowth, a high-dynamic-range nonlinear measurement system was developed using automated analog cancellation. Cancellation depth was previously given as a primary limit to system dynamic range, so the development here focused on maximizing automated cancellation. Extreme cancellation of over 70 dB was achieved through careful calibration of the feedforward signal amplitude and a directly convergent, weakly-iterative algorithm. In application to two-tone nonlinear distortion characterization it was shown that at high levels of cancellation, the cancellation depth does not limit dynamic range performance. Instead the primary limits on system dynamic range are system residual spectral regrowth and the receiver thermal noise floor. In two-tone testing, up to 120 dBc of dynamic range was achieved in two-port transmission measurements, and up to 140 dBc of dynamic range was achieved in one-port reflection measurements for tone frequency separations of at least 1 kHz. Dynamic range performance decreases for 1 Hz tone frequency separations to 94 dBc and 111 dBc, respectively. The flexibility of the canceller-based measurement was demonstrated by characterization common laboratory termination over a tone frequency separation sweep of 1 Hz to 100 MHz at a center frequency of 460 MHz, achieving 21.7% fractional bandwidth without reconfiguration—significantly higher than possible with filter-based systems.

Passive spectral regrowth is difficult to predict theoretically, because the small interaction or coupling involved is often approximated out as insignificant to make governing equations tractable and efficient. Removing these assumptions is essential to understanding the fundamental processes. In particular, new acousto-electromagnetic sources of spectral regrowth were identified in the interaction of an incident RF signal and a vibrating metal plate. Four scattering effects were derived from basic principles, and characterized by their modulation on the scattered RF wave including Doppler phase modulation, amplitude modulation from special relativity, path loss modulation, and modulation of radar cross section. The modulation spectrum for each of these mechanisms were shown to have unique discriminating features. Using the high-dynamic-range nonlinear measurement system, significant spectral regrowth from Doppler phase modulation and radar cross section modulation were observed below the dynamic range of conventional systems. By correlating the measured RF reflected signal with known scattering mechanisms, the RF measurement system also becomes a ground-penetrating radar vibrometer and is shown to detect vibrational displacement as low as 11 nm.

In structures more complex than a simple vibrating plate, the acousto-electromagnetic interaction will be much richer, inducing additional spectral regrowth through intermodulation and self-coupling. This interaction was shown to be significant in broadband antennas used for single aperture applications. Modulation of an RF carrier tone was observed and characterized on antennas remotely stimulated by an acoustic source. This modulation was correlated with the power and frequency of the applied acoustic stimulus, and a complex spectral response was observed, suggesting coupling between the mechanical and electromagnetic resonances of the antenna. The effect of spectral regrowth in antennas was characterized as a limiting factor in the dynamic range of a single aperture system.

6.2 Future Research

The research presented in this dissertation has many fundamental and practical extensions. Each chapter presents unique advancements to draw from on for future work.

There are numerous opportunities to expand on the enhanced canceller performance presented in Chapter 3. The demonstrated maximum cancellation depth exceeded the performance needed to enable high-dynamic-range measurements in the current nonlinear measurement system. This excess cancellation can be exploited in future work, by using higher-power stimulus tones and more sensitive receivers. As the fundamental system limitations are relaxed, the enhanced cancellation would enable even greater dynamic range. As dynamic range is increased, residual system spectral regrowth will become the primary limit on nonlinear sensitivity. As this system is composed of real, physical components, there is a limit to the minimum system-generated spectral regrowth. This spectral content could be removed by analog cancellation

using an additional source at the frequency and amplitude of the residual tone. The process for cancellation would be similar to the process for cancelling the primary high-power tone. By cancelling the residual spectral regrowth, any detected nonlinear content could be assumed to be generated by the target or device-under-test. Alternatively, this process could also provide insight into the relative phase of the spectral tones, since cancellation process determines a phase shift relative to a reference feed-forward signal. The addition of phase measurement would allow for vector characterization of passive spectral regrowth, providing an extra dimension for classification and discrimination.

Nearly all types of RF probing systems may benefit from analog cancellation, as the high-power probing source is commonly the largest source of interference. This extension is demonstrated in Chapter 4, as the modulation spectrum is interpreted so that the measurement system becomes a radar vibrometer. Aside from measurement, any system in need of rejecting a large signal in favor of a small signal will benefit from enhanced cancellation. Feed-forward linearization of power amplifier and radar reverse-power-cancellers, which already use feedforward cancellation techniques, could take advantage of a directly integrated, self-healing canceller based on the directly convergent algorithm. In communications, co-site interference resulting from direct coupling of antennas could be dynamically cancelled, thus enabling greater performance from physically distributed antenna arrays. With careful design, the analog canceller could also be extended to remove external interfering signals, however significant engineering and development would be need to ensure a fast enough procedural loop time to enable truly adaptive cancellation. As currently implemented using discrete components, the system can only respond to environment changes slower than 1 Hz. Cancellation in rapidly-changing environments, as in most wireless systems, will likely require extensive integration at the chip level.

Analytic expressions for the modulation sidebands on acoustically-scattered RF signals were derived in Chapter 4. Each of the effects considered featured a unique discriminating parameter that could be exploited in remote sensing of vibrating objects. The relative power amplitude of the lowest-order modulation tones from amplitude modulation from special relativity and Doppler phase modulation were shown to be equal to the ratio of the RF and vibrational frequencies. Since RF frequencies are typically much greater than vibrational frequencies, the amplitude modulation can generally be ignored. In certain detection techniques, such as in handheld metal detectors, very low RF frequencies are used with ultrasonic vibrations, making the ratio of frequencies much closer to one, and thus making the amplitude modulation significant. Both amplitude modulation from special relativity and path loss modulation were shown to be independant of RF wavelength, expanding the spectrum available for exploitation, however path modulation was also shown to have an inverse relationship with standoff distance, making moderate-to-long-range detection difficult. Modulation of radar cross section was shown only for a simple, symmetrically rocking plate, but significant modulation was detectable, and

a modulation spectrum was derived that suppressed all odd-order tones. The key limitation of these theoretical derivations is the assumption of very simple interaction. While rocking modulation could be generated in a controlled, laboratory environment, inducing the rocking motion using standoff acoustics is a challenging proposition at best. As the motion of vibrating objects from an acoustic stimulus is better understood, new equations could be derived following the general framework presented here. Analysis of more complicated structures and motion could help extend RF measurement of vibration, taking advantage of new high dynamic range techniques and ground-penetrating capability. In addition, this work may be applied in common scenarios where the sources of passive spectral regrowth are poorly understood, such as antennas mounted on moving platforms or vehicles and near the top of windy towers.

Chapter 5 introduced the concept of modulating an RF tone through acoustic stimulation of an antenna. This is both an undesirable noise source to be considered in virtually all antenna environments and a potential new modality for probing electronic equipment. Acoustic stimulation to induce an RF response has the benefit of operating in an orthogonal domain, where interference may be expected to be minimal or non-existent. Aside from standard applications in metal and defect sensing as mentioned in the chapter, acoustic stimulation could be applied to systems known to be sensitive to motion, such as "rusty bolt" connectors. Current methods of testing these connectors on antenna masts rely on a technician to physically tap the connector and measure the resultant response. Integrating an acoustic source into the system would allow for controlled, automated testing of this type of spectral regrowth, reducing time and monetary costs. Perhaps critically, acoustic tests could also be designed to verify antenna performance and immunity from the nonlinear processes considered in Chapter 4, however the coupling mechanisms between acoustics, electromagnetics, and vibration will need to be studied further. The propensity of acousto-electromagnetic coupling mechanisms prevents some practical applications, but new understanding, such as introduced in Chapter 4, could help build the next generation of detection sensors.

REFERENCES

[1] S.-W. Chen, W. Panton, and R. Gilmore, "Effects of nonlinear distortion on CDMA communications systems," *IEEE Trans. Microw. Theory Tech.*, vol. 44, no. 12, pp. 2743–2750, Dec. 1996.

[2] K. G. Gard, H. M. Gutierrez, and M. B. Steer, "Characterization of spectral regrowth in microwave amplifiers based on the nonliner transformation of a complex Gaussian process," *IEEE Trans. Microw. Theory Tech.*, vol. 47, no. 7, pp. 1059–1069, Jul. 1999.

[3] V. Aparin, "Analysis of CDMA signal spectral regrowth and waveform quality," *IEEE Trans. Microw. Theory Tech.*, vol. 49, no. 12, pp. 2306–2314, Dec. 2001.

[4] T. H. Lee, *The Design of CMOS Radio-Frequency Integrated Circuits*, 2nd ed. New York: Cambridge Univ. Press, 2004.

[5] M. Bayrak and F. A. Benson, "Intermodulation products from nonlinearities in transmission lines and connectors at microwave frequencies," *Proc. IEEE*, vol. 122, no. 4, pp. 361–367, Apr. 1975.

[6] F. Arazm and F. A. Benson, "Nonlinearities in metal contacts at microwave frequencies," *IEEE Trans. Electromagn. Compat.*, vol. 22, no. 3, pp. 142–149, Aug. 1980.

[7] M. B. Amin and F. A. Benson, "Nonlinear effects in coaxial cables at microwave frequencies," *Electron. Lett.*, vol. 13, no. 25, pp. 768–770, Dec. 1977.

[8] ——, "Coaxial cables as sources of intermodulation interference at microwave frequencies," *IEEE Trans. Electromagn. Compat.*, vol. 20, no. 3, pp. 376–384, Aug. 1978.

[9] P. L. Lui, "Passive intermodulation interference in communication systems," *Electronics and Communication Engineering*, vol. 2, no. 3, pp. 109–118, Jun. 1990.

[10] M. T. Abuelma'atti, "Prediction of passive intermodulation arising from corrosion," *IEE Proc. Science, Measurement, and Technology*, vol. 150, no. 1, pp. 30–34, Jan. 2003.

[11] M. Vladimirescu, R. Kwiatkowski, and K. Engel, "Tunnel conduction consequences in high frequency microcontacts; passive intermodulation effect," in *50th IEEE Holm Conference on Electrical Contacts*, Sep. 2004, pp. 152–159.

[12] C. Vicente and H. L. Hartnagel, "Passive-intermodulation analysis between rough rectangular waveguide flanges," *IEEE Trans. Microw. Theory Tech.*, vol. 53, no. 8, pp. 2515–2525, Aug. 2005.

[13] A. G. Schuchinsky, J. Francey, and V. F. Fusco, "Distributed sources of passive intermodulation on printed lines," in *Proc. IEEE AP-S Int. Symp.*, Jul. 2005, pp. 447–450.

[14] D. E. Zelenchuk, A. P. Shitvov, A. G. Schuchinsky, and V. F. Fusco, "Passive intermodulation in finite lengths of printed microstrip lines," *IEEE Trans. Microw. Theory Tech.*, vol. 56, no. 11, pp. 2426–2434, Nov. 2008.

[15] J. R. Wilkerson, K. G. Gard, A. G. Schuchinsky, and M. B. Steer, "Electro-thermal theory of intermodulation distortion in lossy microwave components," *IEEE Trans. Microw. Theory Tech.*, vol. 56, no. 12, pp. 2717–2725, Dec. 2008.

[16] J. R. Wilkerson, P. G. Lam, K. G. Gard, and M. Steer, "Distributed passive intermodulation distortion on transmission lines," *IEEE Trans. Microw. Theory Tech.*, vol. 59, no. 5, pp. 1190–1205, May 2011.

[17] G. C. Bailey and A. C. Ehrlich, "A study of RF nonlinearities in nickel," *Appl. Phys.*, vol. 50, no. 1, pp. 453–461.

[18] Y. Yamamoto and N. Kuga, "Short-circuit transmission line method for PIM evaluation of metallic materials," *IEEE Trans. Electromagnetic Compatibility*, vol. 49, no. 3, pp. 682–688, Aug. 2007.

[19] J. Shefer, R. J. Klensch, G. Kaplan, and H. C. Johnson, "Clutter-free radar for cars," *Wireless World*, pp. 117–122, May 1974.

[20] R. O. Hstger, "Harmonic radar systems for near-ground in-foliage nonlinear scatterers," *IEEE Trans. Aerosp. Electron. Syst.*, vol. 12, no. 2, pp. 230–245, May 1976.

[21] D. Mascanzoni and H. Wallin, "The harmonic radar: A new method of tracing insects in the field," *Ecol. Entomol.*, vol. 11, no. 4, pp. 387–390, Nov. 1986.

[22] A. F. Martone, A. K. Mikkilineni, and E. J. Delp, "Forensics of things," in *Proc. IEEE Southwest Symp. Image Analy. Interpretation*, Jun. 2006, pp. 149–152.

[23] J. A. Kosinski, W. D. Palmer, and M. B. Steer, "Unified understanding of RF remote probing," *IEEE Sensors J.*, vol. 11, no. 12, pp. 3055–3063, Dec. 2011.

[24] G. J. Mazarro, M. B. Steer, K. G. Gard, and A. L. Walker, "Response of RF networks to transient waveforms: interference in frequency-hopped communications," *IEEE Trans. Microw. Theory Tech.*, vol. 56, no. 12, pp. 2808–2814, Dec. 2008.

[25] G. J. Mazarro, M. B. Steer, and K. G. Gard, "Filter characaterization using one-port pulsed radio-frequency measurements," *IET Microw., Antennas, Propagat.*, vol. 3, no. 2, pp. 303–309, Mar. 2009.

[26] C. Feige, T. Ostertag, M. Loschonsky, and L. M. Reindl, "Radar assisted detection of passive electronic components," in *Proc. IEEE Radio and Wireless Symp. (RWS)*, Jan. 2010, pp. 200–203.

[27] W. R. Scott, C. T. Schroeder, and J. S. Martin, "A hybrid acoustic/electromagnetic technique for locating land mines," in *Proc. Int. Geosci. Remote Sensing Symp.*, Jun. 1998, pp. 216–218.

[28] A. Stelzer, C. G. Diskus, K. Lübke, and H. W. Thim, "A microwave position sensor with submillimeter accuracy," *IEEE Trans. Microw. Theory Tech.*, vol. 47, no. 12, pp. 2621–2624, Dec. 1999.

[29] S. Kim and C. Nguyen, "On the development of a multifunction millimeter-wave sensor for displacement sensing and low-velocity measurement," *IEEE Trans. Microw. Theory Tech.*, vol. 52, no. 11, pp. 2503–2512, Nov. 2004.

[30] F. Barbon, G. Vinci, S. Lindner, R. Weigel, and A. Koelpin, "A six-port interferometer based micrometer-accuracy displacement and vibration measurement radar," in *2012 IEEE MTT-S Int. Microw. Symp. Dig.*, Jun. 2012, pp. 1–3.

[31] S. Borkar and R. F. Yang, "Reflection of electromagnetic waves from oscillating surfaces," *IEEE Trans. Antennas Propag.*, vol. 23, no. 1, pp. 122–127, Jan. 1975.

[32] R. Kleinman and R. Mack, "Scattering by linearly vibrating objects," *IEEE Trans. Antennas Propag.*, vol. 27, no. 3, pp. 344–352, May 1979.

[33] D. De Zutter, "Doppler effect from a transmitter in translational motion," *IEE Journal Microwaves, Optics and Acoustics*, vol. 3, no. 2, pp. 85–92, Mar. 1979.

[34] J. Cooper, "Scattering of electromagnetic fields by a moving boundary: the one-dimensional case," *IEEE Trans. Antennas Propag.*, vol. 28, no. 6, pp. 791–795, Nov. 1980.

[35] J. Van Bladel and D. De Zutter, "Reflections from linearly vibrating objects: plane mirror at normal incidence," *IEEE Trans. Antennas Propag.*, vol. 29, no. 4, pp. 629–637, Jul. 1981.

[36] D. De Zutter, "Reflections from linearly vibrating objects: plane mirror at oblique incidence," *IEEE Trans. Antennas Propag.*, vol. 30, no. 5, pp. 898–903, Sep. 1982.

[37] D. Censor, "Theory of the Doppler effect: fact, fiction and approximation," *Radio Sci.*, vol. 19, no. 4, pp. 1027–1040, Jul. 1984.

[38] J. E. Gray and S. R. Addison, "Effect of nonuniform target motion on radar backscattered waveforms," *IEE Proc.-Radar, Sonar, Navig.*, vol. 150, no. 4, pp. 262–70, 2003.

[39] V. C. Chen, F. Li, S.-S. Ho, and H. Wechsler, "Micro-Doppler effect in radar: phenomenon, model, and simulation study," *IEEE Trans. Aerosp. Electron. Syst.*, vol. 42, no. 1, pp. 2–21, Jan. 2006.

[40] D. E. Lawrence and K. Sarabandi, "Acoustic and electromagnetic wave interaction: analytical formulation for acousto-electromagnetic scattering behavior of a dielectric cylinder," *IEEE Trans. Antennas Propag.*, vol. 49, no. 10, pp. 1382–1392, Oct. 2001.

[41] A. H. Waynick, "The reduction of microphonics in triodes," *Appl. Phys.*, vol. 18, no. 2, pp. 239–245, Feb. 1947.

[42] R. Nelson and L. Davidson, "Electrical noise generated from the microphonic effect in capacitors," in *2002 IEEE Int. Symp. Electromagnetic Compatibility*, Aug. 2002, pp. 855–860.

[43] R. Hartman. (2011) SI Series PIM Analyzers - D Model Revision. [Online]. Available: http://www.summitekinstruments.com/passive/docs/Technical Data D.pdf

[44] A. Christianson and W. Chappell, "Measurement of ultra low passive intermodulation with ability to separate current/voltage induced nonlinearities," in *2009 IEEE MTT-S Int. Microwave Symp. Dig.*, Jun. 2009, pp. 1301–1304.

[45] J. K. Cavers, "Adaptation behvaior of a feedforward amplifer linearizer," *IEEE Trans. Veh. Technol.*, vol. 44, no. 1, pp. 31–40, Feb. 1995.

[46] S. P. Stapleton, "Adaptive feedforward linearization for RF power amplifiers," in *55th ARFTG Conf. Dig.-Spring*, Jun. 2000, pp. 1–7.

[47] F. H. Raab, P. Asbeck, S. Cripps, P. B. Kenington, Z. B. Popovic, N. Pothecary, J. F. Sevic, and N. O. Sokal, "Power amplifiers and transmitters for RF and microwave," *IEEE Trans. Microw. Theory Tech.*, vol. 50, no. 3, pp. 814–826, Mar. 2002.

[48] V. Aparin and L. E. Larson, "Analysis and reduction of cross-modulation distortion in CDMA receivers," *IEEE Trans. Microw. Theory Tech.*, vol. 51, no. 5, pp. 1591–1602, May 2003.

[49] J. C. Pedro and N. B. de Carvalho, "Evaluating co-channel distortion ratio in microwave power amplifiers," *IEEE Trans. Microw. Theory Tech.*, vol. 49, no. 10, pp. 1777–1784, Oct. 2001.

[50] O. Andersen, D. Wisell, and N. Keskitalo, "Measurement of ACLR with high dynamic range," in *2008 IEEE MTT-S Int. Microwave Symp. Dig.*, Jun. 2008, pp. 273–277.

[51] A. Roussel, C. Nicholls, and J. Wight, "Frequency agile RF feedforward noise cancellation system," in *2008 IEEE Radio and Wireless Symp.*, Jan. 2008, pp. 109–112.

[52] J. R. Wilkerson, K. G. Gard, and M. B. Steer, "Automated broadband high-dynamic-range nonlinear distortion measurement system," *IEEE Trans. Microw. Theory Tech.*, vol. 58, no. 5, pp. 1273–1282, May 2010.

[53] T. V. den Broeck and J. Verspecht, "Calibrated vectorial non-linear-network analyzers," in *IEEE MTT-S Int. Microw. Symp. Dig.*, May 1994, pp. 1069–1072.

[54] P. Blockley, D. Gunyan, and J. B. Scott, "Mixer-based, vector-corrected, vector signal/network analyzer offering 300kHz–20GHz bandwidth and traceable phase response," in *IEEE MTT-S Int. Microw. Symp. Dig.*, Jun. 2005, pp. 1497–1500.

[55] J. Hu, K. G. Gard, and M. B. Steer, "Calibrated non-linear vector network measurement without using a multi-harmonic generator," *IET Microwaves Antennas and Propagation*, vol. 5, no. 5, pp. 616–624, Apr. 2011.

[56] A. Walker, M. Steer, and K. Gard, "Simple, broadband relative phase measurement of intermodulation products," in *65th ARFTG Conf. Dig.*, Jun. 2005, pp. 123–127.

[57] B. van der Pol, "The nonlinear theory of electric oscillations," *Proc. IRE*, vol. 22, no. 9, pp. 1051–1086, Sep. 1934.

[58] J. G. Proakis and M. Salehi, *Fundamentals of Communication Systems.* Upper Saddle River, N.J.: Pearson Prentice Hall, 2005.

[59] J. R. Wilkerson, "Passive intermodulation distortion in radio frequency communication systems," Ph.D. dissertation, North Carolina State University, 2010.

[60] S. Maas, *Nonlinear Microwave and RF Circuits.* Norwood, MA: Artech House Pub., 2003.

[61] M. B. Steer, *Microwave and RF Design: A Systems Approach*, 1st ed. Raleigh, NC: SciTech Pub., 2010.

[62] M. B. Steer and P. J. Khan, "An algebraic formula for the output of a system with large-signal, multi-frequency excitation," *Proc. IEEE*, vol. 71, no. 1, pp. 177–179, Jan. 1983.

[63] M. B. Steer, C. Chang, and G. W. Rhyne, "An algebraic formula for the output of a system with large-signal, multi-frequency excitation," *Proc. IEEE*, vol. 71, no. 1, pp. 177–179, Jan. 1991.

[64] H. Gutierrez, K. Gard, and M. B. Steer, "Nonlinear gain compression in microwave amplifiers using generalized power-series analysis and transformation of input statistics," *IEEE Trans. Microw. Theory Tech.*, vol. 48, no. 10, pp. 1774–1777, Oct. 2000.

[65] J. F. Sevic, M. B. Steer, and A. M. Pavio, "Nonlinear analysis methods for the simulation of digital wireless communications systems," *Internation Journal of Micowave and Millimeter-Wave Computer-Aided Engineering*, vol. 6, no. 3, pp. 197–216, 1996.

[66] J. F. Sevic and M. B. Steer, "On the significance of envelope peak-to-average ratio for estimating the spectral regrowth of an RF/microwave power amplifier," *IEEE Trans. Microw. Theory Tech.*, vol. 48, no. 6, pp. 1068–1071, Jun. 2000.

[67] E. Bedrosian and S. O. Rice, "The output properties of volterra systems (nonlinear systems with memory) driven by harmonic and Gaussian inputs," *Proc. IEEE*, vol. 59, pp. 1688–1707, Dec. 1971.

[68] S. A. Maas, "Volterra analysis of spectral regrowth," *IEEE Microw. Guided Wave Lett.*, vol. 7, no. 7, pp. 192–193, Jul. 1997.

[69] D. R. Morgan, Z. Ma, J. Kim, M. G. Zierdt, and J. Pastalan, "A generalized memory polynomial model for digital predistortion of RF power amplifiers," *IEEE Trans. Signal Process.*, vol. 54, no. 10, pp. 3852–3860, Oct. 2006.

[70] A. Walker, M. Steer, K. Gard, and K. Gharaibeh, "Multi-slice behavoiral model of RF systems and devices," in *IEEE Radio Wireless Conf.*, Sep. 2004, pp. 71–74.

[71] A. Walker, M. Steer, and K. Gard, "Capturing asymmetry in distortion of an RF system using a multislice behavioral model," *IEEE Microw. Wireless Compon. Lett.*, vol. 16, no. 4, pp. 212–214, Apr. 2006.

[72] G. J. Mazzaro, M. B. Steer, K. G. Gard, and A. L. Walker, "Response of RF networks to transient waveforms: interference in frequency-hopped communications," *IEEE Trans. Microw. Theory Tech.*, vol. 56, no. 12, pp. 2808–2814.

[73] G. J. Mazzaro, M. B. Steer, and K. G. Gard, "Filter characterization using one-port pulsed radio-frequency measurements," *IET Microw. Antennas Propag.*, vol. 3, no. 2, pp. 303–309.

[74] J. G. Simmons, "Generalized formula for the electric tunnel effect between similar electrodes separated by a thin insulating film," *Applied Physics*, vol. 34, no. 6, pp. 1793–1803, Jun. 1963.

[75] C. D. Bond, C. S. Guenzer, and C. A. Carosella, "Intermodulation generation by electron tunneling through aluminum-oxide films," *Proc. IEEE*, vol. 67, no. 12, pp. 1643–1652.

[76] J. Russer, A. Ramachandran, A. Cangellaris, and P. Russer, "Phenomenological modeling of passive intermodulation (PIM) due to electron tunneling at metallic contacts," in *IEEE MTT-S Int. Microw. Symp. Dig.*, Jun. 2006, pp. 1129–1132.

[77] J. Wilcox and P. Molmud, "Thermal heating contribution to intermodulation fields in coaxial waveguides," *IEEE Trans. Commun.*, vol. 24, no. 2, pp. 238–243, Feb. 1976.

[78] M. Bahrami, J. R. Culham, and M. M. Yovanovich, "Modeling thermal contact resistance: a scale analysis approach," *Heat Transfer*, vol. 126, no. 6, pp. 896–905, Jun. 2004.

[79] G. H. Stauss, "Intrinsic sources of im generation," Navy Research Laboratory, Washington, DC, Tech. Rep. NRL Memo. Rep. 4233, Ch.5, 1981.

[80] J. Henrie, "A study of passive intermodulation distortion in coaxial cable connectors," Ph.D. dissertation, Purdue University, 2009.

[81] Y. Wu, W. H. Ku, and J. E. Erickson, "A study of nonlinearities and intermodulation characteristics of 3-port distributed circulators," *IEEE Trans. Microw. Theory Tech.*, vol. 24, no. 2, pp. 69–77, Feb. 1976.

[82] E. Rocas, C. Collado, N. D. Orloff, J. Mateu, A. Padilla, J. M. O'Callaghan, and J. C. Booth, "Passive intermodulation due to self-heating in printed transmission lines," *IEEE Trans. Microw. Theory Tech.*, vol. 59, no. 2, pp. 311–322, Feb. 2011.

[83] A. Albareda, J. H. Kayombo, and J. A. Gorri, "Nonlinear direct and indirect third harmonic generation in piezoelectric resonators by the intermodulation method," *Review of Scientific Instruments*, vol. 72, no. 6, pp. 2742–2749, Jun. 2001.

[84] D. A. Field and D. S. Shim, "Determination of the nonlinear physical constants in a piezoelectric AlN film," in *2010 IEEE Ultrasonics Symp. (IUS)*, Oct. 2010, pp. 277–282.

[85] K. Sarabandi and D. E. Lawrence, "Acoustic and electromagnetic wave interaction: Estimation of Doppler spectrum from an acoustically vibrated metallic circular cylinder," *IEEE Trans. Antennas Propag.*, vol. 51, no. 7, pp. 1499–1507, Jul. 2003.

[86] A. Buerkle and K. Sarabandi, "Analysis of acousto-electromagnetic wave interaction using the finite-difference time-domain method," *IEEE Trans. Antennas Propag.*, vol. 56, no. 8, pp. 2191–2199, Aug. 2008.

[87] M. S. Frankel and A. M. Peterson, "Remote temperature profiling in the lower troposphere," *Radio Sci.*, vol. 11, no. 3, pp. 157–166, Mar. 1976.

[88] J. Nath, D. Ghosh, J.-P. Maria, A. I. Kingon, W. Fathelbab, P. D. Franzon, and M. B. Steer, "An electronically tunable microstrip bandpass filter using thin-film Barium-Strontium-Titanate (BST) varactors," *IEEE Trans. Microw. Theory Tech.*, vol. 53, no. 9, pp. 2707–2712, Sep. 2005.

[89] N. Pothecary, *Feedforward Linear Power Amplifiers.* London, U.K.: Artech House, 1999.

[90] P. D. L. Beasley, A. G. Stove, B. J. Reits, and B.-O. As, "Solving the problems of a single antenna frequency modulated CW radar," in *Record IEEE 1990 Int. Radar Conf.*, May 1990, pp. 391–395.

[91] J. Grajal, A. Asensio, and L. Requejo, "From a high-resolution LFM-CW shipborne radar to an airport surface detection equipment," in *Proc. IEEE 2004 Radar Conf.*, Apr. 2004, pp. 157–160.

[92] M. A. Gonzalez, J. Grajal, A. Asensio, D. Madueno, and L. Requejo, "A detailed study and implementation of an RPC for LFM-CW radar," in *Proc. 36th Eur. Microwave Conf*, Sep. 2006, pp. 1806–1809.

[93] K. Lin, Y. E. Wang, C.-K. Pao, and Y.-C. Shih, "A Ka-Band FMCW radar front-end with adaptive leakage cancellation," *IEEE Trans. Microw. Theory Tech.*, vol. 54, no. 12, pp. 4041–4048, Dec. 2006.

[94] J. Mateu and S. A. S. J. C. Booth, "Frequency tuning and spurious signal generation at microwave frequencies in ferroelectric SrTiO3 thin-film transmission lines," *IEEE Trans. Microw. Theory Tech.*, vol. 55, no. 2, pp. 391–396, Feb. 2007.

[95] J. Henrie, A. Christianson, and W. J. Chappell, "Prediction of passive intermodulation from coaxial connectors in microwave networks," *IEEE Trans. Microw. Theory Tech.*, vol. 56, no. 1, pp. 209–216, Jan.

[96] K.-J. Kim and K. Ahn, "Design of 60 GHz vector modulator based active phase shifter," in *2011 Sixth IEEE International Symposium Electronic Design, Test and Application (DELTA)*, Jan. 2011, pp. 140–143.

[97] J. R. Wilkerson, K. G. Gard, and M. Steer, "Electro-thermal passive intermodulation distortion in microwave attenuators," in *Proc. 36th Eur. Microwave Conf.*, Sep. 2006, pp. 157–160.

[98] A. Buerkle and K. Sarabandi, "Non-destructive evaluation of elastic targets using acousto-electromagnetic wave interaction and time reversal focusing," *IEEE Trans. Antennas Propag.*, vol. 57, no. 11, pp. 3628–3637, Nov. 2009.

[99] J. Van Bladel, "Electromagnetic fields in the presence of rotating bodies," *Proc. IEEE*, vol. 64, pp. 301–318, Mar. 1976.

[100] J. M. Wetherington and M. B. Steer, "Robust analog canceller for high-dynamic-range radio frequency measurement," *IEEE Trans. Microw. Theory Tech.*, vol. 60, no. 6, pp. 1709–1719, Jun. 2012.

[101] ——, "Standoff acoustic modulation of radio frequency signals in a log-periodic dipole array antenna," *IEEE Antennas Wireless Propag. Lett.*, vol. 11, pp. 885–888, 2012.

[102] M. B. Steer, J. R. Wilkerson, N. M. Kriplani, and J. M. Wetherington, "Why it is so hard to find small radio frequency signals in the presence of large signals," in *2012 Workshop on Integrated Nonlinear Microwave and Millimetre-Wave Circuits (INMMIC)*, Sep. 2012, pp. 1–3.

[103] G. Vinci, S. Lindner, F. Barbon, R. Weigel, and A. Koelpin, "Promise of a better position," *IEEE Microw. Mag.*, vol. 13, no. 7, pp. S41–S49, Nov./Dec. 2012.

[104] C. Li and J. Lin, "Non-contact measurement of periodic movements by a 22–40 GHz radar sensor using nonlinear phase modulation," in *2007 IEEE MTT-S Int. Microw. Symp. Dig.*, Jun. 2007, pp. 579–582.

[105] A. Einstein, "Zur Elektrodynamik bewegter Körper," *Annalen der Physik*, pp. 891–921, Jun. 1905, English translation: "On the Electrodynamics of Moving Bodies," translated by W. Perrett and G. B. Jeffery, in *The Principle of Relativity*, Methuen and Company, 1923.

[106] J. W. Crispin, Jr., R. F. Goodrich, and K. M. Siegel, "A theoretical method for the calculation of the radar cross sections of aircraft and missiles," Radiation Lab., Univ. of Michigan, Ann Arbor, MI, Tech. Rep. 2591-1-H, Jul. 1959.

[107] J. W. Crispin, Jr. and A. L. Maffett, "Radar cross-section estimation for simple shapes," *Proc. IEEE*, vol. 53, no. 8, pp. 833–848, Aug. 1965.

[108] R. A. Ross, "Radar cross section of rectangular flat plates as a function of aspect angle," *IEEE Trans. Antennas Propag.*, vol. 14, no. 14, pp. 329–335, May 1966.

[109] B. S. Yurchak, "Assessment of specular radar backscatter from a planar surface using a physical optics approach," *Int. Journal of Remote Sensing*, vol. 33, no. 20, pp. 6446–6458, Oct. 2012.

[110] A. K. Fung and H. J. Eom, "Coherent scattering of a spherical wave from an irregular surface," *IEEE Trans. Antennas Propag.*, vol. 31, no. 1, pp. 68–72, Jan. 1983.

[111] C. Bourlier and P. Pouliguen, "Useful analytical formulae for near-field monostatic radar cross section under the physical optics: far-field criterion," *IEEE Trans. Antennas Propag.*, vol. 57, no. 1, pp. 205–214, Jan. 2009.

[112] C. A. Balanis, *Antenna Theory: Analysis and Design*, 3rd ed. Hoboken, NJ: John Wiley, 2005.

[113] G. Garner, J. Wilkerson, M. M. Skeen, D. F. Patrick, R. D. Hodges, R. D. Schimizzi, S. R. Vora, Z. Feng, K. G. Gard, and M. B. Steer, "Acoustic-RF anechoic chamber construction and evaluation," in *2008 IEEE Radio and Wireless Symp.*, Jan. 2008, pp. 331–334.

[114] J. M. Wetherington and M. B. Steer, "Characterization of the dynamic range of a single aperture communications system," in *2012 Workshop on Integrated Nonlinear Microwave and Millimetre-Wave Circuits (INMMIC)*, Sep. 2012, pp. 1–3.

[115] A. C. Polycarpou, C. A. Balanis, and A. Stefanov, "Helicopter rotor-blade modulation of antenna radiation characteristics," *IEEE Trans. Antennas Propag.*, vol. 49, no. 5, pp. 688–696, May 2001.

[116] J. P. Stockman and K. Sarabandi, "Doppler radar detection of mechanically resonating objects," in *2005 IEEE Antennas and Propagation Society Int. Symp.*, Jul. 2005, pp. 130–133.

[117] G. Scientific. [Online]. Available: http://www.greenwavescientific.com

[118] L. E. Kinsler, A. R. Frey, A. B. Coppens, and J. V. Sanders, *Fundamentals of Acoustics*. New York: Wiley, 1999.

APPENDICES

Appendix A

Automated Analog Canceller System Documentation

A.1 Introduction

This user guide provides an introduction to operating the automated analog canceller system introduced in this dissertation. The analog canceller is a versatile building block for many different experimental detection and measurement systems, so that exact hardware and software specifications are expected to change over time. Details contained within this guide are for the system constructed for the North Carolina State University Electronics Research Laboratory as it existed in June 2013 using the computer designated TERROR. This guide should only be used for reference, and a fully-trained system operator should always be present. For discussion on general analog canceller design, refer to Chapter 3.

A.2 User Interface

Automated hardware control and interfacing is performed using National Instruments' Laboratory Virtual Instrument Engineering Workbench (LabVIEW) scripting language. Individual LabVIEW scripts are referred to as virtual instruments (VIs). Each VI may be treated as a function which may be called within other VIs, and a directory can be organized to form a standard library. The analog canceller code is highly modularized, with many VIs feeding one or more top-level control VIs that the operator interfaces with. The complete canceller VI library is outlined in Appendix B.

Each VI provides a front panel interface providing control of programming inputs and outputs to the operator. An example front panel is shown in Fig. A.1. VIs are executed using the "play" button in the upper left below the menu bar. User inputs (entered before execution)

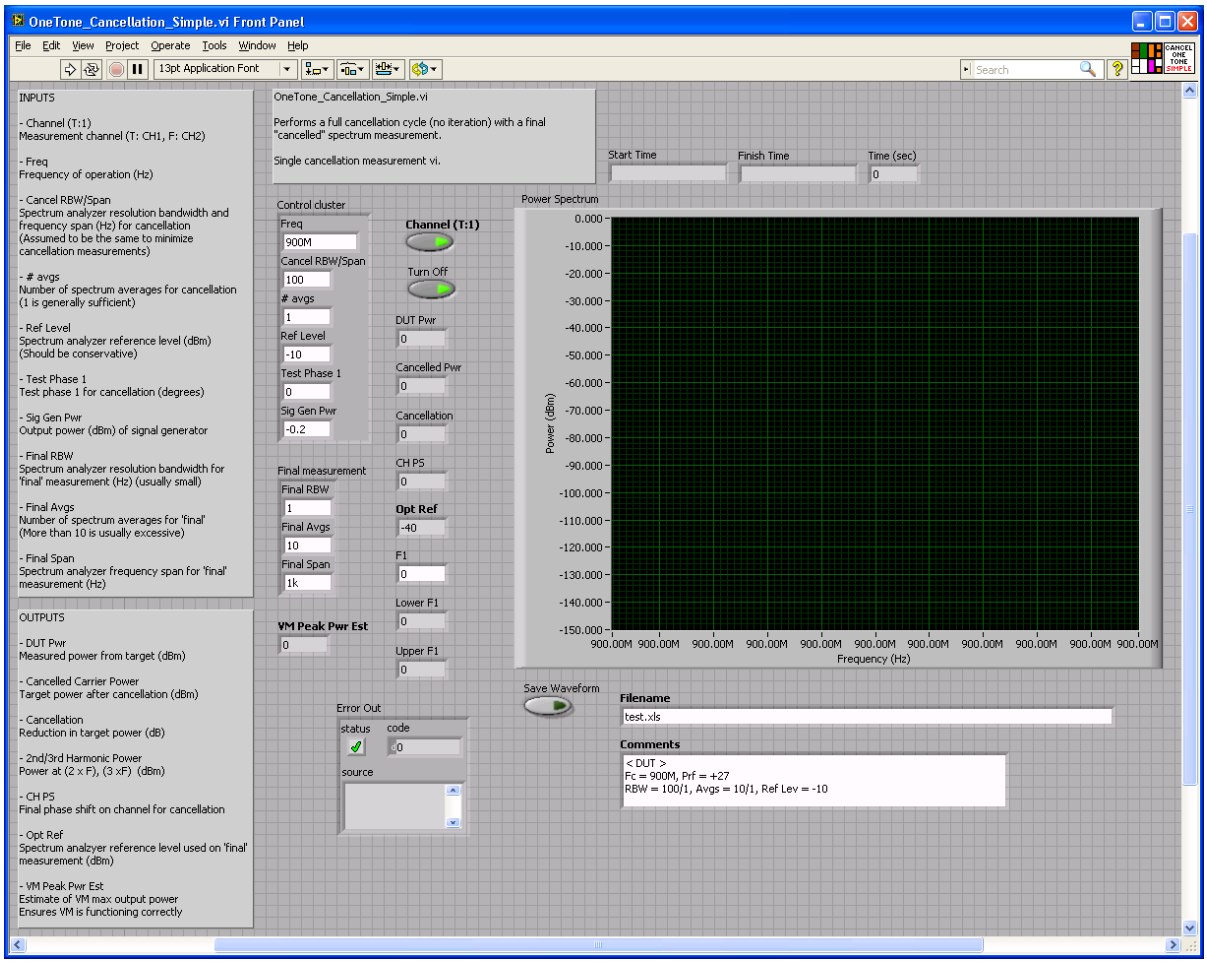

Figure A.1: Example front panel user interface.

are text boxes with a white background and on/off buttons. VI outputs (displayed during and after execution) are text boxes with a grayed background, and in this case a spectrum plot. Description of every input and output can be found in the block comments on the left side.

A.3 Hardware

Most aspects of the hardware architecture and design are discussed in Chapter 3. The complete minimal block diagram for both single-channel and dual-channel configurations are shown here in Fig. A.2 and Fig. A.3, respectively. In this section, hardware specifications are discussed for the implemented system, as well as practical issues encountered in typical configurations.

A list of active components and physical control interfaces used in the analog canceller is given in Table A.1. A key capability for the majority of the active hardware, including the

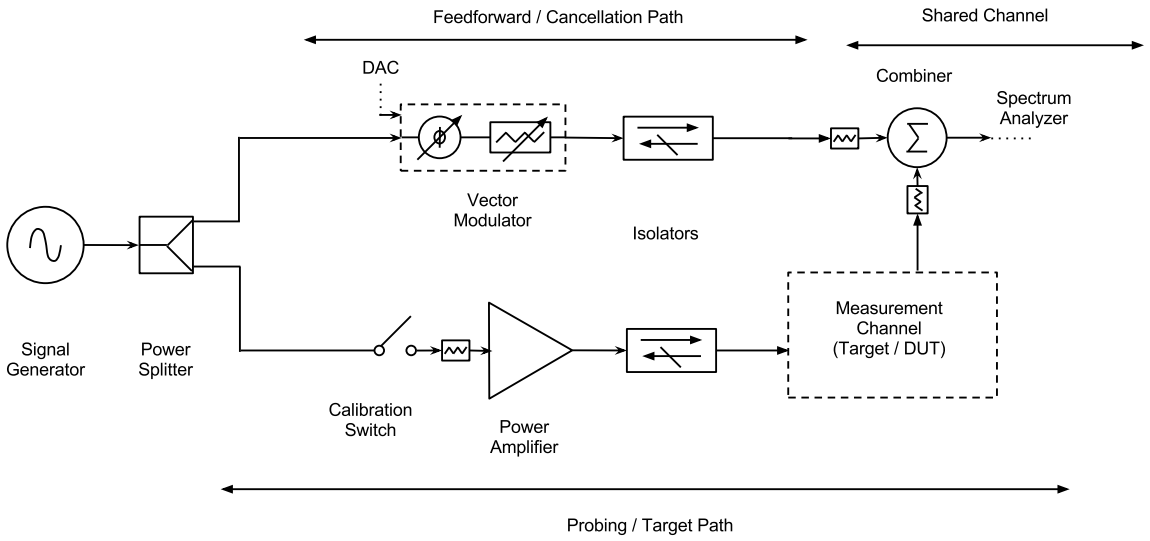

Figure A.2: Hardware architecture for single-channel cancellation.

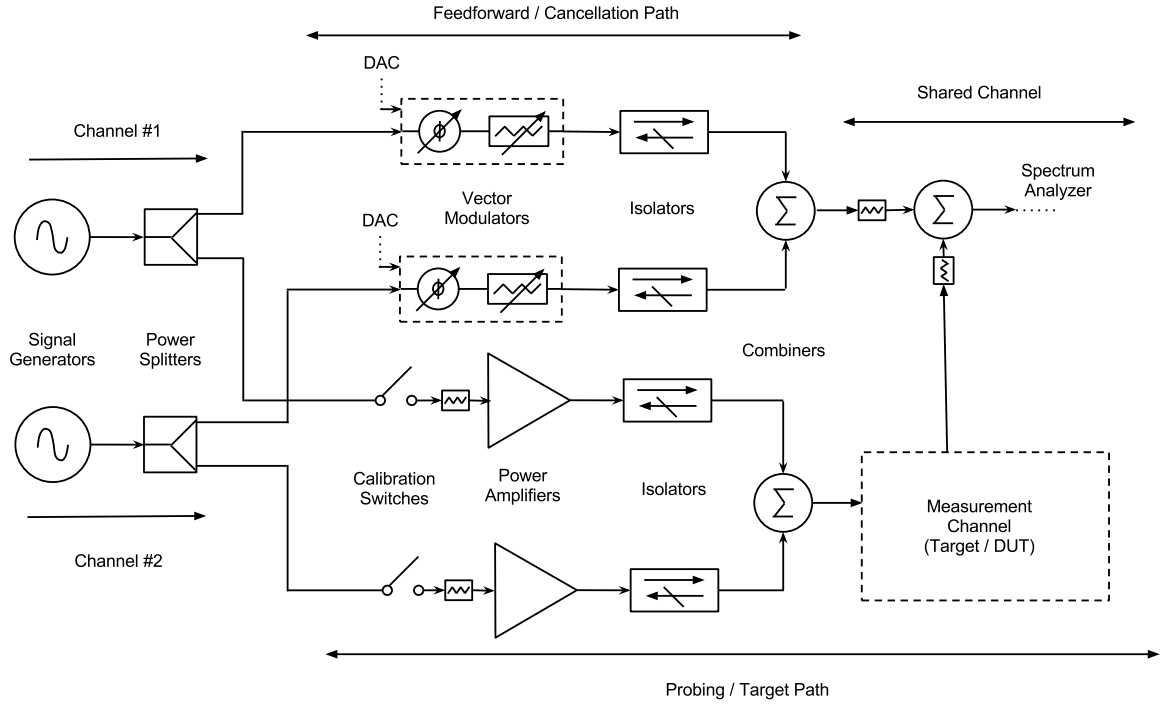

Figure A.3: Hardware architecture for dual-channel cancellation.

signal generators, vector modulators and power amplifiers, is the ability to operate entirely on DC power. This reduces or eliminates 60 Hz harmonics that plague high-dynamic-range,

Table A.1: Hardware used in analog canceller on controller "TERROR"

Component	Vendor	Part	Communication/Control
Signal Generator	IFR	IFR2025	GPIB to Controller
Vector Modulator	Hittite	HMC497LP4	SMA/coax to DAC
DAC	Measurement Computing	USB3103	USB to Controller
Power Amplifier	Mini-Circuits	ZHL-20W-13+	N/A
Spectrum Analyzer	National Instruments	NI PXI-5660	Internal (PXI)
Switches	National Instruments	NI PXI-2597	Internal (PXI)
System Controller	National Instruments	NI PXI-8102	Internal (PXI)

narrowband measurements. The IFR2025 signal generator and ZHL-20W-13+ power amplifier require 24 VDC for operation, while the HMC497LP4 vector modulator requires 5 V. In the current system, a 5 V voltage regulator is used with the vector modulator, such that external power required is >7 V (i.e., 6×AA batteries). For maximum sensitivity, DC power should be provided by batteries, however proper safety precautions should be taken, given the high power involved. Devices with good built-in power supply rejection, such as the signal generators and power amplifier, can be powered using linear power supplies, with no apparent loss of sensitivity. In addition, heatsink cooling fans, common in signal sources and amplifiers, can generate detectable spurious noise through reverse-electromagnetic-interference coupled across a common power supply. Electrically isolating cooling fans from the main device power supply is recommended. The ZHL-20W-13+ power amplifier fan requires 24 V, while the IFR2025 signal generator fan requires 5 V. Proper engineering controls should be maintained to prevent device overheating and damage.

The most critical active components are the vector modulators and digital-to-analog converters (DAC). The vector modulators directly manipulate the feedforward cancellation signal based on inputs from the DAC. As discussed in Chapter 3, the limit of fine control of the cancellation signal has a direct impact on the maximum achievable cancellation. The USB3103 DACs converts a 16-bit control signal provided from the system controller to differential in-phase (I) and quadrature (Q) signals, which are input to the HMC497LP4 vector modulators. In addition to fine control, the linearity of the amplitude output across phase for the vector modulators can greatly impact canceller performance. Although this linearity can be completely handled in software via in-line calibration (see Chapter 3), the vector modulators in the system were pre-screened to minimize amplitude non-linearity over phase, greatly improving typical calibration. The vector modulators are also the largest source of phase noise in the system, due to the degradation of coherence with manipulation of the feedforward signal. Excess noise originating in the vector modulator is lower than typical applications due to the use of DC I

and Q signals and DC battery power, however the vector modulators in the current system were also pre-screened to ensure minimal noise.

The remaining active components are less critical, and can be swapped out to accommodate varying frequency and power specifications. Low noise and linear operation are expected for these devices.

The critical parameters for passive components, including cables, attenuators, terminations, isolators, couplers, and hybrids are discussed Chapter 3 as well as in [52]. The most sensitive areas for PIM generation in passive components occur after the power amplifiers and on the shared channel, which should be kept as linear as possible to prevent overwhelming very low level detection. In general, common laboratory-grade components are usually sufficient to prevent sensitivity loss, but should not be ruled out as a potential noise source.

For the current system using the hardware in Table A.1, attenuators are needed to ensure proper signal levels at several points in the system, particularly at active device inputs and prior to the final combination as shown in Fig. A.2 and A.3. The HMC497LP4 vector modulators have an specified input range of -6 to $+6$ dBm, while the ZHL-20W-13+ power amplifiers have a maximum linear input power of -10 dBm. With a common input source, the inherent signal level discrepancy must be handled by passive attenuators. Attenuators prior to active devices can also roughly improve input impedance matching for these devices, improving performance and stability. At the cancellation signal combination point, the power level of the signal received from the measurement channel can be significantly higher than the maximum output power of the HMC497LP4 vector modulators (limited to +8 dBm), limiting the flexibility of the system to perform high power measurements. Attenuators are added at the end of the feedforward or measurement path to equalize signal power for cancellation, however this can directly impact maximum achievable dynamic range (see Chapter 3). As the dynamic amplitude control of the HMC497LP4 is limited to approximately 20–30 dB, for best performance, the expected maximum power from the measurement signal should be as close to the maximum output of the vector modulators as possible.

A.4 Canceller Algorithms

Central to automated signal cancellation is the ability to determine the correct amplitude and phase for the feedforward signal to fully cancel the measurement signal. As discussed in Chapter 3, this is accomplished using only power measurements and the phase-shift equation

$$\phi_s = \pi \pm 2 \arccos\left(\frac{\beta}{2\alpha}\right) \tag{A.1}$$

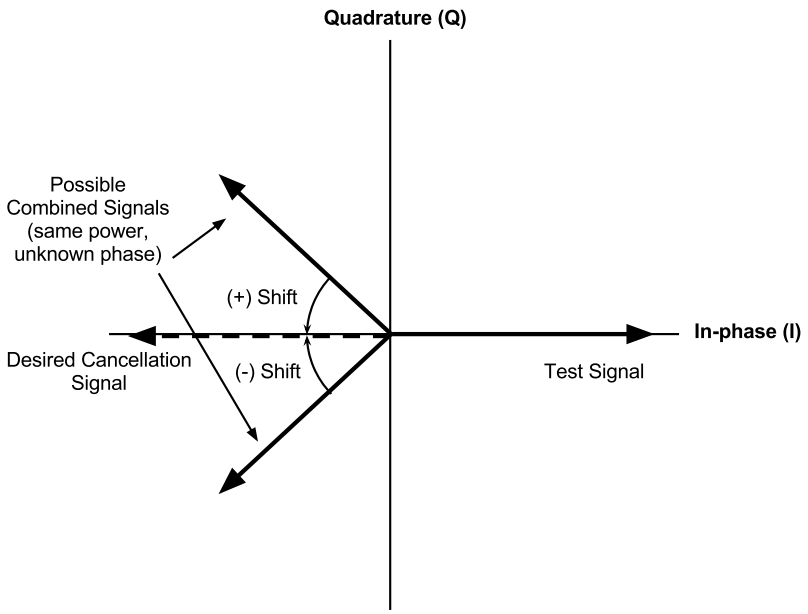

Figure A.4: Phase ambiguity from application of the phase-shift equation (A.1).

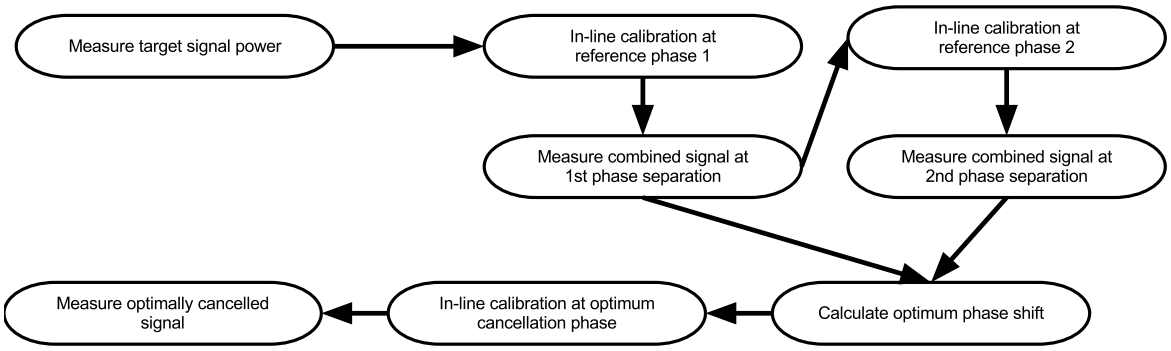

Figure A.5: Procedural flow for a non-iterative feedforward cancellation measurement.

where ϕ_s is the additional phase shift needed on an arbitrary measured cancellation signal to cancel a measurement signal with amplitude, α, given the combined amplitude of the measurement signal and the observed cancellation signal is β. The ambiguous sign is a result of two independent trigonometric solutions, as illustrated in Fig. A.4. To resolve the correct sign, an extra measurement is needed for the cancellation at a new phase offset.

The steps for a full cancellation routine are shown in Fig. A.5. The canceller must first determine the amplitude of the measurement signal to be cancelled, α in (A.1). The vector

modulator is nominally set to this power. The vector modulator is set to the first reference phase for measurement, and must perform in-line calibration to enforce amplitude matching with the measurement signal. During vector modulator calibration, the measurement path is disabled using an RF switch at the input to the power amplifier (see Fig. A.2). The amplitude-calibrated cancellation signal is then combined with the measurement signal to determine the combined, cancelled signal amplitude, β in (A.1). This process is repeated for the second reference phase. Inspection of the phase shift solution from each measurement will yield one common solution (performed by comparing the difference of the calculated phase shifts with the difference of the reference phases). After applying the optimal phase shift to the vector modulator, the cancellation amplitude must be in-line calibrated a final time, then the final cancelled signal can be measured. This is the procedure executed in control VI "OneTone_Cancellation_Simple.vi". For a dual-channel configuration, this routine is completed in parallel for both channels. As each channel tone is at a different frequency, both measurements can generally be completed simultaneously, as executed in the control VI "TwoTone_Cancellation_Simple.vi", given the resolution bandwidth of the measurement is less than the tone separation. For extremely small tone separations, the cancellation operation can only be done on one channel at a time, while the other channel is disabled, as executed in control VI "TwoTone_Cancellation_Split.vi". This can slightly degrade cancellation performance on the first channel, while waiting for the second channel cancellation optimization to finish.

The one-step phase shift, (A.1), assumes perfectly linear, ideal signal combination at any phase offset between the measured signal and the reference cancellation signal. In practice, the cancellation procedure works best at phase offsets near 180° (ideal cancellation), due to local linearity with the desired solution. Sometimes, the automated canceller simply benefits from a second attempt due to the first attempt weakened by random error. In these cases, a weakly iterative scheme can be introduced. The simplest iterative method is to loop the procedure in Fig. A.5, repeating the full cancellation operation. Alternatively, iterative cancellation can be achieved more efficiently by only considering a single reference phase in each loop, and referring to the reference phase measurement in the previous iteration to determine the phase shift sign in (A.1). The calculated optimal phase shift on each iteration is used as the reference phase for the next loop. This "fast" iteration method is shown in Fig. A.6, and is executed in "OneTone_-Cancellation_Repeater_Fast.vi" and "TwoTone_Cancellation_Split_Repeater_Fast.vi" for single-channel and dual-channel configurations, respectively. The iteration considered in this process is not a "true" iteration, due to the lack of direct feedback and de-coupling of the control function (the vector modulator phase shift) and the error function (cancellation depth). Thus, secondary control inputs are necessary to prevent the iteration from going unstable. At each iteration, the cancellation depth is compared to the desired cancellation, and the iteration count is compared to the maximum allowed iterations. If either metric exceeds the input control value, the loop is

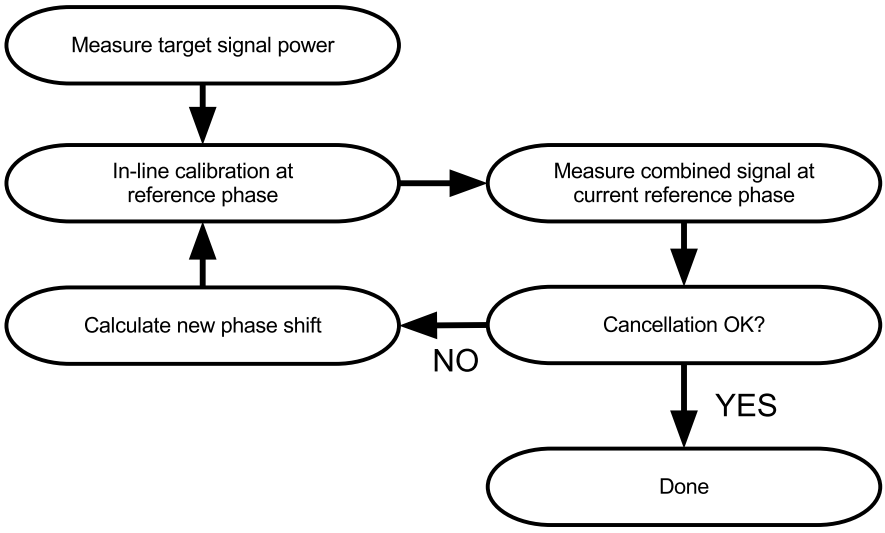

Figure A.6: Procedural flow for an efficient, semi-iterative feedforward cancellation measurement.

stopped. Removing these controls will create a infinite loop, useful for adaptive cancellation in time-dynamic environments.

A.5 Sample Measurement Walkthrough

This section provides step-by-step instructions for performing a one-shot, high-dynamic-range, two-tone third-order intermodulation (IM3) measurement with analog cancellation using "TwoTone_Cancel_Simple.vi". Each of the two tones operate on separate physical channels, and the VI completes the cancellation procedure shown in Fig. A.5 simultaneously for each channel. At the end of the cancellation process, cancellation depth is checked, and the receiver is optimally adjusted for high-sensitivity measurement. A final high-fidelity measurement occurs for detection of the IM3 tones. A screenshot of the front panel is shown in Fig. A.7. This VI provides a large number of user-defined inputs, numerical outputs, and a spectral plot for the final IM3 measurement. The user inputs are grouped into two clusters. The main "Control" cluster is used to set test signal and cancellation measurement parameters. The "Final Measurement" cluster sets measurement parameters for the final IM3 measurement. The numerical outputs give an overview of the cancellation measurements and statistics for troubleshooting, as well as the measured power of the IM3 tones. A clock and timer are also included for convenience.

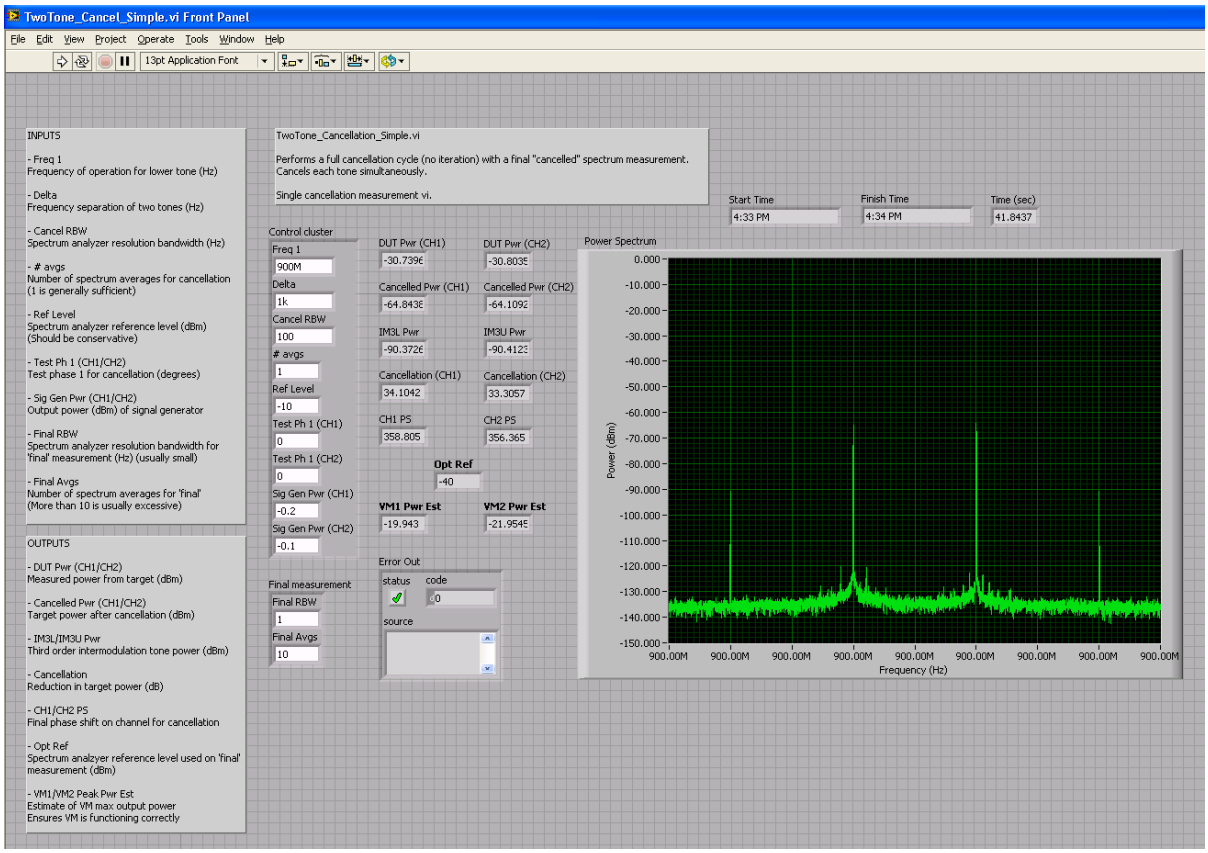

Figure A.7: Front panel user interface for "TwoTone_Cancel_Simple.vi".

A.5.1 Setup

Before the measurement, the physical system should be checked to match the architecture shown in Fig. A.3 and all active devices should be powered and properly communicating with the system controller. The measurement channel should be prepared with a target or device-under-test (DUT) to produce the proper reflection or transmission measurement. For two-port transmission tests the channel will slot directly in the diagram as shown in Fig. A.3. For one-port reflection tests, a coupler may be used to capture the reflected signal, which is then sent to the combiner for cancellation. Use of circulators for reflection tests should be avoided due to inherent high non-linearity.

User-input test signal parameters include test signal frequency, frequency separation between the two tones, initial reference phase for each tone, and signal generator output power for each tone. The Channel 1 frequency is set to the test signal frequency "Freq 1" and the Channel 2 frequency is set to the sum of the test signal frequency "Freq 1" and the frequency separation "Delta". The initial reference phases "Test Ph 1 (CH1)" and "Test Ph 2 (CH2)" set

the initial phase offset of the vector modulator for each channel and may be used to improve non-iterative cancellation by providing a better starting condition, as suggested in Section 3.2. The cancellation procedure is robust enough that these inputs may generally be ignored. The second reference phase for cancellation is automatically set to the initial reference phase advanced by 90°. The signal power of each tone applied to the measurement channel is directly proportional the to signal generator output, set by "Sig Gen Pwr (CH1)" and "Sig Gen Pwr (CH2)". The path between the signal generators and the measurement channel is highly linear, as long as the power amplifiers are not driven into compression. Input signals to the power amplifiers should be kept at least 10 dB below compression to ensure maximum linearity. For the ZHL-20W-13+ power amplifier, this implies a maximum tone power of 30 dBm can be applied to the measurement channel. The conversion from signal generator output power to applied tone power can be directly measured by feeding input of the measurement channel directly to a power meter or spectrum analyzer. Care must be taken to ensure that power is below the maximum input threshold of the measurement device.

User-input cancellation parameters include resolution bandwidth, averaging, and receiver reference level. The cancellation resolution bandwidth "Cancel RBW" sets the resolution bandwidth in the reference and interim measurements used to optimize cancellation. For two-tone tests, this must be less than the frequency separation of the two tones, or the canceller will not be able to resolve the separate channels. Since the cancellation tones are usually much higher in power than anything within the bandwidth, the resolution bandwidth can be set as high as possible to speed up the cancellation procedure. Averaging allows the receiver to repeat the spectral measurement sequentially a number of times indicated by "# avgs", and average the spectral power linearly. This will reduce the effect of zero-mean additive random noise. Again, since the cancellation tones are much higher in power than noise with the bandwidth, averaging is not needed and the number of averages may be set to one to reduce cancellation time. The reference level is the maximum expected total input power for the receiver and is used to set internal attenuation and mixer levels. Prior to cancellation, this level needs to be high, and can be set up to -10 on the NI PXI-5660 spectrum analyzer without activating internal attenuation. Setting this parameter may result in inaccurate measurement without proper equipment calibration. It is up to the user to ensure that the measurement signal reaching the spectrum analyzer does not exceed the reference level setting.

User-input final measurement parameters again include resolution bandwidth and averaging. These parameters function exactly as described above, but are used only for the final IM3 measurement. During the cancellation process, the final reference level is automatically set based on achieved cancellation depth to prevent damage to the spectrum analyzer. On the NI PXI-5660 spectrum analyzer, the resolution bandwidth may be set as low as 1 Hz to minimize total noise from the finite spectral bandwidth. This measurement is very slow, but provides

the greatest sensitivity. Averaging may also be used reduce noise, at the cost of additional test time. Generally, 10 averaged measurements provide a good trade-off between additional test time and noise reduction.

When the user has completed setup, the VI can be executed by pressing the "Play" button (a white right-facing arrow) in the upper left corner of the window, below the menu bar. Cancellation and measurement will be executed, taking roughly 30 seconds to 2 minutes depending on input settings, and then the VI will stop, displaying numerical and graphical results.

A.5.2 Reading the Output

Once the VI has finished executing, all output numerical fields should be populated. For each channel, the power of the un-cancelled received measurement tone ("DUT Pwr"), the power of the cancelled measurement tone ("Cancelled Pwr"), the cancellation depth ("Cancellation"), the vector modulator optimal phase shift ("PS"), and the vector modulator estimated maximum output power ("VM Pwr Est") is shown. In addition, the power of the upper and lower third-order modulation tones ("IM3U Pwr" and "IM3L Pwr") and optimized reference level ("Opt Ref") are shown. Finding the power of the IM3 tones is the goal of the measurement and the most relevant output. The remaining outputs indicate the quality of the measurement. For maximum sensitivity, the optimal reference level should be at the minimum for the receiver (-40 dBm for the NI PXI-5660). This level is automatically set based on the detected cancelled signal power, and will never be lower the values given by those outputs. The cancelled measurement tone power should be very low (< -50 dBm) and may be the result of good cancellation depth (typically, >30 dB) or high-loss measurement channels (revealed by a very low un-cancelled tone power). In cases of poor cancellation, the maximum output power of the vector modulators is usually found to be less than the un-cancelled measurements tones, limiting the achievable cancellation. Attentuation and signal levels in the system should be checked, as well as ensuring the vector modulators are properly powered.

At completion, the VI will also display a power spectrum for the final IM3 measurement with a frequency span wide enough to display the cancelled-input and IM3 tones. Aside from the expected tones, other spurious spectral content may appear. Analysis of the complete spectrum is useful for interpreting the measured results in relation to the measurement noise floor and interference.

The front panel screenshot given in Fig. A.7 shows a strong, high-quality measurement with a low noise floor and good cancellation. In contrast, Fig. A.8 is an example of a measurement with poor cancellation. In this situation, there is a problem with the Channel 1 vector modulator, as evident by the maximum output power being roughly the measurement noise floor. Good cancellation is achieved on Channel 2, however the final measurement is limited by the lack of

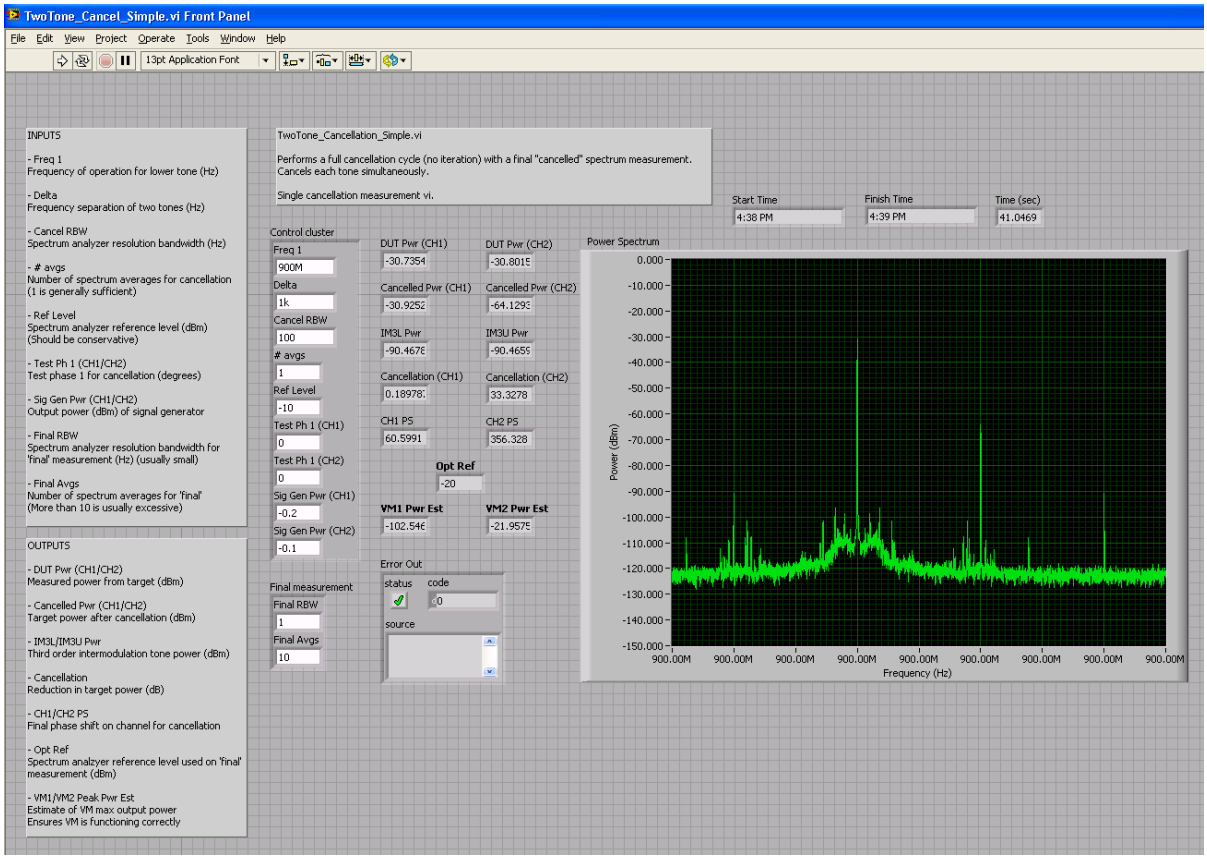

Figure A.8: Measurement with poor cancellation depth.

cancellation on Channel 1, leading to a high un-cancelled signal power and an increased final reference level. Analysis of the spectral graph indicates that the power of the IM3 tones is 30 dB above the broadband noise floor (approximately -120 dBm in this measurement), thus this measurement may be considered good. Measurement of passive intermodulation (PIM) often requires much lower levels, so the quality of this measurement would not suffice. Cancellation depth would be would be expected to improve by fixing the issue with the Channel 1 vector modulator, which in this case was un-powered.

Appendix B

LabVIEW Analog Canceller VI Directory

This appendix provides a light documentation of the .vi files used in the operation of the analog canceller. All .vi files are listed in alphabetical order with a short description detailing their purpose and operation. Complete description and documentation may be found by opening the individual .vi files within the LabVIEW environment. Control files provide high-level functionality with user input for controlling hardware and performing cancellation and spectral measurements. Support "sub-VI" files provide automated low-level functionality embedded in the control, performing mathematical algorithms and physical communication with hardware equipment. Sweep files provide an additional higher layer above the control files, allowing for automated test sweeps across useful parameters, with data collection capability.

B.1 Control Files

- OneTone_Cancellation_Harmonics.vi
  - Performs a full cancellation cycle (no iteration) with a final "cancelled" spectrum measurement, including harmonic spectra.
  - Single cancellation measurement vi.

- OneTone_Cancellation_Repeater_Fast.vi
  - Performs iterative cancellation with a final "cancelled" spectrum measurement.
  - Single cancellation measurement vi.

- OneTone_Cancellation_Simple.vi
  - Performs a full cancellation cycle (no iteration) with a final "cancelled" spectrum measurement.

- Single cancellation measurement vi.

- Sig_Gen_Control.vi
  - Signal generator control (IFR2024).
  - Sig gen control only.

- SpectrumAnalyzer.vi
  - Grabs power spectrum from spectrum analyzer, and provides controls for signal generators.
  - Measurement vi, no VM control.

- TwoTone_Cancellation_Simple.vi
  - Performs a full cancellation cycle (no iteration) with a final "cancelled" spectrum measurement.
  - Cancels each tone simultaneously.
  - Single cancellation measurement vi.

- TwoTone_Cancellation_Split.vi
  - Performs a full cancellation cycle (no iteration) with a final "cancelled" spectrum measurement.
  - Cancels each tone individually.
  - Single cancellation measurement vi.

- TwoTone_Cancellation_Split_Repeater_Fast.vi
  - Performs iterative cancellation with a final "cancelled" spectrum measurement.
  - Cancels each tone individually (full iteration).
  - Single cancellation measurement vi.

- VM_Calibration.vi
  - Performs VM I/Q power calibration (high-level control of VM_CH_Characterization.vi), including mandatory switching.
  - Calibration vi, stores data to file.

- VM_Quick_Phase.vi
  - High-level control of vector modulator (frequency, power, phase)
  - VM control only.

B.2 Support Files

- AngleConversion.vi
  - Converts between radians and degrees. Use appropriate input/output.

- BoundPhase.vi
  - Converts input phase (degrees) to equivalent phase in range of 0-360 degrees

- CancellationPhaseShift_Deg.vi
  - Given combined tone power and cancellation tone power, calculates phase shift required for cancellation
  - Assumes positive sign in phase shift equation, must be handled appropriately by calling vi.

- CancelOneTone.vi
  - Performs one full cancellation procedure on a given channel, with two reference phases, then sets vector modulator to calculated phase shift.
  - Calling vi must handle initialization of signal generator and spectrum analyzer, and ensure VM is pre-calibrated

- CancelOneToneRepeat.vi
  - Performs iterative cancellation procedure on a given channel, vector modulator is set to final phase shift used.
  - Following measurement not guaranteed to exceed cancellation target!
  - Calling vi must handle initialization of signal generator and spectrum analyzer, and ensure VM is pre-calibrated

- CancelTwoTone.vi
  - Performs one full cancellation procedure on both channels, with two reference phases, then sets vector modulators to calculated phase shifts.
  - Calling vi must handle initialization of sig gen and receiver, and ensure VMs are pre-calibrated.

- CloseDUT.vi
  - Closes calibration switches on both channels (enables DUT/probing path)

- CloseDUT_CH1.vi
  - Closes calibration switches on channel 1 (enables DUT/probing path)

- CloseDUT_CH2.vi
  - Closes calibration switches on channel 2 (enables DUT/probing path)

- CP_calc.vi
  - Calculates approximate cancellation limit based on quantization of I/Q data sent to DAC/VM.
  - Accuracy questionable.

- DataFetch.vi
  - Extract fundamental and two-tone intermodulation products based on settings and grabs spectrum data centered between carrier frequencies over given bandwidth.
  - Full spectrum data disabled for very large spans relative to resolution bandwidth.
  - Receiver must be initializer by calling vi.

- DataFetchMulti.vi
  - Extract power for input frequencies and grabs spectrum data centered around fundamental frequency over given bandwidth.
  - Full spectrum data disabled for very large spans relative to resolution bandwidth.
  - Receiver must be initializer by calling vi.

- DataFetchSingle.vi
  - Extract power for input frequency and grabs spectrum data centered around fundamental frequency over given bandwidth.
  - Full spectrum data disabled for very large spans relative to resolution bandwidth.
  - Receiver must be initializer by calling vi.

- dBm_mW.vi
  - Converts between dBm and mW. Use appropriate input/output.

- dBm_V.vi
  - Converts between dBm and V assuming 50 ohms. Use appropriate input/output.

- FindPeaks2.vi
  - Finds the power at two frequencies within a spectrum using the SMT Spectrum Peak Search.

- FindPeaks2Single.vi
  - Finds the power at a frequency within a spectrum using the SMT Spectrum Peak Search.

- FindRefLevel.vi
  - Determines an appropriate spectrum analyzer reference level based on expected input power.

- FindSpectrumValue.vi
  - Finds the power at two frequencies within a spectrum directly using array indexing.

- FindVMParamsHittite.vi
  - Linear extrapolation of I/Q conversion using VM I/Q calibration data.

- Folders.vi
  - Contains hard-coded path names for calibration and data directories for loading/storing data.

- Get_LO_cal.vi
  - Reads LO calibration file to get sig gen output setting for a desired DUT/target power.
  - See vi for LO_cal file details.

- get_switch_positions.vi
  - Reads switch states.
  - Switch equipment settings are hard-coded here.

- GetPhaseShift.vi
  - Given combined power at two reference phases, determines new cancellation phase shift.
  - The output phase shift is chosen from the reference phase with the lower combined power (better cancellation).
  - Extends (CancellationPhaseShift_Deg.vi) by adding correct sign handling.

- Interpolate_Channel_Char.vi
  - Frequency interpolation of VM I/Q calibration data.

- IQsettingsHittite.vi
  - Determines I/Q input voltages for given RF power and phase based on linear I/Q conversion equation from (FindVMParamsHittite.vi)

- ni5600_init.vi
  - Initializes ni5660 spectrum analyzer.
  - Spectrum analyzer equipment settings are hard-coded here.

- NI5660_IFR2024_init.vi
  - Initializes both ni5660 and IFR2024.
  - Combined vi for Convenience.

- OpenDUT.vi
  - Opens calibration switches on both channel (disables DUT/probing path)

- OpenDUT_CH1.vi
  - Opens calibration switches on channel 1 (disables DUT/probing path)

- OpenDUT_CH2.vi
  - Opens calibration switches on channel 2 (disables DUT/probing path)

- PeakPwrEst.vi
  - Approximates VM peak power output based on linear I/Q conversion equation from (FindVMParamsHittite.vi)
  - Primarily used to check VM functionality.

- ReadCalFile.vi
  - Loads a single column data array from file.

- SF_Channel_Char.vi
  - Measures VM output power at hard-coded test voltages.
  - Receiver must be initializer by calling vi.

- switch_control.vi
  - Set arbitrary positions on switches.
  - Switch equipment settings are hard-coded here.

- switch_control_DUT.vi
  - Set arbitrary positions on switches.
  - Switch equipment settings are hard-coded here.

- switch_control_with_pos.vi
  - Set arbitrary positions on switches and reads all switch states.
  - Switch equipment settings are hard-coded here.

- USBBinaryDACcontrol.vi
  - Converts analog channel voltages from (USBDiffDACcontrolHittite.vi) to bits, and sends to the DAC.

- USBDACstop.vi
  - Sends all 0's to the given channel DAC (disables DC bias of VM -¿ no VM output power)

- USBDiffDACcontrolHittite.vi
  - Converts I/Q voltages from (IQsettingsHittite.vi) into differential analog channel voltages.

- VM_Adjust_One_Ch.vi
  - Performs in-line calibration of VM on given channel using two-point interpolation.
  - VM is "properly" set on exit.
  - Marginally slower than single-point most of the time, and usually slightly more accurate.

- VM_Adjust_One_Ch_single.vi
  - Performs in-line calibration of VM on given channel using single-point shift.

- VM is “properly” set on exit.
- Marginally faster than two-point interpolation most of the time, and slightly less accurate.

- VM_Adjust_Two_Ch.vi
  - Performs in-line calibration of VM on both channels using two-point interpolation.
  - VMs are “properly” set on exit.
  - Marginally slower than single-point most of the time, and usually slightly more accurate.

- VM_Adjust_Two_Ch_single.vi
  - Performs in-line calibration of VM on both channels using single-point shift.
  - VMs are “properly” set on exit.
  - Marginally faster than two-point interpolation most of the time, and slightly less accurate.

- VM_CH_Characterization.vi
  - Initializes sig gen and spectrum analyzer for (SF_Channel_Char.vi), and stores calibration data to files.

- VM_Stop.vi
  - Disables output of both VMs. Sends all zero’s (hard stop).

- VM_Stop_CH1.vi
  - Disables output of channel 1 VM. Sends all zero’s (hard stop).

- VM_Stop_CH2.vi
  - Disables output of channel 2 VM. Sends all zero’s (hard stop).

- WriteDataFile.vi
  - Stores a vertical 1D or 2D data array to a file with a text comment, label array, and current time.

- WriteDataFooter.vi
  - Writes the current time to a file, and ends file with a ‘-’.

- WriteDataHeader.vi
  - Writes a text comment, current time, and label array to a file.

- WriteDataLine.vi
  - Writes a horizontal 1D data array to a file.

B.3 Sweep Files

- OneTone_Cancel_FreqSwp.vi
  - Automated frequency linear sweep using (OneTone_Cancellation_Harmonics.vi)
  - Sweeping cancellation measurement vi, stores data to file.

- SpectrumSweep.vi
  - Automated frequency linear sweep, grabs power spectrum for fundamental from spectrum analyzer.
  - Sweeping measurement vi, no VM control, stores data to file.

- SpectrumSweep_Harmonics.vi
  - Automated frequency linear sweep, grabs power spectrum for fundamental + harmonics from spectrum analyzer.
  - Sweeping measurement vi, no VM control, stores data to file.

- Timing_Test_SingleCh.vi
  - Grabs power spectrum from spectrum analyzer at given intervals. Enables sig gen for a given channel.
  - Sweeping measurement vi, no VM control, stores data to file.

- Timing_Test_TwoCh.vi
  - Grabs power spectrum from spectrum analyzer at given intervals. Enables sig gen for both channels.
  - Sweeping measurement vi, no VM control, stores data to file.

- TwoTone_FreqSwp.vi
  - Automated frequency linear sweep using (TwoTone_Cancellation_Simple.vi).
  - Sweeping cancellation measurement vi, stores data to file.

- TwoTone_LogDeltaSwp.vi
  - Automated tone frequency separation log sweep using (TwoTone_Cancellation_Simple.vi).
  - Sweeping cancellation measurement vi, stores data to file.

- VM_Sweep_Phase.vi
  - Sweeps the vector modulator phase to measure amplitude variation, with optional in-line calibration.
  - Sweeping measurement vi, stores data to file.

- VM_Sweep_Phase_Adv.vi
  - Sweeps the vector modulator phase to measure amplitude variation, with optional combined power measurement and in-line calibration.
  - Sweeping measurement vi, stores data to file.

- VM_Sweep_Phase_Cancel.vi
  - Automated vector modulator phase sweep using single channel canceller. Vector modulator phase is inserted as reference phase 1 in the canceller.
  - Sweeping cancellation measurement vi, stores data to file.

Appendix C

MATLAB functions

C.1 Nonlinear Intermodulation

The function "nonlinear_series.m" is a time-domain simulation of the simple nonlinear functions in Section 2.2.2. Time-stepping is less than one-tenth the period of the input sinusoids and runs for thousands of cycles. A high-fidelity fast-Fourier-transform is performed on the output signal to produce the spectra in Figures 2.1 and 2.2.

```
function nonlinear_series
% Simple nonlinear intermodulation
% Used to produce Figs. 2.1 and 2.2

close all hidden; clear all; clc;

dt = 0.5e-2;
t = 0:dt:1000; % time stepping

f1 = 10; f2 = 12; w1 = 2*pi*f1; w2 = 2*pi*f2; % tone frequency
A1 = 1; A2 = 1; % tone amplitude
phi1 = 0; phi2 = 0; % tone phase
phi1 = phi1/180*pi; phi2 = phi2/180*pi;

s1 = A1*cos(w1*t+phi1); % input tone 1
s2 = A2*cos(w2*t+phi2); % input tone 2

% x_in = s1; x = x_in; % single tone input
x_in = s1+s2; x = x_in; % two tone input
```

```
x = 1/10*(x).^5; % nonliner function

L = length(t); dt = t(2)-t(1);
Fs = 1/dt; NFFT = 2^22; % FFT variables

Y_in = (fft(x_in,NFFT)/L); % perform FFT on input signal
f = Fs/2*linspace(0,1,NFFT/2+1);
Ymag_in = 2*abs(Y_in(1:NFFT/2+1));

subplot(1,2,1); plot(f,20*log10(abs(Ymag_in)), 'LineWidth',2)
axis([0 80 -40 5])
xlabel('Frequency (Hz)'); ylabel('Input Signal Amplitude (dB)');

Y = (fft(x,NFFT)/L); % perform FFT on output signal
f = Fs/2*linspace(0,1,NFFT/2+1);
Ymag = 2*abs(Y(1:NFFT/2+1));

subplot(1,2,2); plot(f,20*log10(abs(Ymag)), 'LineWidth',2)
axis([0 80 -40 5])
xlabel('Frequency (Hz)'); ylabel('Output Signal Amplitude (dB)');

end
```

C.2 Projected Cancellation from Amplitude-to-Phase Error

The function "ampl_to_ph_err.m" computes the degraded cancellation resulting from an amplitude offset or amplitude noise in the phase-shift equation, (3.2), at every possible phase separation between the feedforward signal and the signal to be cancelled. The mismatched amplitude is used to generate new values of α and β, then the phase-shift equation is used to calculate a phase offset with the new values. This phase offset is compared to the theoretical offset, and the error is inserted into the achievable cancellation equation, (3.1), to produce the maximum theoretical analog cancellation versus phase separation as shown in Fig. 3.2.

```
function ampl_to_ph_err
% Determines degraded cancellation resulting
%   from amplitude mismatch in phase-shift
%   equation.
```

```
% Produces Fig. 3.2

close all hidden; clear all ;clc;

phase_sep = 0:1:180; % phase sweep stepping (degrees)

ampl_err_db = [0.001 0.01 0.05 0.1]; % amplitude mismatch parameters
alpha = 10.^(ampl_err_db/20);

% determine "correct" phase shift
correct_ph = 2*acosd(sqrt((1+cosd(phase_sep'))/2));

% determine beta/2alpha using ampl. mismatch
a = (alpha/2).^2;
b = 1/4+1/2*cosd(phase_sep')*alpha;
for i=1:length(phase_sep)
    c(i,:) = b(i,:)+a;
    for j=1:length(alpha)
        if c(i,j) > 1
            c(i,j) = 1;
        end
    end
end
wrong_ph = 2*acosd(sqrt(c)); % determine "new" phase shift after
    ampl. error
ph_err = abs(wrong_ph - [correct_ph correct_ph correct_ph correct_ph
    ]);
ph_err_cp = -10*log10(2*(1-cosd(ph_err)));

for i=1:length(alpha)
    ph_ampl_err_cp(:,i) = -10*log10(1+alpha(i)^2-2*alpha(i)*cosd(
        ph_err(:,i)));
end

plot(phase_sep,ph_err_cp);
xlabel('Phase Separation (Deg)'), ylabel('Analog Cancellation (dB)')
    ;
```

```
38 legend({'0.001 dB (a)','0.01 dB (b)','0.05 dB (c)','0.1 dB (d)'});
39 set(gca,'XTick',0:45:180);
40
41 end
```

C.3 Calculated Modulation Tone Power

The function "AM_PM_compare.m" computes the theoretical modulation tone power for the vibratory modulation forms discussed in Chapter 4. The Doppler phase modulation tones are computed using the appropriate Bessel function (4.16). Tones from special relativity amplitude modulation, (4.32), and path loss modulation, (4.49), are calculated using the first ten terms of the full series expansion. For rocking amplitude modulation, only the lowest-order Bessel term in (4.63) is used for each tone.

```
1  function AM_PM_Compare
2  % Computes theoretical modulation tone power (dBc) from Table 4.1
3  % Produces Figs. 4.4 and 4.5
4
5  close all hidden; clear all; clc;
6
7  w_max = 10; % highest order tone to calculate
8
9  c = 3e8; f = 900e6; fv = f/9e5; % radar parameters
10 lambda = c/f; k = 2*pi/lambda;
11
12 beta = 3e-2*lambda; % vibration amplitude
13 D0 = 3*lambda; % standoff distance
14
15 % AM (RCS)
16 a = 0.9*lambda; % RCS parameters
17 varphi_deg = 2; varphi = varphi_deg/180*pi;
18 kay = k*a*varphi;
19
20 for n = 1:w_max % tone sweep
21     AM_RCS(n) = 0;
22     i = 0;
23     AM_RCS(n) = AM_RCS(n) + besselj(2*i+1+n,kay);
```

```
24      AM_RCS(n) = AM_RCS(n)*4/(kay);
25  end
26  AM_RCS = abs(AM_RCS/2); % from RF mixing
27  AM_RCS_dB = 20*log10(AM_RCS);
28  AM_RCS_dB = [0  0  AM_RCS_dB];
29
30  % AM (Path Loss)
31  B = beta/D0; % path-loss parameter
32  for n = 1:w_max % tone sweep
33      AM(n) = 0;
34      for i=0:10
35          AM(n) = AM(n) + (i+1)*(B/2)^(2*i)*nchoosek(2*i+1+n,i+1);
36      end
37      AM(n) = AM(n)*2*(B/2)^n;
38  end
39  AM = abs(AM/2); % from RF mixing
40  AM_dB = 20*log10(AM);
41
42  % AM (Relativity)
43  K = beta*2*pi*fv/c; % Spec. Rel. parameter
44  for n = 1:w_max % tone sweep
45      AMr(n) = 0;
46      for i=0:10
47          AMr(n) = AMr(n) + (K/2)^(2*i)*nchoosek(2*i+n,i);
48      end
49      AMr(n) = AMr(n)*4*(K/2)^n;
50  end
51  AMr = abs(AMr/2); % from RF mixing
52  AMr_dB = 20*log10(AMr);
53
54  % PM (Doppler)
55  for n = 1:w_max % tone sweep
56      PM(n) = (besselj(n,2*k*beta));
57  end
58  PM = abs(PM);
59  PM_dB = 20*log10(PM);
60
```

```
% Plot comparison between modulation types
TN = 0:2:10;
plot(PM_dB,'Marker','s','MarkerSize',10); hold all;
plot(AMr_dB,'Marker','^','MarkerSize',10); hold all;
plot(AM_dB,'Marker','o','MarkerSize',10); hold all;
plot(TN,AM_RCS_dB(2:2:end),'Marker','v','MarkerSize',10); hold all;
legend('PM (Doppler)','AM (Special Relativity)',...
    'AM (Path Loss)', 'AM (Rotational)')
xlabel('Tone Number, \it{n}');
ylabel('Normalized Modulation Tone Amplitude (dBc)');
axis([1 5 -250 0]);
plot([0,10],[-140 -140],'LineWidth',2.5,'LineStyle','--')

% AM (RCS) - 0.1 degrees
a = 0.9*lambda;
varphi_deg = 0.1; varphi = varphi_deg/180*pi;
kay = k*a*varphi;
for n = 1:w_max
    AM_RCS(n) = 0;
    AM_RCS(n) = AM_RCS(n) + besselj(1+n,kay);
    AM_RCS(n) = AM_RCS(n)*4/(kay);
end
AM_RCS = abs(AM_RCS/2); % from RF mixing
AM_RCS_dB = 20*log10(AM_RCS);
AM_RCS1_dB = [0 0 AM_RCS_dB];

% AM (RCS) - 1 degree
a = 0.9*lambda;
varphi_deg = 1.0; varphi = varphi_deg/180*pi;
kay = k*a*varphi;

for n = 1:w_max
    AM_RCS(n) = 0;
    AM_RCS(n) = AM_RCS(n) + besselj(1+n,kay);
    AM_RCS(n) = AM_RCS(n)*4/(kay);
end
AM_RCS = abs(AM_RCS/2); % from RF mixing
```

```
AM_RCS_dB = 20*log10(AM_RCS);
AM_RCS2_dB = [0 0 AM_RCS_dB];

% AM (RCS) - 6.6 degrees
a = 0.9*lambda;
varphi_deg = 6.6; varphi = varphi_deg/180*pi;
kay = k*a*varphi;

for n = 1:w_max
    AM_RCS(n) = 0;
    AM_RCS(n) = AM_RCS(n) + besselj(1+n,kay);
    AM_RCS(n) = AM_RCS(n)*4/(kay);
end
AM_RCS = abs(AM_RCS/2); % from RF mixing
AM_RCS_dB = 20*log10(AM_RCS);
AM_RCS3_dB = [0 0 AM_RCS_dB];

% AM (RCS) - 10 degrees
a = 0.9*lambda;
varphi_deg = 10; varphi = varphi_deg/180*pi;
kay = k*a*varphi;

for n = 1:w_max
    AM_RCS(n) = 0;
    AM_RCS(n) = AM_RCS(n) + besselj(1+n,kay);
    AM_RCS(n) = AM_RCS(n)*4/(kay);
end
AM_RCS = abs(AM_RCS/2); % from RF mixing
AM_RCS_dB = 20*log10(AM_RCS);
AM_RCS4_dB = [0 0 AM_RCS_dB];

% Plot comparison between rotational vibration amplitude
figure; plot(PM_dB,'Marker','s','MarkerSize',10); hold all;
TN = 0:2:10;
plot(TN,AM_RCS1_dB(2:2:end),'Marker','^','MarkerSize',10); hold all;
plot(TN,AM_RCS2_dB(2:2:end),'Marker','o','MarkerSize',10); hold all;
plot(TN,AM_RCS3_dB(2:2:end),'Marker','v','MarkerSize',10); hold all;
```

```
135 plot(TN,AM_RCS4_dB(2:2:end),'Marker','d','MarkerSize',10); hold all;
136 hl = legend('PM (Doppler)','$$\varphi$$ = 0.1$$^\circ$$', ...
137     '$$\varphi$$ = 1$$^\circ$$','$$\varphi$$ = 6.6$$^\circ$$', ...
138     '$$\varphi$$ = 10$$^\circ$$');
139 xlabel('Tone Number, \it{n}');
140 ylabel('Normalized Modulation Tone Amplitude (dBc)');
141 axis([1 8 -200 0]); set(hl,'Interpreter','latex')
142
143 end
```